Modelling the dispersion of a passive tracer in complex open channel flows using random walk, particle tracking techniques

Barry Gwyn Hankin, Bsc

This thesis is submitted for the degree of Doctor of Philosophy
at Lancaster University

February, 1995

Abstract

A random walk, particle tracking model is used to study the dispersion characteristics of passive tracers in three different turbulent shear flows of varying geometric and hydrodynamic complexity.

The first half of the thesis is concerned with the application of random walk models to observations of two flows in the Flood Channel Facility at Hydraulics Research, Wallingford (an in-bank, 100mm flow depth and an over-bank, 176mm flow depth). A sensitivity analysis was undertaken in which several different random walk models were applied to the data. These were based on different inferences about the Lagrangian fluctuating velocity field. The different random walk models were used, since the actual form of the Lagrangian velocity statistics for an inhomogeneous flow is not known. The random walk models were semi-empirically fitted to the data, such that the macroscale particle distributions were in close agreement with the observed tracer concentration distributions, at a single measurement cross-section. The calibrated random walk models were then used to predict the statistics of the evolving tracer concentration distribution further downstream. It was found that at both the calibration and prediction stages, random walk models based on different perturbations, were able to match the observed concentration distributions to within the estimated experimental uncertainties. This property will hereinafter be referred to as equifinality.

In the second half of this thesis, a random walk, streamtube-based particle tracking model is used to study the dispersion characteristics of the flow in a meander bend of an upland gravel-bed river. A fieldwork campaign was undertaken in which measurements of velocity, turbulence statistics and rhodamine tracer mass-flux distributions from a dye-tracer experiment, were collected. These measurements were analysed and used to calibrate the random walk model using the same technique as for the channel flows. It was again found that the model could be calibrated such that the particle distributions matched the observed relative tracer mass flux distributions to within the estimated uncertainties.

Acknowledgements

The author wishes to extend his deepest gratitude to Keith Beven for his guidance, ideas and insights into physical and conceptual modelling. Thanks also to Harriet Orr, I.F.E. for shared and sometimes extremely exciting fieldwork. Thanks also to Adrian Kelsey for fluid dynamics discussions, and to Walt for the same, plus his expertise with field equipment. Thanks to Paul Carling at I.F.E. for the the use of field equipment. Thanks to Hannah Green for information francais pour le Fluorimeteur. Thanks to Adrian Morgan, Miranda Foster, Jenny McArthur, Neil Thomasson, Adrian Kelsey and Walt for help with fieldwork on the River Lune. Thanks to Charles Blakely for assistance with field equipment. Thanks to Ian Guymer for the Flood Channel Facility tracer data. Thanks to Walt, Adrian Kelsey and Kev Buckley for their assistence with computing in general. Finally thanks are due to all who have worked (and lived) in and around room A532 over the last 3 years.

Nomenclature

symbol	meaning
a	constant
A	constant of integration
A_1, A_2, A_3	empirical constants
b	spacing between velocity measurements
B_V	ratio of area under concentration distribution curve at any depth to the area under the same curve at measurement site closest to the surface.
B_1, B_2, B_3	empirical constants
B	magnetic field
C	concentration of a passive, conservative tracer or as a constant in equation 1.43
c	mean (time averaged) concentration
c'	fluctuating concentration
c_d	depth average concentration.
c_∞	concentration of well mixed tracer.
C_{KO}	Kolmogorov/Obukhov constant
Cov(t,H)	Covariance of fast fractional Gaussian noise, of dimension H
ch1-ch4	measured channel potentials
chu,chv,chw	channel potentials corresponding to u,v,w velocities
ct,st	calibration and sample temperature
d	displacement height
d.u.	digital unit
D_{50}	b diameter of bed material for which 50% of material has smaller diameter
D	diameter
e_x, e_y	downstream /transverse dispersion coefficients
E(k)	Energy spectrum
E_u, E_v	electromotive forces (electric potentials)
E_x, E_y, E_z	dispersivity coefficients
f_U, f_V, f_W	variable parameters- multipliers to downstream, transverse and vertical step sizes
$f_1 - f_6$	coefficients
F	body force per unit volume
F_i	Force acting on particle i.
F( )	function of
F.O.D.	factor of diffusion in partial cumulative discharge diffusion equation.
F_{max}	maximum frequency
$F_{corrected}, F_{signal}$	temperature corrected and uncorrected measurement of fluorescence
G( )	function of.
k	wave number

K	downstream dispersion coefficient for 1d flow
K_{ij}	kinetic energy per unit mass tensor
h	channel / water depth
H	scaling exponent
L	length scale
L_L	Eulerian integral length scale
L.B.,R.B.	Left and right banks
L.H.S./R.H.S.	Left hand side/ right hand side
m	mass flux of tracer
m_i	mass flux input
m_x, m_y, m_z	metric coefficients
M_x, M_y	number of knots linking splines in bi-cubic spline approximations in x and y directions
M_i, N_i	values of splines
n	number of steps in a random walk or as a suffix meaning in the normal direction a surface
N	number of particles
N_b	index corresponding to right bank
N_M	number of measurement sites
N_r	number of discretised intervals in y direction within one streamtube.
N_S	number of active degrees of freedom.
Nvw	Total number of combinations of f_V and f_W in optimisation of objective functions
O( )	to the order of ...
obj1,obj2,obj3	objective functions.
P	pressure
P( )	probabiltiy of ...(distribution defined)
P_{ij}	spline coefficients
Q	discharge
Q_{meas}	discharge on day of velocity measurements
Q_{tracer}	discharge on day of tracer experiment
Q_e	source discharge
q	discharge per streamtube
q_c	partial cumulative discharge
r'	non-dimensional radius of curvature of projected particle path
r_{UV}	correlation coefficient for u',w' fluctuating velocities
r_U, r_V, r_w	autocorrelations in the u',v' and w' fluctuating velocity time series
R( )	Correlation coefficient
R_{ij}	Correlation tensor
R_e	Reynolds number
s	variance (specified)
s(x,y)	surface fitted to a 2d velocity field.
S	parameter to determine extent of approximation to a bi-cubic spline approximation

t	time coordinate
t'	dummy time variable
t_1, t_2	specified times
Δt	small time interval/step
T	time scale
T_L	Lagrangian integral timescale
T_E	Eulerian time scale
T_{ECM}	1/e time constant derived from fluctuating velocity time series measured using E.C.M.
T_{tracer}	1/e time constant derived from fluctuating concentration time series measured using the flurometer.
T_{uu}, T_{vv}, T_{ww}	estimated 1/e time scales from u,v,w fluctuating velocity time series
u	vector velocity.
u,v,w	downstream, cross stream, vertical time averaged mean velocities.
u_d	depth averaged velocity.
u_n	velocity component normal to surface.
U,V,W	downstream, cross stream, vertical velocities.
u_{depth}	depth averaged mean velocity
u_{45}	mean velocity component measured at 45 degrees to the downstream direction
u_X	mean cross stream velocity
u',v',w'	fluctuating downstream, cross stream, vertical velocities
u'',v'',w''	random part of fluctuating downstream, cross stream, vertical velocities
$\overline{u_i' u_j'}$	Reynolds stresses
u'_{ieff}	effective fluctuating velocity
u*	shear velocity
u_∞	free stream velocity
U_{max}	maximum velocity
w''	completely random part of fluctuating velocity.
$w_{effective}$	effective fluctuating velocity, taking into account autocorrelation
x,y,z	Cartesian coordinates
x'	displacement of particle
Δx	size of single step in random walk
y_{min}, y_{max}	boundaries in y direction
Y_L, Y_R	left and right streamtube boundaries
Zo	roughness height
z'	non dimensional length in boundary layer
z''	non dimensional length in viscous sublayer
δ	boundary layer thickness
δ_{ij}	Dirac delta function

$\Delta( )$	preceding an observable, this implies the estimation of the uncertainty in that observable
ε	energy dissipation per unit mass
ε_x, ε_y, ε_z	eddy diffusivity components.
ϕ	angle
$\phi_{1\text{-}7}$	coefficients in first order autocorrelation equation.
γ	intermittency.
η	non dimensionalised partial cumulative discharge or a random number taken from a normal Gaussian distribution with zero mean and unit variance
κ	Von-Karman constant
κ_m	molecular diffusivity
κ_t	turbulent diffusivity
λ	scaling constant
ν	kinematic viscosity of water
ρ	density of water
σ	standard deviation from the mean
$\sigma_{w'}$	standard deviation from mean for fluctuating velocity field, w'.
σ_{model}, σ_{data}	estimations of the spread in the particle and concentration distributions
τ	shear stress
τ_{xy}, τ_{zy}	components of the Reynolds shear stresses.
τ_b	bed shear stress.
ω	angular velocity.
ω_1	downstream vorticity component.
ξ	non dimensionalised downstream distance

List of Figures for chapters 1-9.

Chapter 1 : Classical fluid dynamics and tracer dispersion.

Chapter 2: Random walk models and their application to complex flows.

Chapter 3: Description of velocity and tracer concentration measurements in the Flood Channel Facility, Wallingford.

Chapter 4: Sensitivity analysis of different random walk models using the measurements from the Flood Channel Facility.

Chapter 5: Field measurements of velocities, turbulence and tracer dispersion in a meander bend of an upland gravel bed river (River Lune).

Chapter 6: Analysis of field measurements from the River Lune.

Chapter 7: Construction of a random particle tracking model based on streamtubes to simulate the observed dispersion of a passive tracer in the River Lune.

Chapter 8: Sensitivity analysis of a random particle tracking model of the tracer dispersion characteristics in the reach of the River Lune.

Chapter 9: No figures

List of Tables for chapters 1-9.

Chapter 1 and chapter 2 : No tables

Chapter 3: Description of velocity and tracer concentration measurements in the Flood Channel Facility, Wallingford.

Chapter 4: Sensitivity analysis of different random walk models using the measurements from the Flood Channel Facility.

Chapter 5: Field measurements of velocities, turbulence and tracer dispersion in a meander bend of an upland gravel bed river (River Lune).

Chapter 6: Analysis of field measurements from the River Lune.

Chapter 7: Construction of a random particle tracking model based on streamtubes to simulate the observed dispersion of a passive tracer in the River Lune.

Chapter 8: Sensitivity analysis of a random particle tracking model of the tracer dispersion characteristics in the reach of the River Lune.

Contents: chapters 1-9.

Chapter 4: Sensitivity analysis of different random walk models using the measurements from the Flood Channel Facility.

Chapter 5: Field measurements of velocities, turbulence and tracer dispersion in a meander bend of an upland gravel bed river (River Lune).

Chapter 6: Analysis of field measurements from the River Lune.

Chapter 7: Construction of a random particle tracking model based on streamtubes to simulate the observed dispersion of a passive tracer in the River Lune.

Introduction.

The research which is presented in this thesis is concerned with the understanding of pollutant dispersion in rivers; which placed in context, is a small but important aspect of water quality control. The management of river water quality is vital for both our good health and the health of the complex natural ecosystems which exist in and along the river corridors. This provides more than a sufficient gravamen to undertake the following research.

Recent integrated catchment management approaches, which have lately been adopted by bodies such as the National Rivers Authority have recognised the inescapable interconnectedness of river usage. The intensity of modern-day agricultural and industrial techniques, along with the domestic waste produced by a large population, puts an enormous strain upon water resources. The natural capacity of a river to dilute and 'make safe' our waste can easily be exceeded, a concept which has only relatively recently been acknowledged. Every effort should therefore be made to understand each stage of water quality control, in order that techniques can be used to minimise the harm to the human (and therefore social) and natural environment, which are intimately connected.

Computer models of river mixing can be used as aides to the understanding of the transportation, accumulation and eventual transformation of the pollutants which we create as residuals from one or other process. Bodies which require to use such models to predict the mixing of pollutants include the waste disposer (water company), the water quality regulator (National Rivers Authority), the water resources scientist, fishery scientists and aquatic botanists and ecologists. However, there are many

complex natural processes which control the dispersion rates of pollutants in rivers, of which turbulence, topographic effects and non-linear interactions are the most significant. These factors make a quantitative description of river mixing difficult, and as a result predictive modelling has large uncertainties associated with it. Moreover, there are no exact solutions to the equations which govern the mixing of pollutants in a river flow, and so direct physical modelling is often supplemented using empiricism. This gives a model a more conceptual, rather than mathematically rigorous basis. Semi-empirical models require the calibration of parameters, and it is generally true to say that the fewer parameters which are used, and which are therefore required to be calibrated, the less the fieldwork is required, and therefore costs are kept low. All of the above mentioned groups generally require a simple, but flexible predictive technique with which to analyse the mixing problems, and the random walk model used in this thesis is suggested to meet these requirements.

In random walk particle tracking models, thousands of particles representing fluid elements are advected under the influence of a simulated mean flow field, whilst being subjected to random perturbations to simulate the effects of turbulence. In order to calibrate the models, the sizes of the perturbations are adjusted at the particle scale, until the large scale ensemble particle distributions are in agreement with the measured concentration distributions at sites downstream.

In this study, the models were first investigated in an artificial channel flow (at the Flood Channel Facility, Hydraulics Research, Wallingford) and were calibrated and then tested predictively against what was considered to be the most accurate set of hydrodynamic and tracer dispersion data available (so far as is known at the time of

writing). Having undergone testing on the channel flows, the random walk model was applied to a more complex, natural flow in a bend of an upland gravel bed river.

For each of the above flows the study concentrated on the mixing of the dye immediately after release, before it becomes fully mixed. It is in this region, just after an outfall or spillage enters the river, that the highest concentrations of the pollutant exist, and where the most damage to aquatic organisms and the ecosystem occur.

The first chapter forms a review of literature pertaining to the fluid dynamics of a turbulent flow, and to the dispersion of a passive tracer within it, which lays the foundations for the assumptions which were made in the modelling work. The second chapter describes the principles of random walk models and their mode of application to complex flows.

In chapters three and four, the random walk model was applied to the aforementioned flume flows. Several different models which made different inferences about the form of the velocity perturbations were investigated within this well defined flow domain. Many of the different models could be calibrated simply by altering the sizes of the perturbations in the random walk, and that the random walk was sufficiently versatile to account for the effects which the massive range of scales of motion in the flow had upon the tracer dispersion. Further, many of the models were successful in predicting the tracer distributions to within estimated experimental uncertainties for two different flume geometries.

The random walk model was then applied to the more complex natural flow in the bend of a typical upland gravel bedded river (the River Lune) in chapters five to eight. Chapter five describes the velocity and tracer experiment measurements which

were made on the river bend during the course of this research. The analysis of these measurements was described in chapter six, and the measurements were used in chapter seven to describe the construction of a mean flow model based upon the framework of streamtubes.

The eighth chapter describes a sensitivity analysis of the random particle tracking model. It was found once more that the model could be calibrated to fit the observed concentration distributions to within the estimated uncertainties.

Chapter nine forms a summary and discussion of chapters 1 to 8 and outlines the potential for future work. Here it is suggested that a momentum-exchange particle tracking model is a natural and desirable predecessor to mass transport modelling using random particle tracking techniques. The construction of a parallel computer-based momenta exchange algorithm is alluded to in chapter 9, as a suggestion for future work.

Chapter 1

Classical fluid dynamics and tracer dispersion.

1.1 Introduction.

This chapter is split up into three principal sections, which deal with the classical equations of fluid motion, the equations of mass continuity for a passive pollutant and the hydrodynamics of river flows.

Section 1.2 describes the classical equations of fluid motion. The Reynolds number and the significance of the non-linear term in the momentum conservation equation are described. The difficulty in constructing a numerical model for a high Reynolds number flow has lead to many different approximate models of the equations of fluid dynamics. Some of these modelling techniques are investigated since they shed light on the underlying physics of the fluid motion.

Section 1.3 describes the advective diffusion equation for a passive tracer in turbulent flows. The different assumptions and approximations which have to be made when the equations are applied to realistic flows are discussed. The concept of streamtubes is introduced, and solutions to the cumulative discharge diffusion equation are examined since they can be compared with solutions from the random particle tracking model, which is used in the major part of the modelling studies used here.

Section 1.4 describes some aspects of the hydrodynamics of channel and river flows which are relevant to this study. The use of the logarithmic equation of the wall to model vertical velocity profiles is described. Finally, section 1.5 summarises this

chapter, and indicates where the different pieces of classical theory have been drawn upon in later chapters.

1.2 The Equations of fluid motion

The two principal conservation laws in fluid mechanics are expressed in terms of the rates of change of mass and momentum per unit volume of the fluid. This draws upon the continuum hypothesis, which supposes that there is a continuity in these quantities from point to point. This in turn necessitates a definition of the spatial resolution of the equations, and in fluid mechanics this means the smallest volume of fluid which can be attributed the macroscopic properties (such as density, temperature, etc.) of the fluid in bulk. The relevant scale is greater than the scale at which the erratic molecular motions are resolvable, yet smaller than the scale at which the macroscopic quantities of the flow vary appreciably due to external influences.

The equations described in the following sections are applicable to a Newtonian fluid, which is defined as one for which the rate of strain is directly proportional to the applied shear stress.

1.2.1 The Navier Stokes and mass continuity equations

The continuity equation is a statement of the law of conservation of mass for a volume of fluid within the flow domain. It equates the mass flux of the fluid across the closed surface of the volume of fluid, to the rate of change in the mass of that volume of fluid in time, and is given by equation 1.1:

$$\frac{\partial \rho}{\partial t} + \frac{\partial (\rho U_i)}{\partial x_i} = 0 \qquad (1.1)$$

where U_i are the three orthogonal components of the vector velocity field, U_1,U_2 and U_3 and ρ is the fluid density. The flows which are investigated in this thesis are incompressible, such that the density of the fluid is constant throughout the flow field, and the velocities are small compared to the speed of sound in water. Under these assumptions, (1.1) simplifies to the incompressible form given by equation 1.2:

$$\frac{\partial U_i}{\partial x_i} = 0 \qquad (1.2)$$

The equivalent momentum conservation equation is called the Navier Stokes (NS) equation, which expresses the rates of change of momentum of a fluid element in a frame of reference which follows that fluid element (Lagrangian framework). This is given by the substantive derivative, which expresses the changes in the fluid element's momentum as it moves from place to place in the velocity field, and also as a result of temporal variations in the velocity field. The substantive derivative is given by the bracketed terms in the expression (1.3) below, where it is used as an operator on the momentum per unit volume of a fluid element:

$$\left(\frac{\partial}{\partial t} + U_j \frac{\partial}{\partial x_j} \cdot \right) \rho U_i \qquad (1.3)$$

The rate of change of momentum of the fluid element is equated to the pressure gradient, viscous and external forces acting on it. This balance is expressed in equation 1.4, and is a statement of Newton's second law of motion (e.g.Tritton,1990):

$$\frac{\partial U_i}{\partial t} + U_j \cdot \frac{\partial U_i}{\partial x_j} = -\frac{1}{\rho}\frac{\partial p}{\partial x_i} + \nu \nabla^2 U_i + \frac{1}{\rho}\mathbf{F} \qquad (1.4)$$

where u_i is the velocity of a fluid element, ρ is the fluid density, ν is the kinematic viscosity of a Newtonian fluid, P is the pressure field and **F** represents external forces acting on the fluid.

1.2.2 The Reynolds number

Reynolds demonstrated the existence of two different flow regimes of laminar and turbulent flow (see for example, Acheson, 1990). The laminar flow regime is characterised by smoothly varying flow, where the predominant forces are due to the action of the fluid viscosity. Turbulent flow is characterised by rapidly varying velocity field, with a loss in predictability of the values of flow parameters. The two regimes coexist, and a wide range of flows intermittently switch between the two regimes. Reynold's experiment of 1883 demonstrated the transition of the laminar to the turbulent flow regime in a pipe flow, both regimes being solutions to the NS equation. The difference between the two regimes depends upon the relative importance of the different forces in the NS equation, which can be measured using the ratio of the inertial to the viscous terms as in equation 1.4. Dimensional analysis of this ratio

reduces the ratio to the familiar form of the Reynolds number on the RHS of equation 1.5:

$$\mathrm{Re} = \frac{U_i \,\partial U_j / \partial x_i}{\nu \nabla^2 U_i} \rightarrow \frac{U^2 / L}{\nu U / L^2} = \frac{LU}{\nu} \qquad (1.5)$$

(Acheson,1990). For a slow, viscous flow the non-linear term is relatively unimportant and any perturbations to the flow are rapidly damped out by the action of viscosity. However, if the inertial forces are large, then the non-linear term becomes important and the motion becomes highly unpredictable and results in turbulence.

1.2.3 The non-linear term in the Navier Stokes equations

The non-linear term in equation 1.4 (second term on the L.H.S.) is responsible for the spreading of the kinetic energy of the motion between the continuum of scales present in the flow. Every scale of motion can essentially interact with any other scale of motion. Small disturbances may become amplified by the mean flow causing greater instability, and it is this form of interaction which leads to the transition from laminar to turbulent flow. Moreover, this form of mean flow - driven instability is an important mechanism in the momentum exchange between the bed and the bulk of the flow in fully developed turbulence.

At the smallest scales of motion the action of viscosity turns kinetic energy into heat, which acts as a sink to the turbulent energy (see for example, Tritton,1990). This dissipation requires a continual supply of kinetic energy down to the small scales from

the large energy producing scales. If the flow is in equilibrium then the transfer of energy through the energy cascade must also be in equilibrium with the dissipation.

The non-linear term in the Navier Stokes equation essentially leads to loss of predictability of the flow and sensitive dependence on initial and boundary conditions. This makes the measurement of observables (for examples velocity, temperature) at the same point in a flow unrepeatable so the only information which can be used to characterise the flow must be statistical in nature.

1.2.4 Numerical modelling of the Navier Stokes equations

There is no general analytical solution to the NS equations, although they have been solved numerically for some small scale or specialised flows (e.g. Marcus and Bell, 1994). The understanding of fluid dynamics has consequently relied upon a large amount of experimental work, and numerous approximations to the terms in the NS equation in order to make more soluble equations.

The difficulty of forming a numerical solution to anything other than the simplest flow is exemplified by investigating the number of degrees of freedom in a high Reynolds number flow, which must be resolved in the numerical problem. Each of these degrees of freedom have spatio-temporal constraints (boundary conditions) which must also be accounted for in the numerical model. The vast number of dynamically significant scales of motion varies from the heat dissipation scales to the characteristic scales of the flow domain. The number of active degrees of freedom can be approximated as the ratio of the largest scales to the smallest scales of motion,

which can be expressed in terms of the Reynolds number (Frisch and Orzag,1990), given by equation 1.6:

$$N_S \approx \mathrm{Re}^{9/4} \qquad (1.6)$$

where N_S is the number of degrees of freedom per unit volume. For the river flow which is studied in later chapters, where Re ~ 50000, the number of degrees of freedom per unit volume is approximately: 4^{10} .The problem is compounded by the absence of any distinct separation of scales in turbulence (Bowles, 1994).

If a single degree of freedom requires a single grid point in a numerical model, then reversing the relationship in equation 1.6, the Re number of the flow which can modelled increases by less than the square root of N_S (McComb, 1991). Clearly numerical modelling of large Re number flows is likely to remain an intractable for some time to come, despite enormous advances in computing power.

This justifies further the simplifications and approximations to the governing equations of fluid motion which will be discussed in sections below.

1.2.5 Kolmogorov scaling

Kolmogorov postulated that intermediate scales of motion could be considered as being solely dependent on the flux of energy from larger to smaller scales. These intermediate or inertial sub-range scales become independent of viscosity for fully developed turbulence, a phenomenon called Reynolds number similarity. With this

assumption, the Navier Stokes equations are invariant if the distance, velocity and time are dependant on a length scale, λ in the way given by equations 1.7:

$$l \to \frac{l}{\lambda}, \quad u \to \frac{u}{\lambda^H}, \quad t \to \frac{t}{\lambda^{1-H}} \qquad (1.7)$$

where H is a scaling exponent. Kolmogorov scaling theory requires that average quantities are scale invariant although infers nothing about the finer structure such as the form of the distributions which the velocity fluctuations take (Lovejoy and Schertzer, 1992). The energy flux per unit mass, ε, passing through an intermediate scale, l, is assumed to depend only on l and observables local to it. Given that the dimensions of the energy flux are energy per unit mass per unit time, the energy dissipation per unit mass is given by equation 1.8:

$$\varepsilon \approx \frac{v_l^3}{l} \qquad (1.8)$$

where v_l is the velocity at scale l. Inserting the scalings given in 1.7 into equation 1.8, gives equation 1.9:

$$\varepsilon \to \frac{\varepsilon}{\lambda^{3H-1}} \qquad (1.9)$$

However, if ε is assumed to be scale invariant in the inertial sub-range, this demands that H = 1/3 (Frisch and Orszag,1990). Given the value of H = 1/3, the scaling properties of other observables such as the energy spectrum can be derived. The energy spectrum (E) expresses the kinetic energy per unit mass as a function of wave number (k), and is an important quantity in the study of homogeneous turbulence.

Essentially, the energy spectrum gives the contribution to the kinetic energy per unit mass from the different length scales (associated with eddies) of motion present in the flow. Using Kolmogorov scaling, and the value of H = 1/3, the energy spectrum scales in accordance with equation 1.10, otherwise known as the Kolmogorov-Obukhov(KO) law:

$$E(k) = C_{KO}\varepsilon^{2/3}k^{-5/3} \qquad (1.10)$$

where C_{KO} is a scaling coefficient. This has been found to be in agreement with measurements in high Reynolds number, homogeneous flows in many instances (for example Grant et al.,1962).

Kolmogorov originally used the scaling law to investigate the local velocity structure functions, rather than the energy spectrum. However, the energy spectrum assumes length scales (or Fourier modes) which are global to the entire flow and are therefore only truly represented in a homogeneous flow. The Fourier representation cannot be extended to describe inhomogeneous turbulence, where the velocity structure (functions) can vary from place to place. Studies have moved towards new representations of the spectra of inhomogeneous flows in order that the KO law might be studied for this more general flow (for example, Moser,1994).

Despite the close agreement of experiment with the KO law reported above, the assumption that ε is invariant is not theoretically an exact description due to the intermittent nature of turbulence. This is explained by considering that intermittency results in there being active and inactive eddies present at all scales. At the smaller scales, the ratio of active to inactive regions is smaller than at larger scales of motion,

which requires that a greater energy flux per unit volume occurs in the smaller scales - in contradiction to the hypothesis of invariant energy flux. Corrections to the theory point towards a scaling exponent slightly larger than 5/3 in equation 1.10 (Tritton, 1990).

Further, corrections to the theory have been made by considering that structures within the flow scale with a range of values of H, each structure comprising a fractal set with dimension dependent on H (Frisch and Orzag,1990). This multifractal approach has met with some success and can be incorporated into the Lagrangian framework, as will be described in later sections. The scaling theory does not give any information about the sizes of the constants in equations, such as C_{KO} in 1.10.

1.2.6 Reynolds averaging

To represent the turbulent fluctuations in the flow, statistical quantities are introduced to equations 1.1 and 1.4 by decomposing the observables into statistical time averaged mean and fluctuating components in a process called Reynolds decomposition in accordance with equation 1.11:

$$U_i = u_i + u_i' \qquad (1.11)$$

Inserting (1.11) into (1.2) yields different statistical combinations of u_i and u_i' which are assumed to follow the linear Reynolds averaging rules (Tennekes and Lumley,1972) in accordance with equations 1.12:

$$\overline{u'_i} = 0$$
$$\overline{u_i u_j} = \bar{u}_i \bar{u}_j + \overline{u'_i u'_j} \qquad (1.12)$$
$$\overline{u'_i u_j} = 0$$

For the case when the averages are time averages, substitution of 1.12 in equation 1.4, gives the Reynolds averaged Navier Stokes(RNS) equations, which for statistically steady homogeneous flows gives equation 1.13 (where the external body forces in 1.4 have been removed for simplicity) :

$$\frac{\partial u_i}{\partial t} + u_j \cdot \frac{\partial u_i}{\partial x_j} = -\frac{1}{\rho}\frac{\partial p}{\partial x_i} + \nu \nabla^2 u_i - \frac{\partial \overline{u'_i u'_j}}{\partial x_j} \qquad (1.13)$$

(for example, see Speziale,1985).The last term on the RHS expresses the rate of change of the time averaged product of u'_i and u'_j , called the Reynolds stress tensor. The different products must be estimated in order that (1.13) become fully 'closed', a process which is described in the next section.

1.2.7 The closure problem

There has been a considerable amount of effort gone into closing the RNS equations (see Speziale,1985; Younis, 1992; for reviews of closure models, and a clear description of the problem in McComb, 1990). The problem arises because there is no complementary equation to 1.13 which defines the non-linear term without using higher order products of the fluctuating velocities. These higher order terms have equations which can only be stipulated in terms of even higher order terms, and so on.

As a consequence of the closure problem, finite difference modelling of the RNS equations has to make a compromise between accuracy (i.e. the order in u_i to which the closure is made) and computation time. The greater the order in u_i at which the closure is made, so the finer the scales which can be resolved with accuracy.

The closure problem is closely related to the problem of determining the scales of the displacements or velocity fluctuations in a random walk, which will be discussed in later chapters.

1.2.8 The Lagrangian Integral Time Scale (T_L).

The location, X, of a fluid particle with velocity U in a stationary homogeneous and isotropic turbulent velocity field, is defined by the integral of the particle velocity over the time t of interest, given by equation 1.14:

$$X(t) = \int_0^t U dt \qquad (1.14)$$

where the frame of reference is chosen such that the time averaged mean value of U is zero. The ensemble averaged value of the square of particle displacement for a large number of particles experiencing the same velocity field can be written in terms of the autocorrelation function R(s), given by equation 1.15 (Taylor, 1921):

$$\left\langle X^2(t) \right\rangle = 2\left\langle U^2 \right\rangle \int_0^t (t-s) R(s) ds \qquad (1.15)$$

where s is a time lag between consecutive observations, and the angled brackets represent ensemble averaged quantities. The autocorrelation function is defined by equation 1.16:

$$R(t-0) = \langle U(t)U(0)\rangle / \langle U^2\rangle \qquad (1.16)$$

From the assumption that the autocorrelation function approaches zero as time approaches infinity, the expectation of the square of the particle position (the variance of the particle positions over time t), approaches the value given in equation 1.17 (Fischer et al.,1979):

$$\langle X^2\rangle \rightarrow 2\langle U^2\rangle T_l.t + const. \qquad (1.17)$$

where the quantity T_L is the Taylor integral time scale given by equation 1.18:

$$T_L = \int_0^\infty R(t)dt \qquad (1.18)$$

From 1.17, it can be seen that, following the Lagrangian time scale, the variance of the particle position will grow linearly with time. T_L is also called a decorrelation time scale, since it is a measure of the average time it takes a particle to forget its initial velocity (Fischer,1979).

1.2.9 Taylor's hypothesis

Taylor's frozen turbulence hypothesis assumes that the rate at which an eddy deforms is much slower than the rate at which it is being advected past a fixed point (Taylor, 1938). This hypothesis can be used to estimate Eulerian length scales from single point velocity integral time scales, and can be expressed in terms of the fluctuating velocity, and the variance of the fluctuating velocity of different particles passing a fixed position, given by equations 1.19:

$$L_L = \frac{U}{\sigma_{u'}^2}\int_0^\infty \overline{u'(t)u'(t+s)}ds$$
$$L_L \approx \langle U \rangle T_L \qquad (1.19)$$

where $\sigma_{u'}$ is the standard deviation from the time averaged mean of the fluctuating velocity, and <U> is the mean downstream velocity. This provides an estimate of the length scale associated with the spatial decorrelation (Raupach et al.,1991), otherwise called the Taylor integral length scale, L_L.

1.3 Dispersion of a passive tracer.

When a passive tracer is injected into an open channel flow, the cloud of tracer evolves in two main stages. Initially, the tracer mixes well in the vertical and the concentration distribution is drawn out longitudinally due to the vertical velocity gradient. Simultaneously, the pollutant has been stretched out in the longitudinal

direction due to the transverse velocity gradients, but due to the cross-stream dimension being relatively large, the pollutant takes a longer period in order to mix well in the cross sectional direction.

These actions create a concentration gradient within the cloud, across which the turbulent diffusive mixing becomes important during the second stage of mixing, often called the Taylor period. The equations which describe the tracer dispersion in this stage, are described in section 1.3.2.

1.3.1 The gradient flux hypothesis

Molecules in a free gas obey the Fickian diffusion relationship, whereby the flux of molecules in a given direction is proportional to the concentration gradient of the molecules in that direction, given by equation 1.20:

$$m = -\kappa_m \frac{\partial C}{\partial x} \qquad (1.20)$$

where κ_m is the constant of molecular diffusivity, m is the mass flux of particles in the x direction and C is the concentration of molecules. This linear relationship is only true if there are distinct length and velocity scales which are universal to the entire medium (Fischer,1979). This is the case for a cloud of molecules, since there are distinct length and velocity scales associated with the mean free path, and mean molecular velocity.

The mass flux of molecules out of an element Δx represents a temporal change in the concentration, expressed by the balance:

$$\frac{m(x+\Delta x,t)-m(x,t)}{\Delta x}_{\lim \Delta x \to 0} = \frac{\partial m}{\partial x} = -\frac{\partial C}{\partial t} \qquad (1.21)$$

inserting 1.20 into 1.21 gives equation 1.22, which is called the diffusion equation:

$$\frac{\partial C}{\partial t} = \kappa_m \frac{\partial^2 C}{\partial x^2} \qquad (1.22)$$

1.3.2 Equation of mass continuity for an advecting passive scalar.

The substantive derivative used in section 1.2 is now applied to a conservative (non decaying), passive scalar (one which has indistinguishable physical properties to the carrier fluid) within a turbulent flow. The continuity equation, is simply a balance between advective and diffusive motions of the tracer, given by equation 1.23:

$$\frac{\partial C}{\partial t} + U\nabla C = \kappa_m \nabla^2 C \qquad (1.23)$$

where $C = C(\underline{x},t)$ is the concentration of the dispersing tracer, determined by the turbulent velocity field $U = U(\underline{x},t)$ and molecular diffusivity κ_m (e.g. Sullivan and Chatwin,1993).

This equation is insoluble for all but the most simple flows, since both the concentration and velocity fields are vector fields with random components, and again

the products of the fluctuating parts of each field must be estimated. This requires knowledge of the complete velocity field, and once more the closure problem is encountered. For this reason, approximate solutions must again be looked for.

1.3.3 Reynolds averaging the mass continuity equation.

Equation (1.23) is now Reynolds decomposed and time averaged as with the Navier Stokes equation, which produces products like $\overline{u'c'}$, which are required to be estimated once more. Since these terms represent a flux of tracer, the gradient flux hypothesis is often drawn upon to form the closure, whereby an analogy is made with molecular diffusion, to give equations 1.24 (the tensor notation for the velocities is dropped for clarity from heronin, $u = u_1$, $v = u_2$ and $w = u_3$):

$$\overline{u'c'} = -\varepsilon_X \frac{\partial c}{\partial x} \quad \overline{v'c'} = -\varepsilon_Y \frac{\partial c}{\partial y} \quad \overline{w'c'} = -\varepsilon_Z \frac{\partial c}{\partial z} \qquad (1.24)$$

where ε_X, ε_Y and ε_Z are called the eddy diffusivities in the x, y and z directions respectively. These are fundamentally different to the molecular diffusivity, since they are a property of the flow and not the flow medium. The use of eddy diffusivities assumes a distinct separation of length and velocity scales in the turbulent flow. This is a great simplification of the actual case, since there is a continuum of scales of motion, which are all interacting due to the non-linear terms in the NS equations, as discussed earlier in section 1.2.4.

These eddy diffusivities form a linear closure to the transport equation, although in regions of the flow where the Reynolds stresses and the velocity gradient do not share the same zeros, such an eddy diffusivity becomes singular (Younis, 1992) and the model breaks down. The development of solutions to, for example, the Reynolds stress transport equations overcomes this particular problem but requires much more computational power, and inevitably higher order closures, so have consequently only been used in some specialised flows (e.g. So et al. ,1991).

The closed, time averaged advective diffusion equation is now given by equation 1.25:

$$\frac{\partial c}{\partial t}+u\frac{\partial c}{\partial x}+\mathrm{v}\frac{\partial c}{\partial y}+\mathrm{w}\frac{\partial c}{\partial z}=\frac{\partial}{\partial x}\left(\varepsilon_x\frac{\partial c}{\partial x}\right)+\frac{\partial}{\partial y}\left(\varepsilon_y\frac{\partial c}{\partial y}\right)+\frac{\partial}{\partial z}\left(\varepsilon_z\frac{\partial c}{\partial z}\right) \qquad (1.25)$$

This equation has been further simplified in many different studies and applied to various flows (see for example Chatwin and Allen, 1985). The most fundamental approach was that of Taylor(1954) for pipe flow, and Elder(1959) for an infinitely wide two dimensional flow, concerning the one dimensional dispersion of a well mixed tracer in a homogeneous flow. This analysis is well documented in Fischer (1979). The most important consequence of Taylor's analysis when applied to a shear flow, is that after the tracer has become well mixed in the vertical and cross-stream directions in a homogeneous isotropic flow, there is a balance between the downstream dispersion due to the velocity gradients and the diffusive action of turbulence in the cross-stream direction. The balance is expressed in terms of a one-dimensional advection diffusion equation (such as equation 1.22), with a downstream longitudinal dispersion

coefficient. However, for complex river flows, the flow is generally anisotropic, inhomogeneous and there are large secondary advections (flow perpendicular to the downstream direction) giving rise to enhanced longitudinal dispersion characteristics (for example see Beltaos, 1981). For river flows, the mixing is inescapably three dimensional (Rutherford,1994) in the near-field (the region between the tracer becoming vertically well mixed and well mixed in the transverse dimension) and mid-field (the region where the tracer is released until it becomes vertically well mixed). In the far-field (the region following complete vertical and transverse mixing), Taylor's one-dimensional analysis can be applied, since the large scale secondary advections become associated with the stochastic mixing on the scale of a very long reach.

This study is concerned with an examination of the near-field and principally the mid-field dispersion characteristics. Clearly, in these regions Taylor's hypothesis does not hold, and the analysis is required to be three or possibly two-dimensional. Nonetheless, it is clearly important to make use of any simplifying procedures which ultimately would result in equations which would make physical sense in three-dimensions, while only requiring the measurements of bulk flow parameters (Knight et al., 1989).

The next section discusses some of the simplifications to the Reynolds averaged advection diffusion equation which are relevant to the application of the advection diffusion equation to a complex channel flow.

1.3.4 Two and three-dimensional mixing models

Where the channel topography is changing or there is curvature, there is also transport by transverse velocities (for example see Rutherford ,1994). Further, under these non-uniform flow conditions, plots of concentration versus transverse distance do not necessarily conserve mass across a transect (Yotsukura and Sayre, 1976). Concentration versus transverse distance curves are often skewed and shifted in the transverse direction. The skewness arises primarily from the non-uniform distribution of flow across the channel, whereas the lateral displacement is due to transverse advective transport (Holley, 1971).

The true distribution of tracer in a non-uniform flow has to be examined in terms of the mass flux distribution in order to conserve mass and avoid this skewing effect. This can be achieved by examining the transverse distributions of the product, cq, (where q is the partial cumulative discharge integrated from the bank). Holley et al.(1972) derived a method for evaluating the longitudinal dispersion coefficient based upon measurements of the solute fluxes at different cross sections based in Cartesian co-ordinates, which took into account secondary advection. Yotsukura and Cobb (1972) suggested an alternative approach which simplified the analysis, whereby concentration is calculated as a function of partial cumulative discharge (which also maintains mass conservation). This approach was generalised by Yotsukura and Sayre (1976) into orthogonal curvilinear co-ordinates which are more adaptable to complex natural geometries.

The equation of mass continuity and the advective diffusion equation have so far been written in Cartesian co-ordinates, which are not very suitable for the complex geometries of natural flows. For this reason, the equations of mass conservation and mass transport are re-written in curvilinear co-ordinates (Yotsukura and Sayre, 1976) to give equations 1.26 and 1.27:

$$\frac{\partial}{\partial x}(m_y u) + m_x m_y \frac{\partial w}{\partial z} + \frac{\partial}{\partial y}(m_x v) = 0 \qquad (1.26)$$

$$m_x m_y \frac{\partial c}{\partial t} + \frac{\partial}{\partial x}(m_y cu) + m_x m_y \frac{\partial}{\partial z}(cw) + \frac{\partial}{\partial y}(m_x vc) = \frac{\partial}{\partial x}\left(\frac{m_y}{m_x}\varepsilon_x \frac{\partial c}{\partial x}\right) + m_x m_y \frac{\partial}{\partial y}\left(\varepsilon_z \frac{\partial c}{\partial z}\right) + \frac{\partial}{\partial y}\left(\frac{m_x}{m_y}\varepsilon_y \frac{\partial c}{\partial y}\right) \qquad (1.27)$$

where u,v,w are the local mean velocity components, ε_X, ε_Y and ε_Z are the local turbulent mass diffusivities in the downstream, cross-stream and vertical directions, c is the local mean solute concentration and all these quantities have been time averaged over a suitable record length. The coefficients, m_x, m_y and m_z are metrics which account for changes along one basis due to changes along the other bases; m_z is unity since the vertical axis is always perpendicular to the other two axes. These equations can be reduced to two-dimensional form by integrating each term over the depth, the details of which are given in Rutherford (1994). The depth integrated equations (1.28 and 1.29) are given here in full, since they contain the products to which approximations are then made in the case of non-uniform channel flow.

$$m_x m_y \frac{\partial h}{\partial t} + \frac{\partial}{\partial x}(m_y h\langle u\rangle) + \frac{\partial}{\partial y}(m_x h\langle \mathrm{v}\rangle) = 0 \qquad (1.28)$$

$$m_x m_y \frac{\partial}{\partial t} h\langle c\rangle + \frac{\partial}{\partial x}(m_y h\langle uc\rangle) + \frac{\partial}{\partial y}(m_x h\langle \mathrm{v}c\rangle) = \frac{\partial}{\partial x}\left(\frac{m_z}{m_x} h\left\langle \varepsilon_x \frac{\partial c}{\partial x}\right\rangle\right) + \frac{\partial}{\partial y}\left(\frac{m_x}{m_y} h\left\langle \varepsilon_y \frac{\partial c}{\partial y}\right\rangle\right) \qquad (1.29)$$

The angle brackets in these equations represent depth-averaged quantities. The products such as <uc> and $< \varepsilon_x \partial c/\partial x >$ are approximated by applying the Reynolds averaging procedure, making use of equations 1.30 :

$$\langle uc\rangle = \langle u\rangle\langle c\rangle + \langle u'c'\rangle$$
$$\left\langle \varepsilon_x \frac{\partial c}{\partial x}\right\rangle = \langle \varepsilon_x\rangle \frac{\partial\langle c\rangle}{\partial x} + \left\langle \varepsilon_x' \frac{\partial c'}{\partial x}\right\rangle \qquad (1.30)$$

where the prime here denotes deviation of local values from the depth-averaged value. The covariance term (<u'c'>) was then approximated using a gradient flux term, of the form used by Taylor (1954) and Elder(1959), given by equation 1.31:

$$\langle u'c'\rangle = -\frac{E_x}{m_x}\frac{\partial\langle c\rangle}{\partial x} \qquad (1.31)$$

where E_x is a dispersivity coefficient expressing the net effect of differential advection by u' coupled with vertical turbulent diffusion. The covariance term, in 1.30, $\left\langle \varepsilon_x' \frac{\partial c'}{\partial x}\right\rangle$,

is eliminated, under the assumption that the vertical variability of the longitudinal diffusion coefficient is negligible. The last two equations are then combined to give the single mixing coefficient, e_x:

$$\frac{e_x}{m_x}\frac{\partial < c >}{\partial x} = \frac{1}{m_x}\left\langle \varepsilon_x \frac{\partial c}{\partial x} \right\rangle - \langle u' c' \rangle$$

where (1.32)

$$e_x = \langle \varepsilon_x \rangle + E_x$$

where e_x is the longitudinal coefficient of dispersivity, which includes the combined effects of depth averaged turbulent diffusion and advective dispersion. Similar approximations are made in the transverse direction, to produce a transverse dispersivity coefficient, e_y. The resulting equations in curvilinear co-ordinates are given by equations 1.33 and 1.34:

$$m_x m_y \frac{\partial h}{\partial t} + \frac{\partial}{\partial x}(m_y h < u >) + \frac{\partial}{\partial y}(m_x h < v >) = 0 \qquad (1.33)$$

$$m_x m_y \frac{\partial}{\partial t}(h < c >) + \frac{\partial}{\partial x}(m_y h < u >< c >) + \frac{\partial}{\partial y}(m_x h < v >< c >) = \frac{\partial}{\partial x}\left(\frac{m_y}{m_x} h \left\langle e_x \frac{\partial c}{\partial x} \right\rangle\right)$$

$$+ \frac{\partial}{\partial y}\left(\frac{m_x}{m_y} h \left\langle e_y \frac{\partial c}{\partial y} \right\rangle\right) \qquad (1.34)$$

These equations have been solved numerically for a number of flows (see in Elhadi et al., 1984), but do not as yet have general analytical solution.

For the case of a continuous, steady release of tracer, in a river with a steady flow, these equations lose the time derivatives, and the turbulent-diffusive mixing in the downstream direction becomes small compared to the downstream mixing due to differential advection. The first term of equation 1.33 is set to zero, and the advective diffusion equation becomes equation 1.35, for which the angled brackets for the depth averaged concentration and velocity have been dropped for clarity:

$$\frac{\partial}{\partial x}(m_y huc) + \frac{\partial}{\partial y}(m_x hvc) = \frac{\partial}{\partial y}\left(\frac{m_x}{m_y} h\left\langle e_y \frac{\partial c}{\partial y}\right\rangle\right) \qquad (1.35)$$

which again has no analytical solution, but has been solved numerically (see Elhadi et al.,1984).

1.3.5 A streamtube model

Equation 1.35 has the form of an advective diffusive equation, which can be further simplified into a diffusion equation from the transformation of the transverse co-ordinate (y) to the cumulative discharge, q_c, given by equation 1.36:

$$q_c = \int_0^y m_y h U_d dy \qquad (1.36)$$

where q_c is the cumulative discharge, integrated from the left bank, and where U_d is the depth averaged velocity. Carrying out this transformation of 1.36 gives equation 1.37, called the partial cumulative discharge diffusion equation:

$$\frac{\partial C}{\partial x} = \frac{\partial}{\partial q_c}\left(Uh^2 m_x E_y \frac{\partial C}{\partial q_c}\right) \qquad (1.37)$$

Where the product, $\left(Uh^2 m_x E_y\right)$, is referred to as the factor of diffusion (FOD). The FOD varies across the channel for most natural streams, which implies that the equation can only be solved numerically (Lau and Krishnappan, 1981).

However, if the FOD is assumed to be constant across the cross section, a rough solution can be determined from the analytical solution (Elhadi et al., 1984). The solutions still account for the transverse advections to some extent.

1.3.6 Solutions to the cumulative discharge diffusion equation

Analytical solutions to the equations exist for a point source located at one bank, and for a continuous line source, stretching across the river to a width marking a specified fraction (r) of the total discharge at the input (Elhadi et al.,1984). The second solution is examined here since it is relevant to the study carried out on the river Lune, and is given by equation 1.38:

$$\frac{c}{c_\infty} = \frac{1}{2r}\left[erf\frac{(r-\eta)}{\sqrt{2\xi}} + erf\frac{(r+\eta)}{\sqrt{2\xi}} + \sum_{m=1}^{\infty} image \quad sources\right] \qquad (1.38)$$

where the image sources are given by equation 1.39 :

$$image \quad sources = \sum_{i=1}^{\infty}\left[erf\frac{2i+r-\eta}{\sqrt{2\xi}} + erf\frac{2i+r+\eta}{\sqrt{2\xi}} - erf\frac{2i-r-\eta}{\sqrt{2\xi}} + erf\frac{2i-r+\eta}{\sqrt{2\xi}}\right] \tag{1.39}$$

and $c_\infty = M/Q$ is the concentration far downstream after the tracer has been completely mixed across the stream. M is the mass of tracer injected per unit time, Q is the total discharge of the stream, $\eta = q_c / Q$, is the normalised cumulative discharge, and $\xi = 2\frac{FOD}{Q^2}x$ is a dimensionless distance.

These solutions have been normalised and plotted in fig.1.1 for different values of the transverse dispersivity coefficient (e_y varied, while all other terms in the FOD held constant) for a reach having cross sectional average quantities corresponding to the study reach examined in chapters 4-8, as an example. The finer details to these plots will be given in chapter 8.

1.4 The hydrodynamics of channel and river flows.

1.4.1 Modelling the vertical velocity profile.

1.4.1.1 The turbulent boundary layer.

The turbulent boundary layer can be divided into three regions in which different length scales are predominant; a division which has been supported by numerous observations (Young, 1989). There is a region very close to the wall where the fluid is at rest due to the non slip condition, which arises due to the viscous forces.

However these are short range forces acting over a length scale of the order ν/u^* (the viscous length scale, where u^* is the friction velocity), beyond which the inertial forces of the main body of the fluid flow become more important.

Moving further away from the influence of the viscous forces, there is an inner region of the boundary where the flow is influenced by velocity scales of the order of the size of the friction velocity, u^*, and a set of length scales characterising the surface roughness and the distance away from the boundary. The outer region, or the remaining 60-80% of the entire boundary region is governed by the friction velocity and length scales of the same order of magnitude as the boundary layer thickness, δ.

The Reynolds stresses are large in the inner region, giving rise to 80-90% of the total turbulent energy production within the boundary layer (Tennekes and Lumley,1972). The region is therefore characterised by continuous turbulent activity, with an intermittency, γ, of unity (where γ is defined as the fraction of the time that the flow is turbulent as oppose to laminar). The inner layer thickness depends on the relative roughness (the ratio of the roughness height to the flow depth) of the flow, but is generally considered to extend to 0.1 - 0.4 δ.

In the outer region, turbulent production drops off and γ decreases to zero at about 1.2 δ, making it difficult to define the precise location of the edge boundary layer.

The inner layer logarithmic law and the outer layer velocity defect law are derived here from asymptotic analysis, which is applicable for both smooth and rough walls (Raupach et al.,1991). The flume flows under study here are smooth walled, but the river flow to be studied later is rough walled with a large relative roughness, so both approaches are addressed here.

1.4.1.2 Smooth walled case

For the smooth walled case, the only length scale of importance in the inner region arising from surface effects is the viscous length scale, to give equation 1.40 by dimensional analysis:

$$\frac{u}{u^*} = F\left(\frac{zu^*}{\nu}\right) \tag{1.40}$$

where u* is the friction velocity. In the outer region, scale effects of the order of the boundary layer thickness, δ, are thought to be prevalent, which gives equation 1.41 by dimensional analysis:

$$\frac{u - u_\infty}{u^*} = G\left(\frac{z}{\delta}\right) \tag{1.41}$$

where u_∞ is the free stream velocity. In the intermediate zone between the two regions, the profile must be continuous, and since the regions do not have any independent parameters in common, the gradients must be constant. The gradients are matched in the intermediate zone using equations 1.42:

$$\frac{\partial u}{\partial z} = \frac{\partial G}{\partial \eta}\frac{\partial \eta}{\partial z} = \frac{\partial F}{\partial \xi}\frac{\partial \xi}{\partial z} = \frac{1}{\kappa}$$
$$\text{where} \quad \eta = \frac{z}{\delta}, \xi = \frac{zu^*}{\nu} \tag{1.42}$$

which when integrated gives equation 1.43 for the inner layer :

$$\frac{u}{u*} = \frac{1}{\kappa}\ln z' + C \qquad (1.43)$$

where z' is the non-dimensionalised depth, and it has been found experimentally, that for smooth walls the integration constant C ~ 5.5 (Allen (1982) used C=5.5 in the construction of a flow domain for a particle tracking model).

1.4.1.3 Rough walled case

Where the roughness of the boundaries is significant, length scales which are representative of the roughness height, roughness element shape and spacing must be considered as scales which can shape the turbulence within the inner region. Moreover, the process of 'eddy shedding' (bursting) of fluid close to the boundary, whereby patches of high vorticity move up through the water column, are thought to influence the outer region as well as the inner (Krogstadt, 1992). Dimensional analysis of parameters relevant to the inner layer for a rough boundary gives equation 1.44:

$$\frac{u}{u*} = F\left(\frac{\nu}{u*}, h, L_i\right) \qquad (1.44)$$

where L_i is the set of length scales characterising the roughness elements and their spacing and h is the roughness height.

The roughness causes the whole flow profile to be displaced upwards by an amount d, the displacement height. It has been shown (Raupach et al., 1991) that d is approximately the mean height of momentum absorption of the wall. However, it is rather difficult to measure, and the most obvious method of ascertaining its value, by fitting the velocity profile to the data set, has been shown to be inaccurate (Raupach et al., 1991).

If an analysis of the vertical velocity gradient, similar to that for the case of the smooth boundary, is carried out for the rough boundary, then a logarithmic shape results once again for the inner layer (Raupach et al.,1991), with the difference that the constant C in equation 1.42 is now dependent on h and L. The constants are often absorbed by again assuming a roughness length scale Zo, which is then interpreted as the height above the displacement height at which the mean velocity is zero, given by equation 1.45:

$$\frac{u}{u^*} = \frac{1}{\kappa} \ln\left(\frac{z-d}{Zo}\right) \qquad (1.45)$$

However, a more empirical approach has been to try and define a more universal value of the constant. This was first done by Nikuradse in 1933 (cited in Raupach et al., 1991), in measurements of fully developed turbulence over a homogeneous layer of fixed sand grain to give equation 1.46:

$$\frac{u}{u^*} = \frac{1}{\kappa} \ln\frac{(z-d)}{Z_o} + 8.5 \qquad (1.46)$$

Subsequently 'equivalent sand grain roughnesses' (which is the inverse logarithm of the constant 8.5 in equation 1.46) have been defined for different flows.

1.4.1.4 Alternative models for the vertical velocity profile

The vertical velocity profile in natural flows is often a more complicated shape than has been so far discussed in this section, and further degrees of freedom are necessary for a better functional representation such as the S shaped Dean profile (for example see Ferro and Biaimonte, 1994). However, this requires the specification of 4 parameters (as oppose to two for the logarithmic profile). This requires an increased number of measurements.

The logarithmic profile has been used over the entire flow depth in previous studies to describe the flow in curved open channels, despite its strict applicability only to the lower 20% of the flow. The velocity measurements made by Bridge and Jarvis (1976) in a river (The River Esk, Scotland) with similar pool and riffle geometry to the reach of the River Lune under study in later chapters of this thesis, suggested that a large number of velocities throughout the water column fell on the logarithmic profile. The presence of helicoidal flow may increase the value of the von-Karman coefficient, κ, because of the enhanced vertical momentum transfer. Measurements such as those of Anwar (1985), have also shown non-compliance with the logarithmic profile in a meandering flow, thus it is important to ascertain the conditions under which the logarithmic profile might be utilised in a meandering flow.

The influence of the roughness height length scale on the flow throughout the depth has, however, been shown to be non-negligible (Krogstadt 1992) since the phenomenon of eddy shedding carries fluid higher into the water column (whereas Zo is not usually included as a dependent variable in the analysis).

1.4.2 Bursts and Sweeps

The presence of intermittency in turbulent flows has already been mentioned in terms of its effect on the Kolmogorov scaling laws and with its association with the occurrence of periodic 'bursts' of fluid motion arising from instabilities which can be amplified by the mean flow. Early flow visualisation techniques employing the use of hydrogen bubbles showed the presence of coherent streaks of fluid motion in the near bed region of a turbulent boundary layer, which after some period would lift upwards, oscillate, and then become unstable and break up (see McComb, 1990). Such an event belongs to a group of behaviours commonly called bursts and sweeps. These phenomena are rapid, coherent upwards or downwards accelerations of fluid. These accelerations of the fluid correspond to both positive and negative correlations between the vertical and downstream fluctuating velocities in either direction. The positive correlations demonstrate the presence of counter velocity gradient momentum transfer, although this has been found to be less significant in the process of momentum exchange between the bed and the mean flow (Lu and Willmarth, 1973).

The four possible kinds of interaction (up and down acceleration, up and down deceleration) have been studied using quadrant analyses (see Lu and Willmarth, 1973 or Kelsey,1994), whereby the different events are identified from measurements of the

near bed shear stress time series. Measurements have shown that the Reynolds shear stress time series consists of long periods of relative quiescence, interspersed with large scale correlated motions from one of the four categories above. Clearly it becomes difficult to define precisely the duration of any particular event, since there must be some imposed definition of a threshold value of shear stress to signify an event. This also makes it difficult to define the average time between events, important for statistical modelling and for testing theory (Luchik and Teiderman, 1986).

Quadrant analysis of shear stress series which were measured over a gravel bedded section in the West Solent by Williams et al. (1989), demonstrated that on average, ejections and inward interactions, or sweeps and outward interactions each contributed ~ 45% of the total stress in only ~28% of the time.

1.4.3 Secondary circulation

Secondary circulation (fluid flow non-parallel to the downstream direction) drastically influences the distribution of stresses exerted by the flow and its ability to disperse contaminant. There are two principle kinds of secondary circulation (Bathurst et al.,1979):

1. Pressure induced secondary motion (Prandtl's flow of the first kind).
2. Turbulence driven secondary motion (Prandtl's flow of the second kind).

The two flume flows under investigation in chapters 3 and 4 are subject to Prandtl's flow of the second kind, and are the same flows which were investigated by

Knight and Shiono(1989). Prandtl's flow of the first kind dominates the secondary advections in the river flow in chapters 5 to 8, although both kinds of flow are present. Straight channel flow has significant three-dimensional structure, despite the relatively simple geometry, which comprises distinct regions of secondary circulation which will be described fully in chapter 3.

The local differences in the three normal stress components of the Reynolds stress tensor, $\overline{u'u'}, \overline{w'w'}, \overline{v'v'}$, are responsible for the generation of the turbulence driven secondary motion, as demonstrated by looking at the longitudinal component of the vorticity equation which is derived by taking the curl of the NS equation. It is the distribution of $\left(\overline{w'^2} - \overline{v'^2}\right)$ that determines the structure of secondary flows. The vorticity equation is given here for the longitudinal vorticity component, ω_1, by equation 1.47 (Tominaga et al.,1989):

$$v\frac{\partial \omega_1}{\partial y} + w\frac{\partial \omega_1}{\partial z} = \frac{\partial^2}{\partial y \partial z}\left(\overline{v'^2} - \overline{w'^2}\right) - \left(\frac{\partial^2}{\partial z^2} - \frac{\partial^2}{\partial y^2}\right)\overline{v'w'} + \upsilon\left(\frac{\partial^2 \omega_1}{\partial y^2} - \frac{\partial^2 \omega_1}{\partial z^2}\right) \tag{1.47}$$

Where ω_1 is the longitudinal vorticity component $\omega_1 = \frac{\partial w}{\partial y} - \frac{\partial v}{\partial z}$, or more in familiar terms, the secondary circulation. It is generally observed that the viscous term is much smaller than the other terms except very close to boundaries, and can be disregarded. The first, and the difference between the second and third terms are of the same order of magnitude, and it is therefore important to model all three terms if the secondary motion is to be correctly simulated.

The flow cannot be reproduced correctly if modelled using, for example, a Bousinesq stress-strain relationship (Cokljat, 1992), since these predict that the Normal Reynolds stresses $\overline{v'^2}, \overline{w'^2}$ are equal.

A model of the NS equations which could account for turbulence induced secondary circulation would therefore require to use a non-linear eddy viscosity for which the normal stresses are not necessarily equal (Younis, 1992).

Pressure, or skew induced secondary currents occur when cross-stream vorticity (caused by e.g. bed friction) is twisted to produce a component of vorticity about the downstream direction. This arises in the case of meandering channels, where the action of the centrifugal forces give rise to twisting.

1.4.4 Flow through a meander.

The flow in a meander is affected by the upstream and downstream flow conditions. Considering a sufficiently long straight approach reach to a meander, such that there are no remnant secondary flows from meanders further upstream, practically all of the isovels are parallel to the flow direction with the exception of those due to small turbulence induced secondary circulation. Such flows were considered in chapter 1, and can be identified by the bulges towards the banks in the primary isovels which they cause, for example see Anwar (1985).

At the bend entrance the flow encounters the non-uniform pressure distribution resulting from the redistribution of flow in the meander. There is a depression of the water surface at the inner bank, which presents a favourable pressure gradient to water flowing into the bend at the inner bank (Demuren and Rodi, 1986).

There is also, therefore, an adverse pressure gradient near to the outer bank which may cause flow separation at high flows (although this is not always a sufficient condition Tritton, 1990). The depression/elevation is significant and has been measured e.g. for a meandering reach of the River Esk having similar geometry to the section of the Lune under study (Bridge and Jarvis, 1976).

Inside the bend the vertical velocity gradient is differentiated by the action of the velocity-dependent centrifugal force such that faster moving water near the surface experiences a greater acceleration towards the outer bank than the slower water close to the bed (the centrifugal acceleration is proportional to the square of the downstream velocity and inversely proportional to the radius of curvature of the thalweg, u^2/r). This causes the vertical velocity profile to become skewed and induces a downstream component of vorticity, causing secondary circulation. The water near to the outer bank therefore elevates. The slower moving water near the bed moves to replace the water which has moved to the outer bank. The secondary flow shifts the primary isovels so that the velocity maximum moves closer to the outer bank, and the maximum shear stress subsequently follows, though there may be some delay. This arises because the secondary circulation actually inhibits the movement of the water close to the bed towards the outer bank (Bathurst et al., 1979).

The strength of the circulation at any transect in a meander depends on the Reynolds number, the distance of the transect downstream from the bend entrance, the aspect ratio of the channel, the ratios of the radius of curvature to width, and the arc angle of the bend, which are all functions of discharge (Bathurst et al., 1979). Secondary velocities have been measured up to 40-50% of the downstream flow velocity.

Instability of the circulating cell arises when the balance between the transverse pressure gradient and the centrifugal force is temporarily broken, resulting in the large cell to break up into a large and a small cell, with the small cell close to the right bank, circulating in the opposite sense to the main cell. This cell is generally observed when there is a steep outer bank (Bridge and Jarvis 1976).

The strength of the secondary flow rate varies with discharge. It has been observed to be the strongest under medium discharges, because there is a decrease in the bulk centrifugal forces at comparatively high or low flows (Bridge and Jarvis, 1976). It is generally agreed that at high flows the mean flow moves outward from the thalweg and at low flows the mean flow slows down. Both of these cause the centrifugal acceleration (u^2/r) to decrease.

At the bend exit the secondary flow continues to circulate to conserve angular momentum, although viscous effects eventually replace the symmetry in the primary isovels after a distance which depends on the nature of the river. In a series of meanders, the secondary flow can be very sensitive to history effects (Anwar,1985).

1.4.5 Separation

In order for flow to separate away from a boundary, the rate of change of velocity in a direction normal to the boundary surface with respect to that same normal direction must be non-zero and positive, as defined by equation 1.48:

$$\frac{\partial u_n}{\partial n} > 0 \qquad (1.48)$$

where u_n is the component of velocity in the direction n, normal to the surface. This is an analytical result which can be derived from making the two-dimensional boundary layer approximation (e.g. see Tritton,1990). For the large separations observed near to the inner bank of flow entering a meander bend, this inequality arises due to the action of centrifugal forces in the direction normal to the inner bank. When the flow separates, it takes with it strong vorticity into the main flow, generating increased shear and enhanced mixing. The inequality more generally arises due an adverse pressure gradient in the direction of flow, expressed by equation 1.49:

$$\frac{\partial P}{\partial x} > 0 \qquad (1.49)$$

Flow can remain attached in the presence of a small adverse pressure gradients under some situations.

1.5 Summary of classical theory, and applications in future chapters.

This section summarises the different theories which have been described in this chapter, which form a background to the assumptions which were made in later chapters, and gives an indication of where in the following chapters these theories were put to use.

In the first few sections some fundamental equations of fluid motion were examined, giving some insight into the origins of the complexity of fluid flow. The Reynolds number was shown to be indicative of the complexity of a flow, and in later

chapters, it was often used as a scaling factor, for example in the estimation of the thickness of the laminar sub-layer at the bed for the particular flows under study. Further, the number of degrees of freedom was shown to increase rapidly with the Reynolds number, which was used to explain the limitations of the use of direct numerical simulations of complex, high Reynolds number flows, and ultimately explains the need for research into models of a conceptual and semi-empirical nature (a point which is discussed in more detail in the final chapter).

Kolmogorov scaling theory was included because it leads to the important, well studied scaling law (Kolmogorov-Obukhov law) for homogeneous, isotropic turbulence, which provides a useful standard to assess the performance of a conceptual model under idealised conditions. This formed the background to further discussion of the random walk model in chapter 2.

The difficulties associated with direct numerical simulations, and the inapplicability of scaling theories to inhomogeneous flows lead to a discussion of the method of Reynolds averaging and the Reynolds averaged momentum conservation equations. These form the basis of most engineering / environmental flow models, and are expressed in terms of the mean and fluctuating parts to the flow observables. The equations require to be 'closed', by the additional specification of the values of the Reynolds stresses, which generally rely upon the assumption of a gradient-flux type of relationship.

The closure models form the closest counterpart in classical hydrodynamics to the conceptually based random walk models, but lack the simplicity, and are more rigid in their applicability to different flows, especially with the higher order closures.

The Lagrangian integral time scale was defined in terms of the Lagrangian autocorrelation function and is later required to be estimated in order to specify a time step between the perturbations in the random walk models. The spatial decorrelation is recovered via Taylors frozen turbulence hypothesis and in later chapters this hypothesis was for example tacit to the Eulerian measurements of the turbulent time scales using the electromagnetic current meters in chapter 5.

Having described the basic equations governing fluid motion, the dispersion of a passive tracer was then described as the balance between the advection and diffusion of a random vector concentration field. Solving the advection diffusion equation has the same problems associated with it as the momentum conservation equation, since the velocity field must first be resolved in order to solve it. The processes of Reynolds averaging, depth averaging and approximating which followed, ultimately resulted in the formulation of a solution to an approximate form of the advection diffusion equation (the streamtube equation). By this stage, the co-ordinates of the equation had been transformed into partial cumulative discharge and downstream distance, and an effective dispersion coefficient had been prescribed which lumped together the effects of turbulent diffusion and secondary advective transport. The simplified, streamtube equation provided a valuable alternative (if approximate) solution to the analysis of tracer dispersion in the final chapter of this thesis.

The analytical treatment of a turbulent boundary layer in the section following this resulted in the logarithmic equation of the wall, which provided a useful tool in chapters 3 and 7 in the interpolation between point velocity measurements.

Finally, the causes of secondary circulation were described since the section of the River Lune which were studied in chapters 5-8 comprises a single 180 degree

meander bend, in which secondary circulation enhances the mixing rate of a tracer. Previous measurements of transverse mixing coefficients are left until chapter 8.

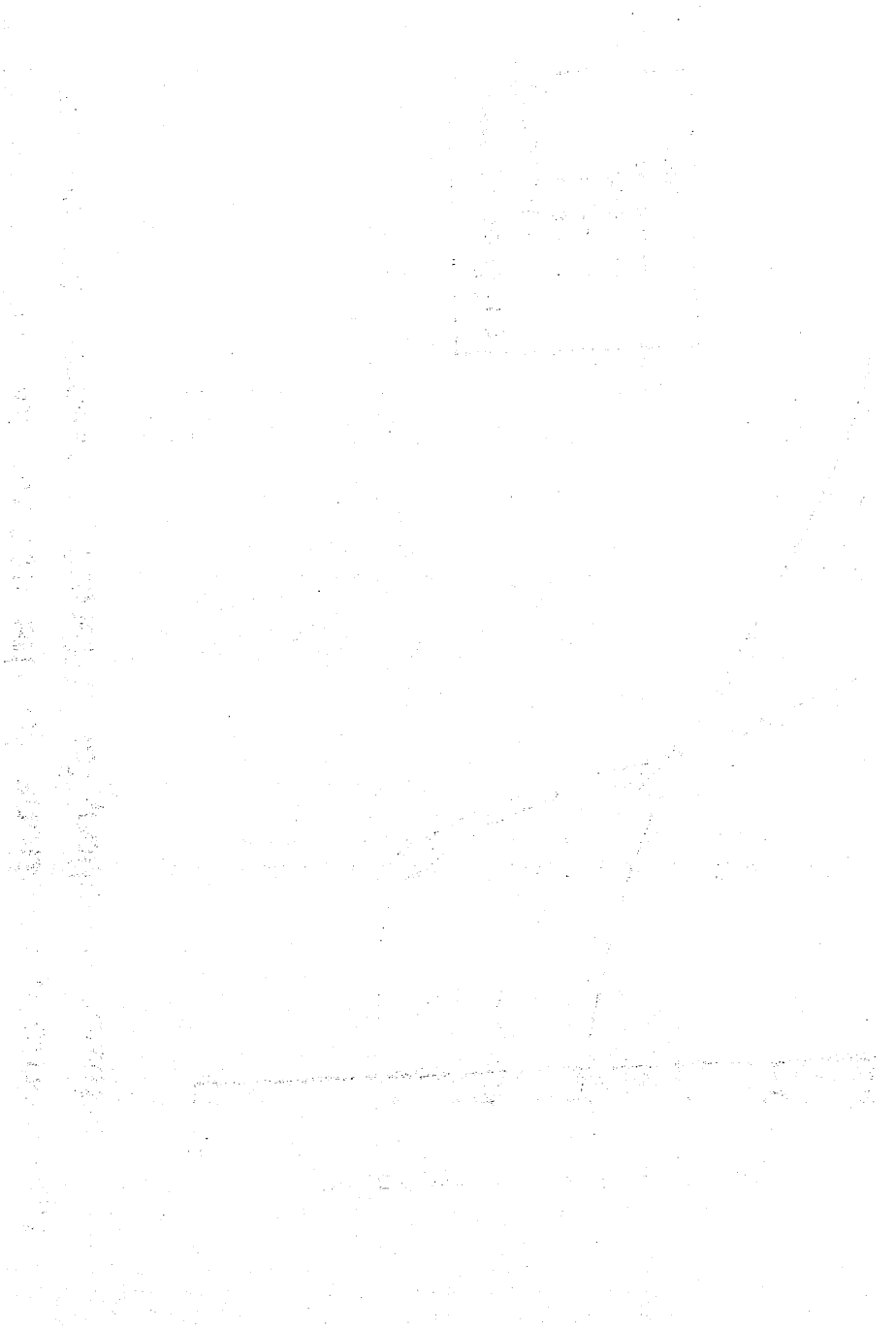

Fig.1.1

Approximate solutions to the partial cumulative discharge diffusion equation, for different transverse diffusivities

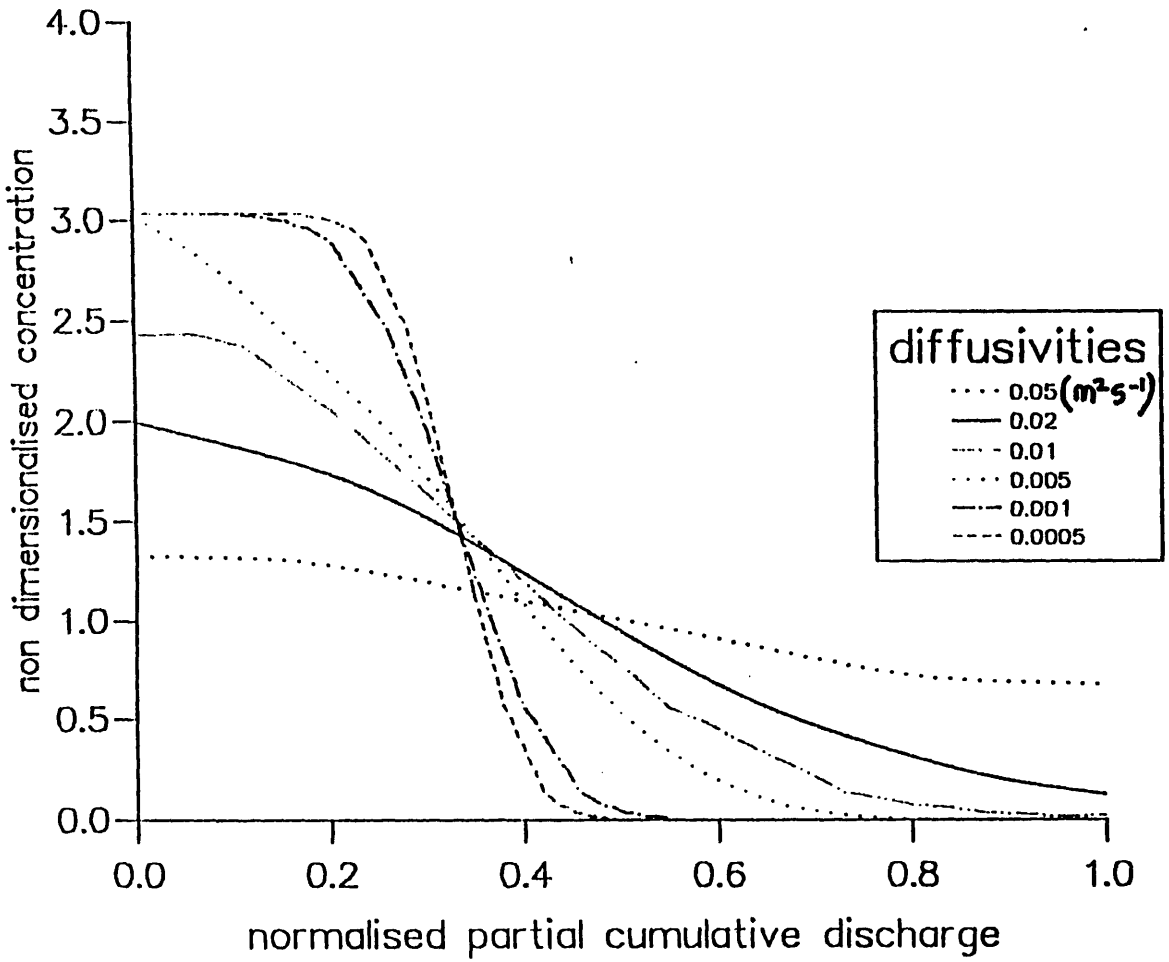

Chapter 2

Random walk models and their application to complex flows.

2.1 Introduction

In the following chapters random particle tracking models are investigated as tools for studying the turbulent dispersion of a passive tracer in several different flows. The imaginary particles undergoing the random walks represent parcels of the fluid which carry the tracer. The various representations of the velocity perturbations which are used in the random walk models described in this chapter draw upon observations and measurements of turbulent motion.

This chapter describes how the random step equation is applied in practice and reviews some of the mathematical properties of random walk models. The implications of applying the model to different kinds of flow, such as non-uniform, inhomogeneous or anisotropic flows are discussed. The random step equation can be formulated such that the particle trajectories include the physical properties observed in fluid flows. Some formulations of the random step equation which have been previously studied are then reviewed.

In section 2.2 the Lagrangian nature of the random walk model is discussed, and the step equation for its application is described. Different properties of single and multiple particles undergoing random walks are then discussed.

Section 2.3 presents the first order Markov chain process which is used (with several different sets of assumptions) as a model for turbulent motion, and several

properties of this type of process are discussed. Section 2.4 discusses further aspects of the application of different random walk models to channel flows.

In section 2.5 the flume geometry for the two different flows is described, since the form of some of the different random walk models which are described in the ensueing sections depend upon it.

Section 2.6 is a description of the different random walk models which are investigated in chapters 3 and 4 in order to test the sensitivity of the large scale dispersion characteristics to the form of the velocity perturbations in the random walk in chapters 3 and 4.

2.2 The random walk model.

2.2.1 Random particle tracking in a Lagrangian framework.

The small scale hydrodynamics of an inhomogeneous turbulent flow play an important part in determining the dispersion of a solute, which makes dispersion a very locally generated phenomenon. In the case of inhomogeneous turbulence a complete picture of dispersion requires a Lagrangian description (Tampieri et al. 1992). However, the parameterisation of Lagrangian particle tracking models is hindered considerably due to the Eulerian nature of most field / flume measurements. Generally the Lagrangian velocity fluctuation variance is assumed to be equal to the Eulerian equivalent (Sawford, 1985), although this is only strictly justifiable for simple homogeneous, isotropic flows. The difficulty with the translation between the two frames arises because the large scales of motion have a sweeping effect on the smaller energy containing eddies and therefore contribute to the correlations measured at a

fixed point. Moreover, there is no generalised theory which defines the extent of the sweeping effect in inhomogeneous turbulent flows. Lagrangian correlations have been measured in small scale turbulent flows using techniques such as particle image velocimetry whereby video images of illuminated particles passing through a laser light sheet are digitised and tracked as described fully in, for example, Perkins and Hunt (1989) or Dalziel (1992). However, it is *large scale flow* Lagrangian measurements in realistic flows which are needed to parameterise the length and time scales for this study.

The random walk has not been derived rigorously from the Navier Stokes equations for inhomogeneous turbulent flows and in these realistic flows it has not been formulated to give an exact solution to the transport equation 1.23 (Van Dop et al 1985). However, it provides a flexible alternative to approximate solutions to the advection-diffusion equation for modelling tracer dispersion, which cannot generally be applied close to a source (in the near field region). Random walk models are exactly mass conserving, and can be applied to the modelling of the dispersion of passive tracers in high Reynolds number, complex turbulence and can take account of inhomogeneneity, unsteadiness and non-Gaussianity in the turbulence velocity distribution (Thomson, 1987). Further, the particle tracking techniques lend themselves well to parallel computing since they are multiple task-orientated, and are potentially more computationally efficient, since calculations only involve marked fluid elements of interest. All of the random walk particle tracking models described here were based on a parallel array of transputers.

2.2.2 The random step equation

For a one dimensional random walk a test particle is repeatedly subjected to randomly orientated displacement, such that there is a 50% probability that the particle will be displaced to the right or to the left at each step. The particle may be considered to be carrying some physical property such as mass (for this study) or momentum from place to place. Fig.2.1 demonstrates an example random walk, where the arrows represent equal probabilities for the two possible orientations at each step.

Fig. 2.1 Schematic diagram of a random walk.

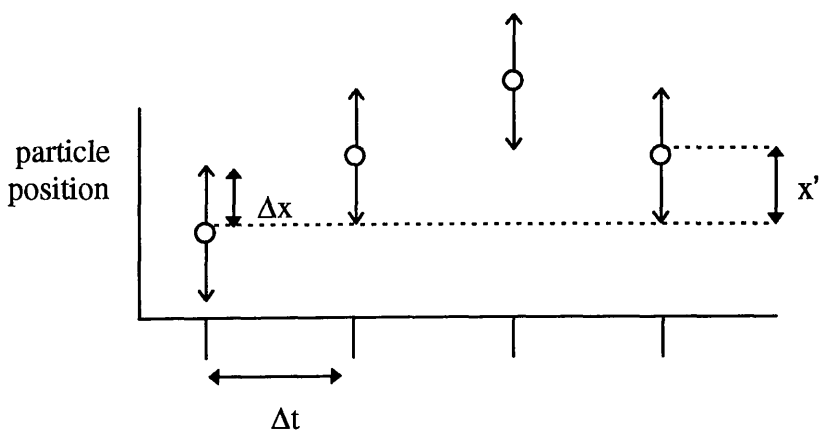

The absisca could equally well be represented by the number of the step from the origin, although it is represented by a cumulative time interval (Δt) between steps here. For the simplified case of one dimension, the net displacement of a particle, x', having undergone a series of random, discrete displacements of distance Δx, in one dimension is described by a symmetric binomial probability distribution P (p), given in equations 2.1:

$$x' = \Delta x \pm \Delta x \pm \Delta x \pm \Delta x \ldots\ldots$$
$$x' = \Delta x(2p - n)$$
where (2.1)
$$P(p) = \binom{n}{p} 0.5^n$$

where p is the number of unit displacements which the particle reaches away from the particle origin after n steps in total.

This distribution rapidly approaches a Normal distribution (Fischer,1979) as the number of displacements surpasses 10 (n=10 gives a fit to second order moments of ~ 2%), although it is only an exact solution to the diffusion equation for an infinitely small time step and an infinite number of steps (Einstein, 1905, cited in van Dam, 1992). It has zero mean and a variance proportional to the number of displacements n, given by equation 2.2:

$$\left\langle \left(x' - \langle x' \rangle\right)^2 \right\rangle = \Delta x^2 n \qquad (2.2)$$

Analogously, the Fickian diffusion equation (1.22) has a solution for a point source, which is a normal Gaussian distribution having a variance which is proportional to t. For comparisons between the two solutions, the time interval is related by: $t = n \Delta t$.

The effective diffusivity for a particle undergoing a random walk is given by equation 2.3:

$$K = \frac{\Delta x^2}{2\Delta t} \qquad (2.3)$$

The next step is to infer that both descriptions can be used to model the rapid, seemingly random motion of turbulence. The most important implication of this is that

it is assumed that there is a distinct separation of turbulent length scales between the diffusive and the advective motions, whereas in reality there is a continuum of scales. Clearly from previous sections, this is not the case in turbulent motion, although an average decorrelation lengthscale can be associated with the eddies for homogeneous, isotropic turbulence (see the discussion of the Taylor integral lengthscale in section 1.29, equation 1.19) .

Based on these assumptions, the random walk is used in the following chapters as a model of the dispersion of a passive tracer in turbulent motion. Numerous amendments will be made to the simplest form of random walk described above, in an attempt to account for additional properties of inhomogeneous flows.

The random walk model allows for more flexibility in its application to real flow dispersion problems than analytical solutions to the advective diffusion equation which are only valid at distances downstream which are greater than the mixing length.

2.2.3 The Central limit theorem.

The Central Limit Theorem states that in the limit (of an infinite sample size), the sum of independent, identically distributed random variables is normally distributed (i.e. that the centroid of the centroids of independent samples from any random distribution approaches the centroid of the normal distribution as the number of samples increases). Therefore one would expect that the ensemble average of the trajectories of a large number of particles in a random walk model would approach the mean trajectory.

2.2.4 The Ergodic hypothesis

A requirement for the particle tracking approach to modelling is that the statistics of the resulting particle concentration field can be compared to the statistics of the pollutant concentration field which is being modelled. This assumption draws upon the Ergodic Hypothesis which approximates the ensemble averaged observed distribution of all spatio-temporal realisations by the time averaged observed concentration distribution. It was emphasised by Allen (1985) that the above assumption requires careful selection of sampling period (which becomes more important in complex environments). This also relates to the fact that the fractal codimension of scaling parameters will always be sample size dependent (Lovejoy and Schertzer,1992); which implies that the probability of occurrence of an event over a threshold being observed depends on the sample size.

2.2.5 Random step equation using a continuum of step sizes taken from a specified distribution.

The simple random walk which has been described so far uses displacements which have a constant size. For this form of random walk, the particles are constrained to lie at discrete distances from the origin, in the case of a point source. This can be overcome by allowing the displacements to be selected from a continuous distribution, whilst maintaining the average magnitude of the displacements (van Dam, 1992). The

effect of this phenomenon on the resulting particle distributions is discussed in chapter 4, where both kinds of random walks are used.

The resulting change to the effective diffusion coefficient for a random walk with displacements which are selected from a distribution was shown by Einstein (1905, cited in Van Dam, 1992) to be given by equation 2.4:

$$K = \frac{1}{\Delta t} \int_{-\infty}^{\infty} \frac{\Delta x^2}{2} P(\Delta x) d(\Delta x) \qquad (2.4)$$

where the only requirements on the probability distribution (P (Δx)) are that it must be an even function, and that its integral over all space is finite. Later in this chapter, a random walk is described for which the distribution of the displacements follows a Normal Gaussian distribution. Inserting this probability distribution into equation 2.4 gives equation 2.5:

$$K = \frac{1}{2\sigma\sqrt{2\pi}\,\Delta t} \int_{-\infty}^{\infty} \Delta x^2 e^{\Delta x^2 / 2\sigma^2} d(\Delta x) \qquad (2.5)$$

for which the integral on the right hand side can be evaluated from tables (Davies, 1987) to give equation 2.6:

$$K = \frac{3\sigma^2}{\Delta t} \qquad (2.6)$$

2.2.6 Self-Consistency problem of autocorrelations for random walk.

If the time series of a particle's velocity is analysed for a simple (constant step size) random walk, then the autocorrelation is zero for times greater than the time step, Δt, and for $t < \Delta t$, there is a $(\Delta t - t)/\Delta t$ chance that the velocity is unchanged between time = 0 and time= t, which results in a triangular function for times less than Δt (Wang and Stock, 1992), given by equations 2.7:

$$R(t) = \frac{\Delta t - t}{\Delta t}, for: t < \Delta t$$
$$R(t) = 0, for: t \geq \Delta t \qquad (2.7)$$

Since the value of the autocorrelation, R (0) is unity, the integral timescale is the area under the triangular function, given by: $1/2 \times 1 \times \Delta t$. If the time interval is simply set as the estimated Lagrangian timescale, then the effective integral timescale, T_L, for the random walk is actually only $T_L/2.0$. By setting $\Delta t = 2T_L$, the desired integral timescale may be achieved. This is termed the self-consistency problem, which clearly becomes more of a problem, the more complicated the step equation. However, for the purposes of this modelling work, whereby the effective diffusivity of the different random walk models is fitted using variable parameters (see section 2.5), the correction can be absorbed into the size of the variable parameter. However, if the autocorrelation functions for the random walk models are analysed, then the correction must be taken into account.

2.3 Markov Processes.

A Markov type process has been included in some of the particle tracking models used in this study, since it provides a framework for the inclusion of autocorrelations and cross-correlations which are observed in measurements of the fluctuating velocities. The exclusion of such correlations might well have an important effect on the accuracy of modelling dispersion in more complex flow. Sawford and Borgas (1993) have shown that discrete random walks (random walks for which the time steps are of the same order of magnitude as the Taylor integral timescale) are inconsistent with Kolmogorov's theory of local isotropy, which requires the Lagrangian velocity to be a continuous function of time.

2.3.1 The step equation for a Markov process.

The Markov process could be said to take the analogy of fluid elements in turbulent motion with microscopic particles in Brownian motion to the extreme. Brownian motion can be described by the Langevin equation (e.g. van Dop et al 1985), given by equation 2.8:

$$dw'(t) = -\frac{w'}{T_L}dt + \sigma_{w'}\sqrt{\frac{2}{T_L}}w'' \qquad (2.8)$$

where dw' is the change in the fluctuating velocity component over a small time increment, dt, and where the standard deviation of the fluctuating velocity component

at time t is given by $\sigma_{w'}$. T_L is the Lagrangian integral time scale and w" is a Gaussian random variable having zero mean and unit variance.

The finite difference form of (2.8) is then the first order Markov chain (see for example Sawford 1985), given by equation 2.9:

$$w'(t+\Delta t) = w'(t)R(\Delta t) + \sigma_{w'}\sqrt{1-R^2(\Delta t)} \cdot w''(t+\Delta t) \qquad (2.9)$$

where R_L is the autocorrelation function, related to the values of the fluctuating velocities at time t and $(t + \Delta t)$ by equation 1.16 . The form of this correlation is known to be exponential for constant time steps, in the limit that Δt approaches zero (Durbin, 1980). The change dw' in equation 2.8 is modelled by the finite difference between the velocities at times t and $(t + \Delta t)$.

2.3.2 Regions of inhomogeneity

In inhomogeneous turbulence there is an unphysical build up of particles in regions of the flow where the time scales are large, since there is on average less opportunity for particles to step out from this region into a region of shorter time scales than in the opposite direction. In other words, the maxima in particle distributions moves away from regions of relatively high diffusivity. Attempts have been made to amend this by the simple addition of a drift term to equation 2.8 (for example, see Sawford 1985), $\left(\frac{\partial \overline{w'^2}}{\partial z}\right)dt$. Van Dop et al (1985) have demonstrated that the formulation of the Langevin equation with this term is approximately in agreement

with solutions of the Eulerian equations for moments up to the second order, of concentration and velocity. Thomson (1987) derived the drift term on a more formal mathematical basis.

2.3.3 Selection of the time step for a Markov process.

An investigation into how large Δt could be (for the sake of saving computation time), without the particle dispersion characteristics deviating away from the correct behaviour, was carried out by Wilson and Zhaung (1989). The problem was addressed by comparing the spreads predicted by Taylor's analytical solution to the diffusion equation for the discrete process (which used the time step T_L) with his time continuous solution (which does not involve a time step). It was found that for a timestep of $0.25T_L$, there was an error in the spread of the discrete solution of over 5%, which was considered too large, especially for models which incorporate further complexities, such as cross-correlations. A timestep of $\Delta t=0.1T_L$ was suggested for homogeneous turbulence, for which the discretisation error in the spread was ~ 2%. Further, the exponential autocorrelation in the velocity series is approximately realised for $\Delta t=0.1T_L$, which is the behaviour in the limiting case, as Δt approaches zero (Wang and Stock, 1992).

2.3.4 First order autocorrelation equation

Equation (2.8) provides a framework to include cross-correlations in the velocity components. The scheme used here was introduced by Zannetti (1991). Often, in vertical shear layer flows, only the cross-correlation r_{uw} is considered as important :

$$r_{uw} = \frac{\overline{u'w'}}{\sqrt{u'^2}\sqrt{w'^2}} \qquad (2.10)$$

Combining this with the single point autocorrelations, the explicit first-order autocorrelation equations are given by equations 2.11:

$$\begin{aligned} u'(t+\Delta t) &= \phi_1 u'(t) + u''(t+\Delta t) \\ v'(t+\Delta t) &= \phi_2 v'(t) + v''(t+\Delta t) \\ w'(t+\Delta t) &= \phi_3 w'(t) + \phi_4 u'(t+\Delta t) + w''(t+\Delta t) \end{aligned} \qquad (2.11)$$

where u', v' and w' are the downstream, transverse and vertical fluctuating velocity components and the parentheses indicate which timestep. The mean advective velocity in the downstream direction is added to the fluctuating component at each generation. The equations are heuristic in origin, since they may or may not be in agreement with solutions to the transport equation (1.23). The ϕ coefficients are algebraic combinations of components of the correlation tensor, the values of which are given by equations 2.12 (Zannetti,1990b):

$$\phi_1 = r_u(\Delta t)$$
$$\phi_2 = r_v(\Delta t)$$
$$\phi_3 = \frac{r_w(\Delta t) - \phi_1 r^2_{uw}(0)}{1 - \phi_1^2 r^2_{uw}(0)} \qquad (2.12)$$
$$\phi_4 = \frac{r_{uw}(0)\sigma_{w'}\left[1 - \phi_1 r_w(\Delta t)\right]}{\sigma_{u'}\left[1 - \phi_1^2 r^2_{uw}(0)\right]}$$

where for example r_u is the component of the correlation tensor corresponding to the autocorrelation in u'. The variance of the completely random components (u",v" and w") in 2.11 are given by equations 2.13:

$$\sigma^2_{u''} = \sigma^2_{u'}\left(1 - \phi_1^2\right)$$
$$\sigma^2_{v''} = \sigma^2_{v'}\left(1 - \phi_2^2\right) \qquad (2.13)$$
$$\sigma^2_{u''} = \sigma^2_{w'}\left(1 - \phi_3^2\right) - \phi_4^2\sigma^2_{u'} - 2\phi_1\phi_3\phi_4 r_{u'w'}(0)\sigma_{u'}\sigma_{w'}$$

where these are the standard deviations away from the means of the components of u'' . The autocorrelations are typically modelled using exponential functions, which in the limit of the discretisation interval, Δt, approaching zero, is known to be the correct behaviour (see Wang and Stock,1992).

The equations can be simplified if the time steps used are greater than the integral time scale, such that the autocorrelations can be ignored and only the cross-correlations are considered to give equations 2.14 and 2.15 (Kelsey, 1994):

$$w' = r_{uw}\frac{\sigma_{w'}}{\sigma_{u'}}u' + w'' \qquad (2.14)$$

$$\sigma_{w''} = \left(1 - r_{uw}^2\right)^{1/2}\sigma_{w'} \qquad (2.15)$$

where w'' is a Gaussian random noise component with standard deviation $\sigma_{w''}$.

The cross-correlation coefficients can be estimated from Eulerian measurements of the u' and w'. The latter has been done by various authors over a wide range of flows using electromagnetic current meters. Heathershaw (1978), measured r_{uw} values between the vertical and down stream fluctuating velocities in the neutrally stratified bottom boundary layer of a tidal current at 100 cm and 150 cm above the bed of -0.18 +/- 0.018 and -0.15 +/- 0.017 respectively. Holland et al., (1990) made turbulence measurements on the river Severn for which, on a straight section, r_{uw} had an ensemble value of approximately -0.4. On the S.E.R.C. Flood Channel Facility (see chapter 3), analysis of the laser-Doppler-anenometer data, carried out on the in-bank 100mm flow depth data, yields an ensemble average value of $r_{uw} = -0.27$.

Alternatively, the correlation r_{uw} may be substituted by r_{uv} and the equations reformulated for the case when the transverse correlation is more significant than the vertical.

Finally, both correlations, r_{uw} and r_{uv} may be included in the form of equation 2.16:

$$\begin{aligned} u' &= u'' \\ v' &= \phi_5 u' + v'' \\ w' &= \phi_6 v' + \phi_7 u' + w'' \end{aligned} \qquad (2.16)$$

where the ϕ coefficients are simple algebraic combinations of the correlation tensor given by equations 2.17 and 2.18:

$$\phi_5 = \frac{r_{uv}\sigma_{v'}}{\sigma_{u'}} \qquad (2.17)$$

$$\phi_6 = \frac{r_{u'v'}r_{u'w'}\sigma_{w'}}{\sigma_{v'}\left(r^2_{u'v'}+1\right)}$$
$$\phi_7 = \frac{r_{u'w'}\sigma_{w'}}{\sigma_{u'}\left(r^2_{u'v'}+1\right)} \qquad (2.18)$$

The correlation between u' and v' and the correlation between u' and w' intimate a correlation between v' and w', hence the inclusion of ϕ_6. The derivation of these coefficients, and the values of the variance of the fluctuating velocities is given in appendix 2A. The variances are given by equations 2.19 and 2.20:

$$\sigma^2_{v''} = \sigma^2_{v'}\left(1-r^2_{uv}\right) \qquad (2.19)$$

$$\sigma^2_{w''} = \sigma^2_{w'} - r^2_{u'w'}.\sigma^2_{w'}\left(\frac{3r^2_{u'v'}-1}{\left(r^2_{u'v'}+1\right)^2}\right) \qquad (2.20)$$

2.3.5 Further properties of the Markov chain.

2.3.5.1 Correction to fluctuating velocity variance.

The spatial variance of the size of the particle cloud is determined from the autocorrelation function in accordance with equation 2.21 (Kampé de Fériet following Taylor (1921), cited in Reid,1978):

$$\sigma_z^2(t) = 2w'^2 \int_0^t (t - t')R(t')dt' \qquad (2.21)$$

where t' is a dummy time variable and σ_z is the spatial variance of the particle cloud distribution.

The use of a discrete time interval, Δt, in the finite difference form of the Langevin equation implies that for this periods of time the autocorrelation in the fluctuating velocity time series is unity. The spatial variance given by 2.21 can only be equal to that for the continuous time case if the velocity variance is modified by a small amount, such that the equality 2.22 holds:

$$w'^2 \int_0^t (t - t')R(t')dt' = w'^2_{effective} \int_0^t (t - t')dt' \qquad (2.22)$$

where $w'_{effective}$ is the modified time averaged fluctuating velocity which accounts for the finite time steps. Evaluating the integrals, using an exponential autocorrelation function, this gives equation 2.23 (Reid,1978):

$$w^2_{effective}{}' = \frac{2T_L^2}{\Delta t^2} \overline{w'^2} \left[\exp - \left(\frac{\Delta t}{T_L} \right) + \frac{\Delta t}{T_L} - 1 \right] \qquad (2.23)$$

where $\Delta t = t - t'$. However, in the studies reported here this correction will automatically be absorbed into the multiplicable factors to the step sizes, which were used as variable parameters in order to calibrate the model, as discussed in section 2.5.

2.3.5.2 Accounting for the effects of intermittency in a Markov chain.

Intermittency is ubiquitous in turbulent flow measurements, and investigations have been carried out into the possibility of integrating its effects into the random walk scheme by Borgas and Sawford (1990). The patchiness of turbulence which arises from intermittency implies that at smaller scales, the ratios of active to inactive regions decreases which should result in there being local variations in the intensity of energy transfer down the energy cascade. This is at odds with the assumption of a constant energy flux which is central to Kolmogorov scaling theory. However, many measurements have been made in approximately homogeneous turbulence, which are somewhat paradoxically in agreement with Kolmogorov's scaling laws. The multifractal scaling approach has met with some success in accounting for the intermittency effects (which on a larger statistical scale change the kurtosis of the velocity distributions). Borgas and Sawford (1993) incorporated this idea into a stochastic model of a one particle dispersion model in which the multifractal scaling was derived from Eulerian measurements. However, the authors concluded that the inclusion of intermittency made little difference to the dispersion, and there were no discernible advantages to its inclusion.

2.4 The application of random walk models to channel and river flows.

2.4.1 Previous studies.

The random walk has been used in relatively few instances to model the dispersion characteristics of the flow in a channel. Recently the model was applied to the flow in the River Severn (Heslop and Allen, 1993). This study was primarily concerned with the longitudinal dispersion characteristics of the reach, and the tracer tests which were carried out showed skewed concentration curves with long tails in the upstream direction. This suggests that there were deadzones or long term correlations present in the flow (e.g. due to deadzones with large storage times or secondary circulation cells) which were not accounted for by the random walk model. The random walks in use were unable to reproduce the observed long tails, a shortfalling which it was said could be improved slightly with the inclusion of deadzone 'storage' effects near the modelled river bed, although results from such a model were not presented. Secondary circulation and dead zones are also present in the river flow which is investigated in chapters 5-8, and efforts are made to account for these features by the inclusion of a variable effective dispersivity coefficient for the random walk.

2.4.2 The scale dependency of the dispersion process.

The effects which the suggested inhomogeneities above can have on solute dispersion are exemplified by considering the case where the diffusion equation is used to predict the transport of the cross-sectional mean concentration of a tracer over a

large distance compared to any meander arc length in the reach. Here the length scales contributing to the constant of dispersivity are large because the large scale circulatory motions of the secondary currents can be considered as random and part of the dispersive motion. If the local concentration is of interest, as in this study, then the constant of dispersivity depends on the scales which are small enough that their motion can be considered random. However, due to the sweeping effect that the larger scales of motion have on these smaller scales, the dispersion equation at this scale is not enough to describe the evolution of the localised concentration. The sweeping effect can give rise to dispersion which is non-Fickian, a problem which is addressed here by the inclusion of an effective memory to the motion of the particles, which can be modelled in many different ways (for example see Kinzelbach, 1990).

2.4.3 Estimating the integral length scale from Lagrangian measurements.

Most of the time and length scales used in the different random walk models which are described below have been based upon the flume photography experiments carried out by Sullivan (1972), and were also employed by Allen (1982; 1992) and Heslop & Allen (1993). Alternatively the scales are based upon the measured Eulerian fluctuating velocity field in the channel flows. The measurements by Sullivan are the largest scale Lagrangian measurements available at the time of writing so far as is known.

Sullivan's Lagrangian measurements were carried out using a camera which was moved along at the mean down stream velocity in a channel flow, recording the positions in two dimensions (three including camera position) of particles having

neutral buoyancy (0.5mm diameters). The flume was 8.95cm deep, with a working width and length of 0.46m and 2.45m. The experiment is outlined below.

The transverse and vertical positions of the particles were projected onto a plane perpendicular to the downstream co-ordinate. The particle paths in this plane could be resolved into a series of circular arcs. Three successive co-ordinate positions were used to define a plane upon which a circular arc could be drawn through the three positions. The radius of the arc was then used to define an instantaneous length scale, r', which is shown in the sketch below:

Flow is into the page

Sketch showing construction of r'

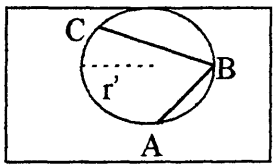

vertical ↑

cross-stream →

The traced particle trajectory, projected onto the x/y plane is ABC. These three points form a unique arc, of radius r'.

r' was non-dimensionalised by the depth, d = 8.95cm. The swept angle made by the arc was divided by two time intervals to define an instantaneous angular velocity, ω (which was non-dimensionalised using [h/u*], where h is the channel depth and u* is the friction velocity). Next an experimental probability density function was defined by fitting the scale and shape parameters of gamma distributions to the observed distributions of instantaneous length scales at ten different depths.

The instantaneous angular velocity of a particle was found to have a definite dependence on the instantaneous length scale. All the values of ω which had the same instantaneous length scales, to within experimental accuracy, were averaged to produce a mean value $\overline{\omega}$, and an experimental relationship was determined of the form given by the relation 2.24:

$$\overline{\omega} = 2.2(r')^{-0.698} \qquad (2.24)$$

The average of the absolute value of the difference between individual $\overline{\omega}$ values and values given by the equation when corresponding values of r' were used was found to be ~ 20-30%.

An ensemble average angular velocity was then determined by inserting the ensemble mean observed length scale which was $\langle r' \rangle$=0.1 into 2.24. This was then used to determine an ensemble average fluctuating velocity magnitude in the y/z plane by putting $\langle u' \rangle = \langle r' \rangle \langle \omega' \rangle$ = 1.0975 in non-dimensional units. This estimate is fundamentally based upon the Lagrangian length and inverse time scales estimated in the experiment. These values were used by Allen (1982 ; 1992) and Heslop and Allen (1993).

2.4.5 The random walk model applied to regions of shear.

A continuous range of step sizes can be used in the random walk, rather than using steps of equal sizes and applied in time steps equal to an estimation of the integral Lagrangian timescale T_L. The major difference that this makes to the dispersion is that the coarseness of the resulting field is reduced. Further, for the random walk having constant step sizes it becomes important to ensure that there are particle trajectories which take odd and even total numbers of steps between release and the sampling cross section since if the particles all take an even number of steps, then they are unable to settle at odd integer numbers of displacements away from the release site. This effect is especially likely to occur when there are small velocity gradients perpendicular to the mean flow direction (such as in the transverse dimension for the in-bank flow, which will be described in the next section).

2.5 Flume geometry and flow conditions.

The hydrodynamic and dye dispersion data used in this report came from two different sets of experiments which were carried out on the Flood Channel Facility at Hydraulics Research, Wallingford. The flume geometry will be described here, since the different random walk models (described in section 2.6) were chosen for the specific flows of interest.

The tracer dispersion tests were carried out by Guymer et al.(1989) for in-bank and over-bank flows for several release points and different depths of flow in a two stage, straight channel with geometry given in fig. 2.2:

Fig. 2.2 Diagram showing flume geometry for Flood Channel Facility, Wallingford (not to scale).

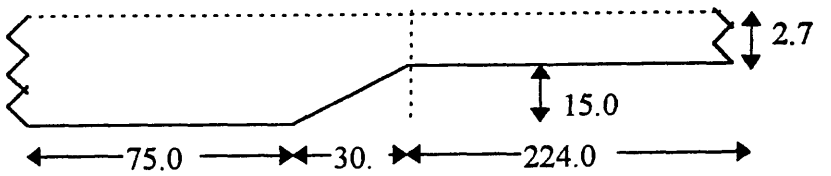

{all measurements in cm.}

The two flows which were examined in this sensitivity analysis corresponded to flow depths of 177mm (over-bank flow) and 100mm (in-bank flow), both having a side wall slope of 2. The dye injection points considered in the analysis were channel side- bank top (depth = 15mm, y= 1.05m) for the over-bank flow, and centreline-water surface for the in-bank flow.

The ratio of the over-bank flow depth to the main flow depth can be considered as similar to that observed on natural rivers, with the side wall slope representing the slope of the inner bank between the flood plain and the main channel.

2.6 Sensitivity of the large scale dispersion characterstics to the form of the velocity perturbations in the random walk model, leading to descriptions of the different formulations which are used in this study.

A variety of random walk models will shortly be described, which make different assumptions about the form of the velocity perturbations in the flume flows. This selection of different models was included because the exact form which the perturbations should take is not known for inhomogeneous turbulence, but it was also included in order to investigate the sensitivity of the macroscale dispersion characteristics of a cloud of particles to the nature of the velocity perturbations which are applied to the individual particles at the microscale. The different models have varying degrees of complexity, ranging from the simple, constant step size type, to a model which takes into account the measured fluctuating velocity field and the fine structure cross correlation and autocorrelation information. The sensitivity analysis also aims to ascertain the worthwhile degree of complexity, baring in mind the additional effort which is required in terms of computation and fieldwork.

The sensitivity analysis of the different random walk models in the next chapters is principally conducted on the more simple, in-bank flow. The best performing models in the in-bank flow will be paid particular attention when studying

the over-bank flow although the best fitting models might not be the same for the two flows.

The various random walks which were used in this study were given names (see parentheses in each section heading below) for identification. All of the velocities, displacements or timescales discussed have been non-dimensionalised using combinations of the depth and the friction velocity of the flume flow. Each of the random walks discussed below incorporated three principal variable parameters, f_u, f_w and f_v which were multipliers to the estimations of the longitudinal, vertical and transverse integral lengthscales respectively. In this way the values of f_u, f_w and f_v ought to be of the order unity if an appropriate model has been defined.

The value of f_u was essentially fixed so that the downstream perturbations were of the correct order of magnitude, since this study concentrated on transverse and vertical mixing. Moreover, the downstream dispersion is controlled more by the differential advection due to cross stream and vertical shear velocity profiles. The values of f_w and f_v , however, were adjusted in size until the predicted particle distribution for each model fitted the measured concentration distributions at the first measurement site downstream (4m). These calibrated values were then fixed, and the particles were allowed to disperse further downstream. The predicted particle distributions were then compared with the measured concentration distributions further downstream.

The over-bank hydrodynamic data available at the time of writing was not as detailed as that for the in-bank flow, so there are differences between the basic forms of random walks which are examined in this section. Wherever possible, the same form of model is used for both flows.

2.6.1 Random walk with a constant step size (JUMP).

This subroutine selects a random real number η from a uniform distribution in the interval (0,1) and if η is greater than 0.5, the particle is displaced a distance $f_w \times L_L$ upwards, if η is less than 0.5, the particle undergoes the same displacement but downwards.L_L is the ensemble Lagrangian length scale estimated in section 2.4. The resulting symmetrical binomial distribution rapidly approaches the normal distribution as discussed in section 2.2. The process is repeated for the remaining two dimensions using corresponding factors f_u and f_v for downstream and cross stream respectively. The steps are applied every integral timescale T_L, which is 0.4 seconds in real time, as estimated from the inverse time scale determined by Sullivan (1972).

2.6.2 Random walk with step sizes selected from a normal random distribution and variance scaled using ensemble average length and velocity scales (NEWJUMP).

This subroutine introduced a continuous range of step sizes such that the particles could in theory sample the entire fluctuating velocity field. The ensemble average fluctuating velocity scale was used to scale the variance of a random number which was generated from a normal Gaussian distribution having zero mean and unit standard deviation, $\beta(0,1)$. The factors f_v, f_w were used once more, such that for example the vertical steps size took the form given by equation 2.25:

$$l_w = f_w \times \beta(0,1) \times L_L \qquad (2.25)$$

where l_w is the resulting particle displacement.

For the over-bank flow, another model (NEWJUMP B) was constructed in which the length and timescales were derived from the measured dimensionless eddy viscosity as determined from the measurements of Knight and Shiono (1990) in which the flume was divided into four subsections in the transverse direction, and each of these given a different effective dispersivity. Knight and Shiono (1990) show numerical solutions to a shear stress model which incorporated such a discretised eddy viscosity, and which greatly improved the fit of the model to the data. One of the sub-regions has been omitted in this work, since the particles never enter the extreme right hand side of the flume in these experiments. In non-dimensional form, the eddy dispersivities,e_y took the values in the intervals given by equations 2.26:

$$\begin{cases} e_y/hu* = 0.07 & 0.00m < y < 0.75m \\ e_y/hu* = 0.16 & 0.75m < y < 1.05m \\ e_y/hu* = 0.07 & 1.05m < y < 3.0m \end{cases} \qquad (2.26)$$

The step sizes were derived from these values by dividing $e_y/hu*$ by the non dimensional Lagrangian velocity scale determined from Sullivan's work (the Lagrangian velocity determined from Sullivan's work scaled using the friction velocity for these flows was $0.029ms^{-1}$).

2.6.3 Random walk scaled using the fluctuating velocity field (TURJ2).

The value of a surface fitted to the vertical fluctuating velocity field and the estimated Lagrangian time scale were used to scale the vertical length scale every step such that : $l_w = f_w(w')T_L$. The transverse fluctuating velocity was scaled similarly, but

using a surface fitted to the transverse fluctuating field : $l_v = f_v(v')T_L$. However, the longitudinal fluctuations were scaled using the vertical fluctuating field, since no data was available for the longitudinal component, thus : $l_u = f_u(w')T_L$.

2.6.4 Random walk with step sizes selected from a continuous range, with displacements scaled using the local velocity (NSCALE).

This subroutine was based on 2.6.2 and 2.6.3 above, with the addition of a scaling factor based on the variation in mean flow velocity. The displacements were scaled as: $l_w = \frac{f_w w' T_L u}{u*}$, where u is the mean downstream velocity, non-dimensionalised using the mean friction velocity.

2.6.5 Random walk with continuous range of step sizes and cross-correlations (CORJ2A, CORJ2B, CORJ3 and CORJ4).

These subroutines were much the same as 2.6.3 above with the addition of a correlation coefficient derived from the measurements of the Reynolds stresses (Shiono and Knight, 1990). The inclusion of cross-correlations attempted to account for the effect that regions of large shear have on the dispersion of a passive contaminant.

The correlation coefficient may either be determined using the local values of Reynolds stresses measured in the flume, or by using an ensemble correlation coefficient value. A surface was fitted to the $\overline{u'w'}$ field (see chapter 3), and the local values of r_{uw} were determined from the interpolated values of the field and the local values of u' and w', using equation 2.10. The coefficient r_{uw} was then incorporated

into the random walk using equations 2.14 and 2.15 for the in-bank flow case (CORJ2A). CORJ2B was the same as CORJ2A, except the ensemble average value for r_{uw} of -0.27 was used.

The fluctuating velocity field measurements were not obtainable for the over-bank flow at the time of writing (although these were available in S.E.R.C. report SR314,1992), although measurements of the transverse shear stress τ_{uv} (Shiono and Knight, 1990) were used tentatively to construct an estimation of r_{uv} . The shape of the transverse shear stress distribution was essentially a saw-tooth with a minimum above the bank top (maximum if absolute value used). The shear stresses were assumed to have a similar distribution, from the relationship 2.27:

$$r_{uv} = -\frac{\tau_{uv}}{\rho\sqrt{\overline{u^2}}\sqrt{\overline{w^2}}} \qquad (2.27)$$

However, the Reynolds stresses were an order of magnitude greater than the bed shear stresses, and consequently the expression above cannot be approximated using the shear velocity in place of the r.m.s. velocities, as is common practice in atmospheric modelling (Zannetti,1990b), since this would yield correlations in excess of unity. A maximum value of correlation was therefore estimated from measurements of $\overline{u'v'}$ for the in-bank flows ($|r_{uv}| = 0.3$). Essentially the effect of a saw-tooth shaped correlation distribution was the important factor in this model. The correlation was then implemented in the modified form of equations 2.14 and 2.15 replacing r_{uw} with r_{uv} (CORJ3) and also in the form of equations 2.16 - 2.19 (CORJ4), which included the correlations in both r_{uw} and r_{uv} . The multiplicative factors f_u, f_v and f_w were then used

in the same way as described for TURJ2 (i.e. $l_w = f_w(w')T_L$, $l_v = f_v(v')T_L$ and $l_u = f_u(w')T_L$).

2.6.6 Markovian random walk (MARKOV).

Here the finite difference equation 2.9 was used and cross-correlations were included in the form of equations 2.11-2.13. The sizes of the displacements were then scaled using the multiplicable factors in the same way as for the model TURJ2 (i.e. $l_w = f_w(w')T_L$, $l_v = f_v(v')T_L$ and $l_u = f_u(w')T_L$). The instantaneous values of the velocity fields were used to estimate the cross-correlations for the in-bank flow.

In the case of the over-bank flow the fluctuating velocity fields were not available at the time of writing (although these were available in S.E.R.C. report SR314,1992), but rather empirical, ensemble average fits to the data were used in the model (MARKOV B) as determined by Knight and Shiono (1990):

$$\begin{aligned} &{u'_i}/{u_*} = A_i \exp(-Bz') \\ &\begin{cases} A_1 = 2.1810 & A_2 = 1.3860 & A_3 = 1.1403 \\ B_1 = 0.6650 & B_2 = 0.6642 & B_3 = 0.5581 \end{cases} \end{aligned} \qquad (2.28)$$

where z' is the depth non-dimensionalised by the total depth of the flow. Unfortunately this method restricted the particles so that they were unable to experience any transverse variation in the effective eddy viscosity, since the fluctuating velocities have been given as a function of depth (z) only. MARKOV A assumed constant values for the fluctuating velocity components (equal to the ensemble averaged values).

2.6.7 Discrete random walk with displacement sizes selected from gamma distributions (SULLIJ)

This random walk was created so that a large amount of the information from the experimental results from the flume photography carried out by Sullivan could be used directly.

The instantaneous length scale was generated using gamma distributions (based on algorithm in Dagpunar, 1990) which used the best fit shape parameters determined in Sullivan's experiment. The local angular velocity was estimated using equation 2.24, with a Gaussian noise component having a standard deviation of 25% (of the local angular velocity) as an attempt to model the degree of disagreement of the power law with the data. This allows the possibility that the local length scale might become negative. If the length scale became negative upon being corrected with noise, the noise term was generated once more and another value returned . Values of r' which fell outside the observed range ($0.01 < r' < 0.5$) in the experiments were also disregarded. Both of these amendments were somewhat ad hoc, and the extent to which the latter affected the distribution is not known. However, the resulting simulated frequency histogram (fig.2.3) shows that the general shape of the gamma distribution was maintained. The instantaneous velocity was then determined as the product of the local length scale and the local angular frequency, ($v_{instant} = r' \times \omega$). The displacement sizes were then determined from: $l_w = f_w \times v_{instant} \times T_L$, $l_v = f_v \times v_{instant} \times T_L$ and $l_u = f_u \times v_{instant} \times T_L$.

2.6.8 Random walk based on fast fractional Gaussian noise (FASTA, FASTB and FASTC).

Some fast fractional Gaussian noise (FFGN) was generated using an algorithm due to Mandelbrot (1971), and was scaled using the ensemble average fluctuating velocity scale in order to produce a series of fluctuations $(v_F)_i$ which could be applied consecutively to the particle trajectories. The displacement sizes were then determined from: $l_w = f_w \times (v_F)_i \times T_L$, $l_v = f_v \times (v_F)_i \times T_L$ and $l_u = f_u \times (v_F)_i \times T_L$.

This kind of noise attempts to model the long term correlations often observed in natural flows by correlating the series of steps that the particles take over their entire journey. The covariance (equivalent of non-normalised autocorrelation function) of the FFGN is given by equation 2.29:

$$Cov(s,H) = 2^{-1}\left(|s+1|^{2H} - 2|s|^{2H} + |s-1|^{2H}\right) \qquad (2.29)$$

where s is a time lag. The extent of the correlation was varied using three different values of the H exponent, 0.65 (FASTA), 0.95 (FASTB) , 0.55 (FASTC). The FFGN which was generated was stored in an array, the dimensions of which were sufficient to accomodate the number of particles plus the the total number of steps which were likely to be taken. The generation of different noises for each of the particles resulted in a large increase in the computation time (or alternatively the storage space required).

Fig.2.3

frequency histogram for modified gamma distribution

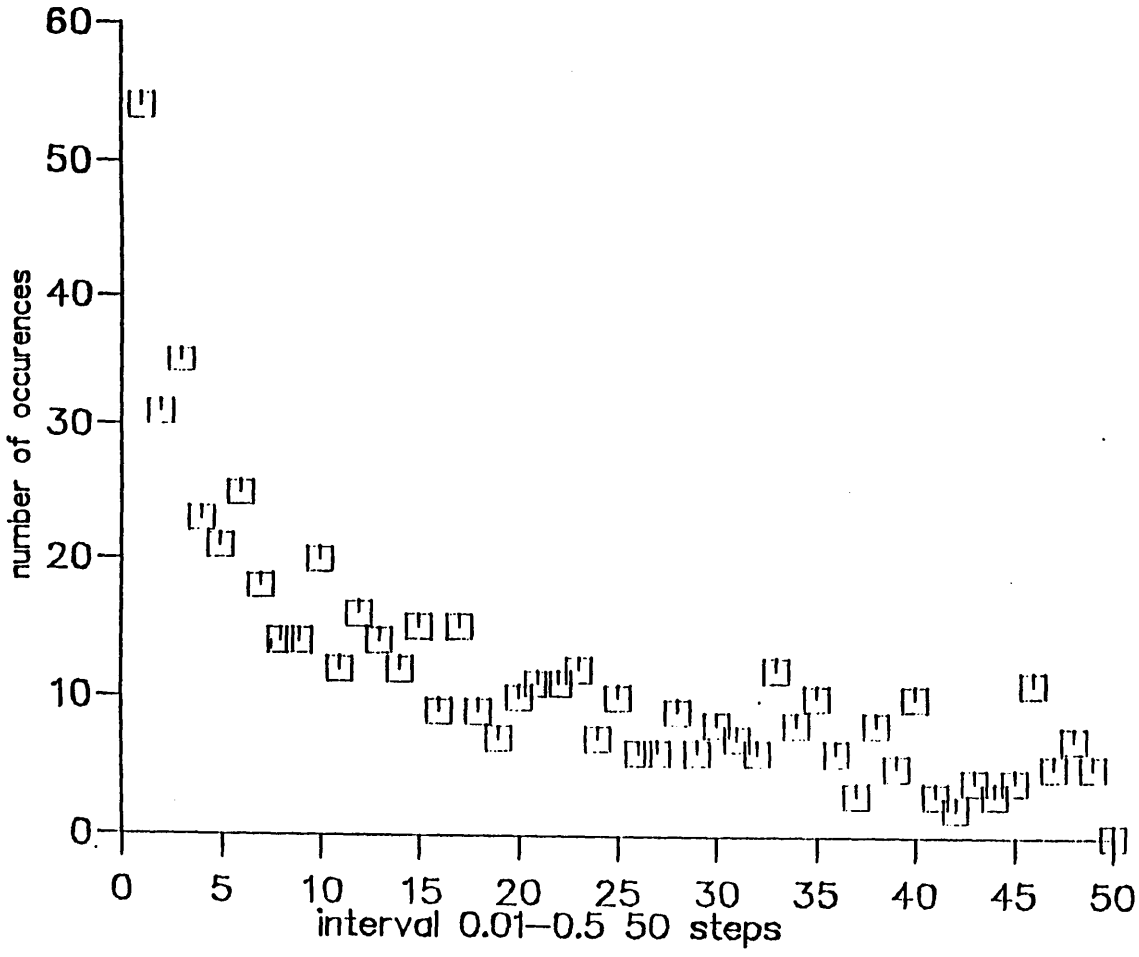

Appendix 2A

Formulation of the autocorrelation equation to include correlation between vertical and streamwise and transverse and streamwise velocity fluctuations.

Here the first order autocorrelation equation is written out in triangular form to give equations A2.1:

$$
\begin{aligned}
u'(t+\Delta t) &= \phi_1 u'(t) + u''(t+\Delta t) \\
v'(t+\Delta t) &= \phi_2 v'(t) + \phi_3 u'(t+\Delta t) + v''(t+\Delta t) \\
w'(t+\Delta t) &= \phi_4 w'(t) + \phi_5 v'(t+\Delta t) + \phi_6 u'(t+\Delta t) + w''(t+\Delta t)
\end{aligned}
\qquad \text{(A2.1)}
$$

Zannetti(1990) gives the full analysis of A2.1 to give the values for each ϕ coefficient. This is achieved by reducing the correlation tensor with appropriate correlations into triangular form and solving a set of simultaneous equations for the unknown coefficients in terms of components of the correlation tensor. However, the autocorrelations are set to zero here, for the simplified case where the time steps in the random walk are the same order as the integral time scale. These assumptions give : $\phi_1 = \phi_2 = \phi_4 = 0$, and reduce ϕ_3 to equation A2.2:

$$
\phi_3 = \frac{r_{uv}(0)\sigma_{v'}}{\sigma_{u'}} \qquad \text{(A2.2)}
$$

which reduces equation A2.1 to A2.3:

$$u' = u''$$
$$v' = \phi_3 u' + v'' \qquad \text{(A2.3)}$$
$$w' = \phi_5 v' + \phi_6 u' + w''$$

The cross-correlation between transverse and vertical components has a negligible effect on the dispersion , although the term ϕ_5 cannot be dropped in solving the equations since there is a mutual correlation between v' and w' , arising from their independent correlations with u'.

The variances of the random parts of the fluctuating velocities are given by A2.4 and A2.5:

$$\sigma_{v''}^2 = \sigma_{v'}^2\left(1 - r_{uv}^2\right) \qquad \text{(A2.4)}$$

and:

$$\sigma_{w''}^2 = \sigma_{w'}^2 - \phi_5^2\sigma_{v'}^2 - \phi_6^2\sigma_{u'}^2 - 2\phi_5\phi_6 r_{uw}\sigma_{u'}\sigma_{w'} \qquad \text{(A2.5)}$$

The values of ϕ_5 and ϕ_6 were obtained through rearranging the autocorrelation equation in terms of the full correlation tensor (r_{ij}) , to the form given by equation A2.6 and by solving the resulting simultaneous equations:

$$\begin{pmatrix} \mathbf{a}_{55} & \mathbf{a}_{56} \\ \mathbf{a}_{65} & \mathbf{a}_{66} \end{pmatrix}\begin{pmatrix} \phi_5 \\ \phi_6 \end{pmatrix} = \begin{pmatrix} \mathbf{b}_5 \\ \mathbf{b}_6 \end{pmatrix} \qquad \text{(A2.6)}$$

where:

$$
\begin{aligned}
\mathbf{a}_{55} &= \phi_3 \sigma_{u'} \\
\mathbf{a}_{56} &= \sigma_{u'} \\
\mathbf{a}_{65} &= \phi_3 \sigma_{u'} . r_{uv} \sigma_{v'} + \sigma^2{}_{v''} \\
\mathbf{a}_{66} &= \phi_3 \sigma_{u'}{}^2 \\
b_5 &= r_{uw} \sigma_{w'} \\
b_6 &= r_{vw} \sigma_{v'} \sigma_{w'}
\end{aligned}
\qquad \text{(A2.7)}
$$

Inserting these values gives simultaneous equations A2.8:

$$
\begin{pmatrix} \phi_3 \sigma_{u'} & \sigma_{u'} \\ \phi_3 \sigma_{u'} r_{uv} \sigma_{v'} + \sigma^2_{v''} & \phi_3 \sigma^2_{u'} \end{pmatrix} \begin{pmatrix} \phi_5 \\ \phi_6 \end{pmatrix} = \begin{pmatrix} r_{uw} \sigma_{w'} \\ 0 \end{pmatrix} \qquad \text{(A2.8)}
$$

Reducing these equations gives equation A2.9 :

$$
\begin{aligned}
\phi_5 &= \frac{r_{uv} r_{uw} \sigma_{w'}}{\sigma_{v'} \left(r^2{}_{uv} + 1 \right)} \\
\phi_6 &= \frac{r_{uw} \sigma_{w'}}{\sigma_{u'} \left(r^2{}_{uv} + 1 \right)}
\end{aligned}
\qquad \text{(A2.9)}
$$

which enables the simplification of the variance of the random component of the fluctuating velocity from equation A2.5 to equation A2.10:

$$
\sigma^2_{w''} = \sigma^2_{w'} - r^2{}_{u'w'} . \sigma^2_{w'} \left(\frac{3 r^2{}_{u'v'} - 1}{\left(r^2{}_{u'v'} + 1 \right)^2} \right) \qquad \text{(A2.10)}
$$

So there is now all the information available to solve equations A2.3.

Chapter 3

Description and interpolation of velocity measurements, and description of tracer concentration measurements in the Flood Channel Facility, Wallingford.

3.1 Introduction.

This chapter summarises aspects of the hydrodynamic (see Knight and Shiono, 1989) and dye dispersion experiments (by Guymer et al, 1989) which were undertaken at the Flood Channel Facility at Hydraulics Research, Wallingford. These experiments were carried out under controlled conditions with a relatively high degree of precision and so provide a good standard by which to assess the performance of hydrodynamic or dispersion models.

Section 3.2 describes the velocity measurements which were taken using laser, Doppler anemometer techniques.

Section 3.3 describes the tracer tests which were carried out using a steady release of fluorescent dye from a point source, and an array of fluorometers with which to measure the concentration distributions at different depths and distances downstream.

Section 3.4 describes how the point measurements of the mean and fluctuating velocities were used to construct interpolated velocity fields. It was important to model the mean flow field accurately, since it determines the extent of the differential advection of the particles in the random particle tracking model.

3.2 Hydrodynamical measurements.

The turbulence and velocity data were collected using a laser Doppler anemometer (L.D.A.). Here a 300mW argon ion laser beam was directed through a fibre optic cable connected to a submersible 15mm diameter probe head. The back-scatter signal was processed and the shift in the frequency between the outgoing signal and the back-scatter was used to measure a continuous velocity time series (see Knight and Shiono,1989). The probe was mounted on a rig, which had three degrees of freedom, so that the probe could be positioned anywhere in the flow, with a spatial resolution of 2mm in the transverse direction and 0.5mm in the vertical direction. The sampling frequency was between 20 and 100 Hz.

3.2.1 Over-bank flow modelling.

Over-bank flow has been much studied since it occurs in most natural rivers during peak flows and is important in the design of flood alleviation schemes (New Scientist,1994). The strong shear layer which exists between the in-bank and relatively slow over-bank regions of flow causes a large amount of momentum transfer, such that the cross-section averaged mean downstream flow velocity is reduced. The studies of the non-linear shear stress distributions in the Flood Channel Facility have led to a greater understanding of how the different shear stresses in the Navier Stokes equation (or in approximations to it) affect the mean flow, as described in the next paragraph.

The distribution of shear stresses on a horizontal plane (τ_{ZX}) through the flow is affected by the distribution of the transverse shear stresses(τ_{ZY}) and the secondary velocities, in addition to the gravitational force per unit area (Knight et al. 1990). If these additional stresses are neglected, the balance results in a logarithmic distribution of the downstream velocity in the vertical direction. By including the additional effects, the velocity profile becomes more complex, altering the depth averaged velocity and consequently discharge calculations at a cross-section. Similarly, the distributions of shear stresses on a vertical plane (τ_{ZY})are also affected by the secondary currents and the distributions of vertical shear stresses.

The analytical models developed for the flume flows have been applied to natural over-bank flows in sections of the River Severn. Knight et al. (1990) report how the model was able to predict the correct depth averaged velocity distributions and total discharges for several cross-sections.

3.2.2 Previous work on the flume flows under study.

There has been a considerable amount of research into measuring the secondary flow structure and into analytical solutions to the depth-averaged momentum equations for the particular flume flows under study (Knight and Shiono 1989; 1990, Tominaga et al., 1989 for a similar flume geometry). It is therefore informative to compare the random walk model results against the detailed flow structure and the conclusions which were arrived at in the analytical approach.

Observations in these studies have shown that the secondary velocities for the trapezoidal in-bank flows are 1-3% of the downstream velocities, and manifest themselves in the form of several coherent cells. In the case of the over-bank flow, similar cells with slightly stronger circulation (1-4% of the downstream velocities) exist. The secondary flow structure is shown schematically in fig. 3.1, which has been reproduced from Shiono and Knight (1991). This structure is well understood in terms of the spatial variation of the different shear stresses and has been reported in detail elsewhere (Shiono and Knight, 1989).

In the case of over-bank flow it was shown by Shiono and Knight (1990) that the use of an eddy viscosity which varied in the transverse direction could vastly improve their analytical model's fit to the observations. It was also found to be essential to include a secondary flow advective term in the model, if no allowance for this variation in eddy viscosity was made. The study showed that if only four different values of dimensionless transverse eddy viscosity were used to model the transverse variation, then the simulations agreed well with observations. References to this work will be made throughout this thesis.

3.3 Tracer data

3.3.1 Instrumentation and sampling strategy

The Rhodamine wt tracer concentrations were measured by Guymer and colleagues (Guymer et al., 1989) using fluorometers which measure the relative fluorescence of the water. The fluorescence is linearly related to the concentration of the tracer, and the constant of proportionality can be determined through calibration

using a standard solution. A vertical array of four fluorometers was traversed across the flume at a chosen cross-section, and the concentrations were measured at different profile positions. The array of fluorometers was then traversed in the opposite direction, but at a different depth, so that the concentrations were now determined at up to eight locations through the vertical and as many as 35 locations in the transverse direction. This gave a resolution of approximately 0.01m in the vertical direction and 0.03m in the transverse direction, for the in-bank flow. For the over-bank flow, the resolution was approximately 0.02m in the vertical and 0.03m in the transverse direction. The concentrations distributions were measured at seven cross-sections in the downstream direction, and an example distribution is given in fig. 3.2 (Guymer et al., 1989). Table 3.1 gives the location of the sites at which the concentration measurements were made:

Table 3.1 Measurement sites for concentration measurements in the Flood Channel Facility.

Flow	downstream measurement sites (m)	measurement positions in vertical (mm)
In-bank	4,6,8,10,12,14,16	24,34,44,54,64,74,84
Over-bank	4,8,12,16	14,34,54,74,94,114,134,154,159

3.3.2 Background fluorescence.

There were several problems with the tracer data which complicated the analysis of the dispersion of the rhodamine tracer. The concentration data was subject

to a cross-sectional sloping background due to the time required for the measurements to be made at each transverse site. However, as fully described elsewhere (Guymer et al. 1989) the background as subtracted from one concentration data set was not consistent when subtracted from another curve for the same cross-section but at a different depth. This resulted in the 'tracer data with background removed' still having some concentration curves with sloping backgrounds, as depicted in fig.3.3a.

However, here the statistical moments of the concentration field were analysed. The position-weighted concentration moments were then calculated up to the third order (centroid, variance and skewness) and after the stage of initial vertical mixing, showed Gaussian-like shape, with consistent centroids and very small skewnesses in the case of the in-bank tracer test. The higher order statistical moments were nonetheless treated with caution.

The systematic error due to sloping background was worse in the data at 16m than at 14m for the in-bank case (as can be seen by comparison of figs.3.3a and 3.3b) which led to the selection of the 14m downstream as being the site at which the different predictive capabilities of the models were assessed.

3.4 Modelling the mean velocity field.

3.4.1 Previous work.

The mean downstream velocity field measurements at each cross section, u(y,z), were represented by fitting a surface s(y,z) using a bi-cubic spline approximation which was advocated by Brockie(1991) following work on the data set.

This surface can be used to infer the vertical velocity profiles at every horizontal location in the flow and, moreover, the shape of these profiles is influenced by the entire velocity field. Brockie (1991) used independent polynomials to interpolate to the velocity distributions in the transverse direction, at each depth of measurement, and the particles in the random particle tracking model were only allowed to reside at the measurement depths.

3.4.2 Modelling the viscous sub-layer

The viscous sub-layer is modelled in the random particle tracking models for smooth walled boundaries, by disallowing the particles to penetrate to within a specified distance of the boundary. The length scales of the displacements applied to the particles in the bulk of the flow would not apply within this thin layer. The thickness of the viscous sub-layer has been estimated from observations as $: Zo = \frac{O(10)}{\mathrm{Re}}$ (m), for example see Young, 1989. Where Re is the Reynolds number and O( ) stands for 'the order of'. Allen (1982) used Zo = 15/Re (m).

The same value of viscous sub-layer thickness which was adopted by Allen was used in this study, which for the over-bank flume flow, with a Reynolds number (based on the friction velocity, depth and molecular viscosity of water) of approximately 2166, gives Zo = 0.007m. The use of a viscous sub-layer confines the flow modelling to a channel with a smooth bed (Allen, 1982, Young, 1989).

3.4.3 Interpolations between point velocity (downstream mean component) measurements for in-bank and over-bank flows.

The in-bank flow was of a regular enough cross-sectional geometry to fit a surface to the entire y-z (transverse, vertical) velocity domain, although it was found that the over-bank flow geometry was too irregular to allow the fitting of a surface to the velocity field. Therefore the over-bank flow was divided into the two regions, as shown in fig. 3.4, and only the in-bank region of the velocity field had a surface fitted to it.

Fig. 3.4 Diagram showing interpolation techniques applied to the Over-bank and in-bank regions of the Flood Channel Facility, Wallingford (not to scale).

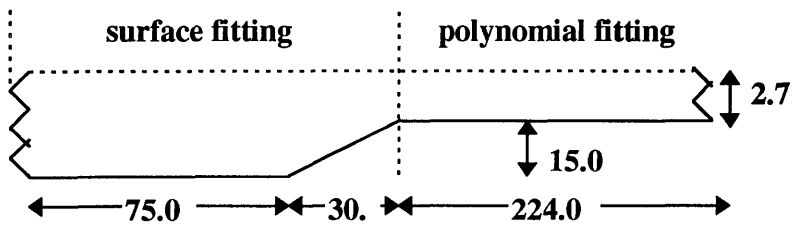

{*all measurements in cm.*}

The over-bank velocity field was divided vertically into three (there were three depths of velocity measurements in this region) and Chebychev polynomials were fitted to each of the resulting horizontals. The velocity field was determined at any vertical through a logarithmic interpolation between these polynomials as described below. The

vertical profile in the over-bank region away from the boundaries is generally agreed to be described by the log law (for example, see Tominaga and Nezu, 1990).

There was no secondary mean advective velocity (i.e. v or w) data available at the time of writing, and the effects of the secondary advections were absorbed into the effective dispersivity coefficients for the random walk model.

Surfaces were also fitted to the distributions of the fluctuating velocity fields u',v' ,w' and Reynolds stress fields, $\overline{u'w'}, \overline{u'v'}$, for the in-bank flow. The process of surface fitting is described in sections below.

3.4.3 Bi-cubic spline approximations

This section describes the use of bi-cubic splines to interpolate between the velocity measurements, using NAG algorithm, E02DDF. The velocity measurements in the vertical and transverse direction formed a surface which could be expanded in terms of normalised bi-cubic splines, given by $M_i(y)$ and $N_j(z)$ in equation 3.1:

$$u_{surface}(y,z) = \sum_{i=1}^{Mx-4} \sum_{j=1}^{My-4} P_{ij} M_i(y) N_j(z) \qquad (3.1)$$

where M_X is the number of knots (linking together cubic splines) in the y direction and M_Y is the number of knots in the z direction. The coefficients, P_{ij}, are then calculated subject to minimising the velocity residuals whilst constraining some function of the curvature such as a second differential (Mackay, pers. comm., 1993). The NAG

algorithm, E02DDF uses a parameter S, the size of which determines the extent of trade off between closeness of fit and smoothness, although the precise functional form of the constraint is not given in the description of the algorithm.

A formal technique for determining the optimum trade off between smoothness and closeness of fit was required. It was evident from the plots of the resulting surfaces (see fig. 3.5) that at the extreme of having the largest permissible number of splines (or knots, limited by the degrees of freedom available) the surface becomes unstable and oscillates. At the other extreme of having the smallest number of knots, the surface is clearly too smooth and ignores the small scale features in the data.

The optimum S factor was estimated using a cross-validation technique which will be described in section 3.5.5. The measured velocity field had a high resolution, and it was relatively simple to visually detect deviations away from the shape of the measured velocity field.

3.4.4 Surface fitting at the flow boundaries

All of the models described in chapter 2 incorporated the mean velocity field interpolations described below. The velocity data sets did not cover the entire flow domain, since velocity measurements could not be made right up to the boundaries. However the random walk model requires the complete flow domain (outside of the viscous boundary layer) if the flow is to be modelled. Consequently a few 'dummy' data points were initially introduced at the boundaries having zero velocities in order that the surface fitted the entire flow domain.

The bi-cubic spline coefficients required to define the surfaces were determined using a program incorporating NAG subroutine E02DDF, and values of the surface were then determined at user defined locations using NAG subroutine E02DFF so that they could be compared with the data.

Since the flume is symmetrical, only half of the flow field was used in the fitting, the opposite half was assumed to be a simple reflection about the centre line, although this would not be true for a non-axis symmetric flow geometry such as that for a meandering channel. This was conveniently implemented through temporarily changing the sign of the transverse position of the particle during the subroutine in which the velocity of the particle was returned.

Similarly in the case of the over-bank region for the over-bank flow case, the polynomial coefficients were determined using NAG routines, E02ADF and E02DDF.

3.4.4.1 In bank flow interpolations close to the boundaries.

The closest velocity measurements which were made to any boundary were between 9 mm and 15mm away from the bed for the in-bank flow (Subsequent to these measurements, the velocities were measured closer to the wall, at 2mm, using the Preston tube technique, although these measurements were not available at the time of writing) . Dummy data points were put in place at the boundaries with zero velocities, although they were given zero weightings. The problem with giving these points zero velocities with weightings, was that for the velocity field to drop to zero in the space of a few millimetres, a large number of knots had to be used with the S factor having a very small value to give good closeness of fit. It is evident from fig. 3.5 that a large number of knots gave rise-

to a large degree of instability elsewhere in the flow domain. However, the exclusion of a weighted, zero velocity point at the boundaries introduces two problems:

(1) A contradiction to the non slip condition.

(2) It can also have the effect of reducing the velocity gradient close to the wall from its true value.

However, the contradiction of the non-slip condition was not experienced by the particles since they were reflected about a point a small distance from the boundaries, this representing the modelled viscous sub-layer (discussed above). This distance represented the viscous sub-layer thickness on the smooth bed of the channel, and was estimated in section 3.5.2 to be 7mm.

The second problem of a reduction in the near bed velocity gradient, caused by excluding the weightings was therefore only a problem in the region of flow between Z = 7mm and z = 9mm or 15mm depending on the local value of the minimum depth of velocity measurement. It was assumed that the uncertainties arising from this form of approximation were smaller than those which were found to arise from using weightings.

In the case of the fluctuating velocity field, the inclusion of weighted zero velocities at the boundary produced a peak in the velocities which was unphysical since it displaced the region of maximum turbulent energy production away from the boundaries, whereas in reality the maximum is very close to the boundary (see Tritton, 1990 or Raupach, 1991). The fluctuating velocity field was therefore not extrapolated to zero at the boundaries, but rather the value of the fluctuating field at an adjacent

measurement site was adopted at the boundary. The same procedure was carried out with the interpolations of the Reynolds stresses.

Finally dummy data points with zero weighting were also placed at the water surface, where there were also no velocity measurements. The behaviour of the velocity profile close to the surface was chosen through criteria described in the sensitivity analysis in section 3.5.5.

3.4.4.2 Over-bank flow interpolations close to the boundaries.

The closest velocity measurements to the bed were 5 mm for the over-bank flow, and since the same value for the viscous sub-layer thickness as for the in-bank flow was used (7mm), neither of the problems which were discussed above were encountered with the over-bank flow model. Extrapolation of the flow domain was not required, and the interpolation was carried out as described above. In the over-bank region (shown in fig. 3.4), 6th order Chebychev polynomials were fitted to the transverse velocity distributions. These required further interpolation in the vertical direction, and this was done during the particle tracking model, through the use of a logarithmic profile derived from the point values in the vertical, the latter having been determined from the values of the polynomials. Table 3.2 shows the values of the polynomials, splines and data at measurement points at the join of the polynomials and the surface. The small discrepancy in these values was considered to be smaller than the uncertainties arising from the use of surfaces or the polynomials in the first instance.

Table 3.2 Values of the surface and polynomial fits to the over-bank flow where they join together above the bank top.

depth (m)	value of surface (m/s)	value of polynomial (m/s)	recorded value (m/s)
0.155	0.421	0.398	0.412
0.16	0.446	0.455	0.460
0.17	0.462	0.440	0.465

Fluctuating velocity data was not available for the over-bank flow at the time of writing, although some large scale empirical relations determined by Knight and Shiono (1990) were used and are discussed later.

3.4.5 Sensitivity analysis applied to fitting the velocity surfaces

The easiest way of examining the surface was to slice through it horizontally and vertically at those levels at which the data was collected. The resulting curves could then be compared to the raw data. The number of knots used and the S factor were adjusted until :

(a)The instability evident in the graphs(e.g. fig. 3.5 for $M_X = 14$, $M_Y = 12$, where M_X, M_Y are the number of knots used) was minimal.

(b)The extrapolated tails of the graphs(fig. 3.5 for $M_X = 14$, $M_Y = 12$ or $M_X = 13$, $M_Y=11$) showed a minimal deviation from the trend of the interpolated region of the graphs.

The worst area of disagreement between the surface and the data set was found to be in a vertical slice adjacent to the corner made between the flume bed and wall at around y = 0.75m. It was thought prudent to carry out the sensitivity analysis in this region, concentrating on one or two particular verticals (plane y = 0.78m in fig.3.5). The closest fitting surface was chosen by inspection and then the surface was examined at a different vertical also adjacent to the corner (y = 0.70 for the in-bank flow as in fig. 3.5, y = 0.75 for the over-bank flow as in fig. 3.6). The surface was split into further slices horizontally and vertically (for example, see fig. 3.7 for the in-bank flow, fig. 3.8 for the over-bank flow) where it could be compared to the data and was considered acceptable.

For the in-bank flow case, the surface was fitted to the fluctuating velocity fields (figs. 3.9 and 3.10) in order that, for some random walk models, the step sizes could be scaled using the local values of the known velocity fluctuations. This introduced the inhomogeneous turbulent flow field of turbulent shear flow to the models which incorporated these fields, which also introduced the complications discussed in chapter two. It was more difficult to fit a surface to the Reynolds stress field because of the large depthwise variation, and fig. 3.11 shows a poor closeness of fit to the data. However, the general shape of the distribution was at least modelled, so that the effect of a cross stream varying Reynolds stress could at least be addressed.

Fig. 3.1

Schematic representation of secondary velocity structure in the over-bank flow examined using a random particle tracking model after Shiono and Knight, 1991.

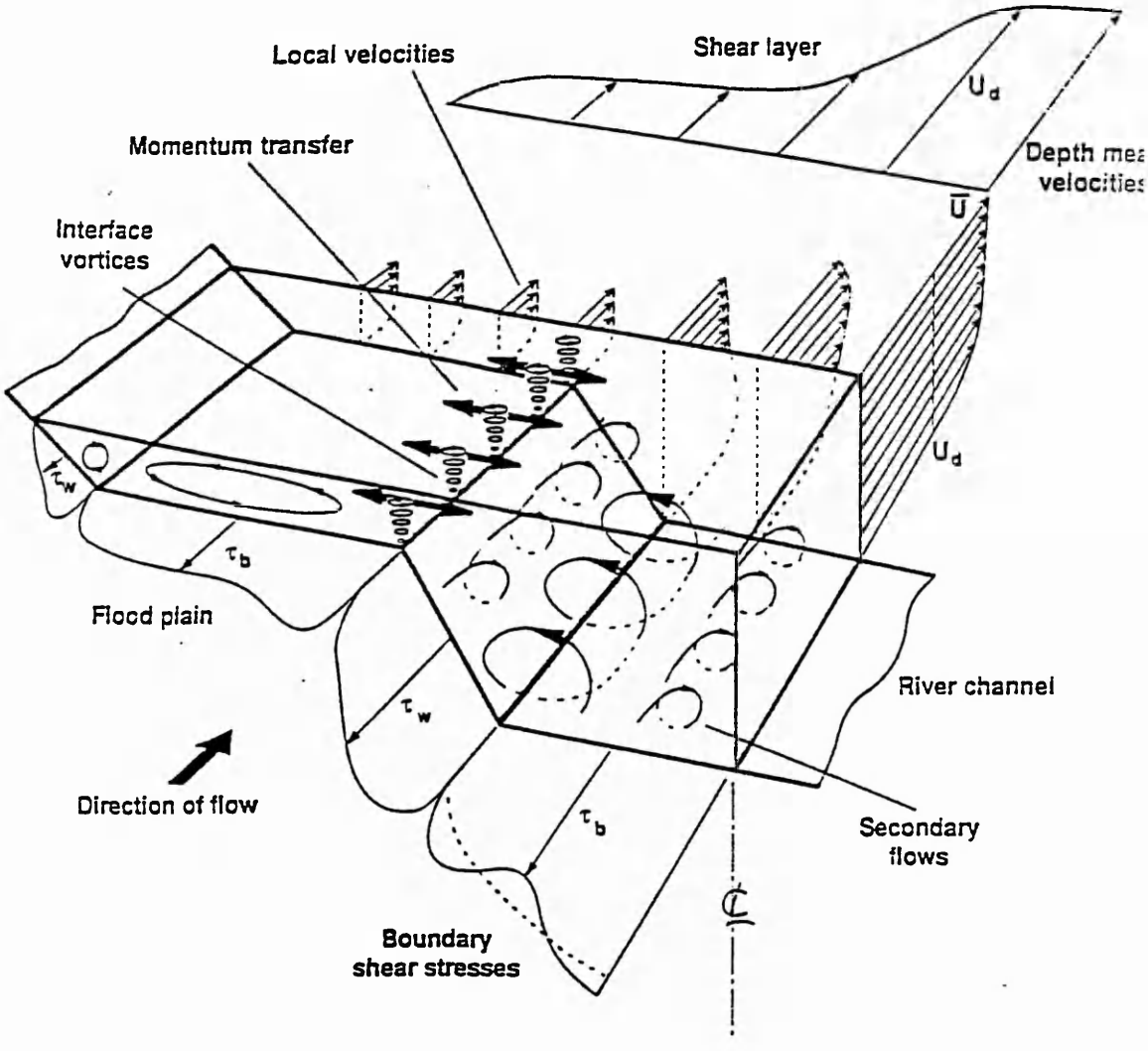

Fig.3.2
Example set of tracer data from the experiments of Guymer and colleagues, 1989

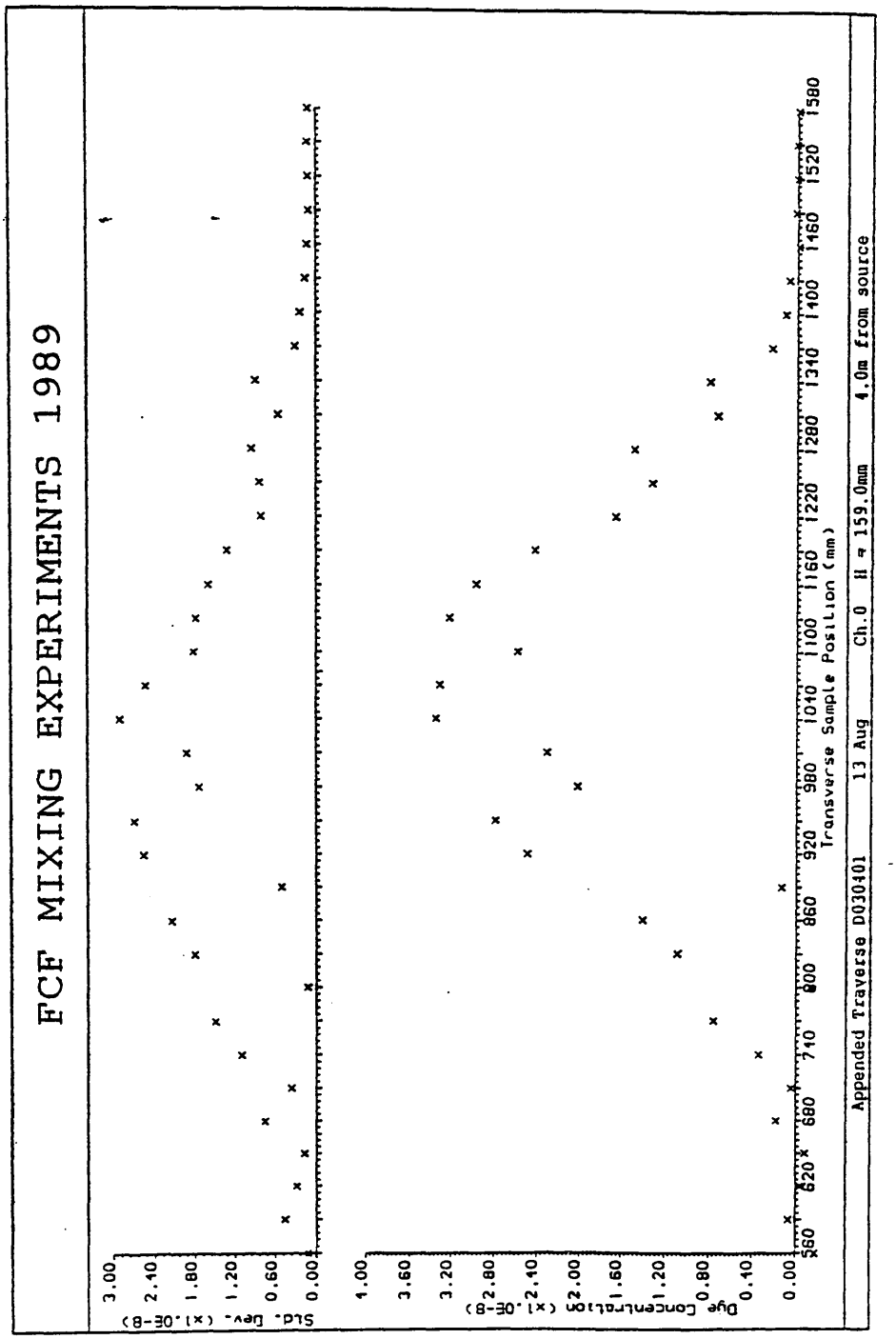

Fig.3.3

Examples of measured concentration distributions with backgrounds removed, showing systematic error at 16m downstream for the in-bank flow.

a

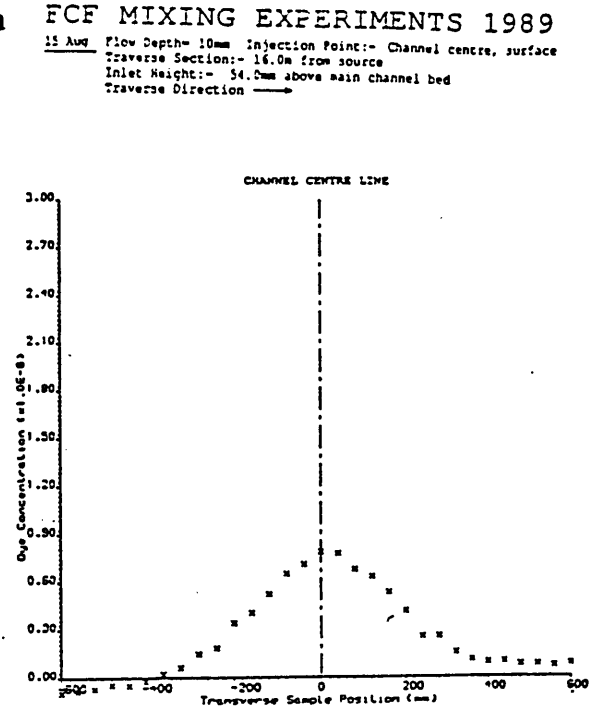

b

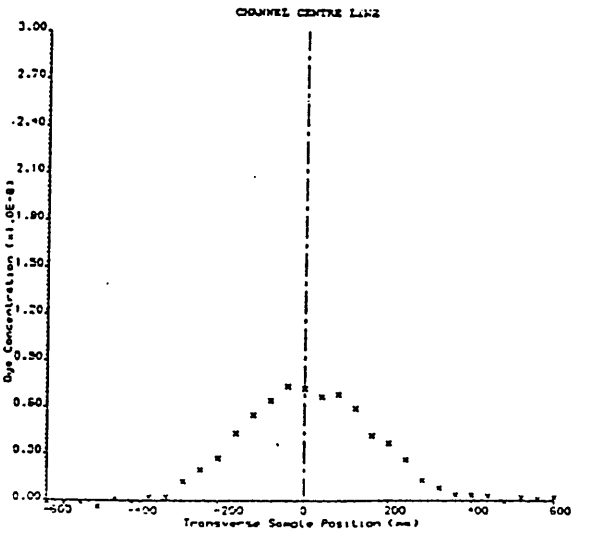

Fig.3.5

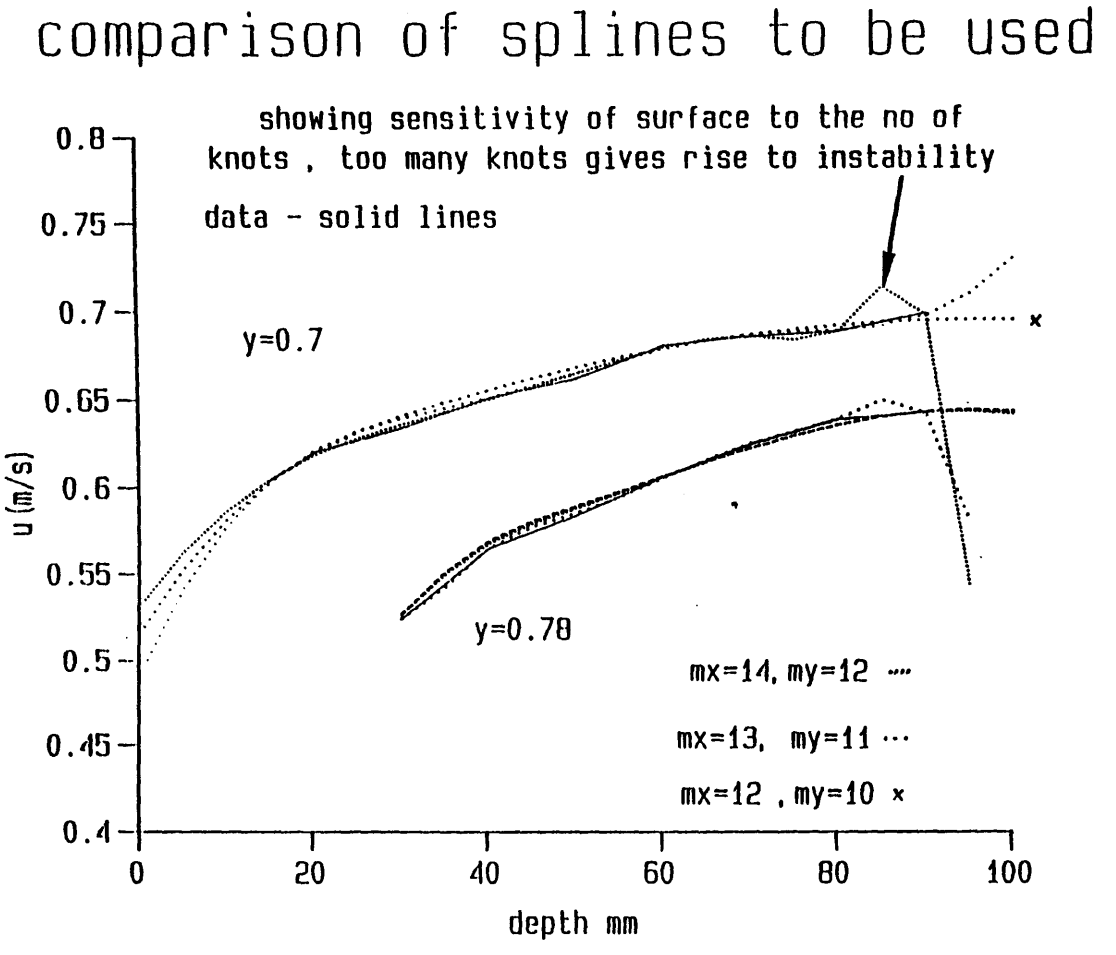
comparison of splines to be used
showing sensitivity of surface to the no of knots , too many knots gives rise to instability
data - solid lines
y=0.7
y=0.78
mx=14, my=12
mx=13, my=11
mx=12 , my=10
u (m/s)
depth mm
0.8
0.75
0.7
0.65
0.6
0.55
0.5
0.45
0.4
0
20
40
60
80
100

Fig.3.6

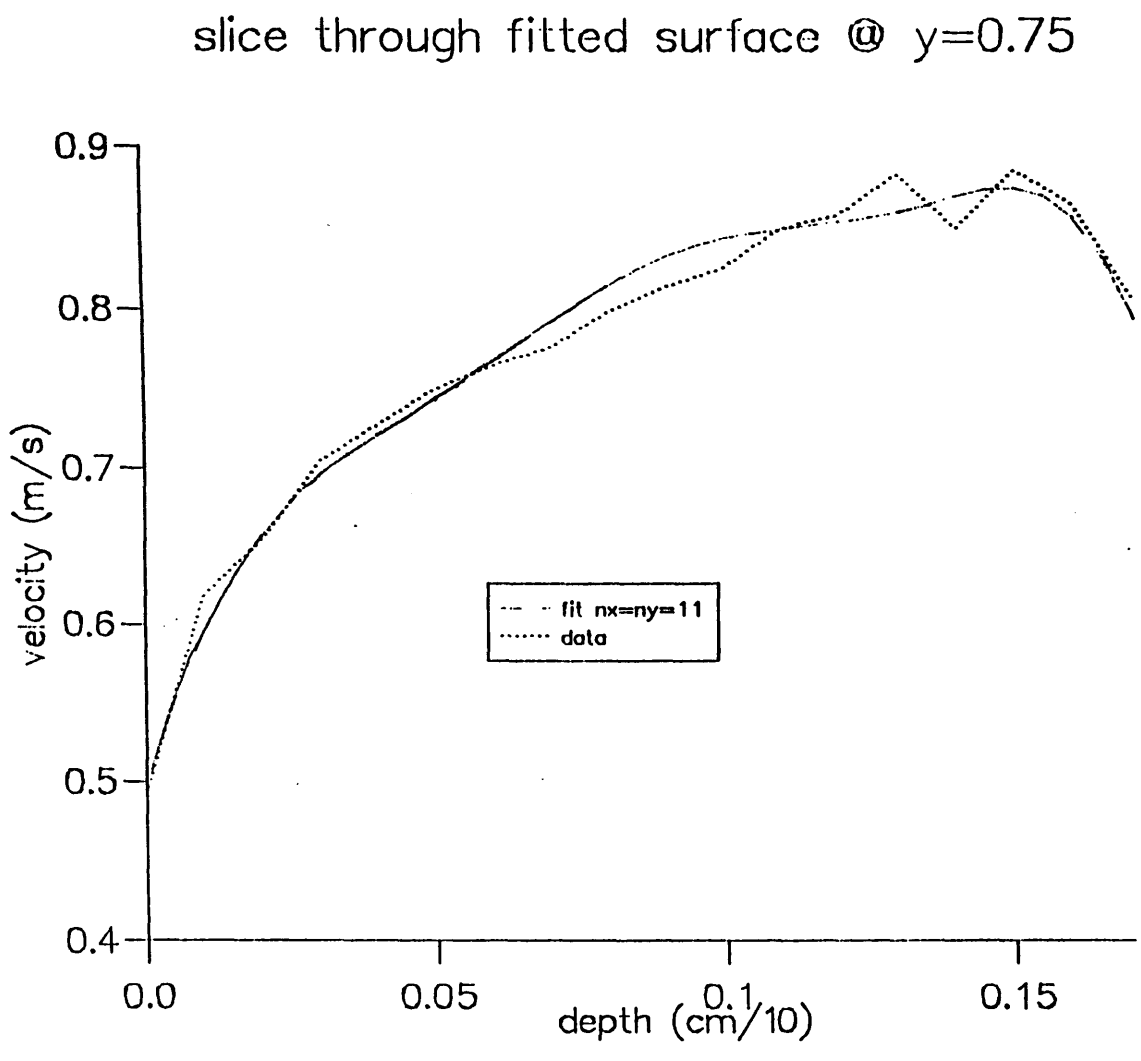
over bank flow , h=0.177
slice through fitted surface @ y=0.75
0.9
0.8
0.7
0.6
0.5
0.4
velocity (m/s)
fit nx=ny=11
data
0.0
0.05
0.1
0.15
depth (cm/10)

Fig.3.7

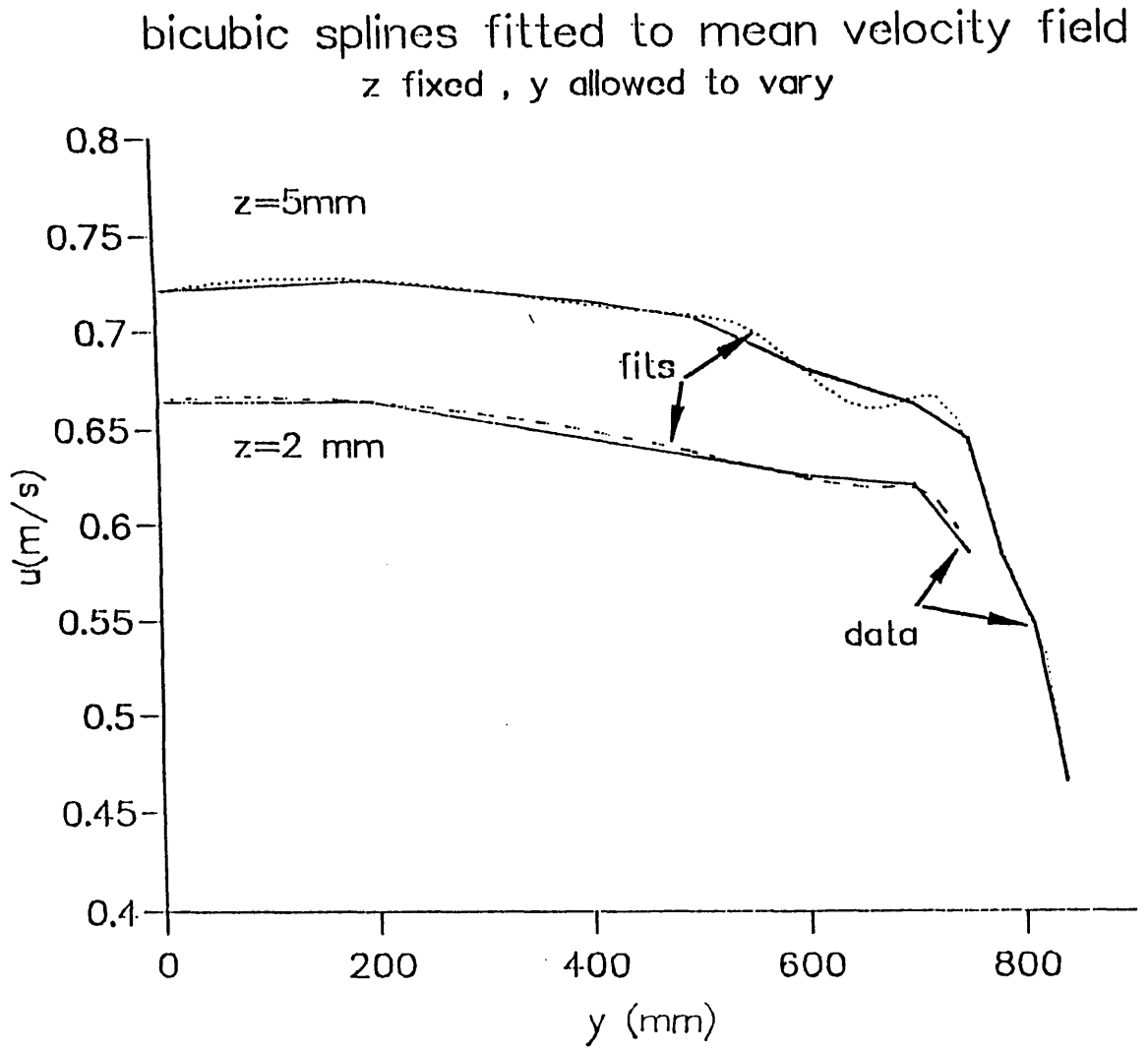
bicubic splines fitted to mean velocity field
z fixed , y allowed to vary
z=5mm
z=2 mm
fits
data
u(m/s)
y (mm)
0.8
0.75
0.7
0.65
0.6
0.55
0.5
0.45
0.4
0
200
400
600
800

Fig.3.8

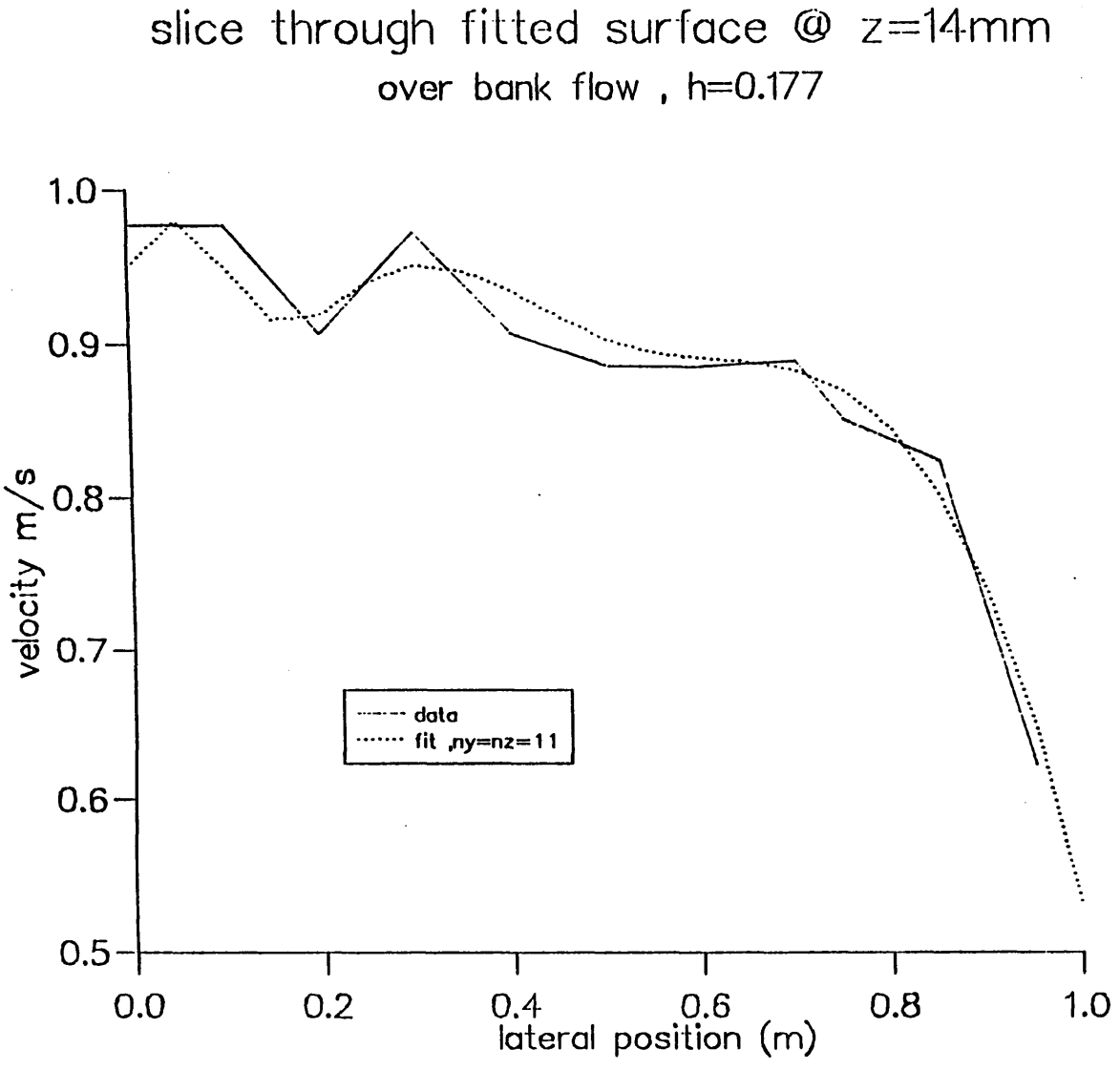
slice through fitted surface @ z=14mm
over bank flow , h=0.177
1.0
0.9
0.8
0.7
0.6
0.5
velocity m/s
data
fit ,ny=nz=11
0.0
0.2
0.4
0.6
0.8
1.0
lateral position (m)

Fig.3.9

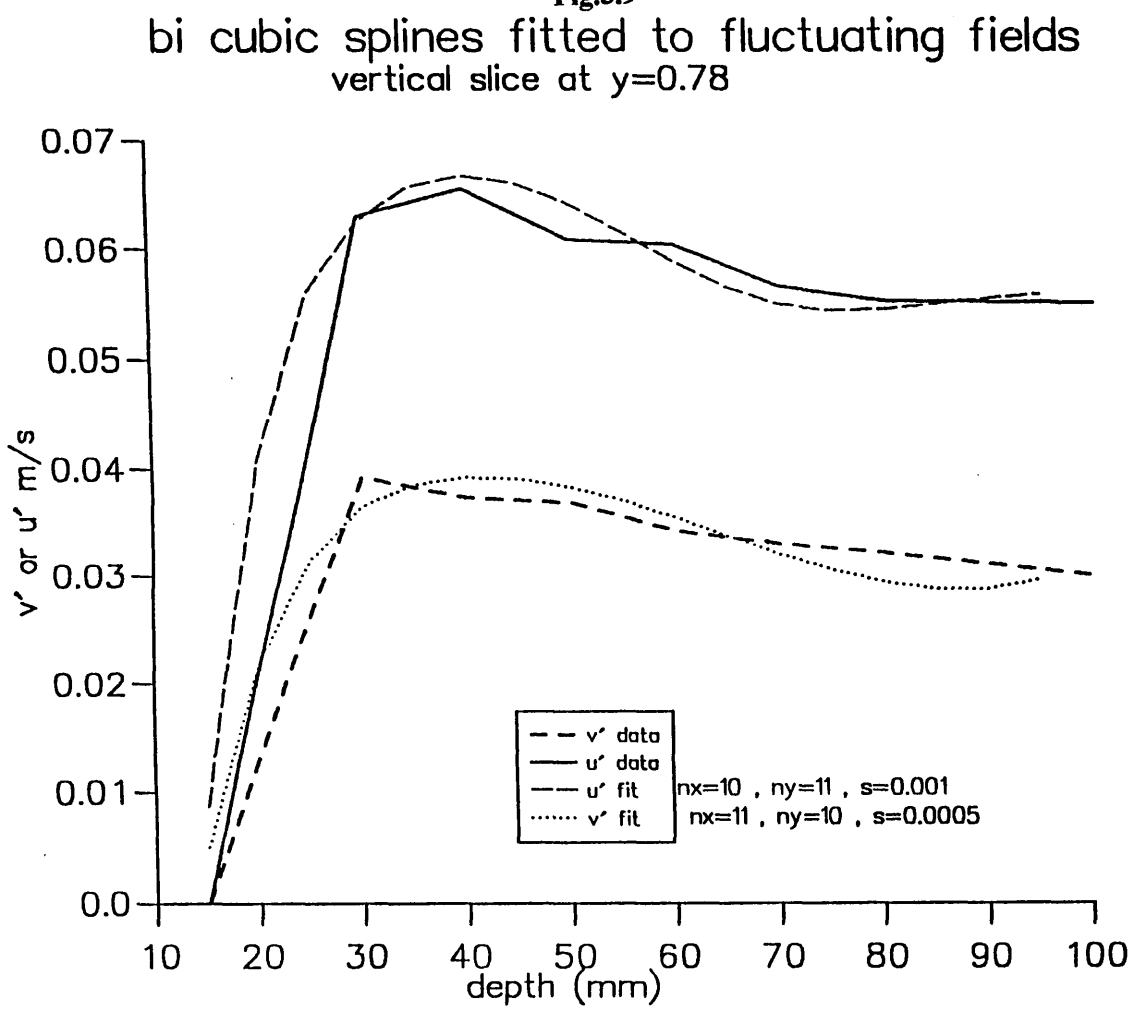
bi cubic splines fitted to fluctuating fields
vertical slice at y=0.78
0.07
0.06
0.05
0.04
0.03
0.02
0.01
0.0
v' or u' m/s
10
20
30
40
50
60
70
80
90
100
depth (mm)
v' data
u' data
u' fit
v' fit
nx=10 , ny=11 , s=0.001
nx=11 , ny=10 , s=0.0005

Fig.3.10

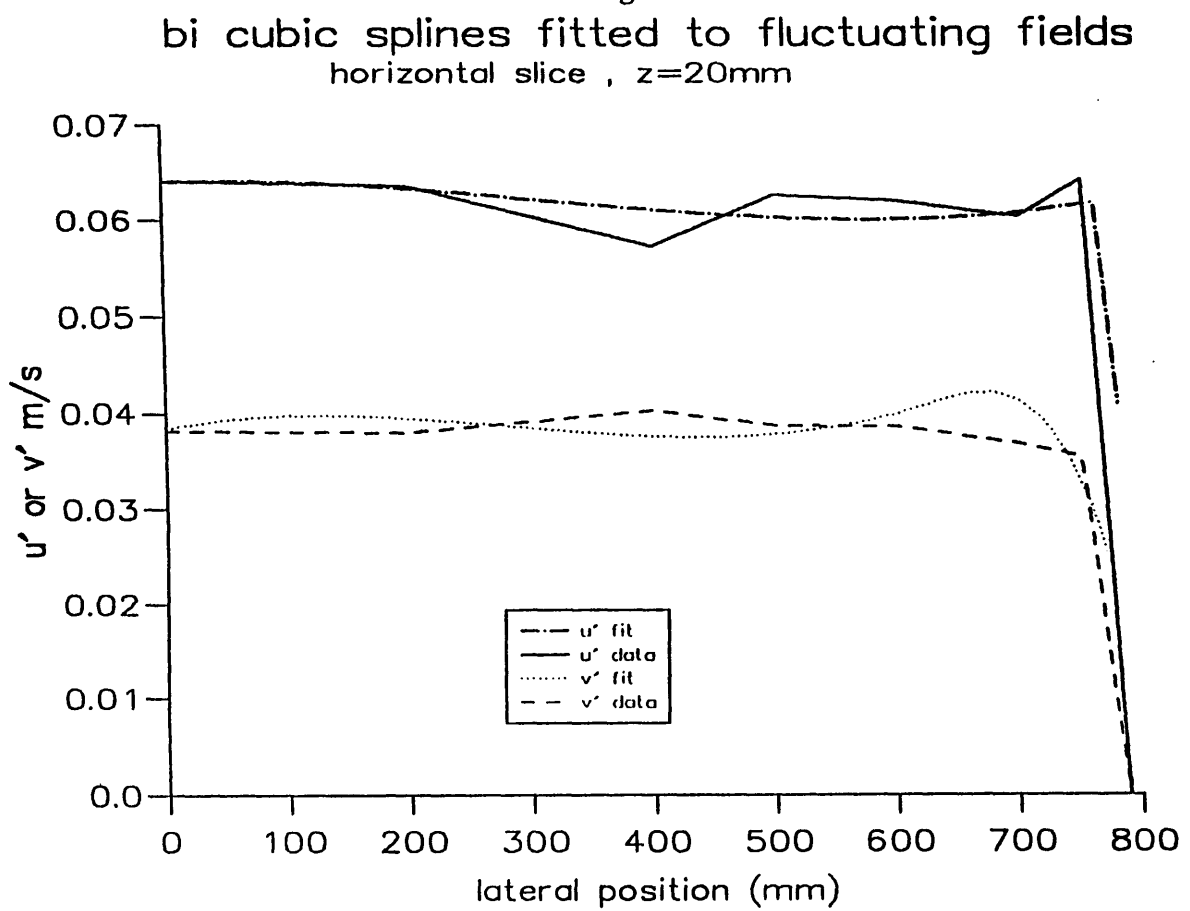
bi cubic splines fitted to fluctuating fields
horizontal slice , z=20mm
u' or v' m/s
0.07
0.06
0.05
0.04
0.03
0.02
0.01
0.0
0
100
200
300
400
500
600
700
800
lateral position (mm)
u' fit
u' data
v' fit
v' data

Fig.3.11

bi cubic splines fitted to fluctuating fields

u'v' field

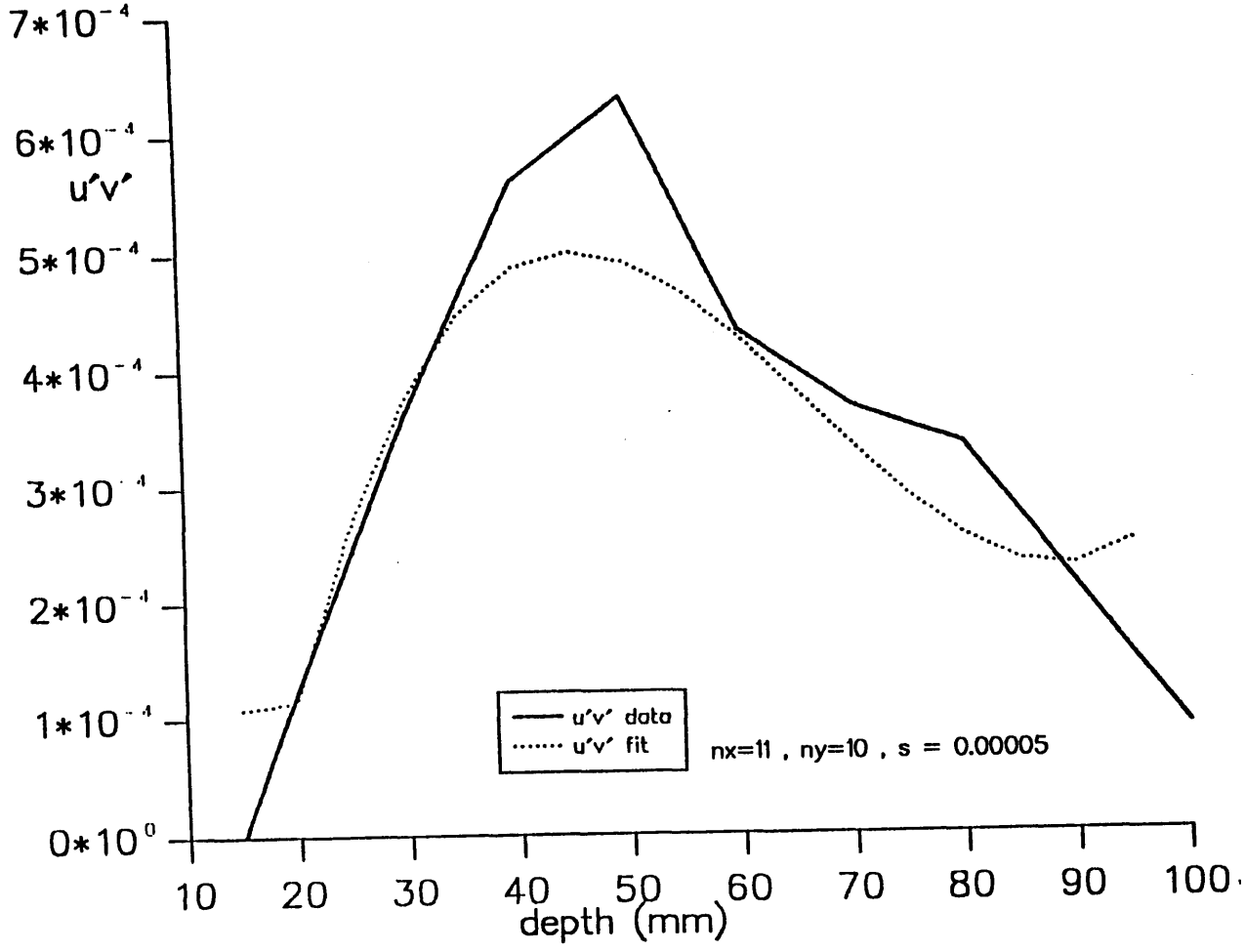

Chapter 4

Sensitivity analysis of different random walk models using the measurements from the Flood Channel Facility.

4.1 Introduction

This chapter aimed to measure the sensitivity of the macroscale particle dispersion characteristics in the two channel flows to the form of the velocity perturbations incorporated in the different random walk models. The more simple of the two flows was studied first, for which more detailed flow measurements were known and which could be incorporated into some of the random walk models. By using two flows of different complexity, the flexibility of the random walk model in general was also tested to some extent, although the sensitivity analysis for the over-bank flow is less detailed.

For each flow one set of concentration measurements at the closest point to the dye-release point were sacrificed in order to calibrate the different models. This was achieved by varying the size of two principal variable parameters (as described in chapter 2, f_v and f_w adjust the size of the displacements in the horizontal and vertical planes respectively), until the macroscale behaviour of the ensemble average particle concentration field was in as far as possible in agreement with the measured concentration field. The closeness of fit of the modelled and measured concentration distributions was assessed in terms of two objective functions, which were based upon the second order moments of the distributions.

The objective functions were optimised to a resolution which was determined as being compatible with the degree of uncertainty of the collected data.

Having forfeited the concentration measurements made at one site downstream, the calibrated models were then used to predict the measured concentration distributions further downstream. The predicted particle distributions were once more compared against the measured concentration distributions at the furthest downstream site, using the same measures for the closeness of fit which were used at the calibration stage. The relative performances of the different models were finally cross-compared for the in-bank and over-bank flows.

Before the main sensitivity analysis described above was carried out, a number of preliminary investigations were undertaken into more general properties of the random walk models, which include an investigation into the number of particles which were necessary to achieve steady particle distributions (section 4.2) and into the behaviour of the distributions in the presence of boundaries (section 4.3). The sensitivity analysis described above was then carried out in sections 4.4 to 4.7 and section 4.7 concludes the first four chapters of this thesis.

4.2 The steady state

The number of particles (N) which was necessary to obtain particle distributions which were in the steady state was established by looking at the variation in the centroids and variances of the particle distributions in the model for repeated releases having different random sequences. The statistical uncertainty in estimates of the second order moments is proportional to $1/\sqrt{N}$ for a one-dimensional continuous

line source, and increases multiplicatively with the number of dimensions (Sawford 1985), so for 20000 particles an uncertainty of approximately 2% in the spread would be expected for a line source. Here the output from the model is examined in three dimensions, and the particles are released from a point source.

The centroid in the particle number or the measured concentration distributions were estimated from an approximation to the integral given by equation 4.1, via the trapezium rule.

$$\text{centroid} = \frac{\int_{-\infty}^{\infty} yCdy}{\int_{-\infty}^{\infty} Cdy} \qquad (4.1)$$

$$\text{centroid} \approx \frac{\sum_{y\,min}^{y\,max} yC\Delta y}{\sum_{y\,min}^{y\,max} C\Delta y}$$

where here C represents either the measured mean concentration or the number of particles, and ymax and ymin determine the limits of the measurement field. Δy is the separation between measurements in meters (or the width of the mesh size for the grid over which the particle numbers are summed in the determination of the particle distributions in the modelling work). The error incurred due to cutting off the tails of the distributions (through the use of finite limits, ymax and ymin) was thought to be minimal, as the concentration distributions were flattened out and close to zero in the vicinity of ymax and ymin.

Similarly, the second order moment (spread) of the measured concentration or particle number distributions were determined from an approximation to the integral given by equation 4.2:

$$(\text{spread})^2 = \frac{\int_{-\infty}^{\infty} C(\text{centroid} - y)^2 dy}{\int_{-\infty}^{\infty} C dy} \qquad (4.2)$$

$$(\text{spread})^2 \approx \frac{\sum_{y\,\text{min}}^{y\,\text{max}} C(\text{centroid} - y)^2 \Delta y}{\sum_{y\,\text{min}}^{y\,\text{max}} C \Delta y}$$

A value of N = 20000 was found to give less than 1% variation in both the position of the depth-averaged centroid and the spread, when six different random number sequences were used for each model, as demonstrated for the random walks, NEWJUMP and CORJUMP2 in table 4.1 below (these were found to be representative all of the random walks).

Table 4.1 Standard deviation away from the mean spread and centroid for repeated runs of the random walk model using 20000 particles for the in-bank flow.

example random walk	coefficient of variability of depth-averaged spread	coefficient of variability of depth-averaged centroid
NEWJUMP	0.002	0.00001
CORJUMP2	0.001	0.00001

4.3 Reflection at boundaries

In this section, the macroscopic behaviour of the particle distributions was investigated in the vicinity of the boundary for different forms of reactions when a particle impinged upon a boundary. The random walk with a displacement size which was selected from a normal Gaussian distribution (NEWJUMP) was used in this part of the study, in order that the particles were not restricted positions at to discrete distances away from the boundary. Cross-correlations in the random walk used here were excluded in order that the behaviour of the particles could be investigated without any other sources of bias. The flow studied here was for a logarithmic vertical velocity (downstream component) profile, with a one dimensional random walk.

The average absolute size of the displacements was chosen so that it was approximately one tenth of the flow depth (a value used by Allen,1982 and Van Dam, 1991), in order that the particles became vertically well mixed. 10000 particles were

used (since this was a simple one dimensional random walk), and each of these were allowed to wander for at least 100 time steps (100 displacements).

The two sorts of interaction which were investigated here, were for the cases for which the particles either reflected on contact with a boundary or remained at the same distance away from the boundary, should the next displacement have taken the particle beyond the boundary.

At the downstream output boundary, the depth was split into thirty sub-divisions, which gave a greater resolution than the average absolute size of the displacements, in case there were small scale effects close to the boundary. The numbers of particles in each sub-division were then determined, and a frequency histogram was constructed for both type of interaction, shown in fig. 4.1.

4.3.1 Results and discussion for the case where particles reflect at the boundaries.

Fig. 4.1 shows that there were no surfeits or dearths of particles close to the boundary (-5 on the abscissa), which were in excess if the random uncertainty associated with the random walk, which was approximately 5 %. There were therefore no discernible facets to the macroscale behaviour due to the presence of the boundary, for the number of particles used, and at the resolution examined.

There is a theoretical discrepancy with the treatment of particles close to the boundaries in this way, although this has evidently not affected the macroscale particle distribution. This discrepancy can be understood schematically using fig. 4.2:

Fig. 4.2 Diagram illustrating the modified particle displacement distribution due to the presence of a boundary for a random walk in which the displacements are selected from a normal Gaussian distribution.

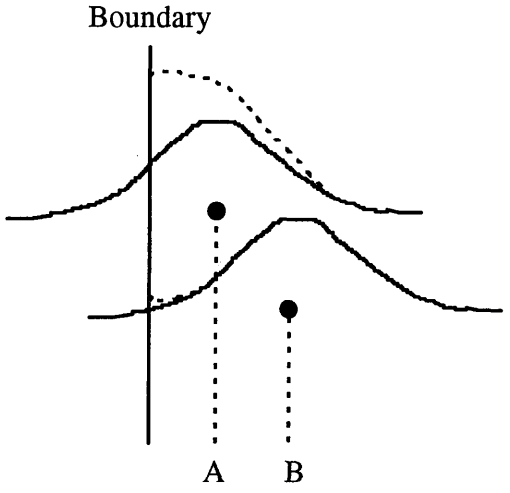

where the solid curved lines represent the Gaussian probability distributions for the next displacement size for particles A and B. The dashed curved lines represent the modified probability distributions due to the presence of the boundary. It now becomes clear that particle A has a greater probability of moving to the location at which particle B is at than particle B has of moving to the location at which particle A is. This asymmetry is a violation of the principle of conservation of mass for the individual particles (or downstream linear momentum, as discussed by Hoogebrugge and Koelman,1992).

This form of boundary interaction was used by Heslop and Allen(1993), and in all of the studies of a random particle tracking model in a bounded flow which are

known about. The study by Heslop and Allen, however, used constant sized steps, so this problem was not encountered.

4.3.2 Results and discussion for the case where particles remain at their present location, if their next step takes the particle across the boundary.

The second form of boundary interaction was examined since it preserves the symmetry which was discussed in the last section. Fig. 4.1 shows that the macroscale particle distributions for this form of interaction were also not affected by the presence of the boundary.

The first sort of behaviour, whereby the particles are reflected was used in the models used in this chapter, for consistency with previous work and since no adverse macroscale effects had been discovered.

4.3.3 Reflection from an inclined surface.

If the particles are reflected about their angle of incidence to an inclined surface then the individual particle momenta are conserved (for example see Matalas,1980). The net result of many of such reflections is to enhance the transverse mixing by a small amount. However, in this study, it was thought that by separating the vertical and transverse mixing of the particles, calibration of the vertical and horizontal displacements in the random walk would be simpler. This allowed for more independent studies of the horizontal and vertical mixing coefficients. For this reason,

most of the random walks only allow for vertical reflection from the boundaries, no matter what the inclination of the bed. This implies that the transverse mixing effects due to vertical motions in the real flow are lumped into the transverse mixing coefficient. Nonetheless, the reflection about an angle of incidence, in the manner shown schematically in fig. 4.3 for the over-bank flow was investigated.

Fig. 4.3 Diagram to illustrate transverse mixing due to a vertical displacement and a non-horizontal surface.

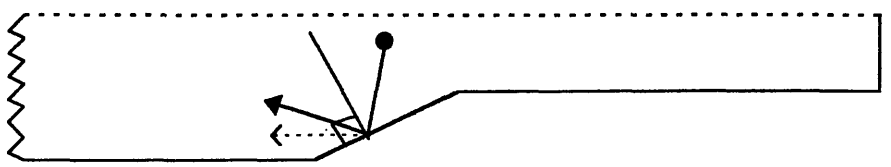

where the solid particle path results from the reflection from the inclined boundary surface, and the dashed arrow represents the transverse component of the reflected particle's velocity.

This form of reflection was likely to have a greater effect in the case of the over-bank flow, for which the particles were released from the top of the bank above the join between the main channel and the over-bank region. In this case, the released particles faced an asymmetrical flow field, and the reflection about an angle of incidence was likely to cause a skewness in the transverse tracer distribution. Results are reported as part of the studies of over-bank flow in section 4.6.

4.4 Sensitivity analysis: Investigation into the ability of different random walks to model the observed concentration distributions.

The different random walks were now calibrated by varying the f_V and f_W parameters until the macroscale particle distributions were in agreement with (as close as was possible, given the sensitivity of the objective functions shortly to be described) the measured concentration distributions at the first cross-section downstream. These calibrated values were then maintained, and the particles were advected further downstream, where their evolving macroscale statistics were compared again to further concentration measurements.

4.4.1 Calibration of different random walk models.

The displacement sizes, or the average magnitude of the displacement sizes for the different random walks were now calibrated using the concentration distributions which were measured at 4m downstream. The time intervals between the displacements for the random walks, which were not intended to model the particle movement at sub-Lagrangian integral time scales, were set at the value of 0.4s from the measurements of Sullivan, described in chapter 2. Since this was only an 'order of magnitude' estimation of the Lagrangian integral time scale, the value was not doubled

in order to achieve a 'self-consistency' in the autocorrelation curves of the random walk. For the Markovian models, a time step which was one tenth of this value was used (0.04s), for which the exponential form of the autocorrelations was consistent with the continuum case, as discussed in chapter two (section 2.2.6). Further details of the different random walks were given in chapter 2.

The random walk algorithms were assessed by their ability to match the observed spread in the data at different depths at a downstream distance of 14m (for the in-bank flow) or 16m (for the over-bank flow), having been optimised to fit the spreads at different depths at a cross-section 4m from the source. The transverse and vertical displacements, together with the time step were considered to be the most important degrees of freedom within the model.

The sizes of the vertical and lateral displacements were adjusted by the varying the multipliers of the estimated Lagrangian integral length scale, f_W and f_V. In this way the values of the multipliers ought to be of the order of unity, if the estimate is good. The estimated length scale was either the ensemble average Lagrangian length scale determined from Sullivan's work, which was described previously, or a local value determined from the Eulerian velocity.

All of the random walks included a downstream random displacement, although the downstream dispersion due to turbulent fluctuations is usually assumed negligible compared to the effects of differential advection (as discussed in chapter 1). However, some of the random walks included cross-correlations, for which it is necessary to include the downstream fluctuating component. Therefore the downstream displacement multiplier, f_U , was included in all the models for consistency. This was

set using the ensemble average measured value of the ratio of w'/ u' = 0.53 for the 100mm in-bank flow and the modelled value of the vertical fluctuating velocity.

4.4.2 Objective function measures.

Two objective functions were devised to measure the closeness of fit of the modelled particle distributions to the measured concentration distributions.

4.4.2.1 An objective function to measure the closeness of fit of the transverse spread of the particle distributions to the corresponding spread of the data.

The squares of the deviation of the spreads in the models (σ_{model}) from the observed spreads of the data (σ_{depth}) at each depth, were summed to make one objective function, called obj1, given by equation 4.3:

$$obj1 = \frac{\sum_{i=1}^{n} (\sigma_{data} - \sigma_{model})^2}{n} \qquad (4.3)$$

where n = number of depths where the concentrations were measured (n = 7 for the in-bank flow, n=1 for the over-bank flow) at and ymax, ymin are the observed bounds to the concentration field in the transverse direction. The spreads were defined earlier, using equation 4.2. Fig. 4.4 shows the variation of spread with depth in the early stages

of mixing (the tracer becomes fully mixed in the vertical direction 10m downstream) for the in-bank flow.

Only a single depth was considered using this objective function for the over-bank flows because the concentration distributions below this depth were highly skewed and would require at least third or fourth order moments to be compared against the particle distributions. The second objective function, shortly to be defined, overcame this problem by comparing the areas under the concentration distribution curves at every depth of measurement with the corresponding measurement for the particle distributions.

4.4.2.2 An objective function to measure the closeness of fit of the modelled and observed vertical mixing.

A second sensitivity factor, obj2, was devised using the ratios of the areas under the particle distribution curves at each depth to the area under the corresponding curve at the surface (the tracer release was at the surface for both flows). These ratios will hereafter be referred to as B_V ratios. The objective function was the sum of the squares of the deviations of the 7 values of the B_V ratio (for the different depths) from the corresponding B_V values constructed from the data, and is given by equation 4.4:

$$obj2 = \frac{1}{(n-1)} \sum_{i=1}^{n-1} \left[\frac{\left(\sum_{y\,min}^{y\,max} C_{model} \Delta y \right)_i}{\left(\sum_{y\,min}^{y\,max} C_{model} \Delta y \right)_n} - \frac{\left(\sum_{y\,min}^{y\,max} C_{data} \Delta y \right)_i}{\left(\sum_{y\,min}^{y\,max} C_{data} \Delta y \right)_n} \right]^2 \qquad (4.4)$$

This sensitivity measure was also minimised through varying the multipliers, f_v and f_w in the way described in the next section. The Bv ratios approach unity for the in-bank flow after 10m downstream, although for the over-bank flow, they are always relatively small because of the effects of the flume geometry on the tracer dispersion (see variation of concentration distributions with depth at 16m downstream in fig.4.5).

The two objective functions which were used in the analyses are not an absolute measure of the performances of the different models. Alternative objective functions could have included a measure of the least square deviations of the model concentration profile away from the data concentration profile, although an argument against this is that the data sets were noisy in themselves, and that only statistical quantities, such as the variance in the overall concentration distributions were less uncertain.

4.4.3 Combination of objective functions.

The values of obj1 and obj2 were normalised individually using the sum of their respective values over all values of f_v and f_w which were investigated. These normalised values were then summed together to create a single objective function, obj3, given by equation 4.5, the value of which could be plotted as a function of fv and fw as a surface.

$$obj3_i = \frac{objl_i}{\sum_{i=1}^{Nvw} objl_i} + \frac{obj2_i}{\sum_{i=1}^{Nvw} obj2_i} \qquad (4.5)$$

where Nvw is the total number of combinations of f_V and f_W used. However, a suitable discretisation interval, or resolution for the f_V and f_W parameters was first required to be determined, which took into the account the uncertainties in the data. In this way the sensitivity analysis could be carried out to a precision which was supported by the resolution of the measurements. The discretisation interval is selected in section 4.4.5 below, following an estimation of the uncertainties in the data.

4.4.4 Estimation of uncertainties in data.

The experimental uncertainty in the measured spread ($\Delta\sigma$) at any particular depth was approximated as the standard deviation of the spread at different depths from the depth-averaged spread at cross-sections were the tracer was considered to be vertically well mixed (from approximately 10m downstream) for the in-bank flow (the experimental error was assumed to be the same for the over-bank flow), given by equation 4.6:

$$\frac{\Delta\sigma}{\sigma} \approx \sum_{i=1}^{7} \frac{\left(\sigma_i^{data} - \overline{\sigma^{data}}\right)}{7\sigma^{data}} \qquad (4.6)$$

where 7 is the number of measurement depths. These fractional standard deviations are given in table 4.2:

Table 4.2 Standard deviations from the depth-averaged spread for the measured tracer concentration distributions for the in-bank flow, when the tracer has become vertically well mixed.

distance downstream(m)	depth-averaged spread (m) (7 depths)	standard deviation from the mean (m)
10m	0.140	0.003 (2%)
12m	0.170	0.004 (2%)
14m	0.184	0.008 (4%)
16m	0.20	0.02 (10%)

The variation of the depth-averaged spread with downstream distance for all of the data (see for example, fig. 4.11) show an irregular relationship, which suggests that the uncertainties in the data are more consistent with the larger deviations in table 4.2. Without further experimental information (such as repeated measurements of the spread at the same depth and transect) the fractional uncertainties in all of the spreads which were determined from the measurements, were assumed to lie between 4% and 10% and a value of 7% was used as an estimate. The large uncertainty at 16m downstream was, however, thought to be in part due to the systematic error which was discussed earlier (due to the incorrect background having been subtracted), and this cross-section was not considered in the sensitivity analysis.

4.4.5 Selection of a discretisation interval for the objective functions taking into account the estimated uncertainties in the data.

The sensitivity of the spread at 4m downstream to varying the factor f_V was investigated for a selection of different models in order to determine a sensible minimum for intervals at which f_V might be discretised . The resulting empirical relationship between f_V and the depth-averaged spread has been plotted in fig. 4.6 for the random walk for which the displacements were taken from a Gaussian distribution (similar plots for the other random walks which were investigated showed a similar relationship). The graphs were approximately linear over the range investigated. From standard error analysis, since this relationship was linear, the fractional uncertainty in f_V could be considered to be approximately the same as the fractional uncertainty in the measured depth-averaged spread. The discretisation interval for the f_V value was therefore made to be approximately 4-5% for the in-bank flow and the over-bank flows. Discretisation intervals of no greater than 5% in the values of f_W were used for the second objective function, since this also depended upon the spreads in the distributions.

4.4.6 Optimisation of combined objective function, obj3.

The surfaces described in section 4.4.3 were examined over ranges of f_V and f_W values which were known to be in the proximity of the best fitting values from experimentation. Two such surfaces are plotted in fig. 4.7, at the downstream measurement site closest to the tracer release point (4m downstream). The combination of the values of f_V and f_W which yielded the smallest value of obj3 were then used to predict the concentration distributions further downstream.

4.4.7 Using the calibrated models to predict distributions further downstream

The predicted particle distributions at cross-sections further downstream were now examined for the different models, using the calibrated values of f_V and f_W in each case. The closeness of fit of each particle distribution to the measured concentration distribution were again examined at the cross-section furthest downstream for each flow (14m for the in-bank flow, 16m for the over-bank flow).

4.5 Results and discussion of sensitivity analysis.

Here the results of the sensitivity analysis for the in-bank flow are presented in section 4.5.1 and discussed in 4.5.2, followed by the presentation of the results for the over-bank flow in section 4.5.3 and the discussion of these results in section 4.5.4.

4.5.1 Results for in-bank flow.

The objective function values for the best fitting (limited by the resolution of the sensitivity analysis) values of f_V and f_W have been arranged in order of increasing total objective function, obj3 (not normalised as in equation 4.5) in table 4.3 (i.e. the closeness of fit to the data is in decreasing order).

Table 4.3 Analysis of particle distributions for the different random walks 4m downstream for the in-bank flow at the calibration stage.

data/model	depth-averaged centroid (m) for release at y=0.0m	depth avgd. spread (m)	obj1* 10^{-4}	obj2* 10^{-3}	obj3* 10^{-3} not norm-alised	f_V	f_W
DATA	-0.0098	0.098 +/- 0.007					
SULLIJA	0.0030	0.099	1.2	0.5	0.6	2.0	0.90
FASTC	0.0086	0.096	0.9	6.6	0.7	2.3	1.10
TURJ2	0.0015	0.100	0.3	0.8	0.9	2.4	1.22
CORJ2A	0.0011	0.101	0.4	0.9	0.9	2.4	1.20
CORJ2B	0.0004	0.100	0.3	1.0	1.0	2.4	1.20
FASTA	0.0014	0.097	1.0	1.2	1.3	2.2	0.94
NSCALE	0.0012	0.099	1.2	2.0	2.1	2.2	0.90
NEWJUMP	0.0011	0.098	1.0	2.0	2.1	2.6	1.14
MARKOV	0.0015	0.095	1.4	2.0	2.2	2.6	1.00
FASTB	0.0029	0.104	1.0	2.9	3.0	1.5	0.78
JUMP	0.0022	0.095	1.1	4.9	5.0	2.9	1.32
JSCALE	0.0012	0.096	1.5	10.0	10.2	2.1	0.98

The optimised f_V and f_W values were kept at the same values, and the particles were allowed to advect further downstream. The evolution of the particle cloud in terms of the increase in depth-averaged spread with downstream distance was compared against the corresponding spreads of the tracer plume. Figs. 4.8,4.9, 4.10

and 4.11 show the variation in depth-averaged spread for the in-bank flow (discussed in section 4.5.2).

The closeness of fit of the different particle distributions to the concentration distributions at 14m downstream, for each random walk, was assessed using the same objective functions as for the calibration stage, and the different models are again arranged in order of decreasing closeness of fit to the data in table 4.4:

Table 4.4 Analysis of particle distributions for the different random walks 14m downstream for the in-bank flow.

data/model	depth-averaged centroid (m)	depth-averaged spread (m)	obj1*10^{-3}	obj2*10^{-3}	obj3*10^{-3}, not normalised
DATA	0.0092	0.184 +/- 0.013			
JSCALE	0.0021	0.179	0.09	1.3	1.4
NSCALE	0.0014	0.184	0.07	2.9	2.9
JUMP	0.0001	0.180	0.11	5.3	5.4
NEWJMP	0.0004	0.185	0.07	5.3	5.4
SULLIJ	0.0019	0.195	0.20	7.5	7.7
FASTC	-0.0015	0.198	0.26	23.2	23.4
FASTA	-0.0019	0.228	1.97	43.4	45.5
MARKOV	0.0011	0.236	2.49	55.4	57.9
TURJ2	-0.0017	0.199	0.27	62.6	62.8
CORJ2A	-0.0023	0.199	0.26	67.4	67.7
CORJ2B	-0.0026	0.198	0.24	71.5	71.8
FASTB	0.0119	0.309	15.62	82.4	98.0
Minimum value of objective function			0.07	1.3	1.4

Fig. 4.12 shows the modelled distributions for the model NEWJUMP, at the calibration and prediction stages (at example depths) and compares these to the measured concentration distributions. These distributions were typical of most of the models, the performance of which is summarised in the tables above. Figs. 4.13 again shows the predicted particle distributions at cross-section 6 for several different models, which are again representative of the results summarised in the tables above.

4.5.2 Discussion of in-bank flow results.

This discussion is split up into four principal sections, which refer to the calibration stage, the evolution of particle cloud with downstream distance, the prediction stage, and several comparisons between models having similar properties.

4.5.2.1 Calibration stage for in-bank flow.

The values of the centroids in the first column of table 4.3 show the presence of a small bias since the centroids were all positive, compared to the small negative value observed for the centre line release, which was consistent to all of the models. However, the centroids deviated by less than a single centimetre in all cases, which was smaller than the resolution of the measurements (3cm: see chapter 3), and consequently acceptable.

The values of the spreads in the second column of table 4.3 demonstrate that all of the models could be calibrated so that the spread of the particle distributions matched the spreads in the measured concentration distributions. The fractional deviations (coefficients of variability) of the modelled spreads from the measured range between: less than 1 % to 3.0%, which is less than the estimated uncertainty in the data due to experimental error (7%).

Using simply the depth-averaged spread as an indication of the ability of the model to fit the model is insufficient, since different vertical distributions of the particles could yield the same depth-averaged spread. It is therefore more informative to examine the sizes of the total objective function, obj3, which has been used to sort the different random walks in decreasing order of closeness of fit in all of the tables. The model SULLIJA was found to be the best fitting model at 4m downstream.

The range in the values of obj3 (which is one order of magnitude) stems from the range in the values of obj2 rather than obj1. The objective function, obj2, is derived from the square of the fractional areas under the concentration or particle distribution curves (called Bv ratios, see section). The actual range of values of the Bv ratios is therefore more like a third of an order of magnitude. For the model, JSCALE, the fractional areas to give a poor fit to the data, and yet the deviation away from the depth averaged spread is small. This could be accounted for if the vertical mixing was too rapid, giving rise to larger than expected Bv ratios, yet maintaining a fairly depth averaged spread similar to that in the data.

In fig. 4.12, the example curve labelled 'newjump, 4,84' confirms the good fit of the modelled particle distribution to the concentration distribution at the calibration stage, at 84mm above the bed.

4.5.2.2 Discussion of the evolution of depth-averaged spread curves for in-bank flow.

The graphs of the variations of depth-averaged spread with downstream distance (figs. 4.8-4.11) show that only relatively few of the random walks agreed with the data, to within the estimated 7% uncertainties, for the entire test reach. The random walk models which fitted into this category were JSCALE and JUMP, but the shape of the spread against downstream distance curves for these models were characteristic of many of the models. This observation has lead to the conclusion that there exists an equifinality in the results, which will be expounded upon in section 4.7.

In order to achieve a closer fit to the distributions throughout the test reach, the other random walk models required further calibration, and could not be used in a predictive sense using a single-stage (data from a single cross-section) calibration only. This will also be discussed further in section 4.7.

4.5.2.3 Prediction stage for in-bank flow.

The centroids of the distributions at 14m downstream were again in agreement with the data to within the measurement resolution of 3cm, although this time the centroids had different signs, which is more indicative of random error about a zero centroid.

All of the models were able to predict the spread in the measured concentration distributions to within the estimated uncertainties, with the exceptions of MARKOV, FASTA and FASTB. The range in the coefficient of variability of the spread is between less than 1% and 68%. The range in the values of obj3 (two orders of magnitude) again stems from the range in the values of obj2 (of two orders of magnitude, resulting from a range of one order of magnitude in the Bv ratios) rather than obj1 (which now has a range of one order of magnitude). This is attributed to the same reason described for the calibration stage.

However, it is evident from comparing tables 4.3 and 4.4, especially for the model JSCALE, that achieving a poor fit to the data at the calibration stage, in terms of the total objective parameter, does not necessarily result in a poor fit at the prediction stage. This could be explained if the variation in the effective dispersivity of the tracer with downstream distance is considered (this variation will be discussed in section 4.7). The model, JSCALE, showed a relatively large value of obj2, which resulted from a poor fit to the data in the vertical direction at 4m downstream. The sizes of the steps in the random walk which gave this result, may have resulted in an effective dispersivity which was more representative of the average dispersivity of the

entire channel from 4m to 14m. This could explain the good fit to the data of the model JSCALE at the downstream site, despite its relatively poor calibration. This indicates a shortfalling in the calibration of the dispersion models using information from a single cross-section, which this sensitivity analysis aimed to do.

Fig. 4.13 gives examples of predicted distributions at 14m downstream and at a depth of 84mm, for the cases of models which do and do not fit the data to within the uncertainties. The models, NEWJUMP, CORJ2A and NSCALE are able to give good fits to the data, whereas the model MARKOV has over predicted the spread in the concentration distribution. The over prediction of the rate of increase of depth averaged spread with downstream distance is common to all of the models which do not fit the data, especially between 4 and 10 m downstream. This will be discussed further in section 4.7.

4.5.2.4 Comparison between the simple random walk (JUMP) and random walk with step size selected from normal distribution (NEWJUMP).

The random walk, JUMP, produced transverse concentration distributions which showed a larger than expected scatter, considering that the binomial distribution should approach a normal distribution after 10 steps (see section 2.22). The average number of steps undertaken by a particle travelling 4m downstream was 20 steps. The discrete intervals between the displacements means that the particles are confined to integral numbers of step sizes away from the centre line release position . If the particles all had similar travel times then the total number of random steps which each

particle undergoes could be coincident, causing there to be a bias in the parity of total numbers of steps. This was found to be the case for the random walk JUMP (with constant step sizes) steps over the first 4m of the flow. This resulted in regularly spaced features or 'oscillations' in the concentration curves having a wavelength which was twice the step size, since particles taking an odd total number of steps could not reside at an even integer number of step lengths away from the release point. As the particle trajectories separated via differential advection, the numbers of odd and even total numbers of steps became approximately equal by 6-8 m downstream as demonstrated in table 4.5a, where 20000 particles were used.

Table 4.5a. Analysis of number of particles taking odd and even total numbers of steps between release and measurement cross section for in-bank flow for model using constant step sizes (called JUMP).

distance downstream(m)	number of particles taking odd total of steps	number of particles taking even total of steps
4	5778	14222
6	9517	10483
16	9779	10221

Since the time step in use was not considered as a variable parameter, and it could therefore not be reduced. This effect is avoided to a large extent when the step size is made variable as for the model NEWJUMP, where the total numbers of steps which are even and odd was close, as shown in table 4.5b. The discrepancy in the total numbers of particles taking odd and even number of steps is not as important for this random walk, since the step sizes come from a continuous distribution, and consequently there are no 'oscillations' in the particle distributions.

Table 4.5b. Analysis of number of particles taking odd and even total numbers of steps between release and measurement cross-section for in-bank flow for model using step sizes taken from normal Gaussian distribution (called NEWJUMP).

distance downstream(m)	number of particles taking odd total of steps	number of particles taking even total of steps
4	8859	11141

4.5.2.5 Comparison between random walks using an ensemble average and a locally determined cross-correlation coefficient.

Fig. 4.11 demonstrates how the use of an ensemble average cross-correlation between u' and w' (r_{UW}) produced very similar results to the case when the local field values estimated from the measured distributions of r_{UW} are used. This suggested that the use of an ensemble average cross-correlation was sufficient for the uniform flow under study, and that nothing was gained by the inclusion of the finer structure.

4.5.2.6 Discussion of random walks which include correlations.

Some run time Lagrangian autocorrelations and cross-correlations are shown in fig. 4.14 for the model, MARKOV, which were determined from the velocity time series of a single, example particle using the NAG algorithm G13DAF (NAG,1987). In

the model, the time steps were 0.04s, and the 1/e time constant in the autocorrelation equation was set at 0.4s, with a cross-correlation, r_{uv} = -0.27.

Using the same NAG algorithm, the above correlations were recovered from analysis of the Lagrangian time series, confirming that the particles were subject to the correct correlations.

A similar analysis of the autocorrelations for the model FASTC was carried out, for which the 1/e time constant was determined to be the same size as the time step, of 0.4s, which is smaller than might be expected due to the long term correlations present in this kind of noise. However, due to the extreme fluctuations between negative and positive values inherent to this kind of noise (W.Kinzelbach, 1990), the time for the particle velocity to drop below 1/e of its initial velocity can be extremely rapid.

4.5.2.7 Variation of the memory term (H) in the fast fractional Gaussian noise random walk model.

The Fast Fractional Gaussian Noise model with the smallest H exponent (which was called FASTC, for which H = 0.55) has been found to be the model in closest agreement with the observations out of the three FFGN models which were used. Fig.4.10 demonstrates the large difference in the behaviour of the modelled evolution of the spread depending on the choice of the H parameter as described above. If H = 0.5, long term correlation is absent, since the covariance determined by equation 2.29 is zero. This suggests that further calibration of the displacement sizes in the random

walk is required (with particle cloud evolution), if random walks with very long term correlations are used. The fact that the best fitting model was FASTC is consistent with there not being any regions in the flume with which to associate long term correlations. The H exponent could be increased for natural flows were such effects are present, but this might entail more calibration points in the downstream direction.

4.5.3 Results for the over-bank flow.

Here the optimised values of the objective function, obj3, were used again to arrange the different models in decreasing order of closeness of fit at the calibration stage, at cross-section 1 (4m downstream), given by table 4.6.

Table 4.5 Analysis of particle distributions for the different random walks 4m downstream for the over-bank flow.

data/ model	cntrd. at depth = 159mm (m)	spread at depth =159mm (m)	obj1* 10^{-6}	obj2* 10^{-3}	obj3* 10^{-3} not norm-alised	opt. f_v value	opt. f_w value
DATA	1.07	0.169 ± 0.012					
MARKOV A	1.11	0.169	0.04	4.2	4.2	1.0	1.0
MARKOV B	1.12	0.169	0.3	5.2	5.2	1.5	0.7
FASTC	1.10	0.167	2.1	5.4	5.4	2.1	1.4
NEWJUMP	1.12	0.168	1.3	5.6	5.6	2.6	1.1
CORJ3	1.11	0.167	3.0	6.0	6.0	2.5	1.6
CORJ4	1.13	0.166	8.4	6.1	6.1	2.6	1.5
NSCALE	1.12	0.170	0.7	6.5	6.5	1.5	1.4
JUMP	1.08	0.166	8.6	7.1	7.1	2.7	1.1
JSCALE	1.12	0.168	1.4	10.3	10.3	2.1	1.4
NEWJUMPB	1.09	0.163	29.7	38.3	38.4	4.0	1.7

The continuing evolution of the spread in the particle distributions with downstream distance, at a depth of 159mm was examined and compared with the corresponding spreads in the concentration distributions in figs. 4.15 and 4.16.

The predicted particle distributions were then examined in detail at cross-section 7 (16m downstream), using the same objective functions described earlier, and the closeness of fit for each model is given in table 4.7:

Table 4.7 Analysis of particle distributions for the different random walks 16m downstream for the over-bank flow.

data/ model	centroid at depth = 159mm (m)	spread at depth = 159mm (m)	ob1*10^{-3}	ob2*10^{-3}	ob3*10^{-3}
DATA	1.05	0.302 ± 0.02			
JSCALE	1.21	0.314	1.4	10.8	10.9
CORJ4	1.22	0.341	1.5	10.3	11.8
NSCALE	1.22	0.323	4.3	12.0	12.4
JUMP	1.14	0.317	0.2	12.4	12.7
MARKOVA	1.17	0.331	0.8	13.2	14.0
NEWJUMP	1.21	0.342	1.5	12.9	14.5
CORJ3	1.21	0.350	2.2	14.2	16.4
FASTC	1.20	0.360	3.4	14.7	18.1
MARKOV B	1.27	0.343	1.7	24.5	26.2
NEWJUMPB	1.14	0.324	0.5	29.3	29.8
Minimum value of objective function			0.2	10.3	10.9

Fig. 4.17 shows the modelled distributions for the model NSCALE, at the calibration and prediction stages (at a depth of 159mm) and compares these to the measured concentration distributions. These distributions were typical of most of the models, the performance of which is summarised in the tables above. Fig. 4.18 again shows the predicted particle distributions at cross-section 7 for several different models, which are again representative of the results summarised in the tables above.

4.5.4 Discussion of over-bank flow models.

This discussion is again split up into four principle sections, which refer to the calibration stage, the evolution of particle cloud with downstream distance, the prediction stage, and several comparisons between models having similar properties

4.5.4.1 Calibration stage for over-bank flow.

The centroids of the particle distributions differed from the data by between 3 and 6 cm, and again showed a positive bias. The discrepancy between the modelled and measured centroids was however of the order of the resolution of the measurements (3cm) and was considered acceptable at 4m downstream.

All of the spreads in the particle distributions at a depth of 159mm agreed to within the estimated experimental uncertainty with the spread in the concentration distributions (the coefficient of variability was in the range from less than 1% to 4%), which is confirmed by the example particle distribution for the model NSCALE labelled 'nscale 40' on fig. 4.17. The predicted particle distribution at 16m downstream (labelled 'nscale 160') on the same figure shows, however, that there are problems to come.

4.5.4.2 Evolution of particle distributions with downstream distance for over-bank flow.

The graphs (fig. 4.15 and 4.16) showing the evolution of the spread at 159mm with downstream distance show that most of the modelled distributions over-predict the measured spread in the concentration distribution. Only one of the models, JSCALE predicts the observed behaviour to within the uncertainties at all of the measurement sites in the downstream direction, although the characteristic shape of the curve is representative of several of the models (NSCALE, JUMP, CORJ3 and CORJ4). This will again be discussed in section 4.7.

The centroids in the particle distributions showed a non-trivial drift in the centroids of approximately 15 cm by cross-section 7, but remained relatively steady in the data as shown in table 4.8 for the model NEWJUMP:

Table 4.8 Variation of centroids with downstream distance for data and two different models.

distance downstream	data centroid (m)	NEWJUMP centroid (m)	NEWJUMP (modified with boundary reflection about angle of incidence) centroid (m)
4m	1.073	1.116	1.084
8m	1.095	1.143	1.111
12m	1.065	1.185	1.129
16m	1.046	1.213	1.143

Fig.4.18 shows the observed and modelled transverse non dimensional concentration distributions for the single depth of 159mm and for the downstream distance 16m in the case of the over-bank flow.

The drift was initially thought to be due to the use of reflections from boundaries, which had previously not properly taken into account the transverse momentum of a particle approaching the sloped side wall of the over bank flow geometry. The particles were now reflected about the normal to the bed slope to conserve momentum (as discussed in section 4.3.3). The drift in the centroid was found to be reduced slightly (see table 4.8 above), although the systematic drift of the centroid remained.

A further investigation into the reason for the drift was undertaken, initially to see if there was any connection between the drift and the difference between the velocities in the over-bank region and those in the main channel. A simulation was undertaken whereby the random walk in the horizontal direction was left the same, but vertical steps were excluded from the trajectories so that the particles all remained at the release depth. This produced good agreement of the model centroid with the observed value. Next the particles were allowed to step vertically, but were restricted to the region of the flow no deeper than the bank top. Again the model and observed centroids were in close agreement.

The above two observations strongly suggested that the misfit in the centroid positions was not due to the relatively large difference in velocities between the in-bank and over-bank regions. This velocity difference might have otherwise given rise

to the sort of drift effect discussed in chapter 2, whereby maxima in particle number densities drift away from regions of high diffusivity, or short time constants.

Having eliminated other possibilities, it was considered that the drift was associated with the asymmetric flow field faced by the particles following their release. Initially, following the injection, an equal number of particles (on average) would disperse either side of the line y = 1.05m. The particles over the main channel would be free to disperse downwards, so that there would then be relatively fewer particles close to the surface (or in the vicinity of z = 159mm at which depth the distributions were examined in detail for the over-bank flow). This would result in there being relatively more particles towards the over-bank region than in the main channel region in the simulation, whereas for the real flow, this was not observed. This facet of the real flow could be explained if the turbulence induced secondary circulation above and adjacent to the bank-top (see fig. 3.1), was increasing the mixing rate of tracer close to the bank-top, on the over-bank side, into the main channel, giving the tracer on average more opportunity to 'escape' into the main channel.

This effect was next attempted to be accounted for by including a transverse varying eddy viscosity as mentioned above, for the random walk, NEWJUMPB. This allowed for a greater effective eddy dispersivity in the region of the bank-top, to simulate this 'enhanced mixing' due to secondary circulatory cells, and was described in section 2.6.2. However, this did not produce any better agreement with the centroids, and by all other accounts (this model was included in the sensitivity analysis above), NEWJUMPB performed badly. It was concluded that in order to investigate

this effect further, more information about the secondary advections was required, which was not available at the time of writing.

4.5.4.3 Prediction stage for over-bank flow.

The predicted spreads in the particle distributions at cross-section 7 for the models JSCALE, NSCALE and JUMP agree with the spreads in the concentration distributions to within estimated uncertainties in the data, with the remaining models deviating by between 10% and 19 % from the observations. However, it is again important to examine the vertical distributions, by inspecting the combined objective function, obj3, which was again used to list the models in decreasing order the closeness of fit in tables 4.4 and 4.5.

4.6 Relative performances of the different models at the calibration and prediction stages for the two flows combined.

The objective functions (obj3) in tables 4.3 to 4.6 stem from normalised measures of closeness of fit. The values at the calibration and prediction stages were combined in order to give an *indication* of which model performed best overall. However, the objective functions, obj2, are not strictly compatible for the two flows, since the Bv ratios were normalised using the areas under the distribution curves close to the surface. Since the concentration distribution close to the surface (159mm) for the over-bank flow-

bank flow is relatively much larger than that at all other depths in the main chanel, the Bv ratios are relatively smaller than their counterparts for the inbank flow.

The different random walk models are nonetheless listed in table 4.9 in order of decreasing closeness of fit using this combination of objective functions, for the in-bank flow and over-bank flows (for the 'best fit' values of objective parameters).

Table 4.9 Comparison of closeness of fit of particle distributions to observed concentration distributions for the different random walk models.

IN-BANK FLOW		OVER-BANK FLOW	
data/model	**sum of objective functions for cross-sections 1 and $6*10^{-3}$**	**data/model**	**sum of objective functions for cross-sections 1 and $6*10^{-3}$**
NSCALE	5.0	**JUMP**	13.4
NEWJUMP	7.5	**NEWJUMP**	15.1
SULLIJA	8.3	**CORJ4**	17.8
JUMP	10.3	**MARKOV A**	18.2
JSCALE	11.6	**NSCALE**	18.2
FASTC	24.1	**JSCALE**	21.2
FASTA	46.8	**CORJ3**	22.4
MARKOV	58.5	**FAST C**	23.5
TURJ2	63.7	**DEBRA**	24.8
CORJ2A	68.6	**MARKOV B**	31.4
CORJ2B	72.8	**NEWJUMP B**	68.2
FASTB	101.0		

If the table is taken literally, then it would appear that the models, NEWJUMP, JUMP and NSCALE perform the best overall. These random walk models are

relatively simple compared to the alternatives, which suggests that the additional degrees of freedom in the other models have not been optimised for the flow as a whole. However, additional physically-based parameters, such as cross-correlations or memories have mainly been based on measured values in the flow (with the exception of the SULLIJ and FAST algorithms), rather than attempting to fit the values in a further calibration analysis.

4.7 Further discussion of the sensitivity analysis for the in-bank and over-bank flows and Conclusions.

The sensitivity of the random walk models to varying the size of the displacements was examined, and a discretisation interval was estimated which was compatible with the uncertainties in the measured concentration distributions. The sizes of the vertical and transverse displacements in the different random walk models were adjusted until the macroscale particle distributions were in close agreement with the concentration distributions for two different flows. It was found that all of the random walks could be calibrated in this way so as to reproduce the observed spread in the measured concentration distributions to within the estimated uncertainties at 4m downstream, for both flows.

The calibrated values of the displacement sizes were then used to predict the evolution of the tracer plume further downstream. As already stated, relatively few of the models for both flows showed the same depth-averaged spread (or spread at z = 159mm for the over-bank flow) as the data at every downstream measurement site. The shape of the spread against downstream distance curves, for those models which

did agree (JSCALE, JUMP for the in-bank flow and JSCALE for the over-bank flow) with the data at every measurement site (to within experimental uncertainties), were characteristic of many of the models.

For the models NSCALE, MARKOV, NEWJUMP, CORJ2A and CORJ2B for the in-bank flow, and the model JUMP for the over-bank flow, the curves could be made to pass through all of the data points to within the estimated uncertainties by reducing the f_v factor slightly. This conditional fitting of the data relies upon the additional information which is gained by examination of more of the concentration data than was used at the calibration stage. The calibration stage of the study was based on the data from a single cross section, and the objective functions effectively assume zero uncertainty in the spread at this cross section. This 'ties' the evolution of spread curve more rigidly to the first data point than is necessarily conducive to obtaining the best overall fit to the entire data set over the whole length of the channel. However, it is highly desirable to be able to calibrate the models based on the measurements at a single cross-section, since this would ultimately lead to less measurements.

Collectively, the models show the greatest deviation from the data at the cross sections 6m, 8m and 10m downstream from release, in the earlier stages of mixing. This was most likely to be due to the models failing to predict the vertical mixing behaviour properly. Inspection of the measured concentration distributions (for the in-bank flow) shows that the tracer becomes fully mixed in the vertical mixing by ~ 10m downstream. The turbulent structures which are generated by the bed shear contain motions of the same order of magnitude as the depth of the flow, but the vertical mixing is being modelled using step sizes of the order 1/10th of the flow depth, which

are supposed to be representative of the average scale of motion in the vertical direction. This could explain the failure of some of the models to model the depthwise mixing process, since they do not explicitly account for these larger scale motions and the correlations which are associated with them. The rate of transverse mixing is affected by the rate of vertical mixing, so if the latter is not modelled correctly in this critical early stage, then the models will not necessarily reproduce the correct transverse spread either.

Most of the models which do not fit the data to within the estimated uncertainties over-predict the depth-averaged transverse mixing in the early stages of mixing, which could be explained by the following. If the transverse dispersivity is actually greater close to the surface (as for example in Prandtl's mixing length theory, where the mixing length in a turbulent boundary layer is proportional to the depth), then for the surface release (this was the case for both flume flows), the mixing would tend to be strongest in the early stages of mixing. As the tracer mixed into greater depths, it would experience a decrease in the effective vertical and transverse dispersivities. Since the models were all calibrated using the tracer data at the first cross-section downstream from the surface release, the calibrated step sizes would reflect this relatively strong initial vertical and horizontal mixing, and could not account for the reduction in the mixing rate as the tracer cloud continues to mix.

The model TURJ2, which included vertical and transverse step sizes scaled with the measured fluctuating velocity fields, would be expected to account for this effect to some extent, but this model in particular still slightly over-predicts the depth-averaged transverse spread at 6 and 8 meters downstream. The behaviour of the tracer is therefore again suggested to be due to larger scale correlations in the flow. Future

work could investigate this, if more information about the secondary currents was made available.

Following the tracer becoming well mixed in the vertical direction, the dispersion process is better represented by the purely stochastic process, since on average, each fluid element (containing tracer) has had the opportunity to experience the dispersivities (in all directions) at every depth. The random walk model therefore gives a better representation of the 'average' mixing process further downstream.

The main sensitivity analysis of the different models was conducted at the furthest downstream location supported by the measurements, in order to put to the test their predictive capabilities. However, from the graphs of the evolution of spread with downstream distance, it is evident that if the analysis had been carried out , for example, 8m downstream, fewer of the models would have collapsed the data to within the estimated uncertainties. However, this does not affect the general conclusions which have been made about the equifinality of the model results for the in-bank flow and to a lesser extent the over-bank flow, since it is the general shape of the graphs which many of the models have in common.

In summary of the predictive capabilities of the models, for the in-bank flow, the models JUMP, NEWJUMP, JSCALE, NSCALE, SULLIJ came within the estimated uncertainty bounds of the measured depth-averaged spread at 14m downstream, and all gave a good fit to the concentration distributions at different depths. These models also possessed the smallest values for the two objective functions. The models TURJ2, CORJ2A and CORJ2B were very close to meeting the same criteria, and were also regarded as successful. The uncertainty bounds are estimates of experimental errors, which should only accommodate 66% of the data

points, if they are truly representative of random error. All of the above models show a similar shape in their respective evolution of depth-averaged spread curves.

For the over-bank flow, the three models, JSCALE, NSCALE and JUMP were successful by the above criteria in reproducing the concentration distributions at 16m downstream. The models MARKOVA, CORJ3 came close to meeting the criteria, and for the same reasons as explained above, these were also regarded as successful models. However, these conclusions are less certain for the over-bank data set, since the data was relatively sparse in the number of downstream measurement sites.

The drift of the modelled centroids away from the observed was unable to be explained in terms of the velocity difference between the over-bank and the main channel flow velocities causing a drift in the particles towards the region of lower velocities (the over-bank region). The drift was reduced to some extent by incorporating boundary reflections which accounted for the angle of incidence. It was considered that the drift was associated with the asymmetric flow field, causing a bias in the relative numbers of particles either side of the injection point (at bank-top at y = 1.05). It was suggested that the drift was not observed in reality, because of the effects of turbulence induced secondary circulation. This was attempted to be modelled by incorporating a spatially varying effective transverse eddy dispersivity, and although it reduced the drift of the particles towards the over-bank, it resulted in a distribution which did not otherwise fit the concentration distributions very well. Future work could explore different versions of this approach, or perhaps, as stated earlier, the secondary advections in the flow could be incorporated into the model.

All of the different models had to be calibrated, including those for which the perturbations were directly based upon the measured Eulerian fluctuating velocity field

(for the in-bank flow only). The calibration of each model simply involved the adjustment of the values of the multipliers to the perturbations for the entire flow field, so that these values were 'global' to the entire flow field. Therefore, in the case of the models which were based upon the Eulerian fluctuating velocity field (for example, TURJ2), and considering that the particle tracking model was essentially based in a Lagrangian framework, it would appear that there existed a simple linear relationship between the Eulerian and Lagrangian fluctuating velocity fields, at the microscale (particle scale), which gave rise to the correct ensemble particle behaviour at the macroscale. The calibrated displacement size for the model TURJ2 is given by equations 4.7:

$$\begin{aligned} L_L &= 2.4 \times \langle v' \rangle \times T_L \\ L_L &= 2.4 \times 0.034 \times 0.4 \\ L_L &= 0.033\text{m} \end{aligned} \qquad (4.7)$$

where <v'> is the cross-section average transverse component of the fluctuating velocity. If this represents the mean Lagrangian 'decorrelation' length scale, then the decorrelation time scale in the downstream direction, using the cross sectional average downstream velocity of $\langle U \rangle = 0.68\ ms^{-1}$, as measured by a stationary laser-Doppler-anenometer, would on average be given by equation 4.8:

$$T_E \approx \frac{L_L}{\langle U \rangle} = \frac{0.033}{0.68} \approx 0.05s \qquad (4.8)$$

Dividing this by the Lagrangian time scale used in the model, of ~ 0.4s, the ratio of Lagrangian to Eulerian time scales is : $T_L / T_E \sim 8.0$. This ratio is larger than the ratio ($T_L / T_E = 3.5$ to 5.0) which was estimated by determined in two separate pieces of work by Engelund (1969) and Hansen (1972), which were also cited in Cotton and West (1980). However, these values were determined from measurements of the motions of buoyant particles in the surface layer at the centre of wide channel flows, so that the particles did not experience wall boundary effects, and nor did they experience the full three dimensional dispersion. These effects would more than likely increase the Lagrangian lengthscale, and lead to a larger ratio.

Since the in-bank flow represented a relatively complex three dimensional shear flow, with anisotropy, secondary advections and inhomogeneities, this simple linear relationship is somewhat surprising, and will be discussed further in chapter 9.

For the application of the particle tracking models to a less accurate set of measurements of velocities and tracer concentrations in a more complex river flow, the use of the simpler random walks is suggested on the basis of this work.

Fig.4.1

Frequency histograms showing the distributions of particles in a 1d bounded flow with different forms of boundary interaction

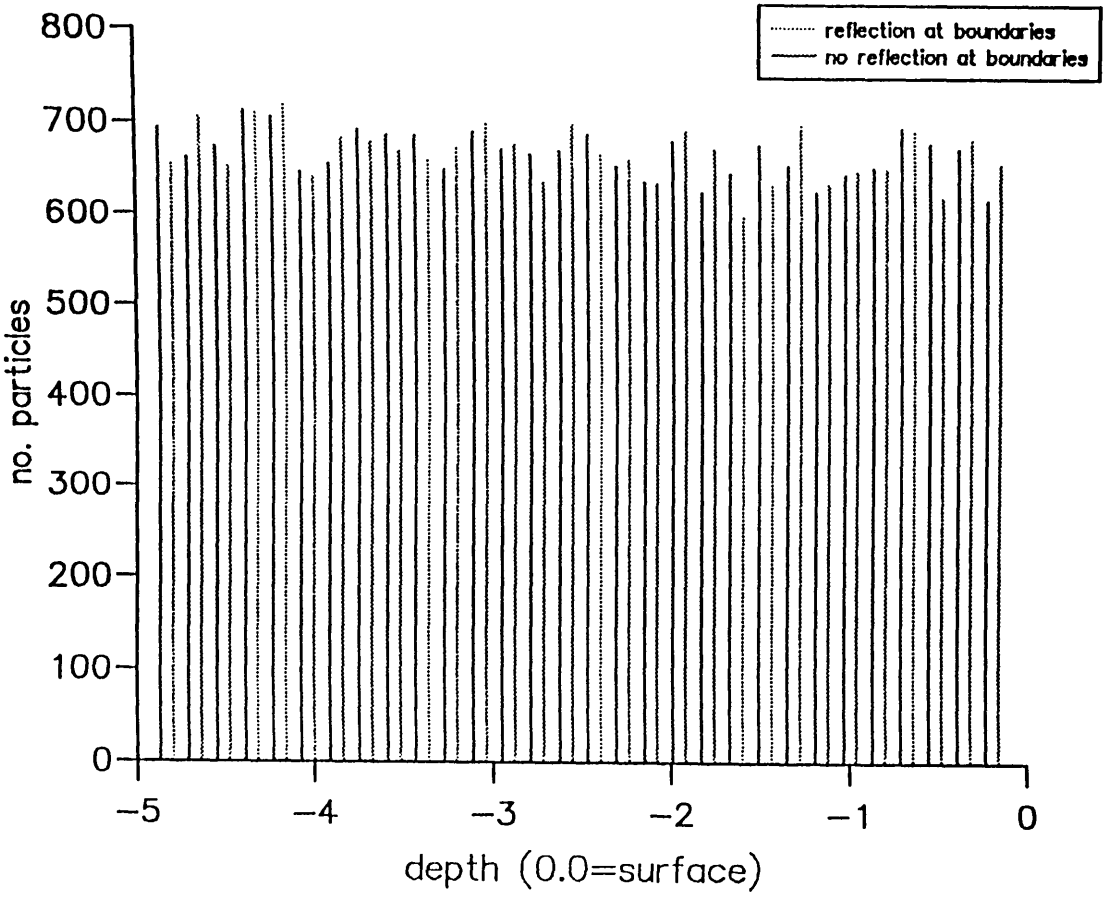

Fig.4.4

Graphs showing the measured concentration distributions at different depths for a downstream distance of 4m, for the in-bank flow.

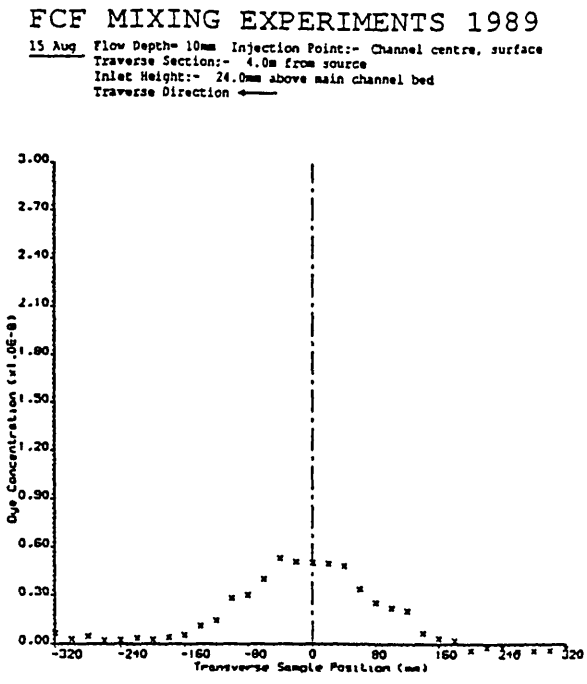

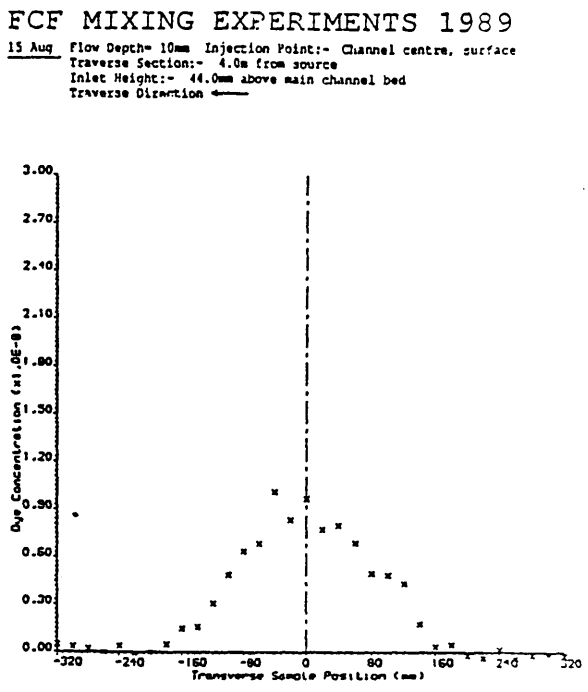

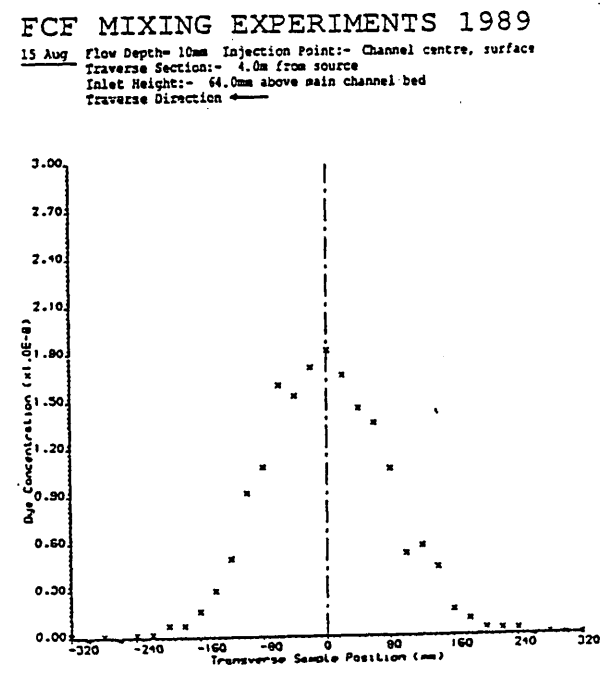

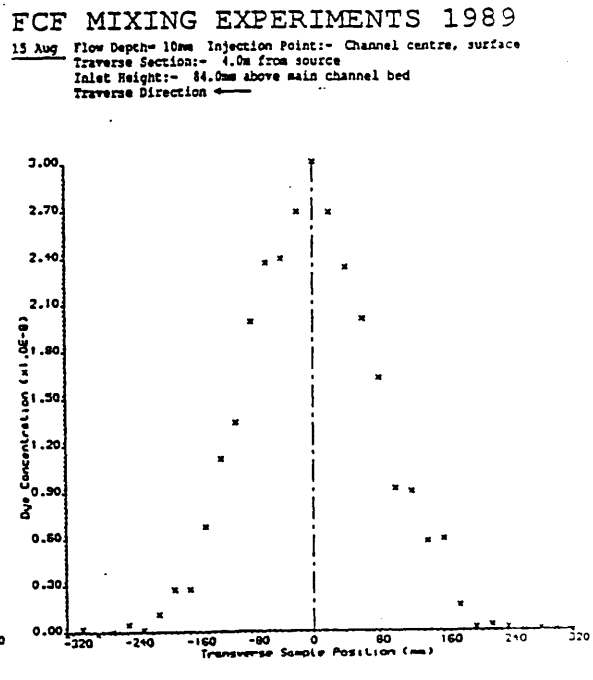

Fig.4.5

Graphs showing the measured concentration distributions at different depths for a downstream distance of 16m, for the over-bank flow.

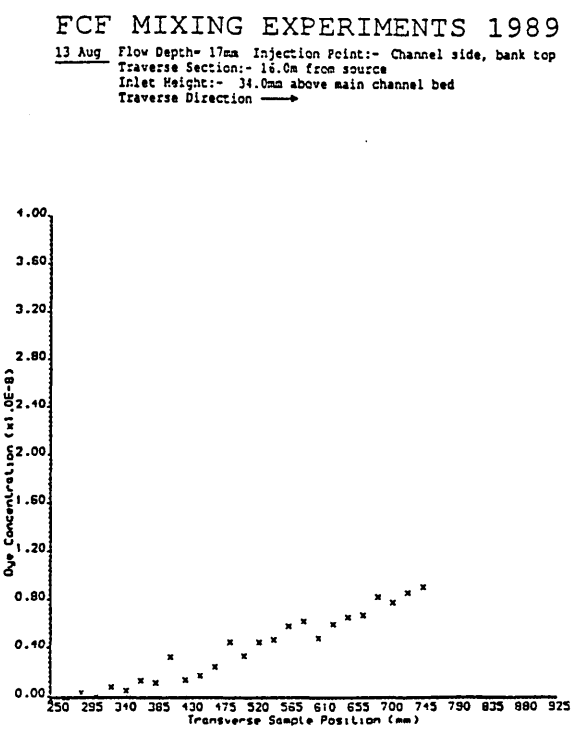

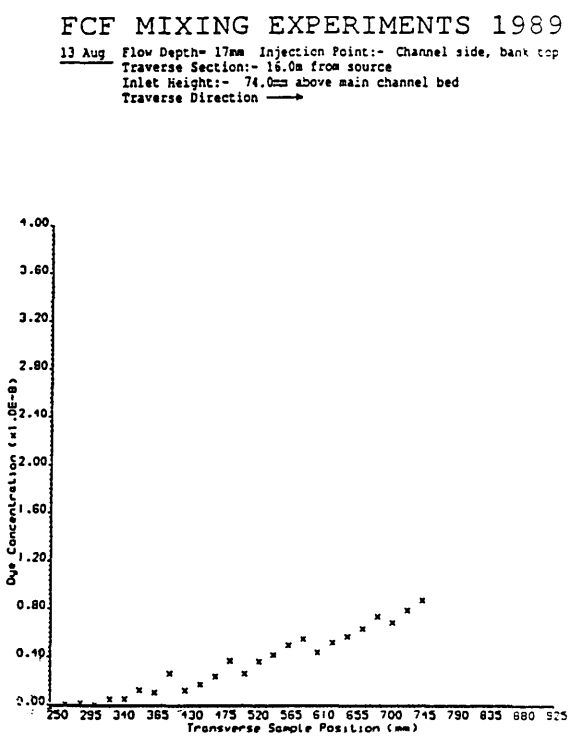

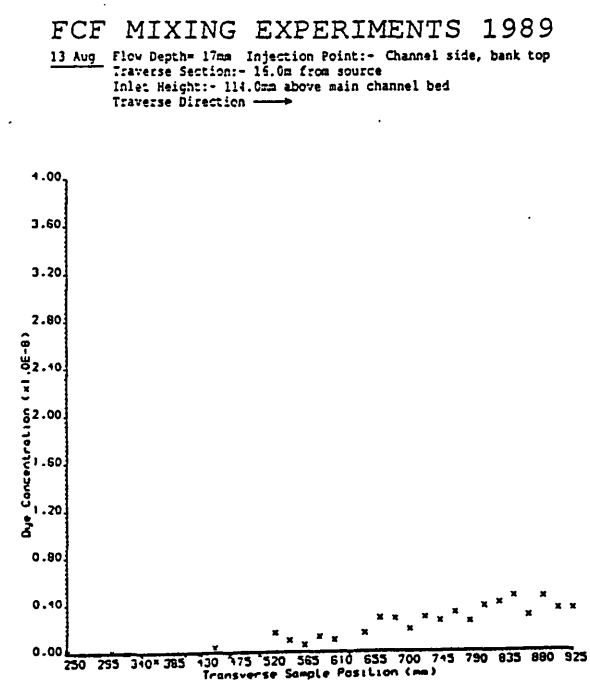

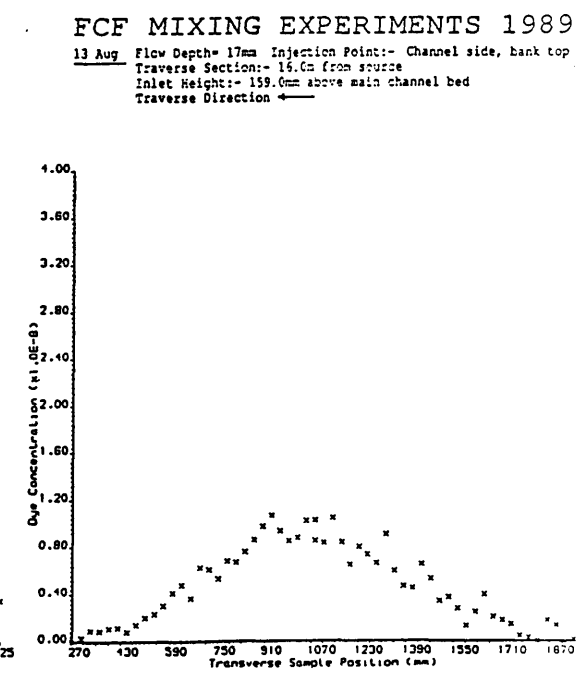

Fig. 4.6

sensitivity of spread to lateral kick multiplier , fv

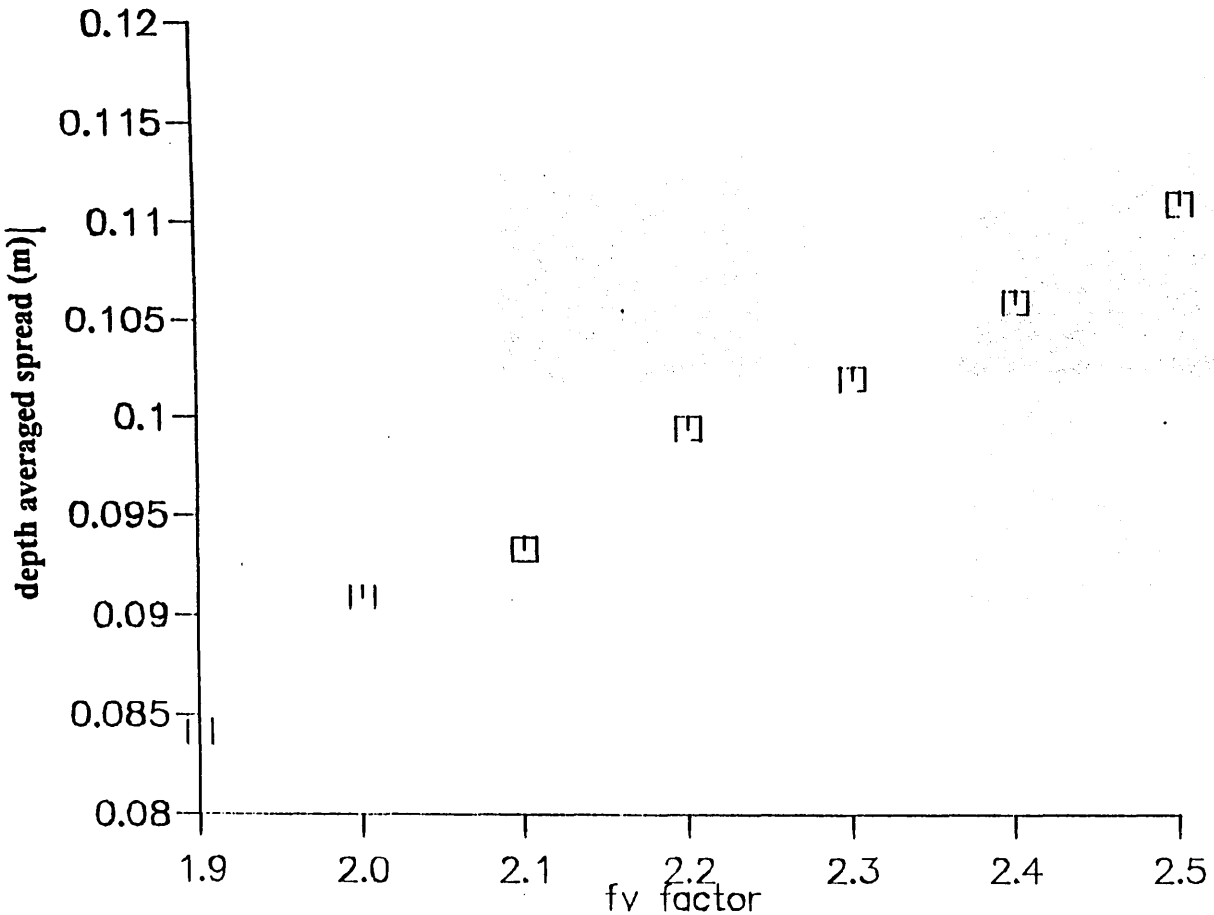

Fig.4.7

Maps to show the minima in some of the objective functions for two example models.

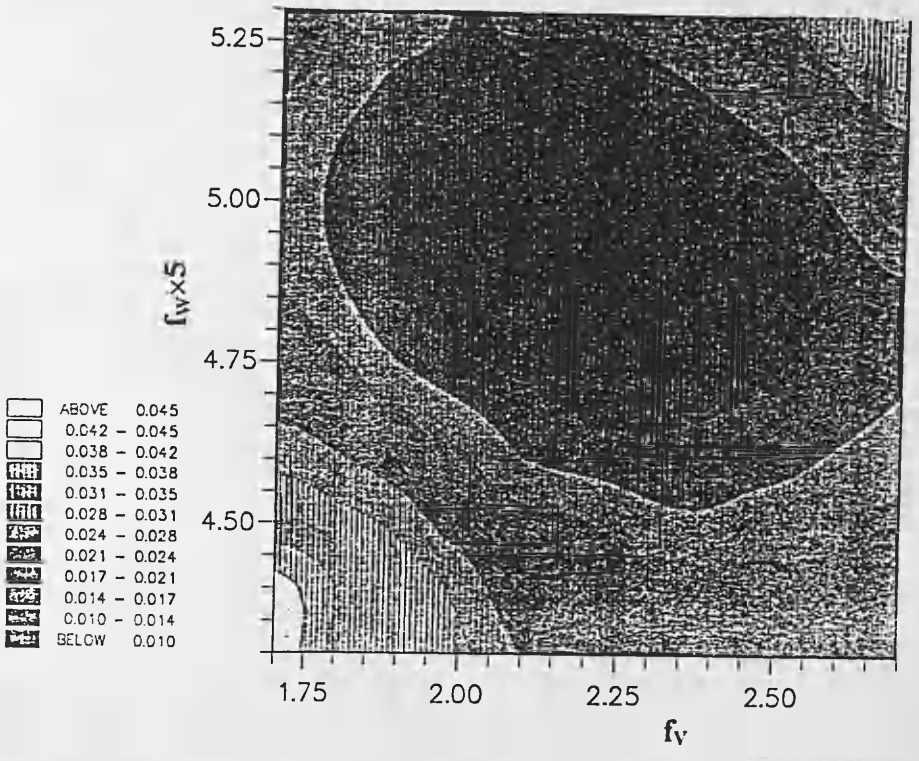

Model JSCALE

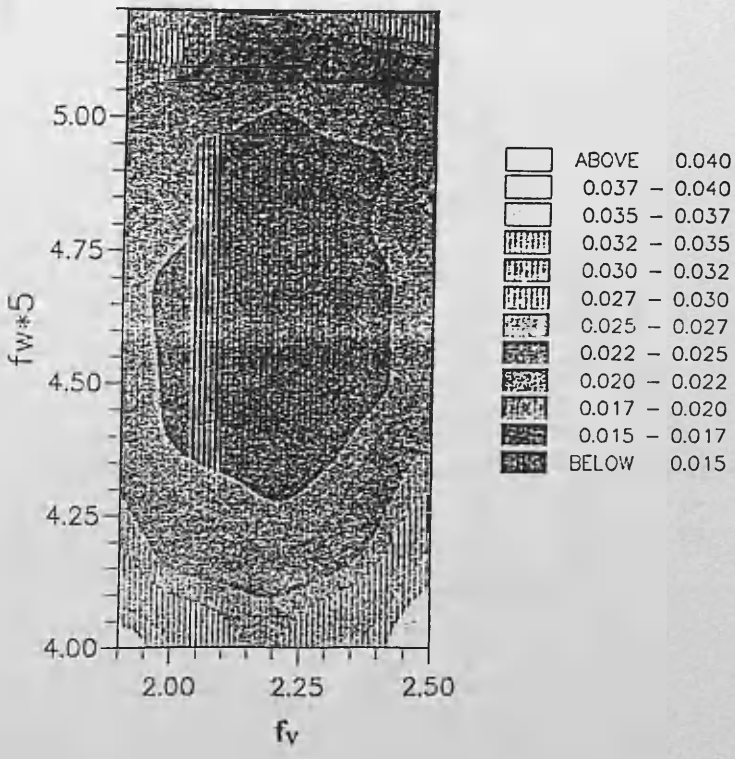

Model NSCALE

Fig.4.8

Evolution of depth averaged spread with downstream distance

(In-bank flow)

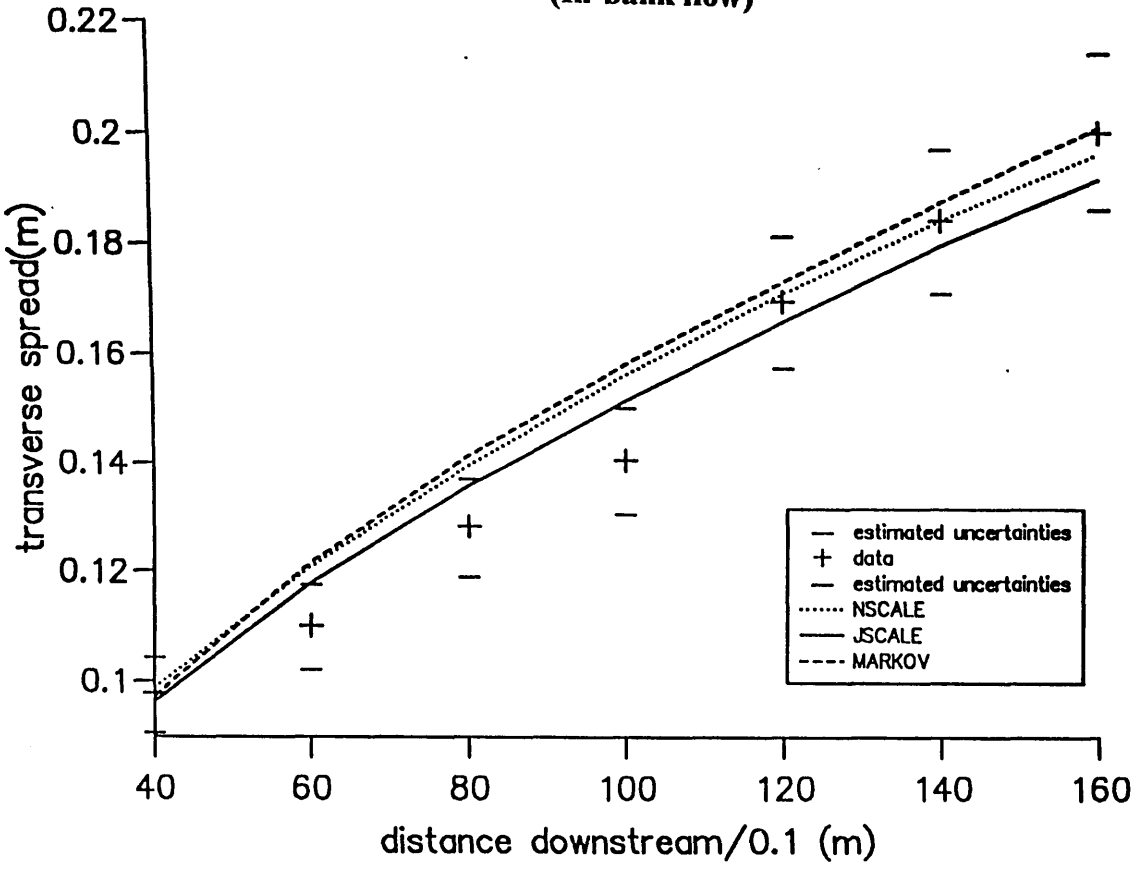

Fig.4.9
Evolution of depth averaged spread with downstream distance
(inbank flow)

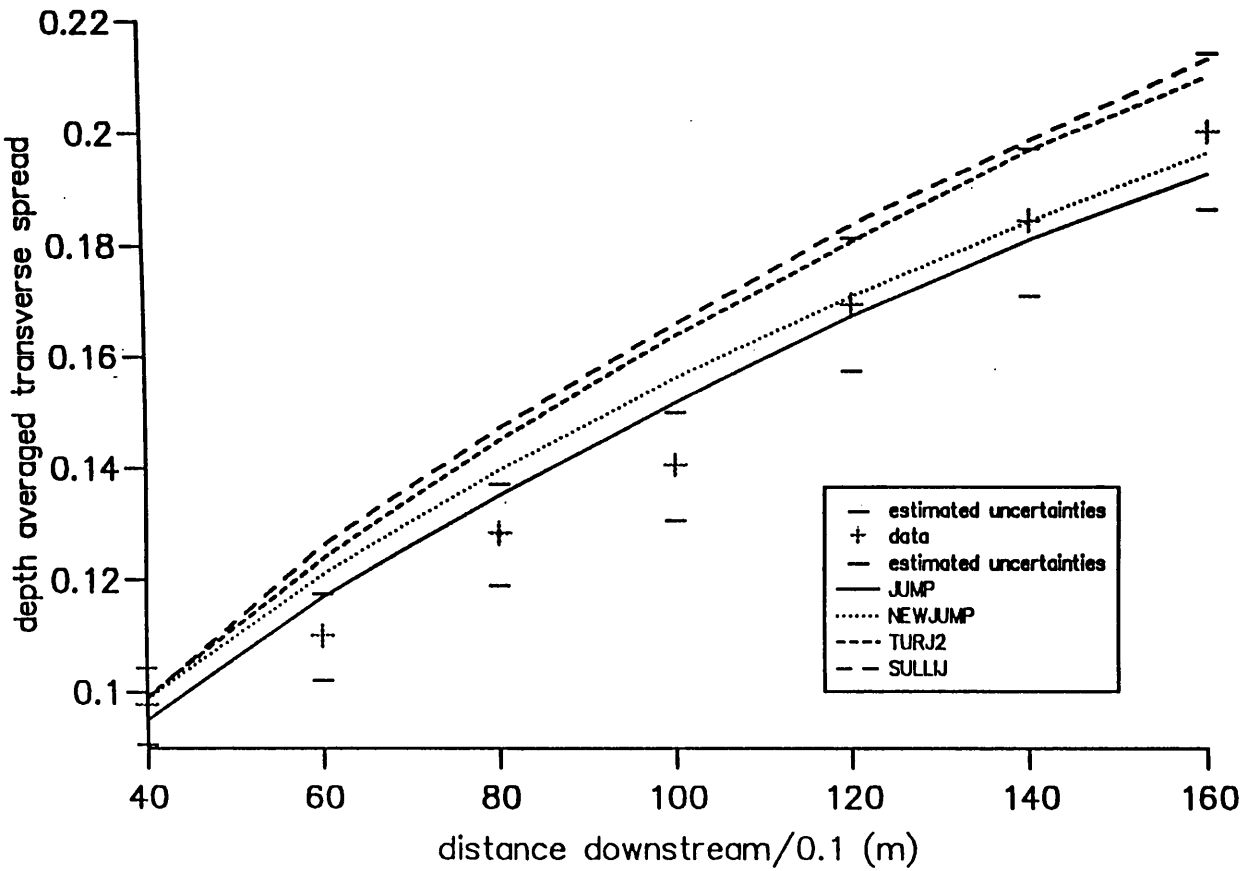

Fig.4.10

Evolution of depth averaged spread with downstream distance

(In-bank flow)

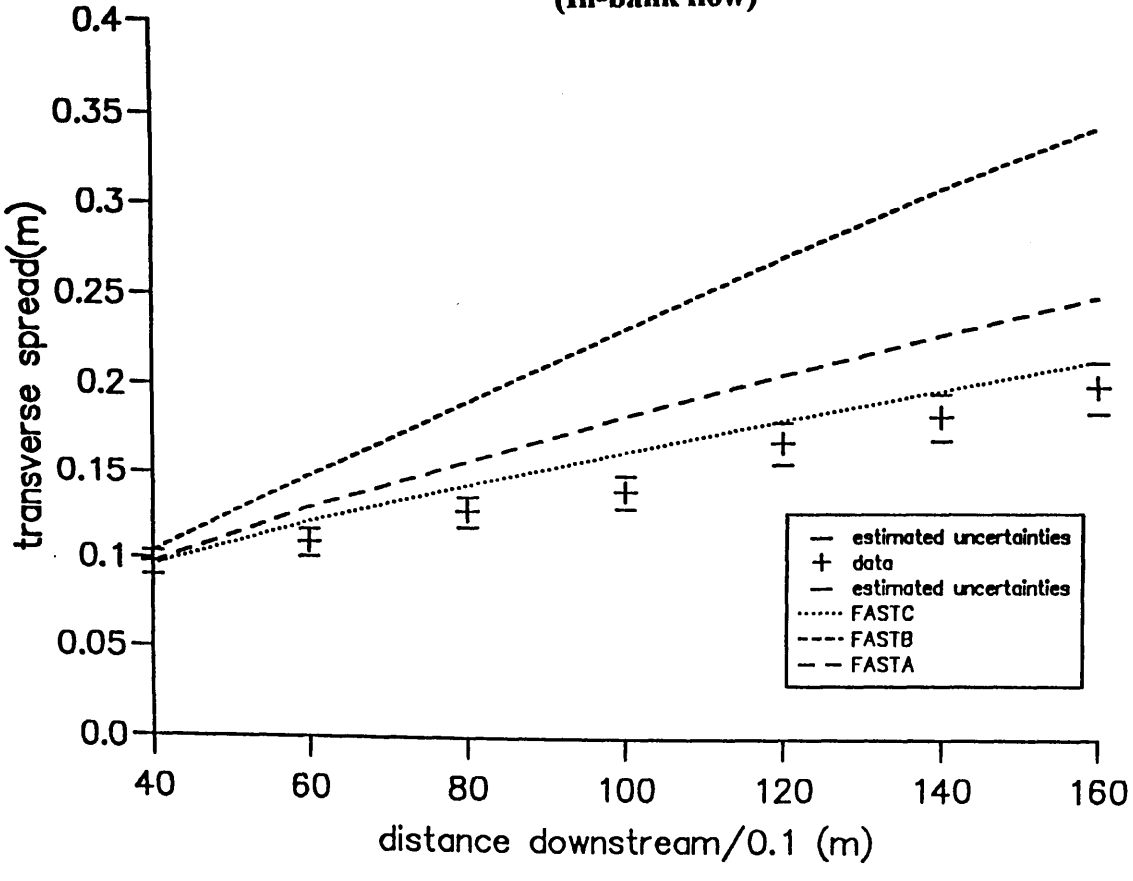

Fig.4.11

Evolution of depth averaged spread with downstream distance

(In-bank flow)

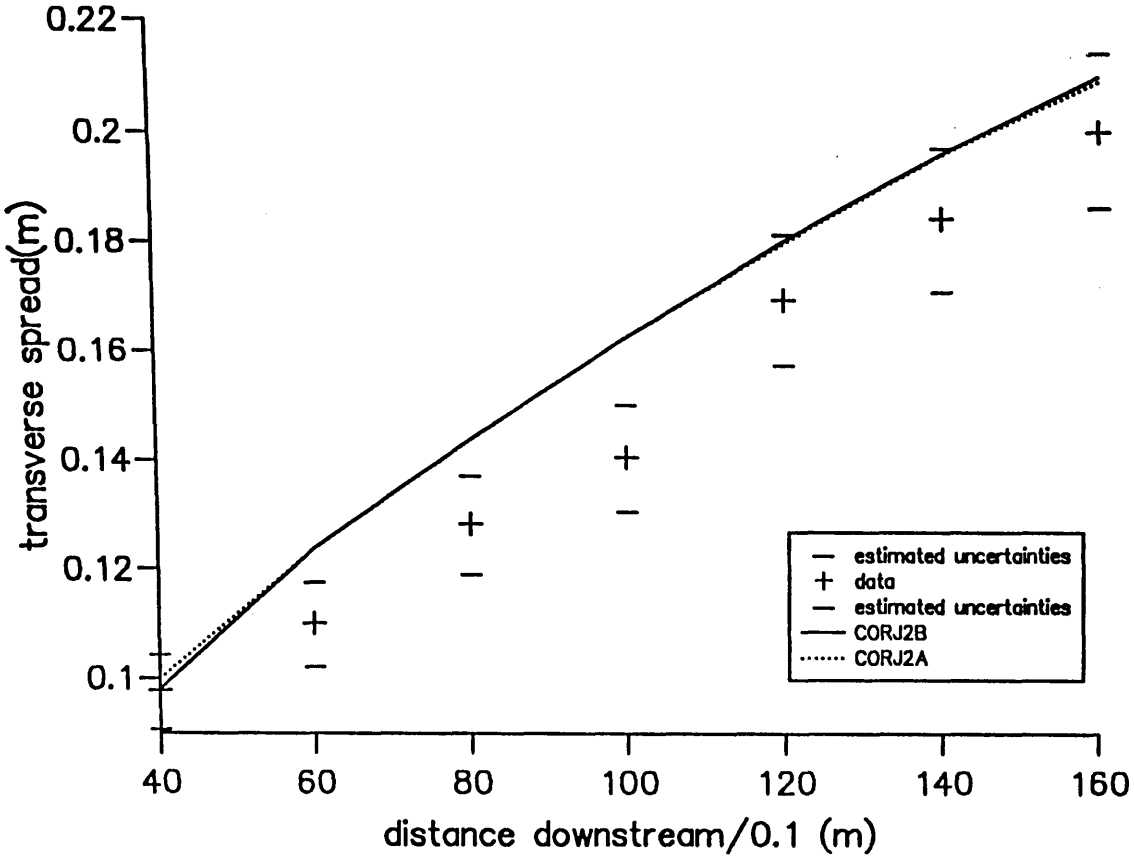

Fig.4.12

Comparison of model and observed lateral concentration distributions at 4m and 14m downstream

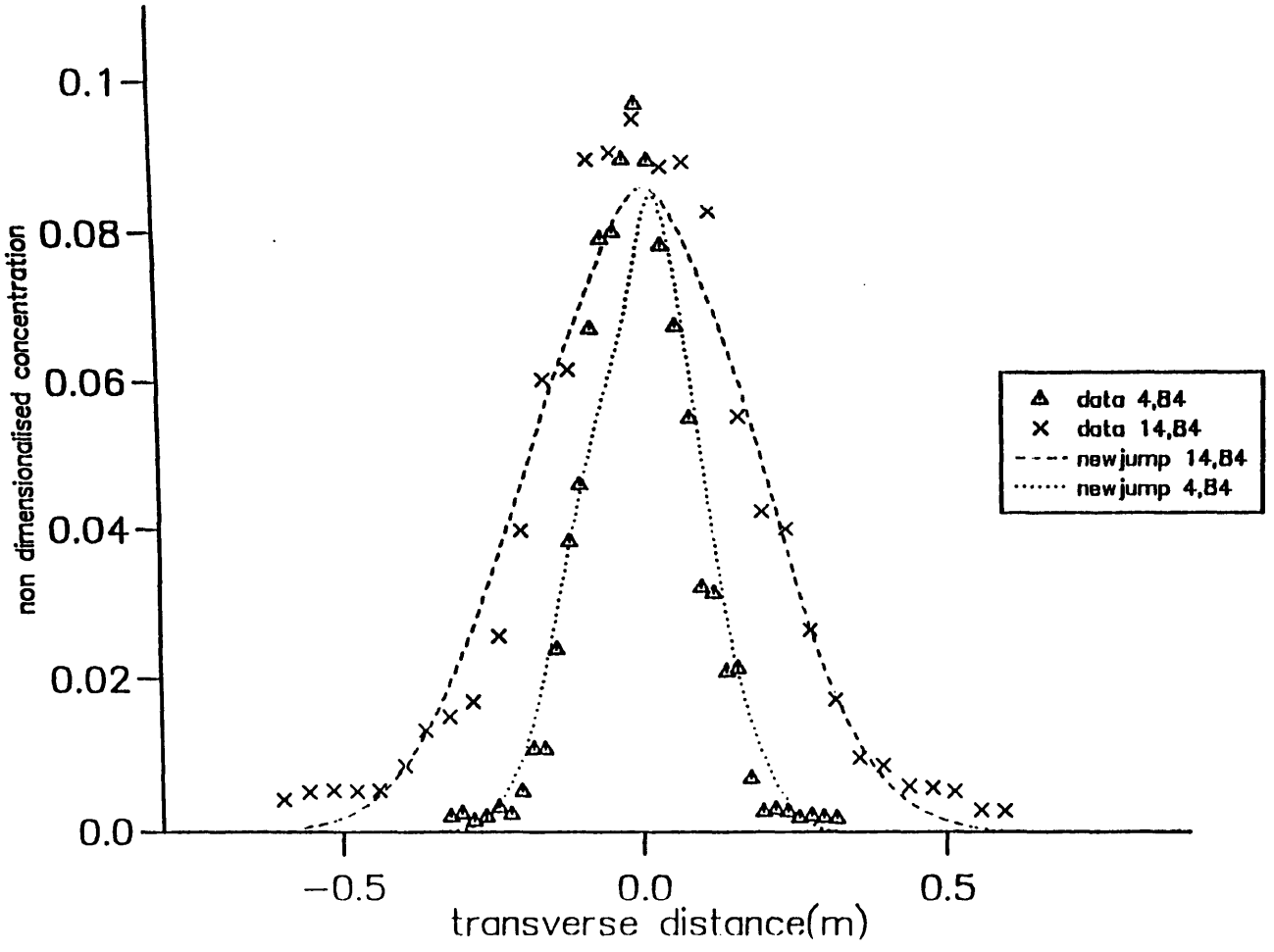

Fig.4.13

Comparison of model and observed lateral concentration distributions at 14m downstream

(In-bank flow)

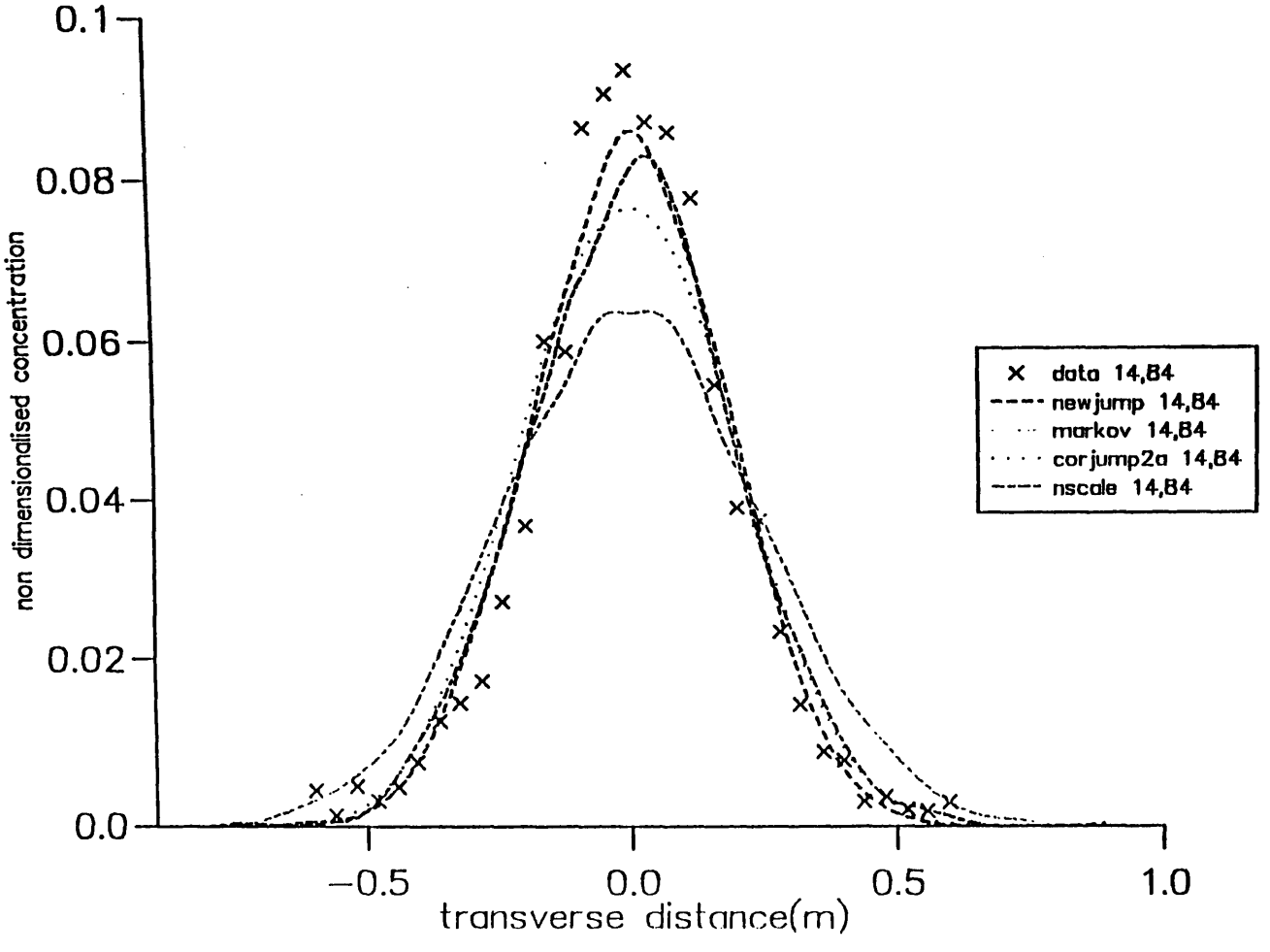

Fig.4.14

Lagrangian cross correlation and autocorrelation coefficients for Markovian model

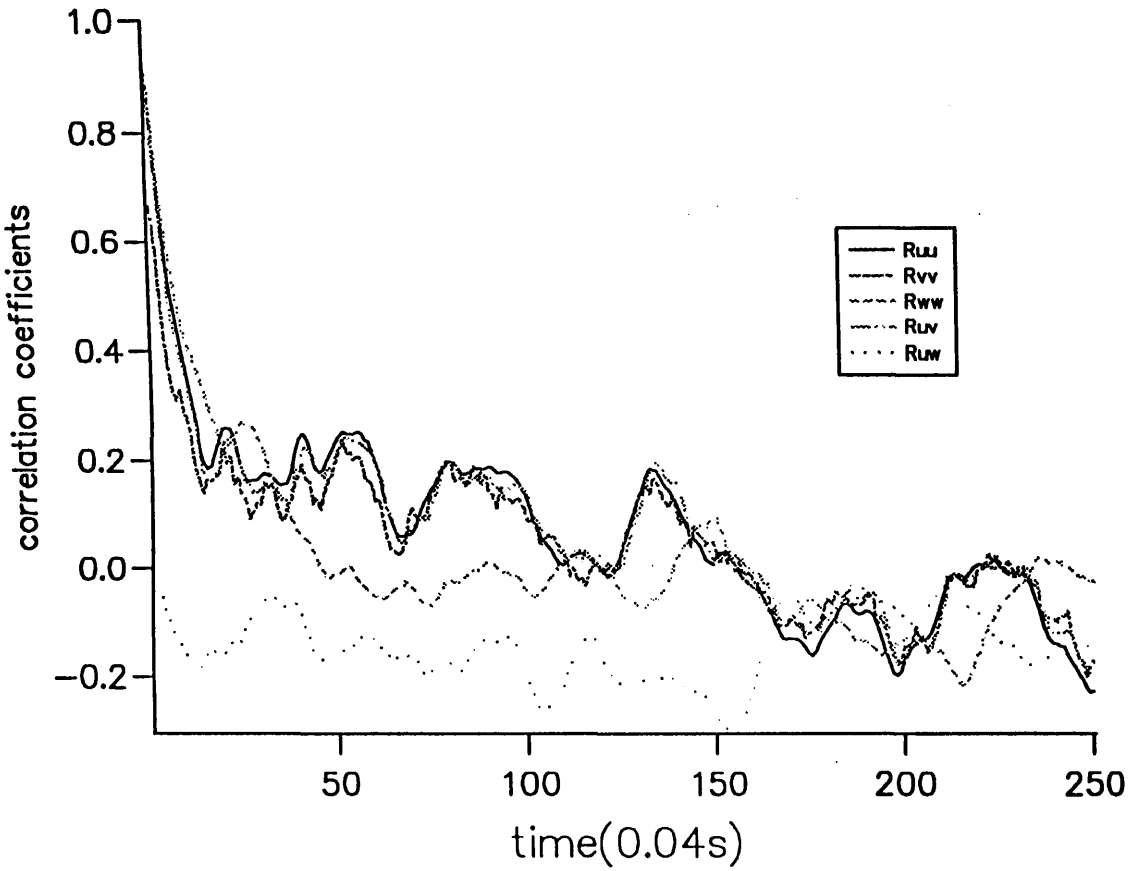

Fig.4.15
Evolution of depth averaged spread with downstream distance
(overbank flow)

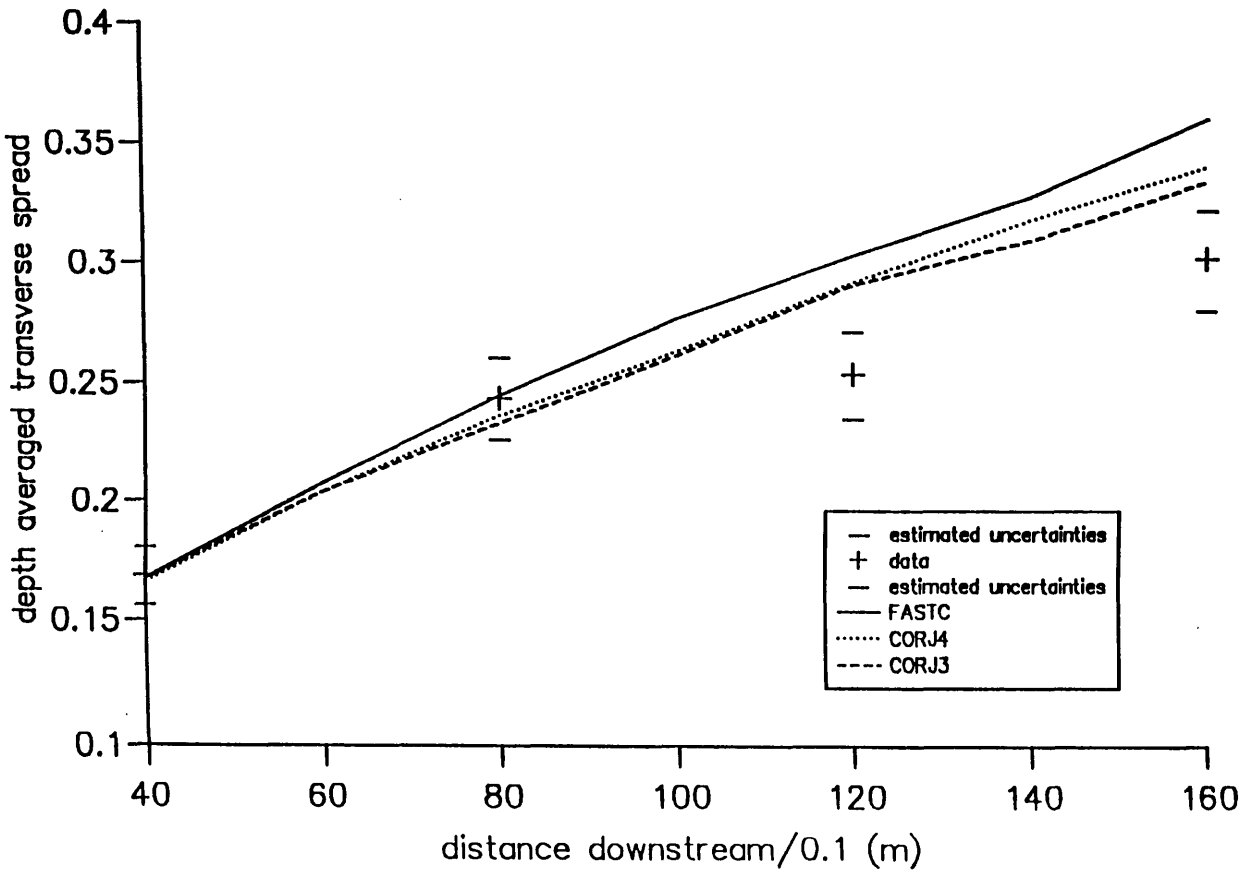

Fig.4.16

Evolution of depth averaged spread with downstream distance
(overbank flow)

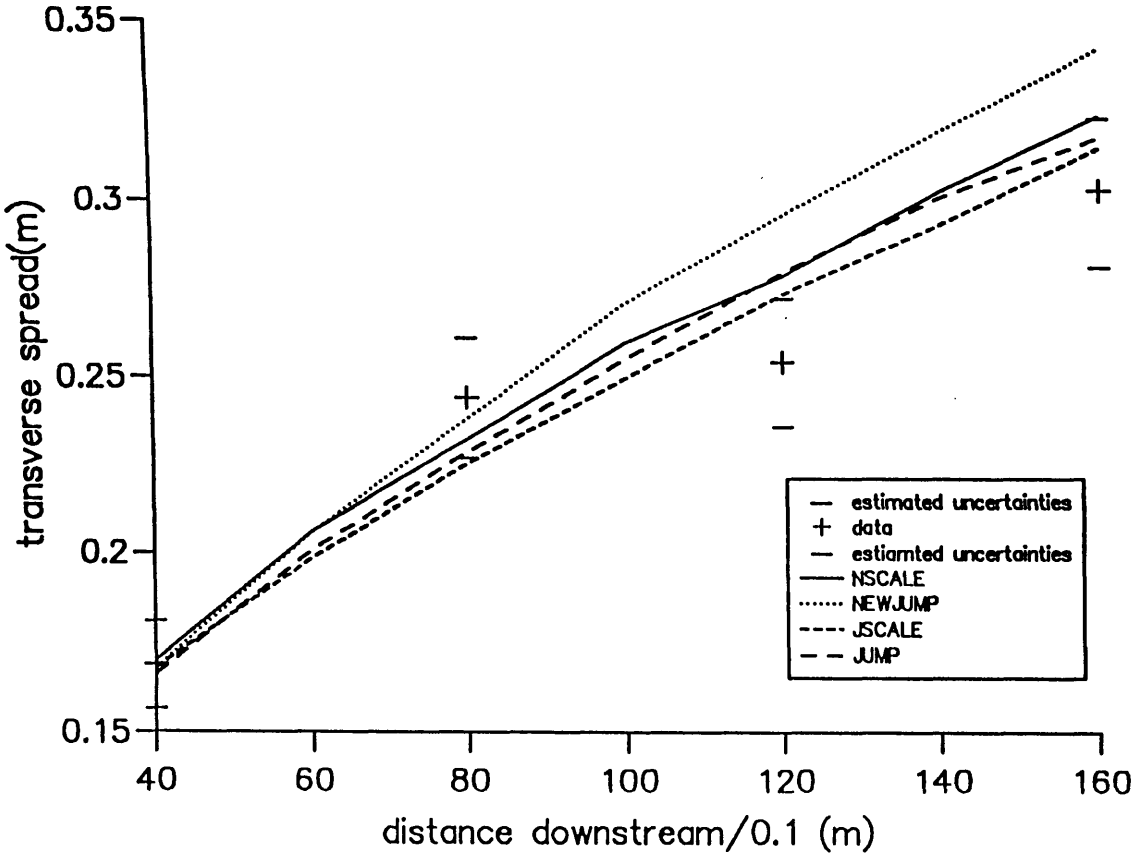

Fig.4.17

predicted and measured transverse concentration distributions at two downstream locations , using the model 'nscale'

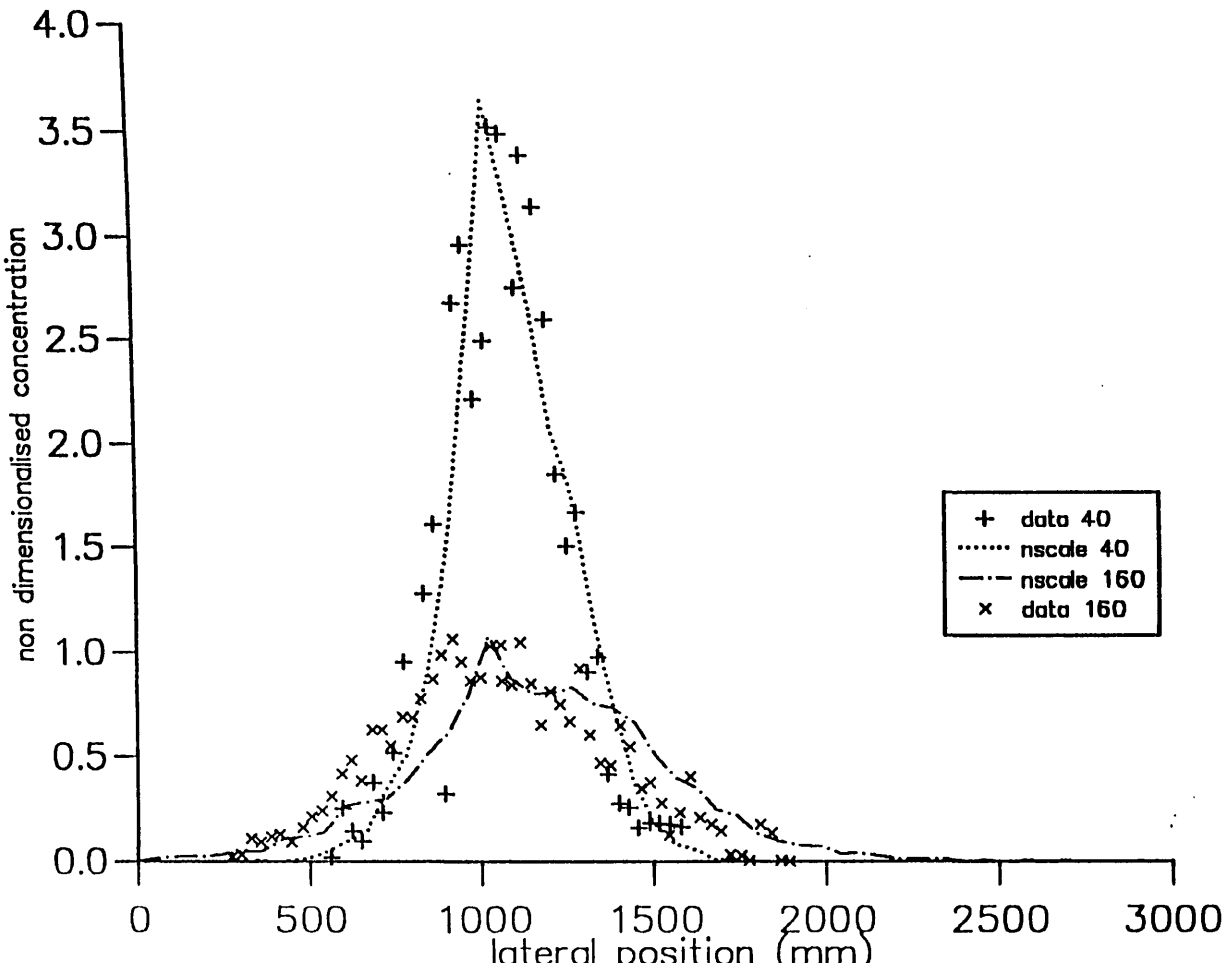

Fig.4.18

Comparison of model and observed lateral concentration distributions at 16m downstream (overbank flow)

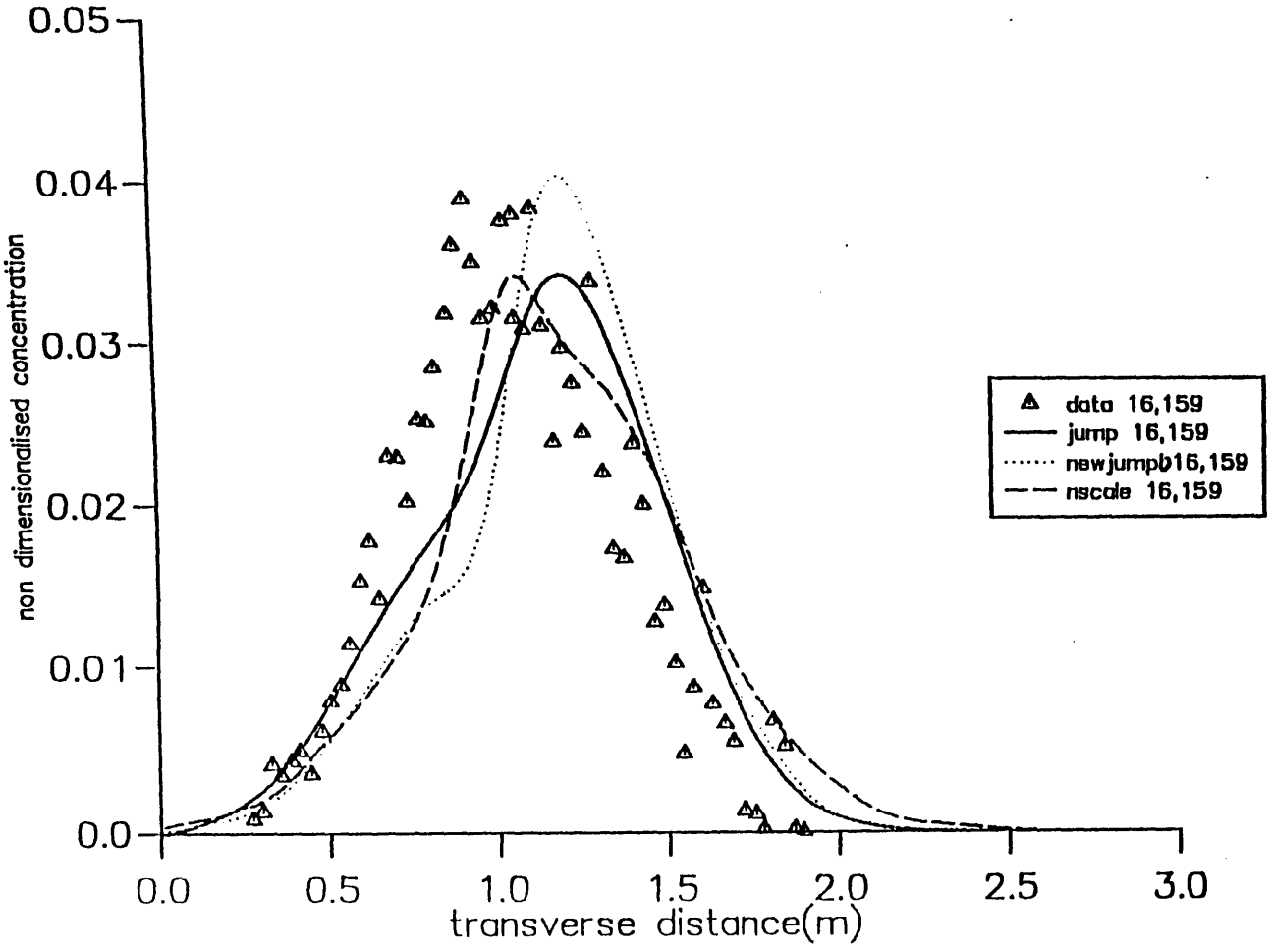

Chapter 5

Field measurements of velocities, turbulence and tracer dispersion in a meander bend of an upland gravel bed river (River Lune).

5.1 Introduction.

This chapter is a description of the laboratory work and fieldwork which was collected for the purpose of constructing a computer model of the mixing characteristics of the flow in a bend of the River Lune. The flow is highly complex, with large scale inhomogeneities, pool sections, riffle sections, deadzones and flow separations. The combined effect of these structures on the flow and its mixing characteristics can only be ascertained with a large degree of uncertainty even with detailed field measurements. The construction of a model of the transport of a tracer within such a complex environmental flow is therefore likely to have an inherently large degree of uncertainty. The experiments must therefore be designed to compensate for the natural variability at every stage, through for example careful selection of sampling periods long enough to accommodate periodic trends in the measurement of observables.

Section 5.2 gives a qualitative description of the study reach and the principle hydrodynamical features. The laboratory and field work comprised four main sets of measurements and instrumentation, which are then described in the four main sections of this chapter. The surveying of the field site is described in section 5.3 and the velocity and stage measurements are described in section 5.4. These measurements

were later used to define the mean velocity field and geometry of the model simulation. Section 5.5 describes the measurements of the fluctuating velocity time series in three dimensions using electromagnetic current metering, which were used to define the characteristic time scales in the random walk model. Section 5.6, describes a dye tracer experiment carried out on the reach, the measurements from which were used to define the input to the model and to calibrate the model.

Each of the four sections are divided into sub-sections (where relevant) on instrumentation, calibration, sampling strategy, results and any further experimentation which was undertaken, such as investigations into experimental uncertainties.

Finally, section 5.7 summarises the data sets which were used in the construction of the random particle tracking model.

5.2 Qualitative description of field site

The field site for this study was a short reach of the river Lune east of Tebay at OS grid reference SD 540 658. The main aspect of the reach was a single large 180 degree meander, within which most of the field measurements were taken. The course of the river is straight for in excess of 200m upstream of the meander, although downstream there were several minor meanders before the river resumed a straight course once more. The river was gravel bedded and had many complex geomorphologic and hydrodynamic features. At the start of this project, some fieldwork had already been carried out at the field site by Harriet Orr of the Institute for Freshwater Ecology (IFE), Windermere, for a study of the bed load transport. This project was also in initial stages and it was clear that the field work which was required

for the two projects conveniently overlapped, sufficiently so that resources could be combined. An overview of the entire test reach on the day of the tracer experiments is given in fig. 5.1.

The bed material in the reach varied from small pebbles to large cobbles and was distributed in a typical pool-and-riffle regime. The river had a mean surface slope of approximately 0.009 (from measurements between the first and last cross-sections, using the distance around the meander bend).

The upstream straight reach comprised a narrow fast flowing channel with a steep left bank which was prone to slumping, and a steep sided shoal along the right bank. As the flow entered the meander there were a number of important features. A small brook (Street Beck) enters the river at an acute angle from to the right bank into a region of relatively still water (noticeable in the top left hand corner of fig.5.2a). Here the flow was slowly flushed by the small volume of water from the brook and was estimated to have a time constant of approximately 7.5 minutes for a moderate flow, which was established by dye dispersion tests in a MSc project by A.Morgan (1993). The still water in this region allowed for a small amount of weed growth. There was a region of strong transverse shear between the slow flow in this pool and the main flow.

On the opposite bank, the main flow separated away at the bend entrance (visible in fig. 5.2a, for a medium stage)and impinged upon the right bank several meters downstream, where an elevation of the water surface was visible in medium to large flows.

Further into the bend the flow close to the right bank separated once more across a small recess in the bank (fig. 5.2a). This separation resulted in a large region

of recirculation over a deep pool which was 1.5-2m deep for a medium stage. The pool extends for 5m downstream where the flow entered the main riffle section of the meander (fig. 5.2b) at cross-section 1. The cross-section widens between cross-sections 2 and 6, and a large point bar forms the outermost of several concentric terraces marking the former course of the river. Between cross-section 1 and 6 the right bank elevates considerably and here it was undermined and eroded extensively during the winter of 1992, as seen in fig.5.2b.

5.4 Surveying of the test reach.

5.4.1 Instrumentation and sampling strategy.

A geodimeter which operated using infra-red wavelength was used to measure the distances and angles between the cross-sections. The survey was carried out on two occasions, due to a landslide which occurred in December 1992 (visible in fig. 5.2b). For each set of measurements the angles between cross-sections were measured relative to a permanent feature of the landscape (A large oak tree).

The meander bend was divided into seven cross-sections, 15-25m apart, which can be identified by the stakes in fig. 5.1. This was considered to give a sufficient resolution in order that the mean flow in the meander could be defined, within the limitations of the time needed to take detailed measurements at each site in a single day. The aim was to have a complete set of measurements at a constant stage.

Cross-section A1 marked the furthest upstream measurements which would define the initial flow and concentration distributions for the model. This cross-section was a few meters downstream of the Street Beck confluence.

5.4.2 Results.

The results from the survey were used to create an overall picture of the reach, shown in fig.5.3a., where the dashed line shows the water line for a moderate flow. Fig. 5.3b. shows the topology at each of the measurement cross-sections for the second survey. The bed topology was measured at each of these transects at intervals of 0.5-1.0 m above an arbitrary datum beneath the bed and the measurements are shown in figs. 5.4 and 5.5. The topology of the river bed was only slightly changed between cross-sections A1-2 (fig.s 5.4a-5.4c), but was different at cross-sections 3-5 (fig.s 5.5a-5.5d). At cross-sections 3 and 4 only, the general shape of the cross-section was shifted towards the left bank (fig. 5.5a, 5.5b), although the shape was changed significantly at cross-section 5 and 6 (fig. 5.5c and 5.5d) following the landslide.

Table 5.1 below gives the separations between the cross-sections along the inner bank and the angles between the surveyed transects for the second set of surveying measurements:

Table 5.1 Surveyed geometry of reach.

measurements between cross-sections:	Separation along inner bank (m)	angle(degrees)
A1-1	24.6	29.8
1-2	21.0	43.5
2-3	26.7	47.0
3-4	18.9	14.9
4-5	18.0	21.8
5-6	14.1	0.05

5.5 Stage and Velocity measurements.

This section is principally concerned with the measurements of the mean downstream flow velocities at different stages, although some measurements of secondary flow were also undertaken.

5.5.1 Instrumentation.

A stage board was set up by H.Orr(I.F.E.) in Autumn 1992, in a pool downstream of the meander which was used in all subsequent work to determine a relative stage.

The velocity measuring equipment was changed over the three year period, due to the acquisition of new equipment by the I.F.E. The first three sets of velocity data were measured using an array of impeller meters (Ott meters) mounted on a single staff. Following these measurements, an electromagnetic current meter (E.C.M.) with a single head, and then an array of E.C.M. meters were purchased by the I.F.E. and were used in subsequent measurements of velocity. The multiple point velocity measurements enabled the structure of the vertical velocity profile to be examined in greater detail.

The E.C.M comprises a coil and a pair of electrodes housed inside a streamlined casing. The coil produces an electromagnetic field around the meter head, which when immersed in a conducting medium such as water, which is in relative motion to the meter head, cause an electro-motive force (E.M.F.) in the water. This

creates a potential gradient which is directly proportional to the relative velocity of the water in accordance with Faraday's law. This E.M.F. is detected by measuring the difference between the potentials of the two electrodes, and it is calibrated to indicate the velocity.

5.5.2. Sampling strategy.

Much of the river catchment is steep sided with high annual rainfall and a rapid runoff response, making the stage subject to flashy responses to precipitation. The hydrodynamic model was steady state only, which required that the field measurements were taken under settled weather conditions. The velocities were measured at as many different stages as possible so that a stage-discharge curve could be determined.

The measurements of the mean downstream velocities were made at approximately 1.0 m intervals in the transverse direction at each cross-section. The local downstream direction, parallel to the mean direction of the two banks, was estimated by eye at each measurement site. The uncertainty in the measurements due to misalignment by eye was estimated from the scatter of repeated measurements in section 5.4.4.

The velocities which were measured using a single E.C.M. were taken at 0.2 and 0.8 of the local flow depths. For the case of the array of E.C.M.'s or Ott meters, the depths of measurement were at fixed distances from the bed (0.05, 0.09, 0.15, 0.25, 0.37, 0.51m and 0.05, 0.09, 0.15, 0.30, 0.46, 0.63m for the E.C.M. and Ott meters respectively), such that in shallow regions only the bottom few probes were under water. There were regions of shallow flow over the point bar, in which it was

only reasonable to make a single velocity measurement in the vertical. In this case the single velocity measurement was used as the depth averaged mean velocity. The velocities at 45 degrees to the downstream direction were also measured for the cases when the E.C.M.'s were used and are described in section 5.4.5.

The sampling time was 30s for all of the measurements, under which conditions suitably stationary velocity time series were found to be obtainable. This was later confirmed by time series analysis of the fluctuating velocity, where the longest 1/e time constant was found to be 6.6s in the deadzone at cross-section A1.

The velocity measurements which had been made using both the Ott and E.C.M. meters described above had to be corrected at a later stage because the original calibrations of the probes were at fault due to an incorrect calibration flume. The corrections were supplied by the I.F.E.

5.5.3. Results

The velocity measurements taken on the different dates are summarised in table 5.2:

Table 5.2 Summary of downstream and secondary velocity measurements made on River Lune.

Date	Stage (m)	Cross-sections examined	Velocity probe used and no. of depths	Secondary velocity measurement
15/9/92	0.52	1-6	impeller meter multiple depths	none
22/9/92	0.58	1-6	as above	none
29/9/92	0.30	1-6	as above	none
3/12/92	0.70	1-6	e.c.m. meter 0.2 and 0.8 of depth	0.2 and 0.8 of depth
10/12/92	0.39	1-6	as above	as above
19/2/93	0.23	A1,A2,1	as above	as above
19/7/93	0.40	1,3,5	multiple e.c.m. probes & depth	multiple probe &depth
1/11/93	0.20	A1,1,4	as above	as above
2/11/93	0.20	7,8	as above	as above

5.4.4 Further experimentation: Estimation of uncertainty in velocity measurements due to misalignment of probe head.

The velocity measurements had a degree of inherent uncertainty due to the error in alignment by eye of the different probes with the mean downstream direction. All of the downstream velocity measurements were taken by holding the different

probes pointing upstream, in a direction which was as parallel to the mean direction of the banks as it was possible to judge by eye. The uncertainty due to misalignment was estimated for the E.C.M. by making repeated measurements at particular locations given in table 5.3a, for which the probe was turned out of alignment and realigned by eye for each measurement.

Table 5.3a Repeated measurements of velocities to ascertain uncertainty due to misalignment of E.C.M. probe.

repeated meas. no.	site 1 velocity m/s	site 2 velocity m/s	site 3 velocity m/s	site 4 velocity m/s	site 5 velocity m/s
1	0.303	0.52	1.09	-0.007	1.06
2	0.304	0.54	1.08	-0.012	1.04
3	0.296	0.51	1.10	-0.007	1.04
4	0.265	0.50	1.07	-0.009	1.05
5	0.286	0.49	1.09	-0.007	1.02
6	0.295	0.49	1.04	-0.008	1.04
7	0.283	0.47	1.07	-0.017	1.01
8	0.272	0.51	1.06	-0.012	1.02
9	0.292	0.56	1.05	-0.009	1.02
10	0.268	0.53	1.07	-0.007	1.03

The different sites were chosen to be representative of the different flow regimes within the channel, and are described in table 5.3b:

Table 5.3b Description of sites at which repeated velocity measurements were made.

site	description
1	0.3 m flow depth, smooth water surface no large scale inhomogeneities
2	0.45m, as above
3	0.80m, water surface characteristic of riffle.
4	0.2m, slow recirculating region of water behind slump - deadzone, negative readings
5	0.2m, long riffle section.

The coefficient of variability (fractional deviation from the mean of a quantity divided by the mean) gives an estimate of the fractional uncertainty for each set of measurements, and is tabled for each set in 5.3c.

Table 5.3c Coefficient of variability for repeated velocity measurements.

site	1	2	3	4	5
mean(m/s)	0.286	0.510	1.071	-0.010	1.031
σ_{n-1}(m/s)	0.015	0.027	0.019	0.003	0.020
σ_{n-1}/mean	0.051	0.053	0.018	0.3	0.019

The uncertainty in most of the measurements ranges from 2-5%, with the exception of site 4, where the flow was negative with respect to the probe orientation due to recirculation (see table 5.3b). The large uncertainty in the measurements at site 4 was thought likely to have been caused by flow separation around the pole to which the probe was attached, interfering with the flow over the probe head. In such instances, the probe should therefore be orientated such that it was pointing upstream.

This observation also cast doubt on the validity of the measurements which were made at 45 degrees to the flow.

5.5.5 Further experimentation: Secondary current measurements by decomposition of velocities measured at 45 degrees and parallel to the downstream flow.

The streamlined shape of the E.C.M. head minimised probe interference with the flow, and it was thought that the probe might also be used to measure the flow at 45 degrees to the downstream direction, by rotating the probe by 45 degrees (using a compass bearing) to the downstream direction. These measurements were combined with their counterpart downstream velocity measurements and the two vectors were resolved in order to determine the secondary velocity strengths using the technique described in chapter 6. The dates for which these measurements were made are also given in table 5.2

5.5 Turbulence measurements using an electromagnetic current meter (E.C.M.).

5.5.1 Instrumentation.

A pair of Valeport series 800 two-axis electromagnetic current meters were used to collect three dimensional velocity measurements. These E.C.M.'s operated on the same principles which were described above, but had an additional pair of electrodes in the plane of the coil, such that the velocity field could be measured in two

dimensions as demonstrated in fig.5.6, where a schematic diagram of the electromagnetic fields is given:

Fig. 5.6 Plan view of E.C.M. head showing electromagnetic fields.

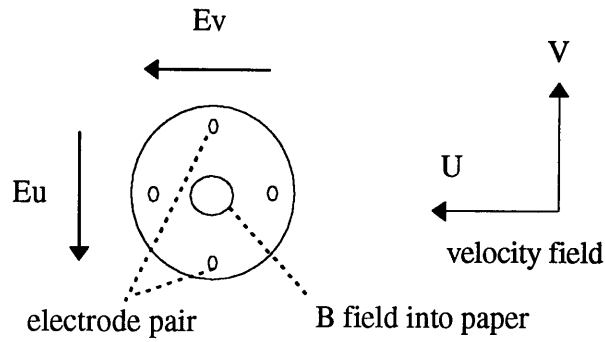

Where Eu is the electric field induced in the water due to the U component of the velocity field, and Ev that due to the V component.

The E.C.M.'s were attached to a rig which had been designed for the purpose of holding two meters at different angles to the flow as demonstrated in fig 5.7.

The two E.M.F.'s for each probe were recorded as digital units by an analogue-to-digital converter attached to a portable computer, and the digital units were converted to voltages (2048 digital units=5.0 volts) such that they could be translated to velocities using the calibration information given by Valeport. The E.C.M. was powered by two 12v batteries in series, and operated with a power consumption of approximately 5 amp-hours.

The probes were held at 45 degrees to the vertical, such that one channel of each probe recorded the downstream velocity time series. The alternate channel for each probe recorded the velocities at 45 degrees to the vertical and transverse directions, such that the velocities in these directions could be determined from the vector superposition of the signals, given by equations (5.1):

$$chU = \frac{(ch1 + ch3)}{2}$$
$$chV = \frac{(ch0 + ch2)}{\sqrt{2}} \qquad (5.1)$$
$$chW = \frac{(ch0 - ch2)}{\sqrt{2}}$$

where ch0-ch3 were the four signals measured by the probes, and chU,chV,chW are the components of the signals corresponding to the desired U,V,W flow directions.

5.5.2 Calibration.

The E.C.M.'s were calibrated by Valeport in 1992. However, the zero offsets for the probes, were investigated before the main set of measurements were made.

5.5.2.1 Laboratory experiments.

Before the E.C.M. rig was taken to the measurement site, it was tested in the laboratory flume, essentially to test that the heads were recording sensible outputs. The heads were then tested for drift in a large metal water tank. The signals which were recorded by the probes when immersed in the tank were discovered to be larger than expected and are detailed below in tables 5.4 and 5.5.

Table 5.4 Measurements of offsets in laboratory test tank for E.C.M. corresponding to Pod C / (yellow pod) .

time	channel 0 (digital units)	channel 1 (digital units)
11:53:34	59.50671	33.62001
11:54:12	58.64996	32.69667
11:58:32	54.7467	30.16334
11:59:23	53.58331	26.54999
12:04:44	49.25337	24.28336
12:15:01	44.87001	24.76003
12:37:52	38.64335	20.76003
13:05:34	34.28001	17.30668
13:07:05	34.07661	17.27334
13:10:37	33.64666	17.72668
13:41:13	30.5535	16.33332
16:09:01	23.27664	13.2533

Table 5.5 Measurements of offsets in laboratory test tank for E.C.M. corresponding to Pod A / (green pod).

time	channel 0 (digital units)	channel 1 (digital units)
11:16:13	-140.8701	-44.09007
11:17:59	-143.5769	-40.60670
11:20:32	-143.2698	-40.15004
11:21:13	-146.8299	-40.06671
11:22:01	-147.2799	-40.14005
11:26:52	-147.2368	-39.56670
11:27:42	-149.8534	-39.50669

Probe C (table 5.4) showed a drift of 40 digital units (~0.02m/s) in the offsets on both channels over a few hours. Probe A (table 5.5) was also found to give a small amount of drift over the quarter of an hour for which it was tested. The probes had recently been re-calibrated by the manufacturer, and it was thought that the drift may have been due to disturbances caused by the immersion of the probes into the water in

a large laboratory tank, not having settled over the period of measurement. At this stage, the probes were taken to the field, to test for the offset drifts in situ, using plastic caps to cover the heads in order to create zero flow around the probe heads.

5.5.2.2 Off-setting in situ.

The offsets were measured in the river by covering the E.C.M. heads with large plastic caps, and by immersing them in the water in the same position as if they were when recording direct measurements. The motion of the water surrounding the plastic caps could still give rise to an induced E.M.F. across the coils of the E.C.M., although the plastic caps were large (10cm diameter), so that the signals induced due to this effect were assumed to be negligible compared to the signals when the plastic caps were removed. The offsets have been called zero offsets, although as discussed above this is not strictly true. Table 5.6 shows the zero offsets which were taken at cross-section A1 on the 12/3/93.

Table 5.6 Measurements of offsets for E.C.M. pods A and C in River Lune on 12/3/93.

	pod C		pod A	
time	channel 0(d.u.)	channel 1(d.u.)	channel 2(d.u.)	channel 3(d.u.)
11:43:35	45.50335	19.66002	-160.2235	-40.03002
11:44:13	45.40994	19.26003	-158.1699	-39.99337
11:45:44	44.86006	18.84336	-157.8633	-41.61663
12:06:58	34.40002	16.61666	-161.0534	-41.61663
14:35:07	27.55671	13.67003	-159.6633	-38.87334
14:35:57	27.38003	13.68668	-159.5134	-38.37335

The offsets were found to be of the same order of magnitude as the laboratory measurements. The offsets for pod C were greater by a factor of at least ten compared to measurements made by Clifford et al.(1993), in which the zero offsets were typically of the order ~ 0.01v , although this will vary between different instruments. However, the offsets which were measured in the laboratory and in the field for the probes belonging to Lancaster University were of the order tenths of a volt . The manufacturer's calibration figures (1992) show that the zero offsets were of the order hundredths of volts, suggesting that the zeros had drifted in the year following these tests.

The calibration given by the manufacturer was non-linear over the entire range of velocities, although the range was split up into three sub ranges within which three different linear calibrations were given. The signals delivered by the heads when immersed in stationary water, fell within the middle sub-range of the calibration. The non-linearity of the calibration was signal size dependant, so the zero offset voltages were translated into velocities before they were subtracted from the velocity measurements.

Table 5.6 also demonstrated that the zeros were not drifting by as much as had been measured in the laboratory for both of the heads. This suggests that the drift in the test tank could have been due to disturbances in the tank. The drifts which were measured over the three hours in the river amounted to systematic deviation of less than 10 digital units in three of the 4 channels and of less than 20 digital units for channel 0. 20 digital units corresponded to a velocity of approximately 0.01 m/s (per 3 hours) which is smaller than the uncertainties associated with misalignment of the E.C.M. rig. for most of the measurements. The signals were therefore considered to

have sufficient stationarity such that time series analysis could be carried out on further velocity measurements.

5.5.3 Sampling strategy.

5.5.3.1 previous work.

The turbulence rig had been used in a previous study by an undergraduate (P.Mullen, 1992) on the straight section of the reach upstream of the meander. This study aimed to ascertain the minimum probe separation that could be attained without the probes interfering with each other. This was important to establish, since the cross-correlations were required to be made in as smaller an area as possible, in order that they were representative of the local flow structure. The report concluded that the minimum acceptable separation of the probes was 6cm, for which the resolved channel signals gave an average correlation of 0.9 over the depth, as shown in fig. 5.8a (due to Mullen,1993). Here x is the correlation between both of the downstream signals and y is the correlation in both of the cross-stream signals. However, more recently a study by Clifford et al.(1993) suggested that the separation which was required was somewhat larger at 20 cm. The value determined by Mullen was adhered to throughout this study, since it was determined using the same turbulence rig.

5.5.3.2 Zero offsets on days of velocity time series measurements.

The zero offsets were collected at the beginning of each set of velocity measurements after a warm up period of at least 15 minutes, but were not collected throughout the experiments. These are given in table 5.7:

Table 5.7 Measurements of offsets for E.C.M. pods A and C in River Lune on 7/5/93.

	pod C		pod A	
date	channel 0	channel 1	channel 2	channel 3
7/5/93	34.76617	-11.05271	-182.7605	-26.82402

These offsets were the same order of magnitude as on all previous tests, and were used with the understanding that they were drifting by at least the same amount as was determined for the measurements on the 12/3/93(i.e. 0.01m/s per 3 hours).

5.5.3.3 Intensity of field measurements.

The report by Mullen(1993) mentioned above found that the variation of the turbulent fluctuations with depth in the water column at any particular cross-sectional position did not show any particular trend in the sections of the reach which were examined (see fig. 5.8b, due to Mullen,1993). In this case, and because the number of measurements which could be made in a field day was limited, it was decided that

turbulence measurements would only be made at a single depth in the water column at each measurement site. This would show up any spatial variations in the turbulent intensities over the reach in the transverse and downstream directions only. However, it is acknowledged that there was a large probability of significant vertical variation in the turbulent intensities in, for example, the deeper regions of the flow.

5.5.3.4 Sampling period and duration for E.C.M measurements

The sampling period used was 7 minutes which was selected as a compromise between the need for a record length long enough to capture long term events in the flow and a record length short enough such that a large number of sites could be sampled at in a single day. The seven minute record lengths were of the same order of magnitude as the 1/e time constant which was estimated from the deadzone tracer experiment mentioned above.

The results from the E.C.M. measurements are not presented here, but are summarised in chapter six following a description of the different analyses carried out.

5.6 Tracer experiments.

The tracer experiments were carried out with two principal aims : 1) to estimate the lateral variation of the concentration of the tracer such that the predictive abilities of the model could be assessed, 2) so that a time series analysis could be carried out on the measured concentration of the passive tracer, which would contain

information about the larger scale mixing processes which the tracer had experienced in the reach.

5.6.1 Instrumentation.

The tracer tests which were carried out on the river Lune made use of four main pieces of apparatus : a fluorometer, a Marriotte (constant head) bottle for the dye injection, a water pump and hosing, a rig to hold the fluorometer in place above the water.

5.6.1.1 Fluorometer design.

The sample chamber dimensions and maximum sampling rate were used to determine the correct pumping rate of water through the sample chamber. Fig. 5.9 shows the sample chamber specifications.

Fig. 5.9 Diagram to show fluorometer sample chamber dimensions.

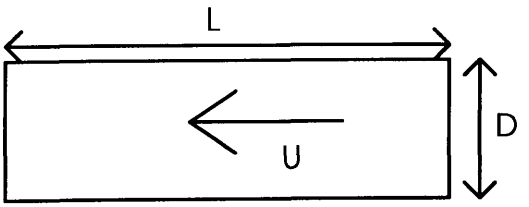

Fmax=1Hz L=0.037m Umax=L*Fmax

Umax=0.037m/s

D=0.018m

The maximum sampling rate was given by the manufacturer as 1 second. This constrained the discharge through the sample chamber to an upper limit, above which the fluorometer would be integrating the fluorescence from a larger volume of water than the capacity of the sampling chamber. In this case the florescence time series as measured by the fluorometer would no longer be the true fluorescence time series which was passing through the tubing.

The theoretical maximum discharge required, if such integration effects were to be avoided was therefore given by equation 5.2:

$$Q_{\max} = U_{\max} . \frac{\pi D^2}{4} \approx 1 \times 10^{-5} \, cumecs \qquad (5.2)$$

However, further integration effects occur from turbulent mixing in the intake pipe, and from the fact that the water is being pumped out of the river at a different rate to the local river flow.

The first effect was reduced through making the intake pipe to the chamber as short as possible. This entailed designing a rig to hold the fluorometer as close to the sampling site as possible. The rig was a simple metal table on which the fluorometer, pump and power supply could be held and is shown in fig.5.10. This effect can also be reduced through having fluted pipework, although there was a small difference in the radii of the intake pipe and the sample chamber, as designed by the manufacturer.

5.6.1.2 Pump specification.

A pump was acquired which had roughly the required discharge. The pumping rate depended on the length of the intake pipe, due to frictional losses increasing with the length of the pipe, so the same length of intake pipe (2.0m) was used in the determination of the pumping rate (table 5.8) and in the field measurements.

Table 5.8a Measurements of pumping rate for fluorometer rig.

intake pipe length(m)	volume pumped(ml)	in time(s)	discharge (cumecs)
2.0	520.0	39.0	0.0000133
2.0	450.0	37.0	0.0000122
2.0	575.0	48.0	0.0000120

Unfortunately, during investigations on the 4/5/93 the pump seal broke and had to be repaired, which reduced the pump rate to:

Table 5.8b Measurements of amended pumping rate.

intake pipe length(m)	volume pumped(ml)	in time(s)	discharge (cumecs)
2.0	2000.0	248.0	0.0000081

Both of these pumping rates were close to the estimated maximum acceptable discharge which was calculated in section 5.6.1.1. The rates were also larger than the minimum recommended pumping rate(8.33×10^{-7} cumecs) of the manufacturer which is necessary to avoid non-trivial heating of the sample during flow through the chamber.

5.6.1.3 Fluorometer calibration.

The fluorometer was calibrated in the laboratory with a $10.06 \mu g l^{-1}$ standard solution of rhodamine wt at 22.4 degrees centigrade in accordance with the manual. The florescent dye used was rhodamine wt, which has a low adsorption rate on inorganic and organic material (Yotsukura et al, 1970) and is believed to have a low toxicity. The rhodamine is sold in caustic solution, which was the main objection to the use of the dye in large quantities put forward by the National Rivers Authority (N.R.A.). However, the small amount of the solution which were used in these experiments (~ 2g rhodamine per day) was acceptable to the NRA.

5.6.1.4 Continuous dye release.

The dye was released into the river from a Marriotte bottle or continuous head device, which was calibrated in the laboratory. The experiments in the field were predicted to last for anything up to 5 hours, so the discharge had to be designed to be slow enough for this. The discharge was essentially governed by the head of the outlet pipe below the level of the air inlet to the Marriotte bottle, and by the bore of the outlet pipe. The bore of the outlet pipe was reduced until the discharge was small enough such that the 20 l capacity would drain in approximately 5 hours for a head of ~ 40cm .

5.6.2 Sampling strategy.

5.6.2.1 Concentration calculations in accordance with N.R.A.

The River Lune is an important salmon river, so the dates of field work and the maximum allowed concentration of dye used had to be prearranged in agreement with the National Rivers Authority. The maximum permissible dye concentration when well mixed in the river was approximately $0.1 \mu g l^{-1}$, so that the tracer experiments had to be designed with this in mind. The fluorometer was capable of discerning concentrations down to $0.01 \mu g l^{-1}$ (Elhadi et al, 1985), but this was limited by the natural background levels of fluorescence. Given the discharge on the day of measurement, the maximum rate of addition of mass to the river was given by equations 5.3:

$$m = 100(\mu g m^{-3}).Q(m^3 s^{-1}) \quad or \quad m = 0.36.Q(g hr^{-1}) \tag{5.3}$$

where m=mass flux and Q=river discharge. For a five hour experiment, the total mass of rhodamine which could be added to the Marriotte bottle, was 1.8Q grammes. For a discharge of 1 cumec, 1.8 g of pure rhodamine or 9g of 20% solution were added.

5.6.2.2. Tracer concentration measurements.

The tracer experiment was undertaken on the 7/5/93 (in conjunction with E.C.M. velocity measurements), for a steady stage of 0.24m.

A measurement of the background fluorescence was taken over a period of 20 minutes before the dye was released. The trace did not show any systematic trends, so this period was considered to be sufficient.

The dye was injected into a turbulent part of the channel 50m upstream of cross-section A1. At least twenty minutes were allowed to elapse before the fluorometer readings were taken, as this was considered long enough for the steady state to have been achieved. The fluorometer was also allowed a 15 minutes warm up period as recommended. The maximum sampling rate of 1s was used, with sampling periods of 3-4 minutes. Table 5.9 summarises the measurements.

Table 5.9 Summary of tracer concentration measurements.

date	stage	cross-sections examined	dye release	sampling intervals
7/5/93	0.24	A1,1,4	left bk. + 3m,(A1-50m)	1s

The fluorometer was deployed at 1m intervals in the transverse direction for each of the transects and at least one minute(or more when there was clearly a large amount of turbidity) was allowed to elapse before the fluorescence was recorded to allow for any disturbance during the movement of the rig.

5.6.7 Results.

The time averaged mean background concentration was measured as:

$$c = 0.046 +/- 0.003 \ \mu g \ l^{-1} . \qquad (5.4)$$

The measurements of the concentration downstream, following the dye release are tabulated below for cross-sections A1,1 and 4, with the temperature corrected and background-subtracted concentrations in the final column. The depth averaged concentrations are displayed graphically in fig.s 5.11, 5.12 and 5.13.

Table 5.10a Tracer concentration measurements at Cross-section A1(7/5/93).

Transverse position(m) from L.bank	Total depth (m)	Meas. height above bed (m)	mean concn. ($\mu g \ l^{-1}$)
1.0	0.32	0.08 0.29	0.623 0.757
2.0	0.30	0.15 0.24	0.253 0.321
3.0	0.40	0.11 0.30	0.253 0.205
4.0	0.31	0.13 0.28	0.326 0.201
5.0	0.46	0.22 0.38	0.358 0.241
6.0	0.43	0.22	0.265
8.0	0.51	0.44	0.278

Table 5.10b Tracer concentration measurements at cross-section 1(7/5/93).

Transverse position(m) from L.bank	Total depth (m)	Meas. height above bed (m)	mean concn. ($\mu g\ l^{-1}$)
1.0	0.32	0.12 0.24 0.31	0.200 0.201 0.245
2.0	0.41	0.15 0.35 0.40	0.366 0.235 0.176
3.0	0.30	0.10 0.27	0.248 0.239
4.0	0.19	0.15	0.178
5.0	0.15	0.10	0.271
6.0	0.09	0.05	0.130
7.0	0.05	0.05	0.165
8.0	0.06	0.02	0.172
11.2	0.26	0.12 0.25	0.247 0.232

Table 5.10c Tracer concentration measurements at cross-section 4(7/5/93).

Transverse position(m) from L.bank	Total depth (m)	Meas. height above bed (m)	mean concn. ($\mu g\ l^{-1}$)
0.1	0.08	0.06	0.115
1.1	0.19	0.10	0.073
2.1	0.22	0.18	0.070
3.1	0.21	0.14	0.080
4.1	0.26	0.22	0.090
5.1	0.30	0.14	0.071
6.1	0.20	0.15	0.089

The temperature correction will be discussed with the rest of the data analysis in chapter 6. The measurements were made at more than a single depth were possible, and around the mid depth in the shallow regions.

5.6.8 Further experimentation: discharge in Street Beck.

Attempts were made to measure the discharge in the brook flowing into the main river, several times using salt dilution gauging. However, the flow was very slow further upstream and there were problems with the salt not mixing adequately. It was estimated from velocity measurements to have a discharge of 0.005-0.01 cumecs, for a medium stage in the River Lune. The brook was also discovered to have a different temperature to the river, by as much as 2 degrees centigrade on more than one occasion. This might act as a useful tracer if the reach was examined in the future using temperature as a tracer.

5.7 Selection of a data set for model calibration.

The different data sets which were collected on the reach were taken on different days, on which there were inevitably small differences in the stage and discharges. This section describes which data sets were used.

The data which was collected on the 7/5/93 for a 0.24 stage was the only complete data set, for which measurements of tracer concentration and turbulence characteristics were made at three cross-sections. This was considered the minimum number of measurements which could be used to characterise the dispersion characteristics of the reach. However, comprehensive velocity measurements were not made at all of the cross-sections A1-6 on this date. A full set of velocity measurements

for all seven of these cross-sections was required in order to create the mean flow model. These measurements had to be corrected for differences in the stage and discharge by making the approximation that the banks were vertical.

The velocity measurements which were made with a stage most similar to 0.24, were taken on 29/9/92, stage=0.3 ; 19/2/93, stage=0.23. The measurements which were taken on 29/9/92 were the more comprehensive, since these were carried out for multiple depths in cross-sections 1-6, although did not include cross-section A1. The measurements of velocity which were taken for the stage of 0.23 were used in the mean flow interpolations between cross-sections A1 and 1. The rescaled velocity field for the entire reach, on which the model is based is given in chapter 6. In summary the data sets in table 5.11 were used:

Table 5.11 Summary of velocity, turbulence and tracer concentration measurements selected to be used for the construction of the computer model.

measurement	date	stage	cross-sections	stage adjustment to:
tracer test	7/5/93	0.24	A1,1,4	-
e.c.m.	7/5/93	0.24	A1,1,4	-
velocity	19/2/93	0.23	A1,1	0.24
velocity	29/9/92	0.30	2,3,4,5,6	0.24

Fig.5.1

Overview of test reach on day of tracer experiment

7/5/93 stage of 0.24

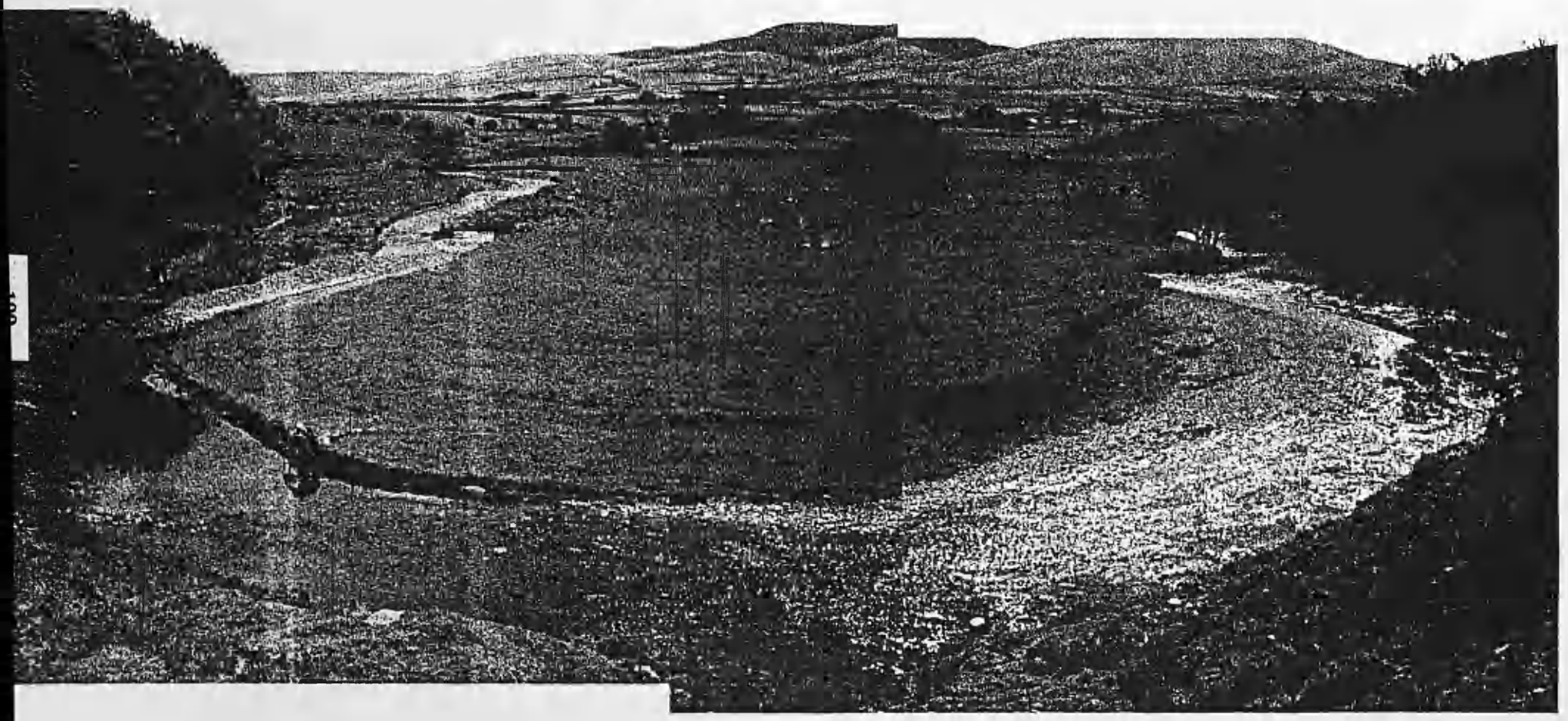

Fig.5.2 Upstream subsection of test reach on 1/2/93 showing secondary currents for stage 0.5m

a

Downstream subsection showing bank erosion

b

Fig.5.3
Contour maps of test reach constructed from survey.

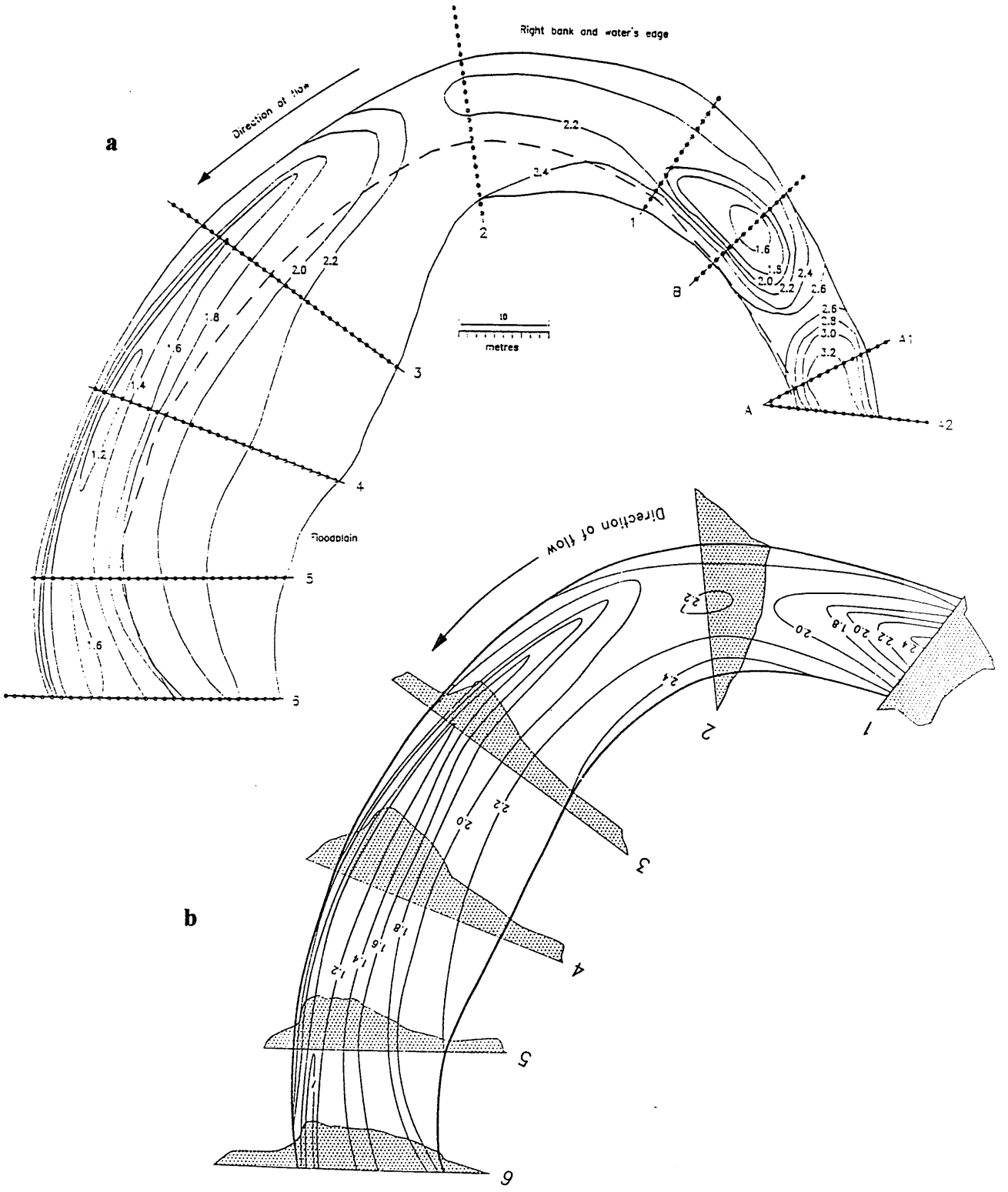

Fig.5.4
Cross-sections of downstream measurements sites, A1, 1 and 2.

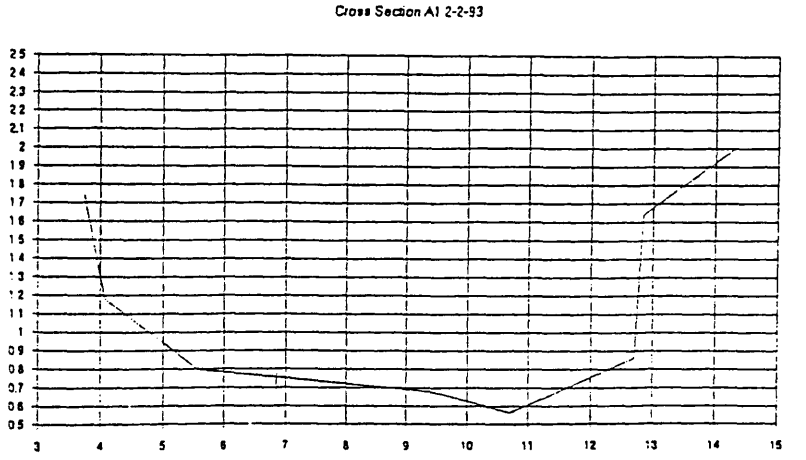

a

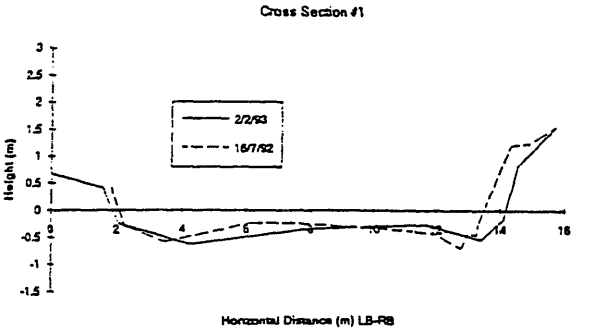

b

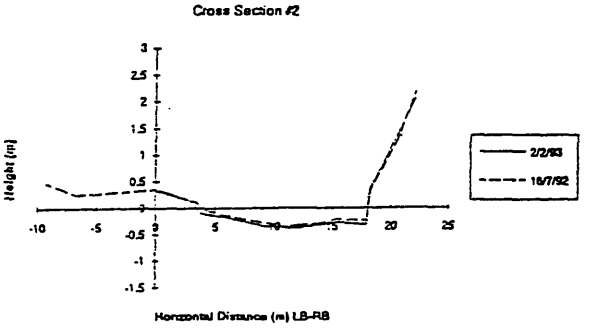

c

Fig.5.5 Cross-sections 3,4,5 and 6 (measurement sites)

a

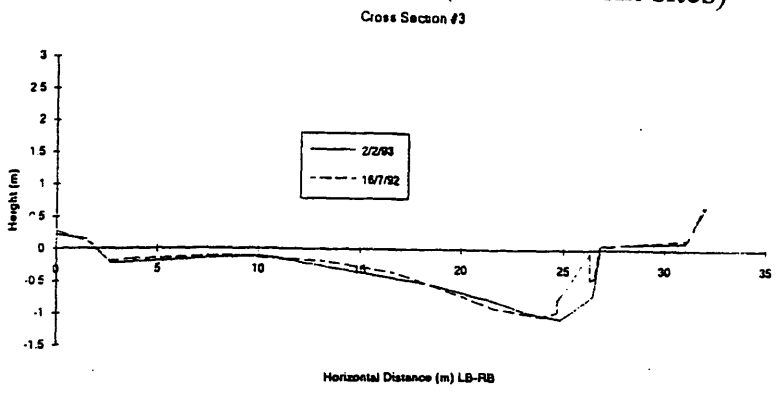

b

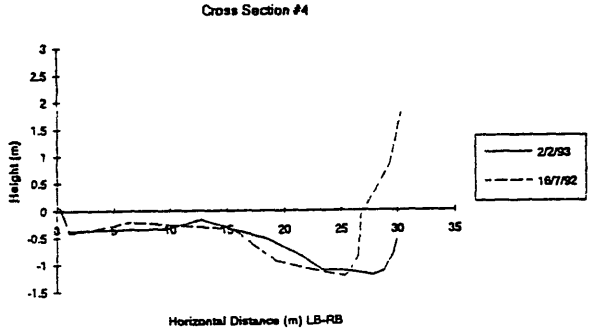

c

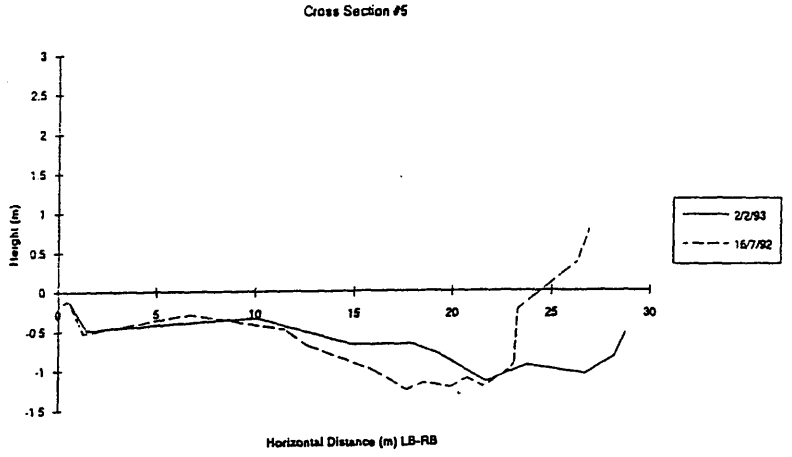

d

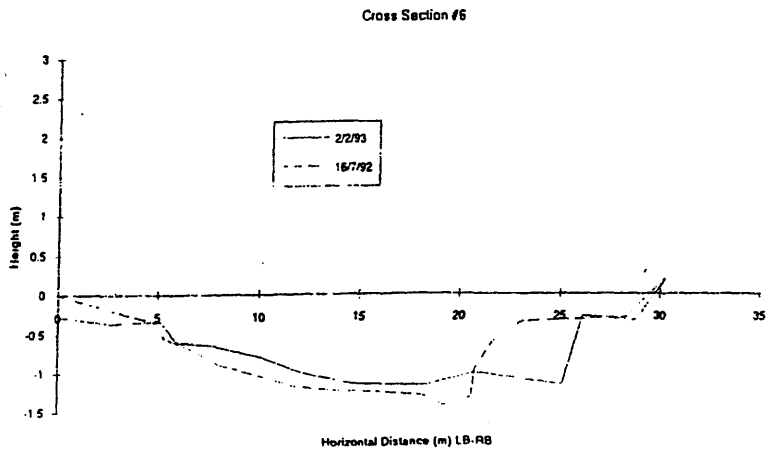

Fig.5.7

Picture of electromagnetic current meter and rig on 7/5/93

stage 0.24

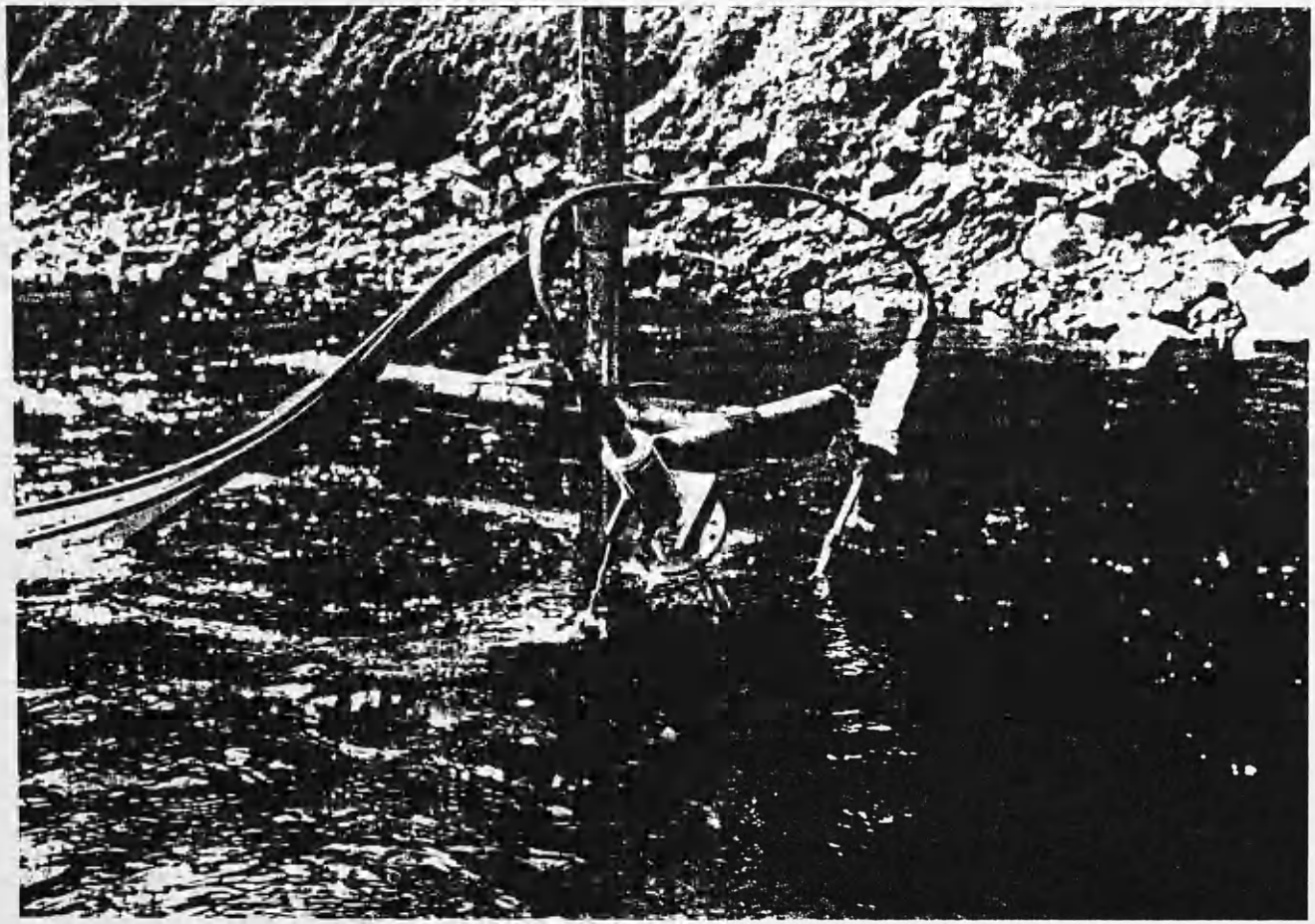

Fig.5.8a Correlations in signals from two E.C.M. probes separated by 6 cm (P.Mullen, 1993).

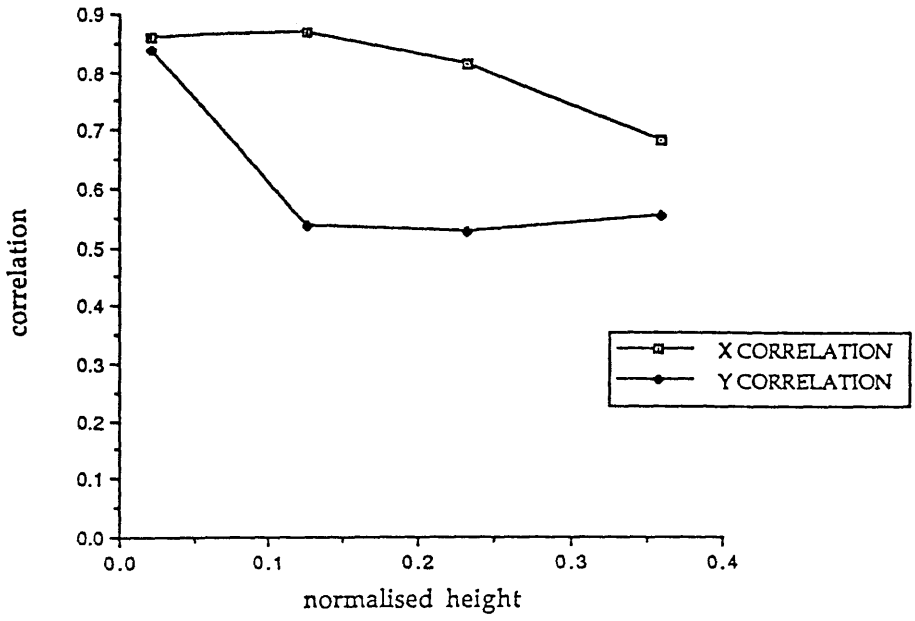

Fig.5.8bR.M.S. Values of siganls ch1,ch2,ch3 and ch4 for E.C.M.'s with probe separation of 6cm (P.Mullen, 1993).

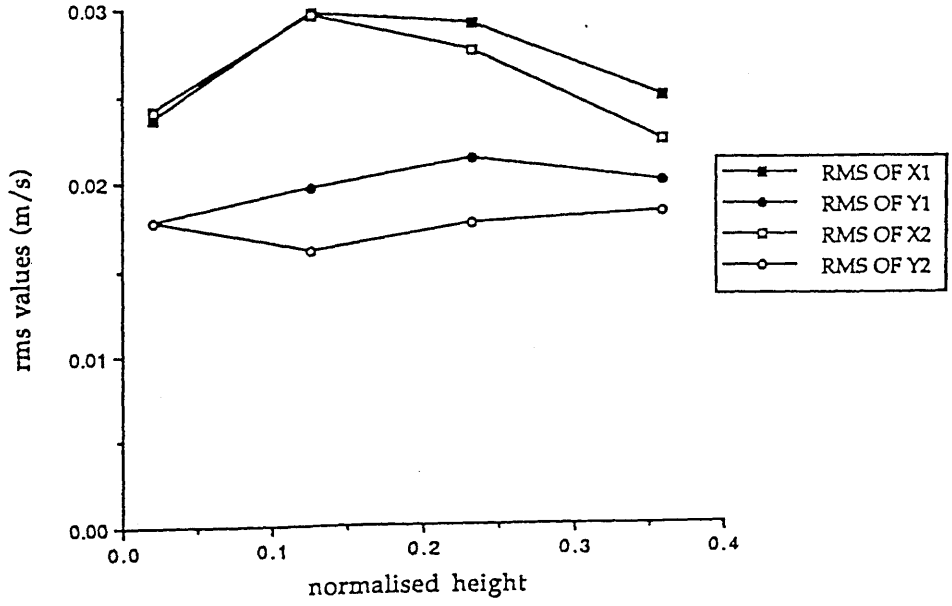

Fig.5.10

Picture of fluorometer and rig on 7/5/93 stage 0.24

Fig.5.11

transverse distributions of depth averaged concentrations,
standard deviations from time averaged mean concentrations,
and the depths at cross section A1

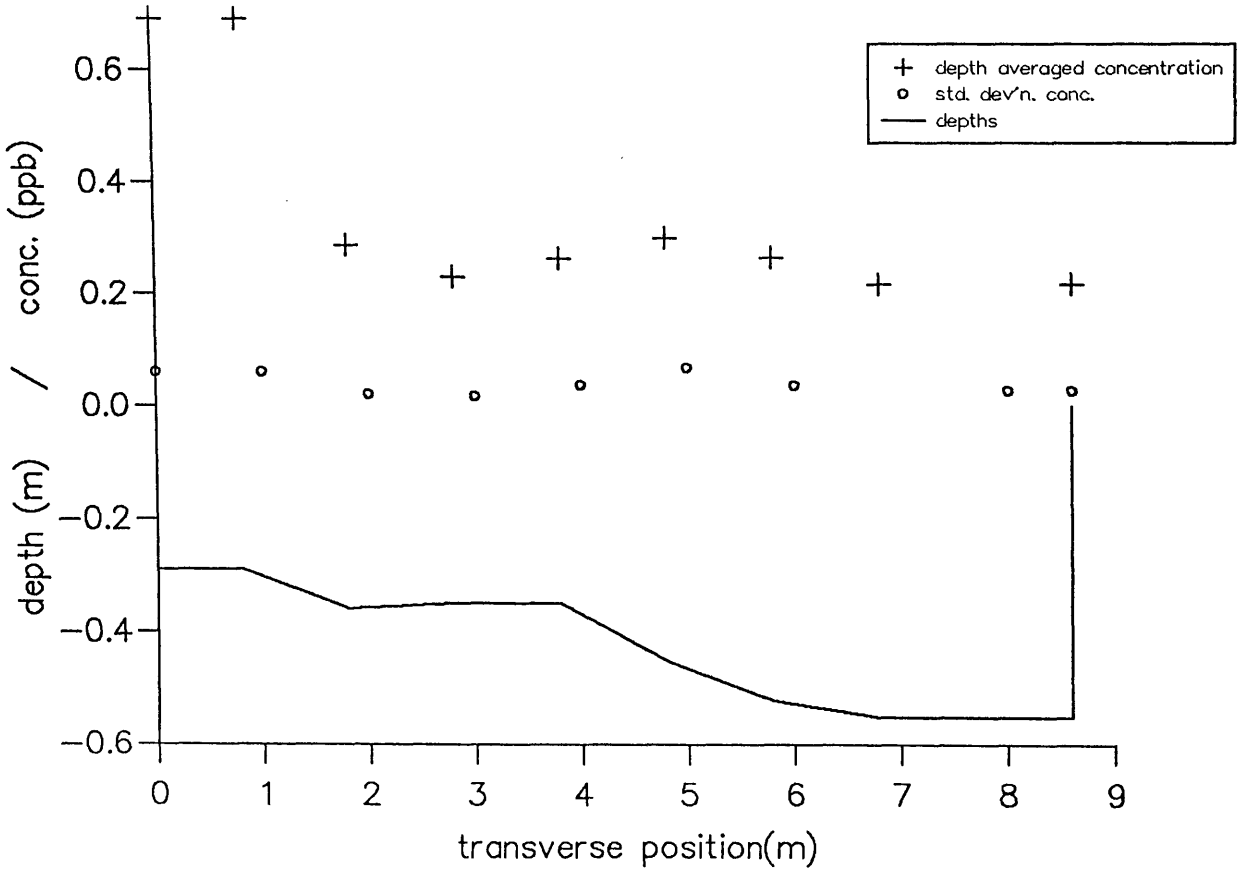

Fig.5.12

transverse distributions of depth averaged concentrations,
standard deviations from time averaged mean concentrations,
and the depths at cross section 1

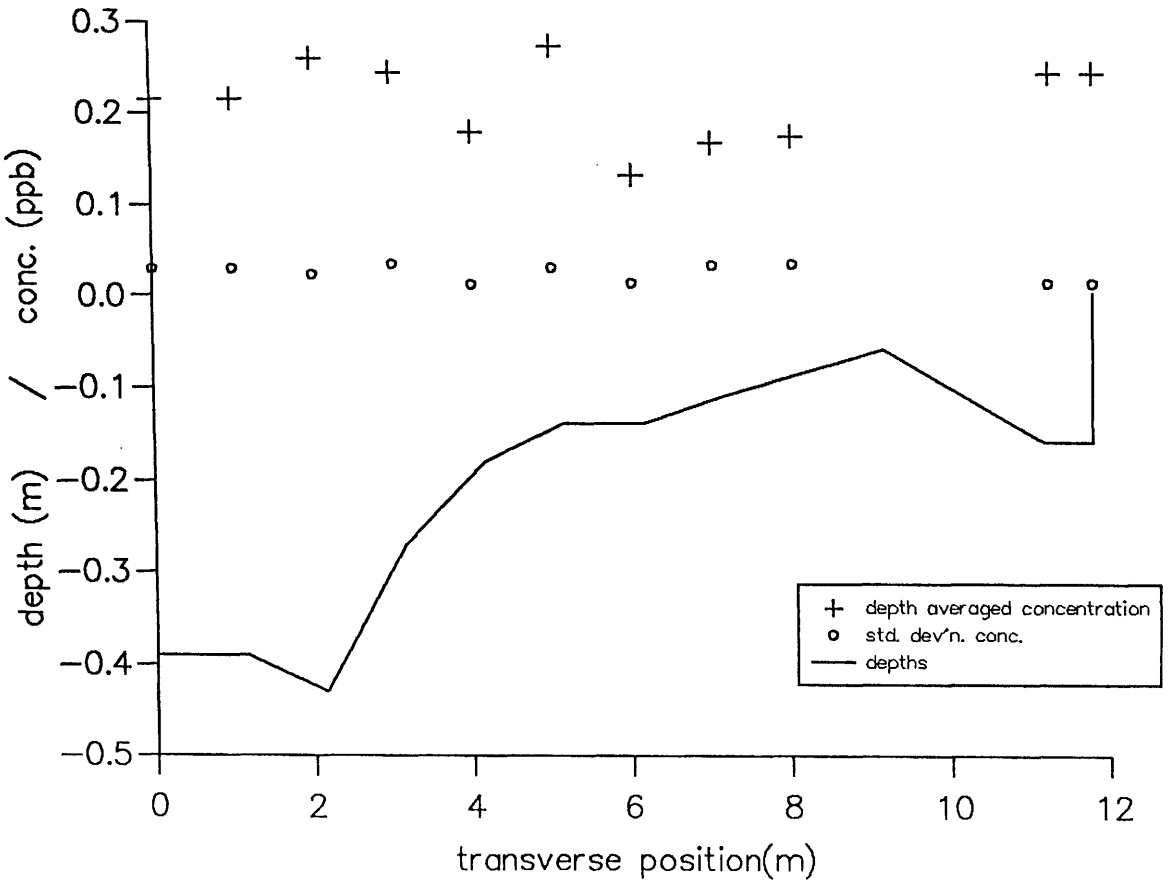

Fig.5.13

transverse distributions of depth averaged concentrations,
standard deviations from time averaged mean concentrations,
and the depths at cross section 4

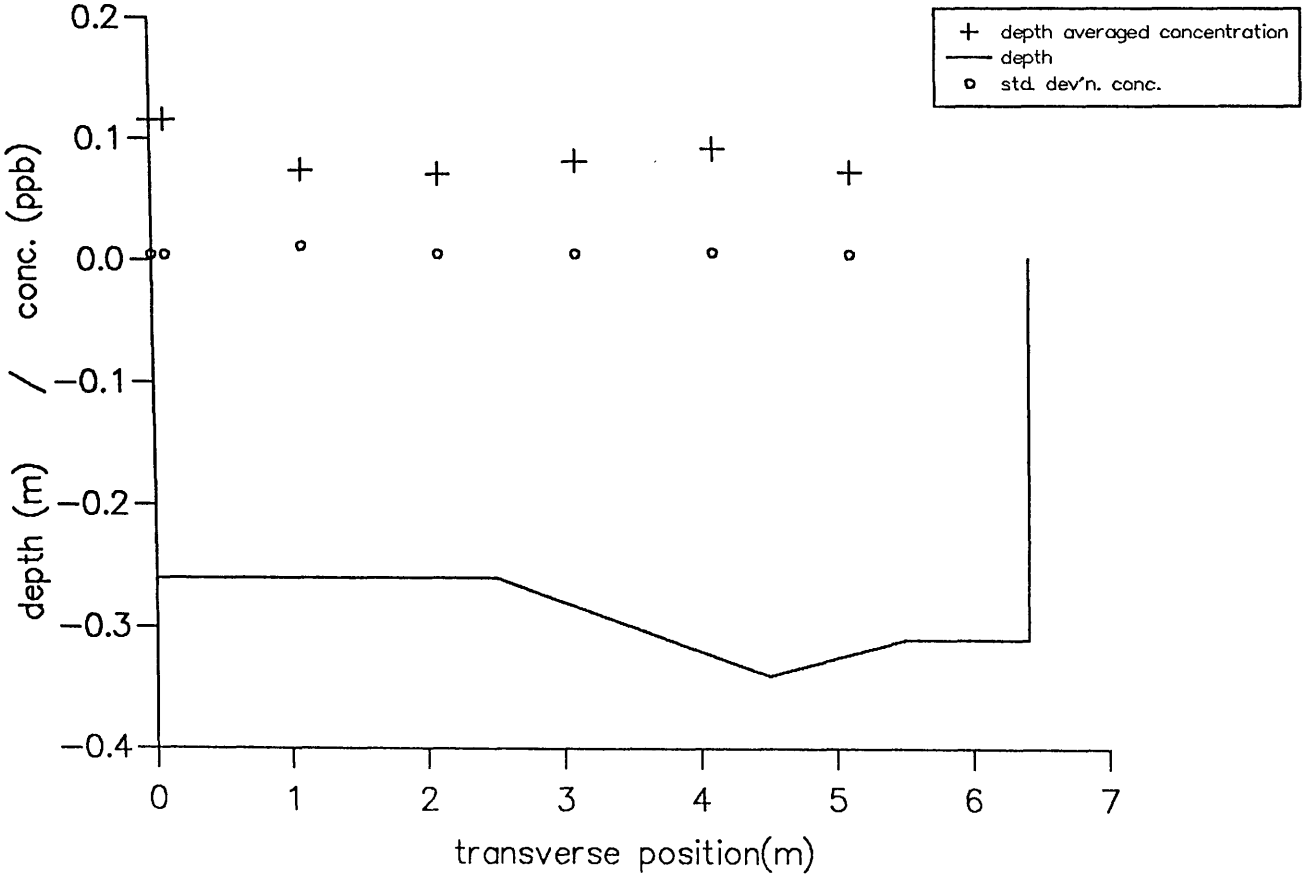

Chapter 6

Analysis of field measurements from the River Lune.

6.1 Introduction.

This chapter describes an analysis of the different measurements which were reported in chapter 5. The analysis can be divided into three principal sections, dealing with the measurements of mean velocities, velocity time series, and tracer concentrations. These sections are further divided into sub-sections which deal with different stages in the analysis including the estimation of uncertainties.

The aim of the analyses was to retrieve enough information from the different data sets to enable the construction of a three dimensional random particle tracking model, which will be described in chapters 7 and 8.

6.2 Analysis of velocity measurements.

In this section the velocities which were recorded on different dates are used to create a stage discharge curve. The vertical velocity profiles are examined and modelled using logarithmic profiles. The measurements of velocities at 45 degrees to the downstream direction are used to estimate the secondary flow velocities. Finally, length scales associated with secondary current speeds are estimated.

6.2.1 Construction of a stage-discharge curve.

The velocity measurements at each cross-section were used to calculate the discharge passing through each section, using the velocity-area method. This technique required the estimation of the depth-averaged velocity at each measurement site. When only one velocity measurement was taken through the depth, due to shallow water, this was taken to be the depth-averaged velocity. When two measurements (at 0.2m and 0.8m of the depth) were used, the average of these velocities was taken to be the depth-averaged mean. When the multiple-head velocity meters were used, and it was possible to fit a logarithmic profile to the data, the depth-averaged mean velocity assuming a logarithmic profile throughout the depth was used (see section 6.2.3). This was generally necessary in order to extrapolate the velocity measurements to the surface, where there were no measurements. The velocity-area method is given by equation 6.1:

$$Q = \sum_{i=1}^{N_M - 1} \frac{\left(u_{d,i} + u_{d,i+1}\right)}{2} \frac{\left(h_{i+1} + h_i\right)}{2} \left(y_{i+1} - y_i\right) \qquad (6.1)$$

where Q is the total discharge through a cross-section, $u_{d,i}$ is the depth-averaged velocity at measurement site i, (which includes the zero velocities at the waters edge) h_i is the total depth at measurement site i, and y_i is the transverse location of measurement site i.N_M is the number of measurement sites plus two (to account for the zero velocities close to the banks).

The discharges for the different stages which were determined this way are given in table 6.1, and the resulting stage / discharge curve is given in fig.6.1.

Table 6.1 Reach averaged discharge and secondary current speeds for the different sets of velocity measurements.

stage(m)	number of depths and cross-sections examined	reach averaged discharge (m^3/s)	reach averaged secondary current speed if recorded (m/s)
0.52	multiple 6	3.4 +/- 0.1 (3%)	-
0.58	multiple 6	4.3 +/- 0.1 (2%)	-
0.30	multiple 6	0.76 +/- 0.07 (9%)	-
0.70	2 6	6.2 +/- 0.3 (5%)	0.22
0.39	2 6	1.36 +/- 0.06 (4%)	0.16
0.23	2 3	0.32 +/- 0.02 (6%)	0.14
0.40	multiple 3	1.41 +/- 0.09 (6%)	0.26
0.20	multiple 3	0.24 +/- 0.02 (8%)	0.11
0.20	multiple 2	0.27	0.14

6.2.2 Uncertainties in the discharges

The discharges are quoted with +/- deviations(and also with fractional deviations expressed as a percentage, given by $\sigma_Q/Q \times 100$) in table 6.1, which are simply the standard deviations from the mean of the discharges which were determined from the different cross-sections examined for each stage. The final measurement set are not quoted with a deviation, since only two cross-sections were examined. The table shows that the scatter is greater when only a few cross-sections are used.

The next step was to approximate the fractional uncertainties in the discharges as the fractional deviations from the mean (σ_Q/Q), but first the expected uncertainties from estimated experimental uncertainties in the measurements of velocity, depths and

transverse distances were examined. This was carried out since it was important to verify the values of uncertainties in the discharges, since these were later used in the estimation of the uncertainties in the tracer mass fluxes.

The discharge between any two measurement sites was calculated in the velocity area method using equation 6.2:

$$q_i = \frac{(u_{i+1} + u_i)}{2} \frac{(h_{i+1} + h_i)}{2} (y_{i+1} - y_i) \qquad (6.2)$$

The uncertainty in each value of q_i, for each cross-section, was estimated from the estimated uncertainties in the measurements of depths, velocities and distances and using standard error analysis of 6.2 to give equation 6.3:

$$\Delta q_i^2 = \left(\frac{\partial q_i}{\partial u_i}\right)^2 \Delta u_i^2 + \left(\frac{\partial q_i}{\partial u_{i+1}}\right)^2 \Delta u_{i+1}^2 + \left(\frac{\partial q_i}{\partial h_i}\right)^2 \Delta h_i^2 + \left(\frac{\partial q_i}{\partial h_{i+1}}\right)^2 \Delta h_{i+1}^2 + \left(\frac{\partial q_i}{\partial y_i}\right)^2 \Delta y_i^2 + \left(\frac{\partial q_i}{\partial y_{i+1}}\right)^2 \Delta y_{i+1}^2 \qquad (6.3)$$

where the fractional uncertainty in the velocity measurements due to misalignment was estimated from the scatter of repeated measurements in chapter 5 to be approximately 5%. The fractional uncertainties in the depth and the transverse distance measurements are estimated as having uncertainties between 3-5% due to the rough geometry of the reach.

The fractional uncertainty in the total discharge at each cross-section can then be determined from standard error analysis of 6.1 to give equation 6.4:

$$\frac{\Delta Q}{Q} = \sqrt{\frac{\sum_{i=1}^{n-1} \Delta q_i^2}{Q^2}} \qquad (6.4)$$

Equations 6.1-6.3 were used to estimate the reach averaged mean of the expected fractional uncertainties in the discharges for the 7 sets of measurements which were used in the construction of the computer model. These 7 sets of measurements were taken from the measurements at stages of 0.23 and 0.3 (discussed in chapter 5).

For the estimates of 3% and 5% in the distance measurements this gave the range of values given by equation 6.5.

$$0.08 < \Delta Q/Q < 0.12 \qquad (6.5)$$

This range of values compares with the range of fractional deviations of 6% and 9% for the 0.23 and 0.3 stages respectively, given in table 6.1.

6.2.3 Vertical velocity profiles.

The number of velocity measurements at each site was limited by the relatively shallow depths involved in the study reach and by the necessity to make measurements at many different sites in a limited amount of time. A low order fit to the profiles was

therefore required to avoid large uncertainties arising from calibrating a large number of parameters.

At measurement sites where it had been possible to measure more than two velocities through the depth, a logarithmic profile was regressed to the data. This made the assumption that lower layer of the turbulent boundary layer extended over the whole of the depth. The dependent variable in the regression analysis is the velocity (Bergeron et al 1992), although it is plotted on the abscissa following normal practice.

Figs. 6.2,6.3 show the velocity measurements at different cross-sections in the form of semi-logarithmic plots of ln(z) against velocity for selected sites where velocities had been measured at 4 locations through the depth. If the logarithmic distributions are suitable, then the points on the graphs should all be in a straight line. However, there are clearly non-linear relationships at some of the of sites, and the gradients of the lines varied by a large amount.

This analysis neglected the zero plane displacement height which was discussed earlier in chapter 1, but the uncertainties caused by this were considered to be smaller than the uncertainties caused by making the assumption of a logarithmic profile throughout the depth.

The shear velocity, u* and the roughness height, Zo were determined from the gradient of the regression and the point of interception of the regression with the ordinate, respectively for measurement sets for which there were more than two measurements of velocity through the depth.

At sites where there was only a single velocity measurement, the single measurement was taken to be the depth-averaged velocity, and this was equated to the depth-averaged velocity assuming a logarithmic profile (in terms of the undetermined

friction velocity and roughness height) . In this case, there are two unknowns, and only one piece of information (the depth-averaged velocity). This was overcome by approximating the roughness height as the cross-section averaged value. These values were used later to determine the downstream velocity at any depth in the flow for the random particle tracking model, and are given in tables 6.2a and 6.2b for the data sets used in the construction of the model.

The data for the 0.23 stage (table 6.2a) comprised two point measurements only (at 0.2 and 0.8 of the depth) and consequently the logarithmic profile could not be fitted with any degree of certainty. In regions were the upper velocity was slower than the lower velocity, for which cases a log profile could not be fitted, the depth averaged velocity was again calculated, and this, in conjunction with the cross-section averaged roughness height were used to determine a friction velocity using the same technique which was described above. This was carried out in the absence of a better data set for the correct stage. It was, however, considered to be the best available form of interpolation, given the data set.

Table 6.2a Depth-averaged velocity, friction velocity and roughness heights determined from measurements of velocity from 0.23 stage for cross-sections A1 and 1.

transverse distance from left bank(m)	depth-averaged downstream velocity(m/s)	friction velocity(m/s)	roughness height(m)
Cross-section A1			
0.0	0.000	0.000	0.000
0.8	0.149	0.020	0.0058
1.8	0.389	0.066	0.015
2.8	0.273	0.080	0.044
3.8	0.121	0.035	0.032
4.8	0.030	0.008	0.032
5.8	0.021	0.005	0.058
6.8	0.012	0.002	0.040
8.6	0.000	0.000	0.000
Cross-section 1			
0.0	0.000	0.000	0.000
1.15	0.168	0.018	0.004
2.15	0.179	0.003	0.002
3.15	0.166	0.017	0.0021
4.15	0.156	0.015	0.0011
5.15	0.133	0.013	0.001
6.15	0.110	0.011	0.002
7.15	0.112	0.009	0.002
9.15	0.040	0.005	0.0002
11.15	0.389	0.030	0.002
11.75	0.000	0.000	0.000

Table 6.2a Depth-averaged velocity, friction velocity and roughness heights determined from measurements of velocity from 0.3 stage for cross-sections 2 to 6.

transverse distance from left bank(m)	depth-averaged downstream velocity(m/s)	friction velocity(m/s)	roughness height(m)
Cross-section 2			
0.0	0.000	0.000	0.000
2.0	0.618	0.091	0.005
4.0	0.525	0.120	0.019
6.0	0.524	0.166	0.040
8.0	0.469	0.079	0.007
10.0	0.614	0.303	0.030
10.5	0.000	0.000	0.000
Cross-section 3			
0.0	0.000	0.000	0.000
1.5	0.140	0.042	0.026
2.5	0.206	0.073	0.043
3.5	0.396	0.128	0.051
4.5	0.816	0.137	0.021
5.0	0.000	0.000	0.000
Cross-section 4			
0.0	0.000	0.000	0.000
2.5	0.424	0.160	0.049
3.5	0.630	0.136	0.021
4.5	0.708	0.213	0.045
5.5	0.658	0.109	0.012
6.4	0.000	0.000	0.000
Cross-section 5			
0.0	0.000	0.000	0.000
2.6	0.607	0.154	0.031
4.6	0.571	0.077	0.006
5.6	0.345	0.122	0.054
6.6	0.357	0.078	0.021
7.1	0.000	0.000	0.000
Cross-section 6			
0.0	0.000	0.000	0.000
0.3	0.492	0.075	0.005
2.3	0.534	0.091	0.008
4.3	0.542	0.150	0.023
6.3	0.292	0.099	0.057
8.3	0.342	0.070	0.028
8.9	0.000	0.000	0.000

The reach averaged friction velocity was determined for each stage from the values determined from the above tables. It was not calculated from the single measurement of the water surface slope which had been made, since the secondary currents have a large influence on the depression/elevation of the water surface (see Bridge and Jarvis, 1976).

6.2.4 Secondary current measurements.

Secondary currents were clearly visible (fig. 5.2a, stage ~ 0.5), and attempts were made to measure them. The cross stream velocity component was estimated from vector addition of the downstream velocity and the velocity at 45 degrees to the downstream direction at the same site. This is demonstrated schematically in fig. 6.4:

Fig.6.4 Definition diagram for vector addition in secondary current velocity analysis.

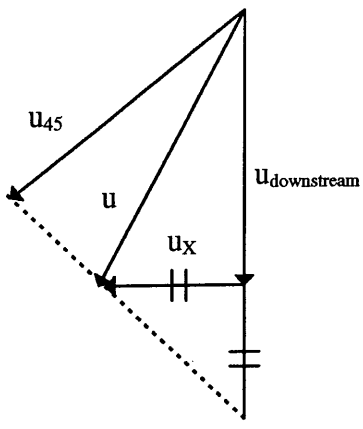

The cross stream velocity, u_X is calculated from equation 6.6:

$$u_X = \frac{u_{45}}{\cos(45)} - u_{downstream} \qquad (6.6)$$

in which u_{45} was the velocity measured at 45 degrees to the downstream direction.

Table 6.2 shows the absolute velocity (u) and secondary currents(u_X) which were estimated for a 0.23 stage at cross-section A1 at two different heights in each profile:

Table 6.2 Secondary velocity measurement at cross-section A1 for a 0.23 stage.

distance from left bank (m)	total depth of water (m)	absolute velocty (m/s) at 0.8h	cross stream component (m/s) at 0.8h	absolute velocty (m/s) at 0.2h	cross stream component (m/s) at 0.2h
0.8	0.29	0.241	-0.155	0.203	-0.168
1.8	0.36	0.533	0.198	0.268	0.039
2.8	0.35	0.386	0.114	0.130	-0.092
3.8	0.35	0.170	-0.125	0.161	-0.096
4.8	0.45	0.326	-0.325	0.227	-0.220
5.8	0.52	0.212	-0.209	0.161	-0.160
6.8	0.55	0.020	0.014	0.008	0.006

The tabulated values were typical of all the measurements, and were selected because of the similar stage to the day of the tracer experiment. The secondary velocities determined in this way did not show a distribution which was characteristic of a large scale coherent motion such as helicoidal flow. The variation of the sense of the signs of the velocity with transverse distance, suggests that the secondary circulation comprised relatively small cells (compared to the channel width) of water rather than a single large cell of gross helicoidal flow. This was thought to be due to the very rough nature of the gravel bed causing strong shear layers and introducing vortical motions into the

main body of the flow, in turn causing instability and the break down of any large scale (channel width) motions. The obvious secondary currents in the photograph (7/5/93) unfortunately occurred just downstream of cross-section A1 on the day of the secondary current measurement.

The use of the velocity probes to measure the velocity at 45 degrees to the downstream direction was thought likely to be highly uncertain, although no detailed studies were made of this problem. The repeated measurements of velocities in a region where there were negative velocities in chapter 5, showed a large scatter which suggested that if the probe was not aligned with the direction of flow, the measurements became inaccurate.

The absolute magnitudes of the velocities were calculated as an indication of the intensity of the secondary advective mixing and are given in table 6.3 for the measurements at cross-section A1 for the 0.23 stage:

Table 6.3 Average secondary current speed over cross-section A1 for 0.23 stage.

cross-sectional average magnitude of secondary velocity at 0.8h	cross-sectional average magnitude of secondary velocity at 0.2h
0.16 m/s	0.11 m/s

The depth-averaged secondary current speeds given in table 6.1 were also determined in this way. Little information can be drawn from these numbers, except that the variation of the average absolute velocities with stage were consistent with observations in other studies such as that of Anwar(1985) where it was found that the secondary currents were strongest for the intermediate stages.

6.2.5 Estimation of length scales associated with secondary current measurements.

The depth-averaged secondary current speeds were used to estimate a length scale associated with the mixing due to transverse advection by dimensional reasoning. This also required the estimation of a Lagrangian time scale, T_L. This was approximated as being equal to the mean of the measured Eulerian 1/e (inverse exponential) time scales which are determined in the section 6.3.1, to give equation 6.7:

$$L_V = u_X . T_L = 0.135 \times 0.7 = 0.09m \qquad (6.7)$$

6.3 Electromagnetic current metering.

In this section the cross-correlations and autocorrelations in the velocity time series are estimated. The 1/e time scales from the autocorrelations are determined, and were later used as the time steps in the random particle tracking model. The vertical / downstream velocity correlations were found to be negative at all sites, which is consistent with a shear layer distribution such as the logarithmic profile. The transverse / cross stream velocity correlations were found to vary in the transverse direction, which is consistent with the variation of the sign of the secondary current velocities in the transverse direction.

No further analysis was carried out on the velocity time series, such as quadrant analysis, or Fourier analysis despite it providing additional valuable information into understanding the processes in the flow. This is justified for two principal reasons:

(1) The studies of the different random walk models in the channel flows in chapters 2-4 suggested that there were no advantages to the inclusion of finer scale structure.

(2) The associated time constants and time averaged cross-correlations at each measurement point were considered to be robust indications of the local flow structure in a highly inhomogeneous flow, and any finer structure was considered to be less significant to the transport process.

6.3.1 Autocorrelations in the velocity time series.

The autocorrelations were determined from the 7 minute record length, velocity time series using a NAG algorithm, G13DAF (NAG,1987). Fig. 6.5 and 6.6 show some selected examples of typical autocorrelation functions. These were approximated as having an exponential decay from unity, and the corresponding 1/e time constants for the three dimensions (Tuu,Tvv and Tww) were determined. Tuu,Tvv and Tww can be associated with the decorrelation times of downstream, cross stream and vertical velocity fluctuations respectively, and are given in the second, third and fourth columns for cross-sections A1, 1 and 4 in tables 6.4a-c:

Table 6.4a Analysis of turbulence time series at cross-section A1.

posit'n (m)	Tuu (s)	Tvv (s)	Tww (s)	Ruv	Ruw	u' var. (m/s)	v' var. (m/s)	w' var (m/s)
LB+1.	1.3	1.0	1.2	0.35	-0.58	0.026	0.036	0.032
+2.0	0.7	0.7	0.8	0.06	-0.48	0.030	0.047	0.056
+3.0	0.7	0.6	0.6	-0.30	-0.20	0.028	0.050	0.055
+4.0	1.6	1.1	1.8	0.47	-0.54	0.013	0.017	0.021
+5.0	4.9	6.6	4.4	0.59	-0.37	0.003	0.004	0.003

Table 6.4b Analysis of turbulence time series at cross-section 1.

+1.4	1.2	1.0	1.2	0.32	-0.53	0.013	0.018	0.018
+2.4	2.1	1.2	2.5	0.05	-0.51	0.010	0.012	0.014
+3.4	0.8	0.7	0.8	0.13	-0.30	0.010	0.012	0.011
+4.4	0.8	0.7	0.6	0.29	-0.44	0.008	0.010	0.010
+5.4	0.5	0.4	0.4	0.16	-0.31	0.020	0.046	0.037

Table 6.4c Analysis of turbulence time series at cross-section 4.

LB+2.	0.6	0.5	0.6	-0.12	-0.24	0.035	0.046	0.038
+3.0	0.4	0.6	0.5	-0.22	-0.10	0.038	0.058	0.054
+4.0	0.5	0.7	0.7	-0.14	-0.50	0.047	0.072	0.089
+5.0	0.5	0.5	0.5	0.39	-0.40	0.028	0.028	0.040

The time constants increase from left to the right bank for cross-section A1, which is consistent with the observation that there is a region of slow moving water in the pool close to the right bank. The time constants at cross-section 1 show a small trend, which may be associated with a region of recirculation just upstream. The time constants show that the turbulent time scales are fairly homogenous at cross-section 4, which was consistent with the observation that the flow across the entire cross-section was characteristic of a riffle.

6.3.2 Cross-correlation

The cross-correlations between the time series of u' and v' (Ruv), and u' and w'(Ruw) were determined using the same NAG routine mentioned above, and are given in the fifth and sixth columns of tables 6.4a-c. The cross-correlation of v' with w' was considered insignificant and was therefore not examined.

If the vertical velocity decreased with depth, then the cross-correlation Ruw would be expected to be negative since an upwardly perturbed element of water would on average carry water from a region of lower downstream velocity to a region of high downstream velocity, causing a negative shear stress (Tritton, 1990). This was found to be the case at all measurement sites, and the scatter plots of u' against w' help to support the significance of the cross-correlations. Fig. 6.7 shows one such scatterplot, which was selected as an example from a region of strong secondary currents at cross-section 1.

The cross-correlations Ruv show a large degree of variability and fluctuate between positive and negative values. The significance of the cross-correlations are again supported by the example scatterplot of u' against v' in fig. 6.8. This was qualitatively consistent with there being multiple cells of transverse motion, which was also intimated by the measurements of secondary velocity.

6.4 Tracer experiments.

In this section the concentration measurements were corrected for differences in the sample temperature at the calibration and measurement stages, and the background measurement of concentration was subtracted from all of the measurements.

A mass balance of the input and tracer concentration measurements was carried out, and several inconsistencies were discovered. The constraints which this imposed upon the modelling work are discussed.

The uncertainties in the concentration measurements, and the additional uncertainties from assuming a depth-averaged concentration are estimated. Finally the autocorrelations in the concentration time series are examined.

6.3.1 Temperature correction.

The fluorescence time series was automatically translated into a concentration time series by the computer in the fluorometer, which used the calibration information that had been determined in the laboratory. This time series was then corrected for the temperature difference between that on the day of measurement and that during calibration, using the correction which was used by Wallis et al.(1987), given by equation 6.8:

$$F_{corrected} = F_{signal} \exp[-0.027(ct - st)] \qquad (6.8)$$

where ct is the calibration temperature, st is the sample temperature and the value 0.027 is a temperature coefficient used by Wallis et al.(1987).

The time averaged concentrations and standard deviations away from the mean concentrations were determined for all of the data. The uncertainties in the concentration measurements are discussed in section 6.3.3.

6.3.2 Mass balance.

A mass balance for the tracer test was carried, the results of which are shown in table 6.5:

Table 6.5 Mass balance of tracer from the input to cross-section 4.

Transect	tracer mass flux μg/s
injection site	49.3
A1	130 +/- 20
1	66 +/- 10
4	25 +/- 4

The mass fluxes which were estimated from the concentration and discharge measurements at each cross-section did not balance. Possible explanations for this will shortly be described, but the problem was overcome for the modelling work by normalising the mass fluxes at each cross-section using the total mass flux at each cross-section, so that only the relative mass fluxes were being examined (this technique was used by Lau and Krishnappan, 1981).

The increase in the mass flux from the injection to cross-section A1 cannot be accounted for by the estimated uncertainties alone. There are a number of possible explanations for the increase, in the absence of instrumental (and calibration) errors. Firstly, at cross-section A1, it is possible that the dye had not become fully mixed in the vertical direction, and that the error incurred due to this was larger than had been estimated from the deviations in the relatively sparse depthwise concentration measurements. The measurements were least intense in the vertical close to the right bank at cross-section A1, were the presence of pond weed prevented the use of the fluorometer, without it becoming choked. Possibly a filter should be used in future

investigations where this sampling technique is used. However, the increase in the total mass flux at cross-section A1 due to the assumption that the tracer was well mixed in the deadzone was at most ~16 $\mu g s^{-1}$, which is insufficient to completely explain the discrepancy. However, if the assumption that the dye was vertically well mixed was incorrect right across the channel, then this could account for the discrepancy.

An alternative explanation could be that there were channels in the flow, down which the tracer advected preferentially, due to for example large obstructions or secondary motions. If the fluorometer had only sampled within these channels, then the readings would be too large. However, the relatively well resolved spatial sampling would tend to make this explanation highly unlikely.

Finally, another explanation could be that the background fluorescence of the water entering the river just upstream of cross-section A1 was relatively high (unfortunately, this was assumed to be the same as the background reading in the river in the experiment). However, this could only lead to relatively large concentrations in the vicinity of the deadzone at cross-section A1, since the water from the brook could not possibly have dispersed right across the main channel width at cross-section A1, thereby influencing all of the concentration measurements. Since the concentrations which were measured in the deadzone only contributed a maximum of ~16$\mu g s^{-1}$ to the total mass flux, passing through cross-section A1, this explanation was also extremely unlikely.

In conclusion, the first of the above suggestions is the most likely explanation for the apparent increase in mass flux. Qualitatively, the concentration measurements showed the expected behaviour of the tracer, in that at cross-section A1, the maxima was close to the left bank, following its release from close to the left bank. Following

the sharp curvature between cross-sections A1 and 1, the tracer had become well mixed in the transverse direction, which was also expected, given the clearly observable secondary currents in this section. Therefore, the normalisation of the mass fluxes, which was described above, so that only the relative mass fluxes were being examined was justified.

The subsequent decrease in the mass flux from cross-section A1 to 4 was more natural if the dye was being lost somehow, although it was also quite extensive. This might be explained if the tracer was being temporarily stored and released over a long period of time. This could occur by two principle mechanisms, due to storage in a stagnant or slow moving region of water (such as the deadzone close to the outer bank at cross-section A1) or by tracer dispersing into the gravels and cobbles of the river bed, and subsequently being released slowly to give smaller concentrations during the time period of the experiment. Such mechanisms were forwarded by Bencala and Walters (1983) to explain this transient storage effect, which were also observed in the concentration measurements of a chloride tracer during investigations in a pool and riffle mountain stream. Further experimentation was carried out in which the interaction of the slow percolation flow in the stream bed material with the stream flow was investigated, this time using a continuous chloride injection (Bencala et al., 1984). This was achieved by comparing concentration measurements in an inflow to the main stream, with concentration measurements upstream and downstream of the inflow. From the observations it was apparent that the chloride entered the inflow via the gravel and returned to the main stream. Further to these observations, increased tracer concentrations were observed in the banks several meters away from the water's edge, again consistent with there being a ground water-main stream interaction.

An alternate, but less likely explanation might be (again) that there were local preferential streams down which the tracer was being advected.

A poor recovery in a similar experiment using rhodamine wt (50% recovery) was found at all cross-sections by Holley and Nerat(1983), for which there was no explanation could be forwarded. In another experiment Lau and Krishnappan (1981) had recovery rates which varied between 77 and 97%, and the losses were attributed to adsorption of the tracer onto bed materials.

6.3.3 Uncertainties in the measured concentrations.

The standard deviations from the mean, σ^t_{n-1}, in the concentration time series measurements and the standard deviation from the depth averaged concentration, σ^d_{n-1}, at sites were more than measurement was made, were used to estimate two different values for the uncertainty in the depth averaged mean concentration (since this was the quantity used in the modelling work). These estimates are given in the next two sections.

6.3.3.1 Estimating the uncertainty in the depth averaged concentration from the standard deviations away from the time average concentrations(σ^t_{n-1}) in each measurement.

For sites where only a single concentration measurement had been made, the fractional uncertainty could only be estimated from the coefficient of variation, σ^t_{n-1}/c.

For sites at which more than one concentration measurement was made, the depth-averaged mean for two (for example) concentration measurements was simply estimated using equation 6.9:

$$c_d = \frac{c_1 + c_2}{2} \qquad (6.9)$$

The uncertainty in the depth-averaged concentration was then determined using standard error treatment of equation 6.9 to give equation 6.10, and by assuming that the uncertainties in c_1 and c_2 could be approximated as the standard deviations from the means(i.e. $\Delta c \approx \sigma^t_{n-1}$) of their respective time series:

$$\Delta c_d^{\,2} = \left(\frac{\partial c_d}{\partial c_1}\right)^2 \Delta c_1^2 + \left(\frac{\partial c_d}{\partial c_2}\right)^2 \Delta c_2^2 \qquad (6.10)$$

which simplifies to equation 6.11:

$$\Delta c_d = \frac{1}{2}\sqrt{\Delta c_1^2 + \Delta c_2^2} \qquad (6.11)$$

This equation was used to produce the first estimate of the uncertainty in the depth averaged concentration, $\Delta c_d/c_d$, given in the fifth columns of tables 6.6a-c below (where it is called $(\sigma^t_{n-1})_d / c_d$).

6.3.3.1 Estimating the uncertainty in the depth averaged mean concentration from the standard deviations away from the depth averaged mean concentrations(σ^d_{n-1}).

Here the fractional uncertainty was simply estimated as the coefficient of variation, σ^d_{n-1}/c_d for sites at which more than one measurement was made. This quantity was highly uncertain due to the small number of measurements through the depth at each site, but is included where relevant in the sixth columns of tables 6.6a-c.

Table 6.6a Analysis of tracer time series at cross-section A1.

transv. distance (m)	depth of meas.(m)	mean conc. c($\mu g l^{-1}$)	std. dev. conc. ($\mu g l^{-1}$)	depth-average conc. c_d ($\mu g l^{-1}$)	$(\sigma^t_{n-1})_d / c_d$	σ^d_{n-1}/c_d
1.0	0.08 0.29	0.623 0.757	0.039 0.084	0.690	0.07	0.14
2.0	0.15 0.24	0.253 0.321	0.023 0.021	0.287	0.07	0.17
3.0	0.11 0.30	0.253 0.205	0.022 0.013	0.229	0.04	0.21
4.0	0.13 0.28	0.326 0.201	0.056 0.020	0.264	0.11	0.3
5.0	0.22 0.38	0.358 0.241	0.022 0.116	0.299	0.20	0.28
6.0	0.22	0.265	0.037	0.265	0.14	
8.0	0.44	0.278	0.028	0.278	0.10	

Table 6.6.b Analysis of tracer time series at cross-section 1.

transv. distance (m)	depth of meas.(m)	mean conc. c($\mu g l^{-1}$)	std. dev. conc. ($\mu g l^{-1}$)	depth-average conc. c_d ($\mu g l^{-1}$)	$(\sigma^t_{n-1})_d / c_d$	σ^d_{n-1}/c_d
1.0	0.12 0.24 0.31	0.200 0.201 0.245	0.038 0.026 0.023	0.215	0.09	0.12
2.0	0.15 0.35 0.40	0.366 0.235 0.176	0.018 0.040 0.008	0.259	0.04	0.38
3.0	0.10 0.27	0.248 0.239	0.027 0.039	0.244	0.09	0.02
4.0	0.15	0.178	0.011	0.178	0.06	
5.0	0.10	0.271	0.029	0.271	0.11	
6.0	0.05	0.130	0.012	0.130	0.09	
7.0	0.05	0.165	0.031	0.165	0.19	
8.0	0.02	0.172	0.032	0.172	0.19	
11.2	0.12 0.25	0.247 0.232	0.012 0.009	0.240	0.04	0.04

Table 6.6c Analysis of tracer time series at cross-section 4.

transv. distance (m)	depth of meas.(m)	mean conc. c($\mu g l^{-1}$)	std. dev. conc. ($\mu g l^{-1}$)	depth-average conc. c_d ($\mu g l^{-1}$)	σ^t_{n-1}/c
0.1	0.06	0.115	0.004	0.115	0.03
1.1	0.10	0.073	0.011	0.073	0.15
2.1	0.18	0.070	0.004	0.070	0.06
3.1	0.14	0.080	0.004	0.080	0.05
4.1	0.22	0.090	0.005	0.090	0.06
5.1	0.14	0.071	0.003	0.071	0.04
6.1	0.15	0.089	0.005	0.089	0.06

There were no consistent and systematic trends to the vertical variation of the concentration measurements. The tracer was assumed to be vertically well mixed such that the depth-averaged concentrations at all of the transverse sites were taken to be the mean of the measurements made through the vertical at each site.

Table 6.7 Reach ensemble coefficients of variability of fluctuating tracer concentration, and depth-averaged tracer concentration.

$<\sigma^{t}_{n-1}/c_d>$	$<\sigma^{d}_{n-1}/c_d>$
0.09	0.18

6.3.4 Time series analysis of concentration measurements.

The autocorrelations in the time series of concentrations which were measured at each site were now examined. The autocorrelations were obtained in a similar manner to the velocity fluctuation autocorrelations, and 1/e time constants were determined and are tabulated in table 6.8, where the transverse coordinate of the measurement sites are in increasing order starting from the left bank, at the same as those in table 5.10:

Table 6.8 1/e time constants for tracer concentration time series for the three cross-sections.

cross-section A1(s)		cross-section 1(s)		cross-section 4(s)	
3 12	7.5	30 20 13	21	2	2
12 2	7	7 11 9	9	35	35
3 2	2.5	2 2	2	3	3
34 3	18.5	3	3	2	2
3 31	17	13	13	3	3
32	32	11	11	3	3
6	6	28	28	4	4
		34	34		
		7 11	9		
mean = 12.9s		**mean = 14.4s**		**mean = 7.4s**	

These time constants showed a greater degree of variability than those determined from the e.c.m. readings, but with similar trends, which will be discussed in the next section.

6.3.5 Discussion of time scales derived from concentration measurements.

The time constants at cross-section A1 show a similar trend to those which were determined from the velocity time series analysis. There is a large time constant close to the right bank, in the deadzone region. Further downstream at cross-section 1, the time constants show a similar trend, with the exception of one measurement of a large time constant close to the left bank. The general trend of large time constants

close to the right bank is in agreement with the tracer having undergone large scale foldings with large time constants close to the right bank between cross-sections A1 and 1 because of the region of slow moving water (deadzone) there.

Finally at the fourth cross-section, all the time constants bar one show small time constants, but otherwise show no trends. The single large time constant is discussed following a more general discussion.

The concentration time series are fundamentally different to the velocity time series because the tracer plume contains information about the history of the fluctuations and differential advection to which it has been subjected since release. This information is lost to a large extent for the point velocity measurements, from the very local nature of the measurement. The velocity series can contain information about any large scale local fluctuations, or remnant advections due to circulations immediately upstream, but the information about the mixing which that local piece of water has undergone in order to reach the measurement site is limited. The tracer data, however, contains information about the large and small scale 'foldings' which the tracer has undergone since release. Therefore, although it might be expected that the small scale fluctuations will become smeared over, the large scale variations or trends in the data might give a better indication of the mixing time scales involved in the reach due to large scale fluctuations or secondary advections.

The presence of large time scales of the order of half a minute, even at cross-sections far downstream in this experiment emphasise the importance of the range of scales of motion in the flow. Such a wide range of scales is ubiquitous of turbulent motion, and highlights its chaotic nature. Moreover, the presence of large time scales (of the order of half a minute) in the concentration time series a riffle section, in which

the turbulent time constants had been measured to be of the order of a second, suggests that large memory effects can remain superimposed onto a highly noisy background of turbulent flow over a rough bed.

The product of the sampling period and the velocity of the river water passed the intake pipe can be used to estimate the minimum spatial dimension over which the sample has been drawn from. If this length scale exceeds the Lagrangian length scale or average eddy size , the time series are insensitive to the concentrations within individual eddies. The transverse and vertical length scales of the sample drawn from the river are dependent on the bore of the intake tubing. Given the intake pipe had a diameter of 0.5cm, and assuming that the sample drawn from the river is cylindrical, then the radius of this cylinder could be approximated as the transverse and vertical dimensions of the sample from the river. For a flow of 0.5m/s ,a 1s sampling period and a pumping rate of 1.2×10^{-5} cumecs, the minimum length of the cylinder is 0.5m with a diameter of 5.5mm . These scales indicate, to an order of magnitude, the resolution of the flurometry measurements.

Fig.6.1

Stage discharge curve for Lune site
with estimated uncertainties

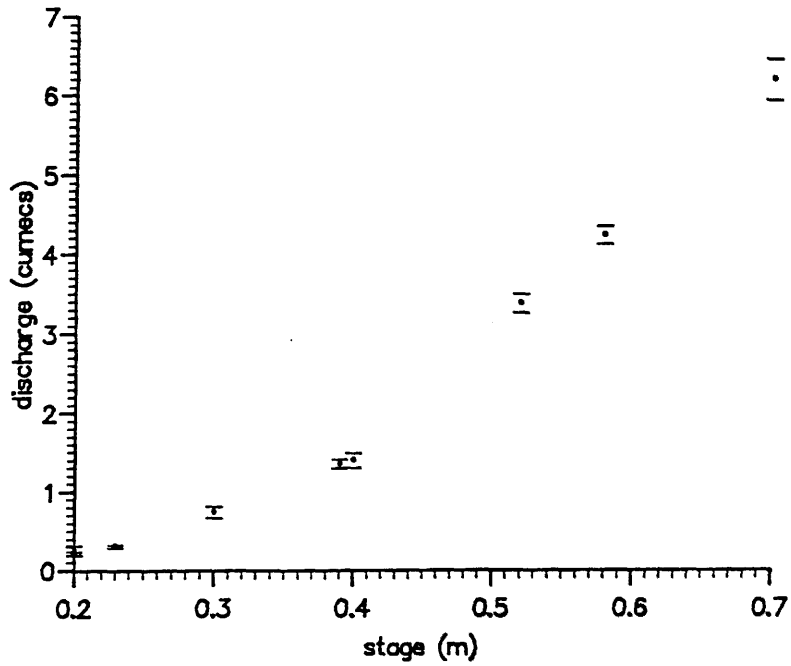

Fig.6.2

Velocity profiles on semi log plot of measurements
at cross sections 1–3 on 29/9/92, stage=0.3m

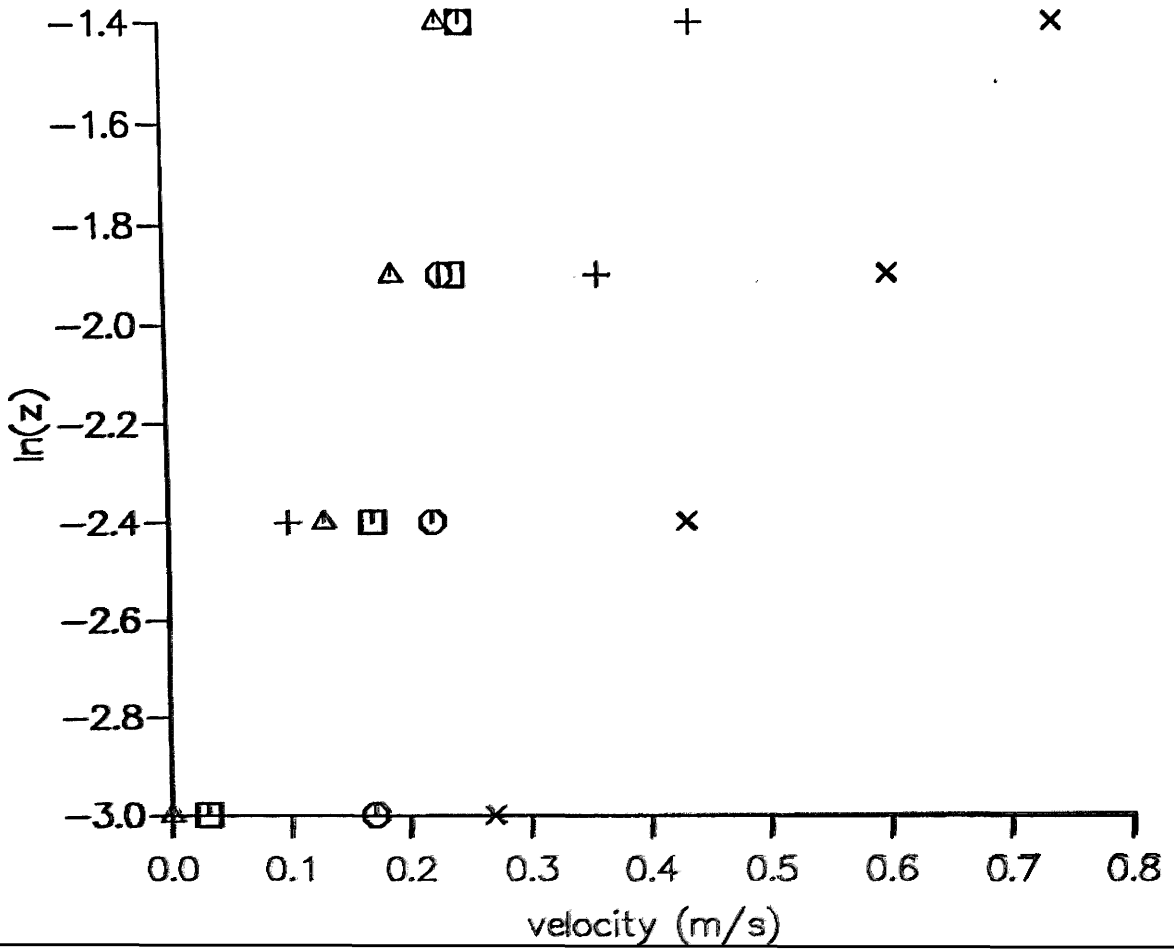

Fig.6.3

Velocity profiles on semi log plot of measurements
at cross sections 4–6 on 29/9/92

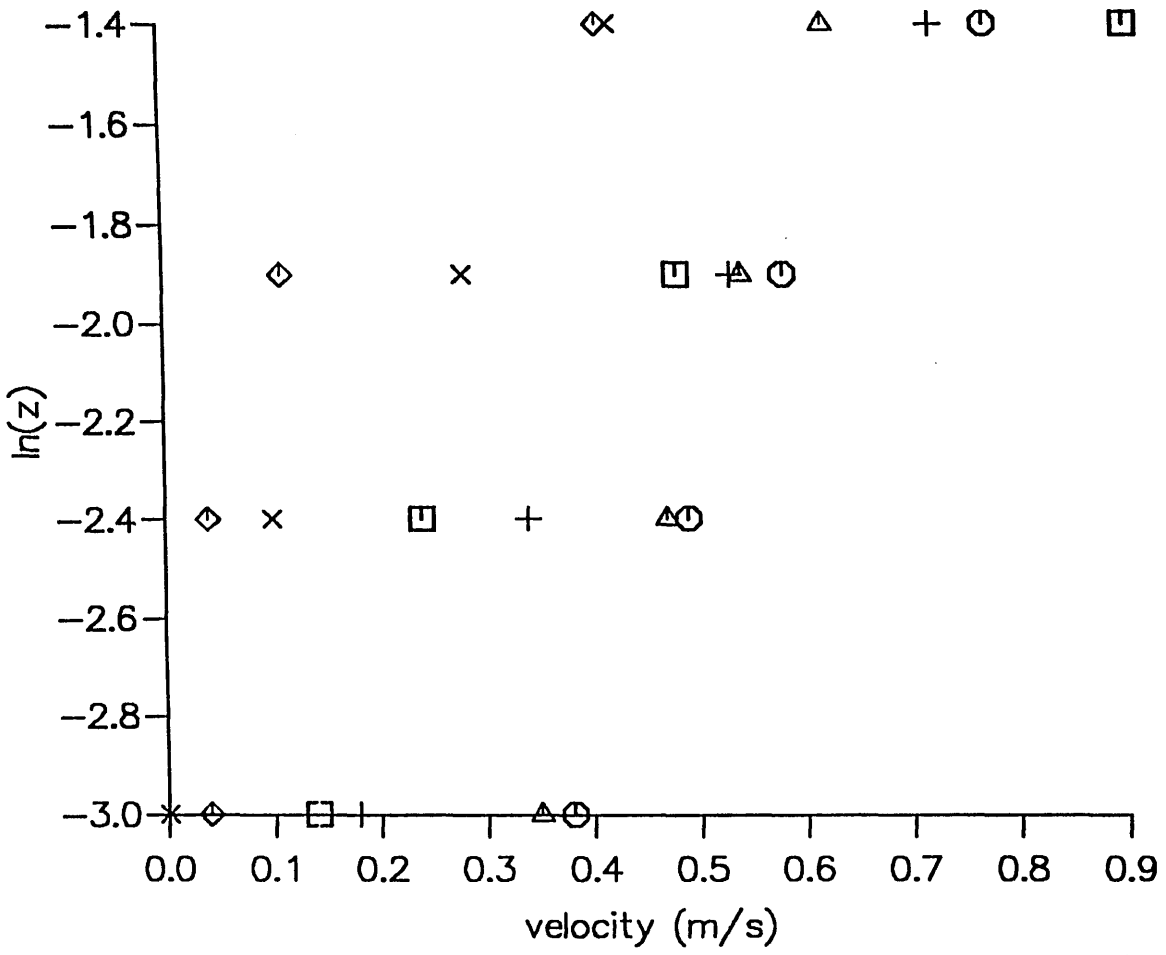

Fig.6.5

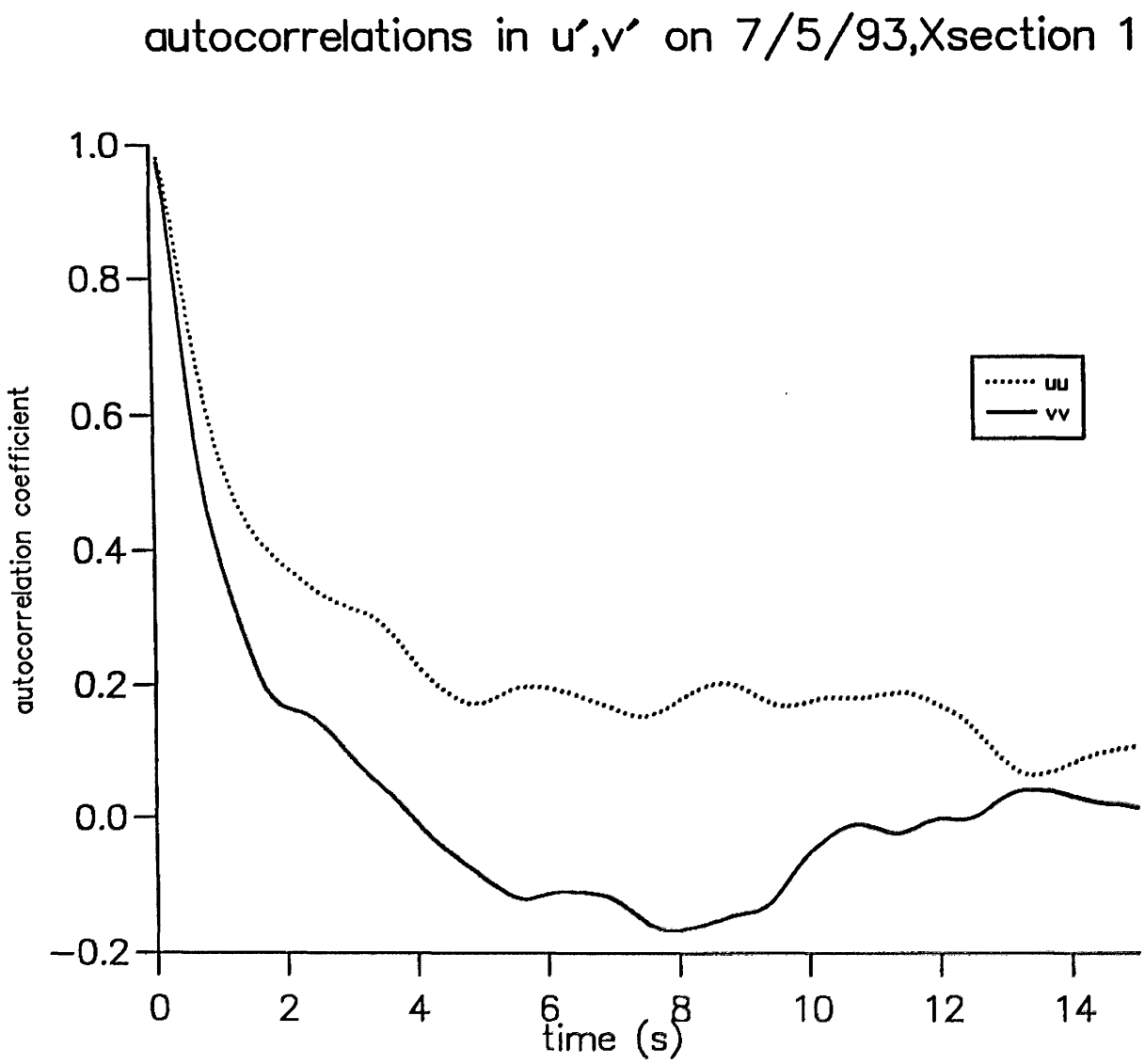
autocorrelations in u',v' on 7/5/93,Xsection 1
1.0
0.8
0.6
0.4
0.2
0.0
-0.2
autocorrelation coefficient
uu
vv
0
2
4
6
8
10
12
14
time (s)

Fig.6.6

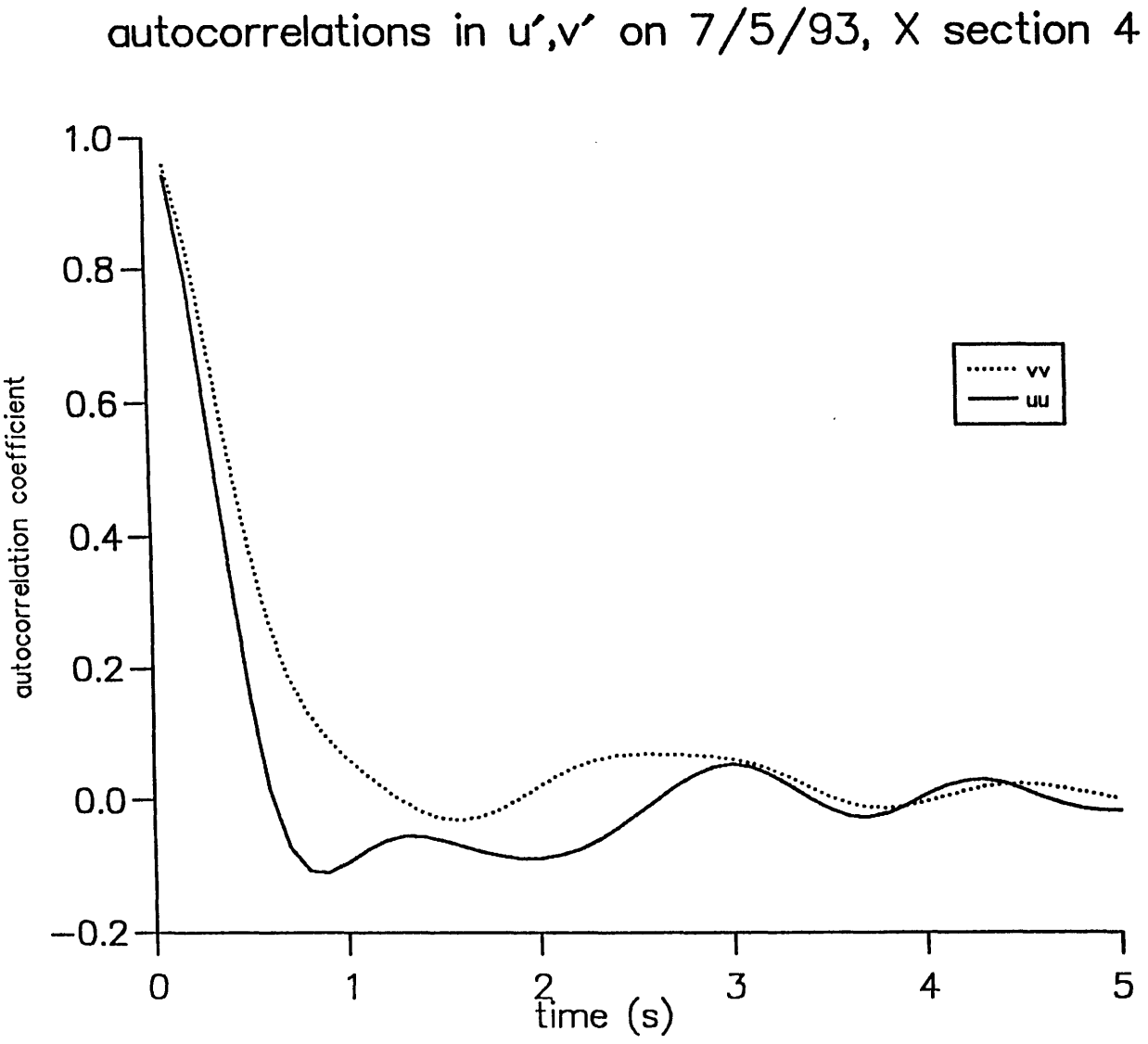
autocorrelations in u′,v′ on 7/5/93, X section 4
1.0
0.8
0.6
0.4
0.2
0.0
−0.2
autocorrelation coefficient
0
1
2
3
4
5
time (s)
vv
uu

Fig.6.8

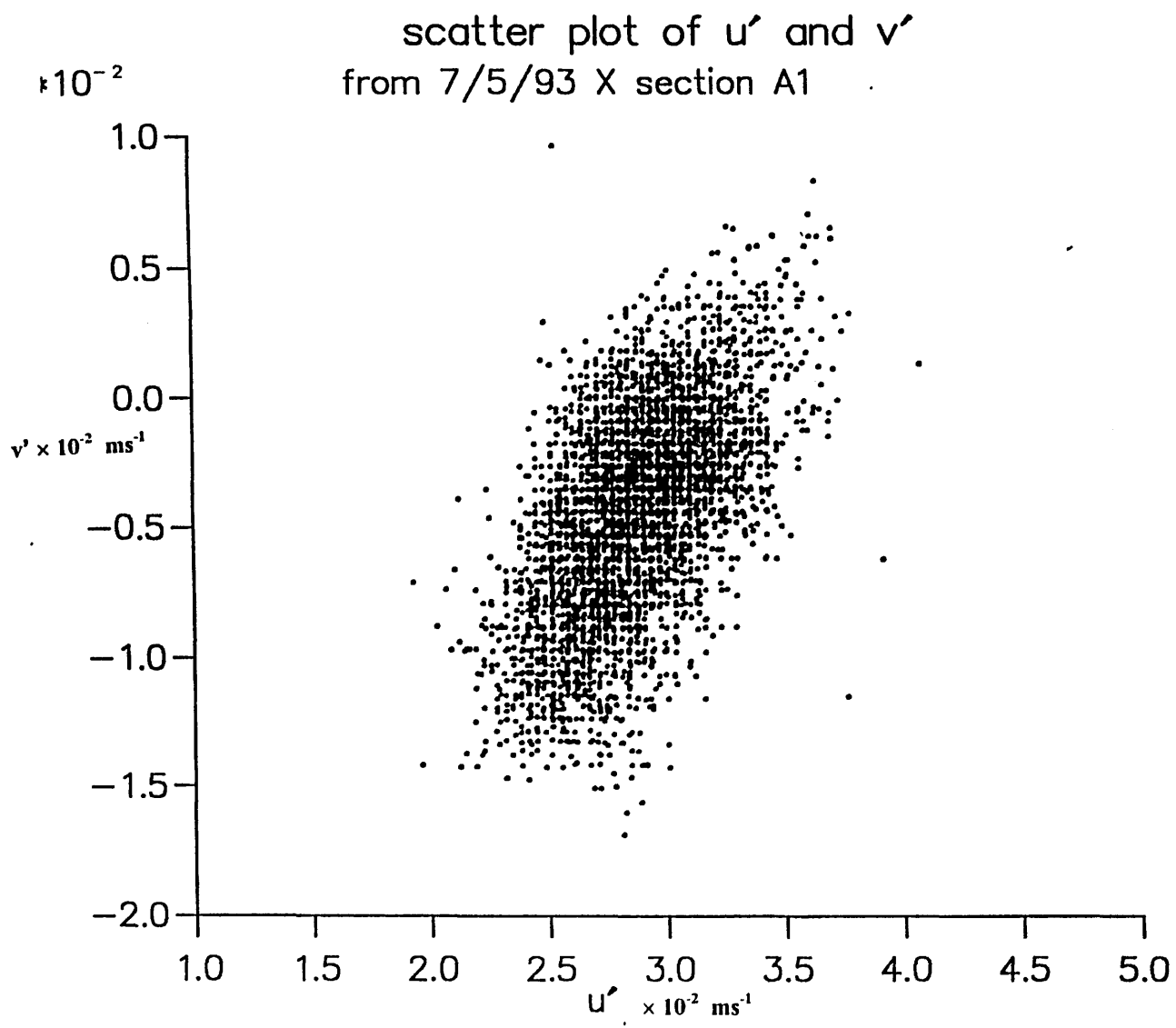
scatter plot of u′ and v′
from 7/5/93 X section A1
×10⁻²
1.0
0.5
0.0
−0.5
−1.0
−1.5
−2.0
v′ × 10⁻² ms⁻¹
1.0
1.5
2.0
2.5
3.0
3.5
4.0
4.5
5.0
u′ × 10⁻² ms⁻¹

Chapter 7

Construction of a random particle tracking model based on streamtubes to simulate the observed dispersion of a passive tracer in the River Lune.

7.1 Introduction.

This chapter describes the construction of a computer simulation of the mean flow in the study reach of the River Lune, based upon the measurements of the topology, geometry and mean velocities which were described in chapters 5 and 6. A random particle tracking model was used once again to simulate the turbulent trajectories of fluid elements within the mean flow field. The resulting particle distributions were studied and compared with the measured dye tracer distributions. The complexity of the system to be modelled is emphasised and uncertainties in the measurements are discussed at each stage.

The model comprised four main stages which can be summarised as: the assimilation of data into a suitable format for the hydrodynamic model, the input to the model, the particle tracking model and the model output. These principal stages can be further divided into sub-sections which relate to distinct functions or algorithms within each stage. A sensitivity analysis of the ensemble dispersion characteristics of particles undergoing random walks within the framework of the hydrodynamic model is undertaken in chapter 8.

7.2 Assimilation of the data sets into a suitable format for the flow interpolations.

In this section, the depths and discharge of the flow at each cross-section are rescaled to those values which corresponded to the day of the tracer experiment; the cross-sections are divided into streamtubes which carry equal discharges and all of the variables are non-dimensionalised.

7.2.1 Rescaling the model depths and velocities to simulate the discharge on the day of tracer experiment.

The flow through each of the modelled cross-sections was rescaled to have a discharge which was estimated from the stage-discharge curve in fig. 6.1 as 0.35 m^3s^{-1} for the day of the tracer dispersion test. This was carried out by making the assumption that the river banks could be approximated as being vertical, and by using the known ratios of the discharges and stages on the days of the tracer experiment and velocity measurements. This information, combined with equation 7.1 was sufficient to rescale the mean velocities, such that the flow in the modelled reach was the same as on the day of the tracer experiment:

$$\frac{Q_{tracer}}{Q_{meas}} = \frac{\sum_{i=1}^{nb} u_{di}' \Delta b_i' \overline{z_i}'}{\sum_{j=1}^{nb} u_{dj} \Delta b_j \overline{z_j}} = \left(\frac{u_d'}{u_d} \frac{\overline{z}'}{\overline{z}} \frac{\Delta b'}{\Delta b} \right) \frac{\sum_{i=1}^{nb} u_{di} \Delta b_i \overline{z_i}}{\sum_{j=1}^{nb} u_{dj} \Delta b_j \overline{z_j}} \qquad (7.1)$$

where Q_{tracer} was discharge estimated on the day of the tracer experiment, Q_{meas} was the discharge on the day of velocity measurements; both were determined using the trapezium rule. The suffices indicate measurements made on the day of the tracer experiment. The index nb corresponds to the measurement site at the right bank. $\Delta b'$, Δb are the intervals in the transverse direction between the velocity measurement sites. u_d' and u_d are depth average velocities for each interval.

The ratio of the depths was known from the ratio of the stages for the two sets of measurements. The widths of the cross-sections, and therefore of the intervals, $\Delta b'$, Δb are constrained to be constant for the two stages, implying that their ratio is unity. This introduced the approximation whereby the banks were assumed to be vertical. Since the ratio of the discharges are known, the velocity ratio for the two stages can be deduced from the law of conservation of mass equations, and equation 7.1, to give equation 7.2:

$$\frac{\bar{z}'}{\bar{z}} = \frac{stage'}{stage}\ \frac{\Delta b'}{\Delta b} = 1$$
$$\left(\frac{u_d'}{u_d}\right) = \frac{Q_{tracer}}{Q_{meas}}\frac{stage}{stage'} \qquad (7.2)$$

The rescaling of the depth averaged velocity in this way implied that the entire velocity profile was shifted by the rescaling ratio. For an assumed logarithmic profile, the friction velocity estimated from a logarithmic fit to the new profile would therefore increase if the velocity rescaling ratio was greater than one. The correction to the friction velocity can be estimated for an assumed logarithmic velocity profile, by

equating the rescaled depth averaged velocity for a particular profile with the integrated depth average of the logarithmic velocity given by equation 7.3:

$$u_d = \frac{\int_{z_o}^{h} u\,dz}{\int_{z_o}^{h} dz} \quad where \quad u = \frac{u^*}{\kappa}\ln\frac{z}{z_o} \qquad (7.3)$$

Integrating this equation by parts gives equation 7.4:

$$u^* = \kappa u_d \frac{[h - z_o]}{\left[h\ln\left(\frac{h}{z_o}\right) - h + z_o\right]} \qquad (7.4)$$

The rescaled depth averaged velocity and the rescaled depths were inserted into 7.4, but before the corrected friction velocity could be determined, an estimation of the new roughness height was required. This was assumed to be approximately equal to the original value which had been determined from the measured velocity profile. The uncertainties which were invoked by making this additional approximation were considered to be smaller than those which had already been invoked due to assuming a logarithmic profile.

7.2.2 Transverse division of each cross-section into streamtubes.

The advantages of dividing the channel into streamtubes or regions of equal discharges, in terms of being able to differentiate between different forms of mixing,

were discussed in relation to solutions of the diffusion equation in chapter one. This section discusses the application of streamtubes to the particle tracking model and moreover it explains the necessity for the use of streamtubes when modelling flows with non uniform geometry in the downstream direction.

7.2.2.1 Reasons to use streamtubes.

The velocities and depths at each cross-section were measured at essentially arbitrary points in the transverse direction at each cross-section. These values had to be interpolated between in the downstream direction in order to construct a complete flow field. However, the channel geometry was non uniform in the downstream direction (largely due to the meandering of the thalweg), so that the discharge between any two measurement sites in the transverse direction was not constant, as depicted for the simplified case in fig. 7.1:

Fig. 7.1 Diagram to aid description of the downstream interpolation technique.

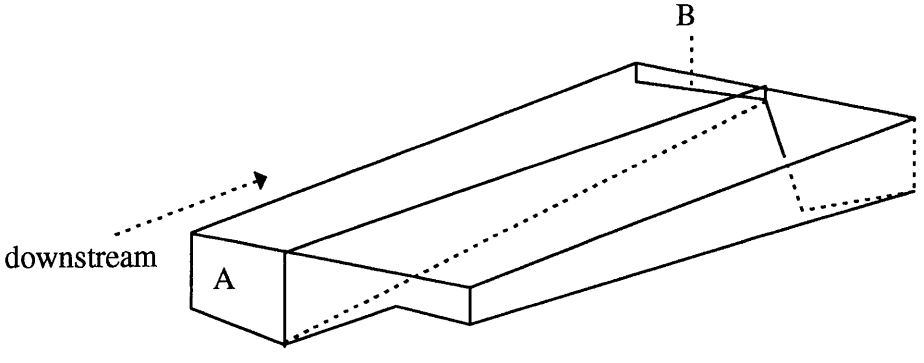

The case is considered when the depths and velocities are simply interpolated between the measurement sites to give the two sub-sections A and B illustrated in fig.7.1. The mass flux of water passing through individual sub-sections is not likely to

be conserved in the downstream direction. Clearly, in the real situation the water diverges or converges under the influences of gravity and the bed topology, so that the total mass flux at each cross-section is conserved. If a number of particles were released into sub-section A in a particle tracking model which simply used interpolation between measurement sites, then these particles would all end up within sub-section B, in the absence of transverse perturbations. For the model to conserve mass, the particles need to follow mean streamlines which conserve the total mass flux. In other words, the mean trajectories of the particles have to follow the same divergent/convergent streamlines which the real flow takes.

The streamlines are difficult to define unless the downstream interpolation is carried out between sub-sections of constant discharge. In this way the mean divergence or convergence of the boundaries which define the streamtubes can be interpreted as following the mean flow divergence/convergence which must have taken place in order that the total mass fluxes be conserved at each cross-section. It then becomes an easy matter to maintain the particle positions relative to these boundaries under the influence of the mean advective velocities only. Tests were devised in the following chapter to demonstrate that this was the case.

7.2.2.2 Determination of streamtube boundaries

Having discussed the necessity for dividing the flow into streamtubes, the depths, widths and velocities which were measured and then rescaled at each cross-section were now used to construct streamtubes. The streamtube boundaries were

determined at each cross-section from an approximation to a cumulative integral of the discharge using equation 7.5:

$$q_c = \int_{Y_L}^{Y_R} u_d z dy \approx \sum_{i=1}^{N_R} u_{di} \bar{z}_i \Delta y \qquad (7.5)$$

Where q_c is the cumulative discharge; Y_L is the left hand boundary of the streamtube, which is initially zero at the left bank; and Y_R is the right hand boundary of the streamtube, which is determined once q_c is equal to the streamtube discharge. The velocity, u_d is the depth averaged mean velocity in the transverse discretisation interval Δy, which was given a value of 1mm, while z is the average depth in this interval. N_R multiplied by Δy gives Y_R, the precision of which depends on the discretisation interval.

Starting at the left bank, the integral is carried out until the cumulative discharge is equal to the total discharge (Q) divided by the number of streamtubes (Ns), and the y coordinate at this point gives the right hand boundary to the first streamtube. The integral is continued, until the discharge reaches 2Q/Ns, which gives the right hand boundary to the second streamtube, and so on. The streamtube boundaries at each cross-section are given following a description of the downstream interpolations.

7.2.2.3 Uncertainties due to the use of streamtubes.

The measured depths and velocities were linearly interpolated between measurement sites in the transverse direction, so that their respective values could be estimated at the boundaries of the streamtubes. However, this incurs an error in the streamtube discharge, when it is re-calculated using the streamtube boundary values of depths and velocities, which is illustrated by fig. 7.2:

Fig.7.2 Diagram to demonstrate the error in approximation caused by interpolation between streamtube boundaries.

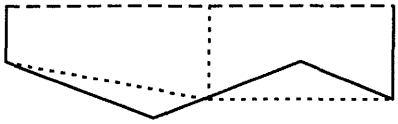

Here the dashed lines represent the new streamtube boundaries and the solid lines represent the measurements. A similar error arises in the velocity interpolations.

Errors which are incurred due to this effect can be minimised by increasing the number of streamtubes, since this reduces the intervals over which the depths and velocities are required to be interpolated. The error cannot be reduced completely due to the finite number of measurements which were made at transverse locations which do not necessarily correspond to streamtube boundaries. Trials were undertaken to examine the variation of this uncertainty with the number of streamtubes which were used, the results of which are given in table 7.1.

Table 7.1 Variation of the uncertainty incurred due to linear interpolations between streamtube boundaries with number of streamtubes used in the transverse direction.

no. streamtubes	σ_q/q
6	0.17
8	0.09
10	0.06
12	0.05
14	0.04

Where σ_q is the standard deviation of the new streamtube discharges calculated from the boundary depths and velocities, away from the discharge per streamtube as calculated from the data (i.e. Q/Ns), with which it has also been normalised. These deviations showed a random scatter, and the factor σ_q/q was approximated as the uncertainty in the streamtube discharges due to the use of streamtubes. The number of streamtubes was therefore chosen such that the factor was smaller or equal to the uncertainty in the discharge calculated from the measurements.

The uncertainty in the discharges calculated from the measurements was estimated in chapter 6. From table 6.1, the fractional uncertainty in the discharge for the two sets of measurements which were utilised in the computer model were estimated as: $\Delta Q/Q = 0.06$ and $\Delta Q/Q = 0.09$ for the 0.23 and 0.30 stages respectively. Assuming that the uncertainties in the modelled discharge due to making the approximation that the banks were vertical were small compared to these uncertainties, it was concluded that the fractional uncertainty in the modelled discharge lay within this range.

The fractional uncertainty in the discharge in each of the streamtubes (q) is the same as the fractional uncertainty in the total discharge since q and Q are linearly related, which gives 7.6:

$$0.06 < \Delta q/q < 0.09 \qquad (7.6)$$

The uncertainty in the discharges which were calculated from the streamtube boundaries had to be at least as small as these estimated uncertainties. Therefore, twelve streamtubes were used for which the factor σ_q/q was approximately half the size of the uncertainty in the discharge (5%).

The tracer concentration measurements had been carried out at approximately half as many locations as this (reach average no. of measurements = 7), so later the streamtubes were coupled together in order that the resolution of the modelled mass fluxes was supported by the resolution of the measurements.

The depth averaged velocities, friction velocities and depths at the streamtube boundaries, along with the transverse co-ordinates were then stored as the boundary conditions to the streamtubes for the particle tracking model. These will be presented following a description of the downstream interpolations.

The fractional uncertainty in the discharge in each of the streamtubes (q) is the same as the fractional uncertainty in the total discharge since q and Q are linearly related, which gives 7.6:

$$0.06 < \Delta q/q < 0.09 \qquad (7.6)$$

The uncertainty in the discharges which were calculated from the streamtube boundaries had to be at least as small as these estimated uncertainties. Therefore, twelve streamtubes were used for which the factor σ_q/q was approximately half the size of the uncertainty in the discharge (4%).

The tracer concentration measurements had been carried out at approximately half as many locations as this (reach average no. of measurements = 7), so later the streamtubes were coupled together in order that the resolution of the modelled mass fluxes was supported by the resolution of the measurements.

The depth averaged velocities, friction velocities and depths at the streamtube boundaries, along with the transverse co-ordinates were then stored as the boundary conditions to the streamtubes for the particle tracking model. These will be presented following a description of the downstream interpolations.

7.2.3 Downstream interpolation of depths and velocities at streamtube boundaries.

The modelled cross-sections were set at the surveyed angles to each other and the channel curvature was approximated using linear interpolations between each cross-section in the downstream direction as shown in fig. 7.3:

Fig. 7.3 Diagram illustrating the form of linear approximation which was made to the downstream curvature.

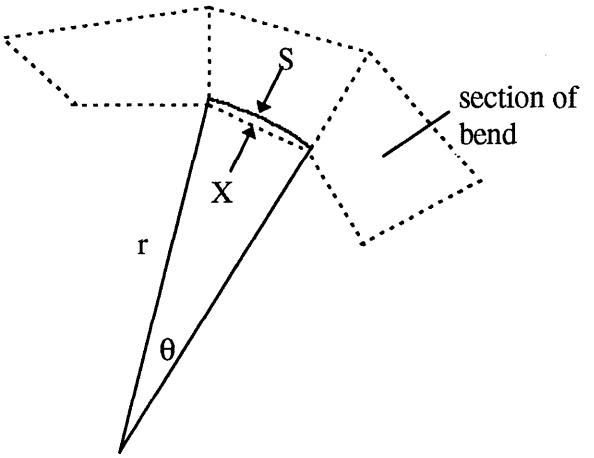

where the dashed lines represent the streamtube boundaries, and the solid curved line is the curvature of the river bank. The distance S was approximated by the distance X in the modelled geometry for each section. The error in this approximation can be estimated from the difference between the distance X and the length along a circular arc (The use of a circular arc is still an approximation to the real curvature, as can be observed from inspection of fig.5.1). With these assumptions, the error in the linear approximation can be estimated for each section using equation 7.7:

$$(S - X) = r(\theta - \sin\theta) \qquad (7.7)$$

where θ is in radians. For an estimated radius of curvature of r = 50m, and a measured value of θ = 29 degrees the approximation is fairly small : (S-X) = 1.07m, or expressed as a fractional error : (S-X)/S = 0.04 = 4%. These values were typical of the reach geometry.

The resulting geometry for the entire reach is shown in fig. 7.4, and should be compared against fig. 5.3 which shows the surveyed boundaries.

Fig. 7.4 also shows the corner points of the transverse streamtube boundaries (using six streamtubes for clarity) for cross-sections A1-6. The boundaries showed convergence and divergence in regions of high and low partial discharges respectively, as might be expected. For example the streamtube near the right bank at cross-section A1 is very wide and corresponds to the 'deadzone' region described earlier.

The geometry, rescaled depths and rescaled velocity field on the streamtube boundaries are shown in figs. 7.5a and 7.5b. The contour maps have been constructed by bi-linear interpolation on a graphics package, which is the same form of interpolation carried out in the model. There are some discrepancies between the two sets of interpolations due to differences choice of interpolation basis axes, although the maps give the correct overall impression.

Linear interpolations of velocities, depths and widths between the measurement sites in the downstream direction were carried out in order that the least amount of information was asserted about the topology, geometry and flow structure between measurement sites. However, discrepancies between the interpolated velocity field and the actual velocity field become apparent when comparisons are made between the

interpolations of fig. 7.5b with the photographs in figs.5.2. Between cross-sections A1 and 1, there are two regions of slow moving water, or deadzones, separated by a region of fast moving water near to the right bank. This sort of detail can only be accounted for through a more intensive fieldwork campaign, in which more cross-sections are examined.

7.2.4 Non-dimensionalising of flow variables.

The reach averaged values of some of the hydraulic parameters were used to non-dimensionalise the velocities, depths and time scales used in the model. The mean friction velocity, u*, was used to non-dimensionalise all of the velocities, and the mean hydraulic radius, r_h, was used to non-dimensionalise the depths. The time scales used in the model were non-dimensionalised using the linear construct r_h/u^*. These values are given in table 7.2:

Table 7.2 Table of parameter values used to non-dimensionalise modelled observables.

hydraulic radius	friction velocity	time scale
0.25 m	0.036m/s	6.94s

This procedure removed the scale dependence of the model observables and enabled the model results to be compared with previous studies more easily.

7.3 Model input.

This section describes how the tracer concentration measurements at cross-section A1 were used to define the input to the flow model. The vertical and transverse distributions are examined.

7.3.1 Transverse distribution of initial mass fluxes.

The spatial intensity or resolution of the concentration measurements was considered insufficient to allow a three dimensional analysis of the model output, and depth averaged concentrations were examined in the modelling work. At sites where several concentration measurements had been made through the depth, there were no systematic and consistent variations of concentration with depth.

The depth averaged concentration measurements which were given in chapter 6, table 6.6, were interpolated linearly in the transverse direction and were averaged over the whole of a streamtube to define an average concentration. These streamtube average concentration values were assumed to be equal to the average concentration within each streamtube, which when multiplied by the discharge per streamtube, q, gave the tracer mass flux through the streamtube. The sum of these values, multiplied by the discharge in a streamtube was therefore the total tracer mass flux through the cross-section.

The tracer mass fluxes in the streamtubes were then normalised by dividing through by the total mass flux. The normalised values could then be used to distribute the total number of particles at the input cross section in such a way that the relative

particle numbers were the same as the relative mass fluxes. The normalised mass flux distributions at the input cross-section (A1) and at the other two cross-sections are shown in fig. 7.6, where the uncertainties have been estimated in the next section.

The particles in any particular streamtube were uniformly distributed between the streamtube boundaries in the transverse direction. This was as a consequence of the chosen minimum discretisation interval which could be supported by the measurements.

The positions of the particles at the input were plotted as a scatterplot against particle number in fig.7.7. The banding in this plot reflects the different numbers of particles which have been distributed uniformly within each streamtube. A frequency histogram (fig. 7.8) demonstrates the form of the corresponding discretised probability distribution function.

7.3.2 Uncertainties in the transverse mass flux distributions.

There were a number of sources contributing to the uncertainty in the measured mass flux distributions. These can be largely attributed to the experimental errors involved in the determination of the discharge and tracer concentrations, from which the mass flux of tracer were derived.

The uncertainty in an individual concentration measurement was approximated as the standard deviation from the time averaged mean of the measured concentration time series. The reach averaged fractional standard deviation calculated in this way was determined in chapter 6 to be: $\langle \sigma^{t}_{n-1} \rangle = 0.09$.

However, if the standard deviation from the depth averaged mean concentration, σ^d_{n-1}, is examined for those measurement sites at which more than one measurement was made through the water column, then the fractional reach averaged standard deviation suggests that the uncertainty in assuming a depth averaged concentration is greater: $<\sigma^d_{n-1}> = 0.18$. The estimates of σ^d_{n-1} are based upon only 2 or 3 samples through the depth, and cannot be estimated for those sites at which only a single measurement was made. For these two reasons these standard deviations could well be an exaggeration of the uncertainty in the depth averaged concentration values.

The fractional uncertainty in the depth averaged concentrations was concluded to lie within the range:

$$0.09 < \Delta c_d/c_d < 0.18 \qquad (7.8)$$

Where Δc_d is the estimated uncertainty in the depth averaged concentration.

Using this range of values, together with the range of uncertainties which were estimated for the streamtube discharges in equation 7.6, the fractional uncertainty in the mass fluxes of tracer per streamtube can now be determined. The mass flux in a streamtube is given by equation 7.9:

$$m = qc_d \qquad (7.9)$$

where q is the discharge in the streamtube and c_d is the depth-averaged concentration within the streamtube. The fractional uncertainty in the mass flux can then be estimated through standard error treatment of 7.9 to give equation 7.10:

$$\Delta m^2 \approx \left(\frac{\partial m}{\partial c_d}\right)^2 \Delta c_d{}^2 + \left(\frac{\partial m}{\partial q}\right)^2 \Delta q^2$$

$$\left(\frac{\Delta m}{m}\right)^2 = \left(\frac{\Delta c_d}{c_d}\right)^2 + \left(\frac{\Delta q}{q}\right)^2 \qquad (7.10)$$

The estimated lower and upper bounds of the fractional uncertainties in q and c_d can be inserted into 7.10 to give the expected bounds on the uncertainty in the tracer mass fluxes, given by 7.11:

$$0.11 < \Delta m/m < 0.20 \qquad (7.11)$$

A fractional uncertainty in the estimated mass fluxes for the streamtubes of 0.15 or 15% was selected as being representative of this range of values.

7.3.3. Vertical distribution of initial mass fluxes.

Given the large uncertainties in the calculated mass fluxes, the output from the model was only examined in terms of depth averaged number of particles per streamtube. However, the model flow domain retained the three dimensions in order that the mass fluxes were correctly maintained, and so that the non-uniform geometry could influence the particle trajectories as in the real situation.

The flow was strongly turbulent, and had been estimated to have a Reynolds number of approximately 50000 for a 0.23 stage, so the vertical mixing was likely to take place in a short distance. The measurements of tracer concentration which had been made in the vertical direction (table 5.4) supported the assumption that the tracer had become well mixed in the vertical direction by the time it reached cross-section A1.

The logarithmic vertical velocity distribution was used to define the relative mass flux of particles through each vertical, with the assumption that the vertical concentration distribution was uniform. Given that only the depth averaged particle numbers were examined at the output, it might be thought that the particles could be distributed uniformly throughout the depth at the input. However, if the eddy coefficient is allowed to vary in the transverse direction, as will be investigated in chapter 8, the vertical mass flux distribution in combination with the channel geometry could have an influence on the transverse mixing. This has been visualised for the simplified case of two adjacent regions of high and low dispersivity for the two forms of distribution shown schematically in fig.7.9:

Fig. 7.9 Diagram to illustrate the importance of using the correct initial vertical distributions of particles in a flow with a laterally varying transverse dispersivity coefficient.

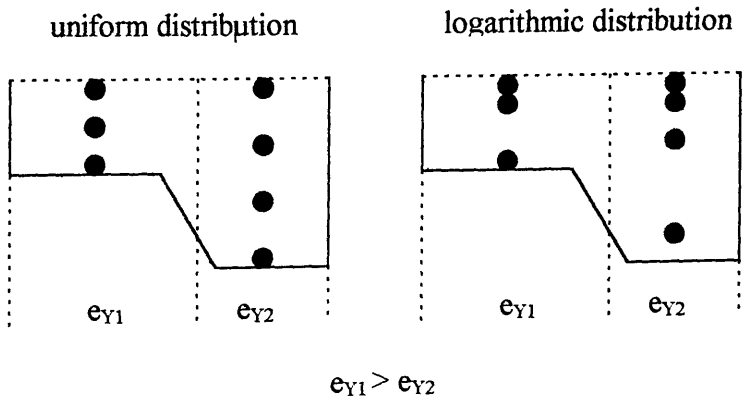

Where e_{y1}, e_{y2} are two different transverse dispersivities and the large particles are representative of the mass fluxes of particles passing through the cross-section. Clearly for the first case, more of the particles on the right hand side are inhibited by the bed topography from entering the region of greater dispersivity, than for the second case. Thus the transverse dispersion for the two cases are likely to differ.

A discretised logarithmic probability distribution was therefore constructed, in order that the relative numbers of particles might be distributed according to the expected mass fluxes for a logarithmic distribution.

The mass flux of water for a one dimensional logarithmic profile between the roughness height and an increment Δz in the vertical direction can be calculated from integrating the velocity profile between these two limits using equation 7.12:

$$m = \rho \int_{z_o}^{z_o+\Delta z} u\,dz \qquad (7.12)$$

where m is the mass flux, u is given by 7.3 and ρ is the density of water. If this integral is carried out for n subdivisions, Δz, of the depth then the relative mass flux per interval can be used to define a discretised probability distribution, using equation 7.13:

$$P(\Delta z) = \frac{\int_{z_o}^{z_o+\Delta z} u\,dz}{\int_{z_o}^{h} u\,dz} \qquad (7.13)$$

Where the sum of the probabilities over the intervals is unity, and h is the flow depth at a particular transverse position. The cumulative probabilities where then used in conjunction with a random number generator which produce a random number in the interval (0.0-1.0). For example, the probability of a particle being in the first interval from the bed was 0.02, and that of a particle being in the second interval was 0.03, then a particle would be assigned to the second interval if the random number which was generated for that particular particle lay between the cumulative probabilities 0.02 and 0.05. The particles were distributed uniformly between the intervals, of which 30 were used. Fig. 7.10 shows a frequency histogram of the particle distribution when they were all confined to a one dimensional profile.

7.3.4 Instantaneous release of particles.

The particles were all released at the same time in the simulations, using the same technique which was used for the channel flow. The modelled flow was steady state, so the instantaneous release represented the input to the reach for all times. This required that all of the particles which were released at one instant to be accounted for at the output. The number of particles which were necessary in order to achieve a steady state was investigated in chapter 8.

7.4 Particle tracking through streamtubes.

This section describes the particle tracking model which was used to examine the dispersion characteristics of the modelled flow field. This comprised the advective

and random parts of the particle motion, the transverse metric correction to the particles following divergent or convergent streamlines, and the modelled behaviour of the particles at the boundaries.

7.4.1 Transformation of particle coordinate system.

Each downstream section of the reach between measurement transects formed a trapezium, which can be observed by inspecting fig. 7.4. The upstream transect and the left bank formed an orthogonal bases set, with the origin in the upstream left hand corner of each trapezium (see fig.7.11 below). Whenever a particle entered a new section of the river in the downstream direction, the origin was moved to the upstream left hand corner of the new section. The particle was assigned downstream and cross stream co-ordinates on these bases, and in addition a streamtube index, depending on which streamtube boundaries it fell between.

Finally, since the transverse and downstream interpolations were all linear, the distances between the streamtube boundaries were rescaled to lie in the interval 0.0-1.0. This necessitated a similar scaling of the particle displacements in the transverse direction. This rescaling process made it simple to define the transverse and downstream boundaries, which were now always 0 or 1, as demonstrated in fig. 7.11:

Fig. 7.11 Diagram showing particle coordinate system in one section of the river and the transformation into a unit square for simplicity in boundary handling.

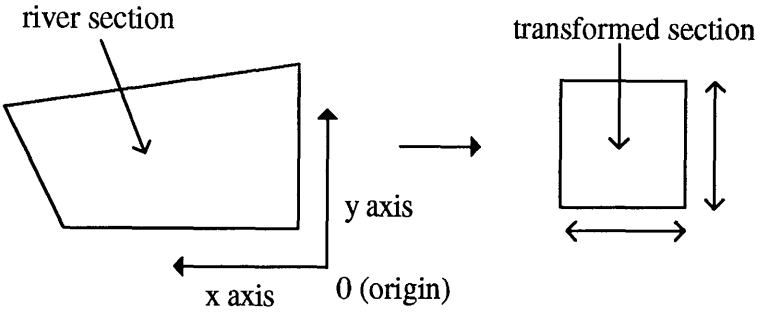

7.4.2 Advection.

Following the initialisation of the particle co-ordinates, the particles were advected through the streamtubes in accordance with the interpolated velocity field. Random displacements were periodically applied to the particle trajectories following the same technique which was described for the channel flow, the lengths and time intervals of which will be discussed in chapter 8. The particles were not subjected to any other body forces, such as a centrifugal acceleration. Centrifugal forces give rise to secondary circulation in the real situation, and these currents strongly influence the mixing characteristics of the reach. However, the enhanced mixing effects due to secondary circulation were absorbed into the transverse dispersion coefficient in the model (a process which was described in chapter 1).

The only effect which the channel curvature had upon the modelled particle trajectories, was in the times of travel between transects. A particle which remained

close to the outer bank would clearly have a longer time of travel than a particle close to the inner bank.

7.4.3 Approximation to a metric due to flow convergence / divergence.

The streamtubes diverged and converged due to changes in the channel width and because of the meandering of the thalweg. The position of a particle relative to its current streamtube boundaries was maintained after the each time step and advection due to the mean velocity. This ensured that the particle followed a streamline which diverged or converged consistently with the streamtube boundaries. When the position of a particle was increased in the downstream direction, the transverse position of the particle was therefore also altered in accordance with the local flow divergence. The random step part of the particle's motion was additional to this correction.

7.4.4 Time steps for the random walk.

The time steps for the random walk were initially set to be constant and homogeneous throughout the flow for simplicity. However, the inhomogeneities in the turbulent time scales, evident from the time series analyses in tables 6.4, suggested that the time steps and therefore the transverse dispersivity coefficient should be allowed to vary, especially in view of the deadzone region. For this reason a varying time step model is investigated in chapter 8.

7.4.5 Form of the displacements for the random walk.

The study of the tracer dispersion in the river model was more restricted than the study which had been undertaken on the flume flow in chapters 3 and 4. The detailed set of measurements which were taken in the flume allowed for an investigation into the sensitivity of the modelled tracer dispersion to a variety of random walk models. It was shown that most of the different forms of random walks could be calibrated to model the observed tracer distributions. However, the river flow was less well defined and the turbulent, topological and geometrical inhomgeneities gave rise to large uncertainties. It was therefore considered that the model would be insensitive to the small differences between different forms of random walk after calibration. Therefore only one random walk model, for which the displacement sizes were selected from a normal Gaussian distribution, was used in the following investigations (equivalent to the model NEWJUMP in the flume flows). This random walk was selected since it allowed for a more rapid sampling of the entire flow field than the random walk which used a single and constant displacement size.

The size of the variance for this random walk was changed through alteration of the size of the transverse step size multiplier, $\mathbf{f_v}$, in equation 7.14, using the same technique which was used the flume model:

$$l_v = f_v L_v \mu(0,1) \qquad (7.14)$$

where l_v is the displacement, $\mu(0,1)$ is a random number generated from a normal Gaussian distribution with zero mean and unit variance and L_v is an estimation of the expected length scale due to secondary advections(from dimensional arguments). L_v was included in order that the calibration of the step size should result in $\mathbf{f_v}$ having a value close to unity for convenience. L_v was considered by dimensional reasoning in chapter 6 (equation 6.7) to be of the order 0.1m. The step length was therefore fixed at the calibrated value, although the transverse dispersivity coefficient could still be varied through varying the size of the time steps.

7.5 Output from model.

Although twelve streamtubes had been used in order to minimise the errors arising from interpolations (described in section 7.2.2), there were insufficient concentration measurements at cross-sections 1 and 4 to support this degree of spatial resolution, especially considering the uncertainties involved. There were on average seven concentration measurements in the transverse direction from which the tracer mass fluxes per streamtube were estimated. For this reason, the streamtubes were paired together at the outputs, in order that there were now six larger streamtubes. The spatial resolution of the modelled mass fluxes was now more compatible with that of the measurements.

The numbers of particles which the model predicted to be in each streamtube at a measurement cross-section were compared against the normalised measured mass fluxes (which were rescaled using the total number of particles used in the model). The

predicted and measured numbers of particles per streamtube are presented in either tabular or graphical form for comparison, in the next chapter.

7.6 Summary of particle tracking, streamtube model.

The computer model of the flow through the reach of the River Lune comprised a random walk, particle tracking model based within a simple streamtube structure. This structure was incorporated since it allowed for the conservation of mass (and momentum) of the particles within the non-uniform flow field. The streamtubes were based on linear interpolations between point measurements in the cross-stream direction. The curvature of the river in the downstream was approximated by a series of trapezoidal streamtube sections joined end on end. As the particles advected in the downstream direction, their changes in cross-stream position (whilst allowing for the turbulent perturbations) due to the changing geometry and relative discharge were accounted for by metrics.

The entire data set was not collected for a single stage, which made it necessary to rescale the velocities and flow depths in order that the model was able to simulate the flow on the day of the tracer experiment. The vertical velocity profiles were approximated as logarithmic profiles, although only the depth averaged mass flux distributions were later examined. The model output was examined in terms of the number of particles occupying regions of equal partial cumulative discharge in the cross-stream direction. These relative number of particles per streamtube were compared against the relative measured mass fluxes for the streamtubes in a sensitivity analysis carried out in chapter 8.

Fig.7.4

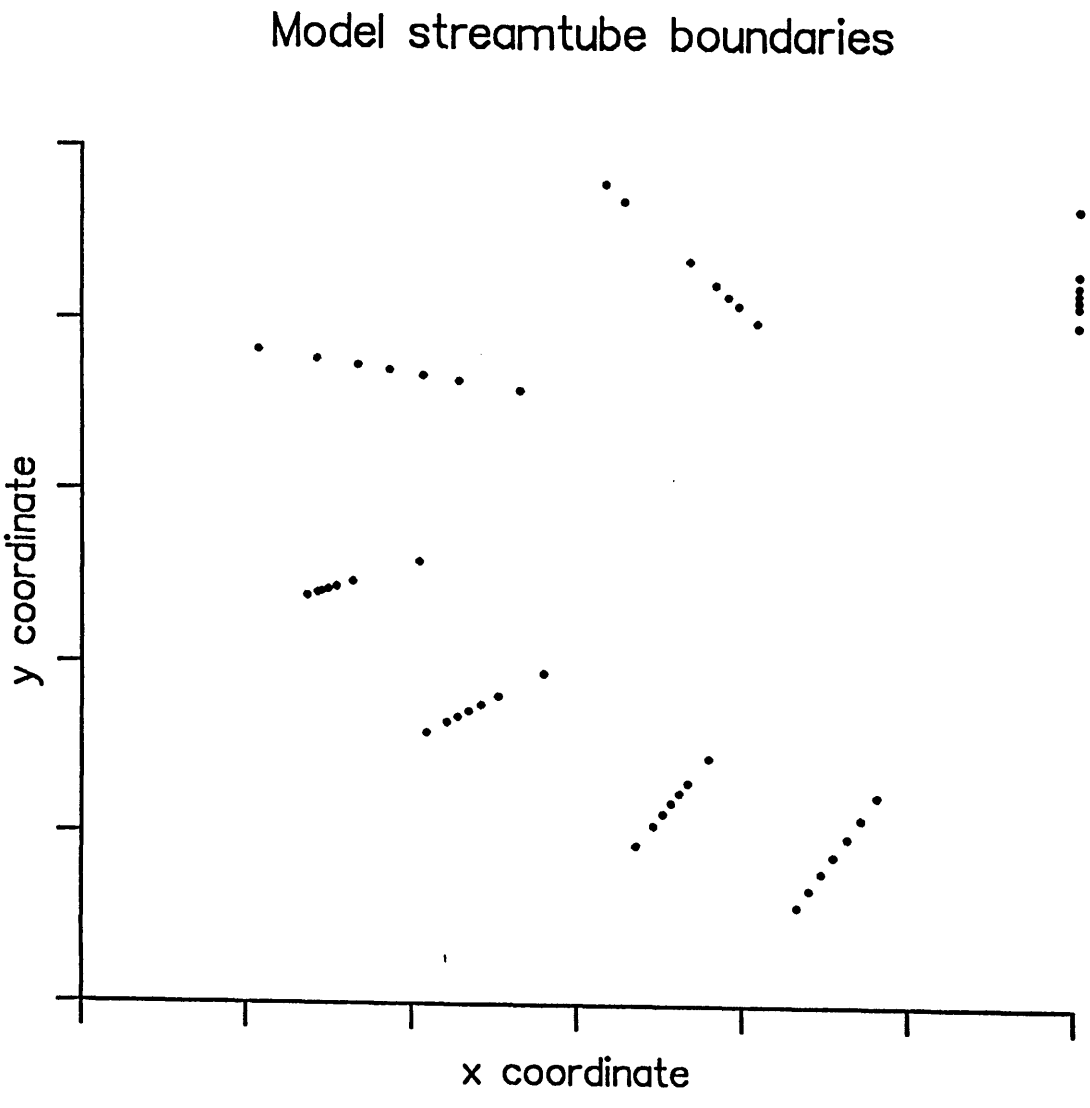

Fig.7.5

Bi–linear interpolations of reach characteristics
with exaggerated width to length scale

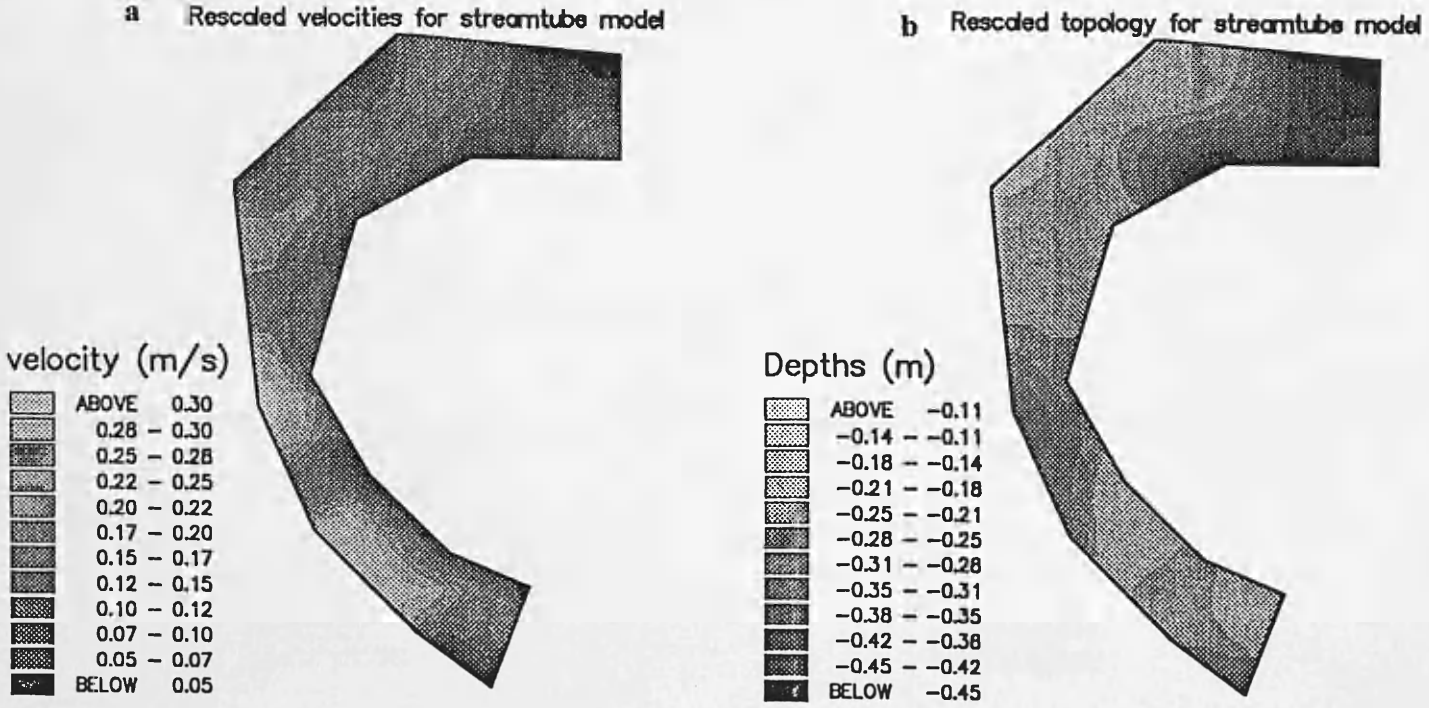

Fig.7.6

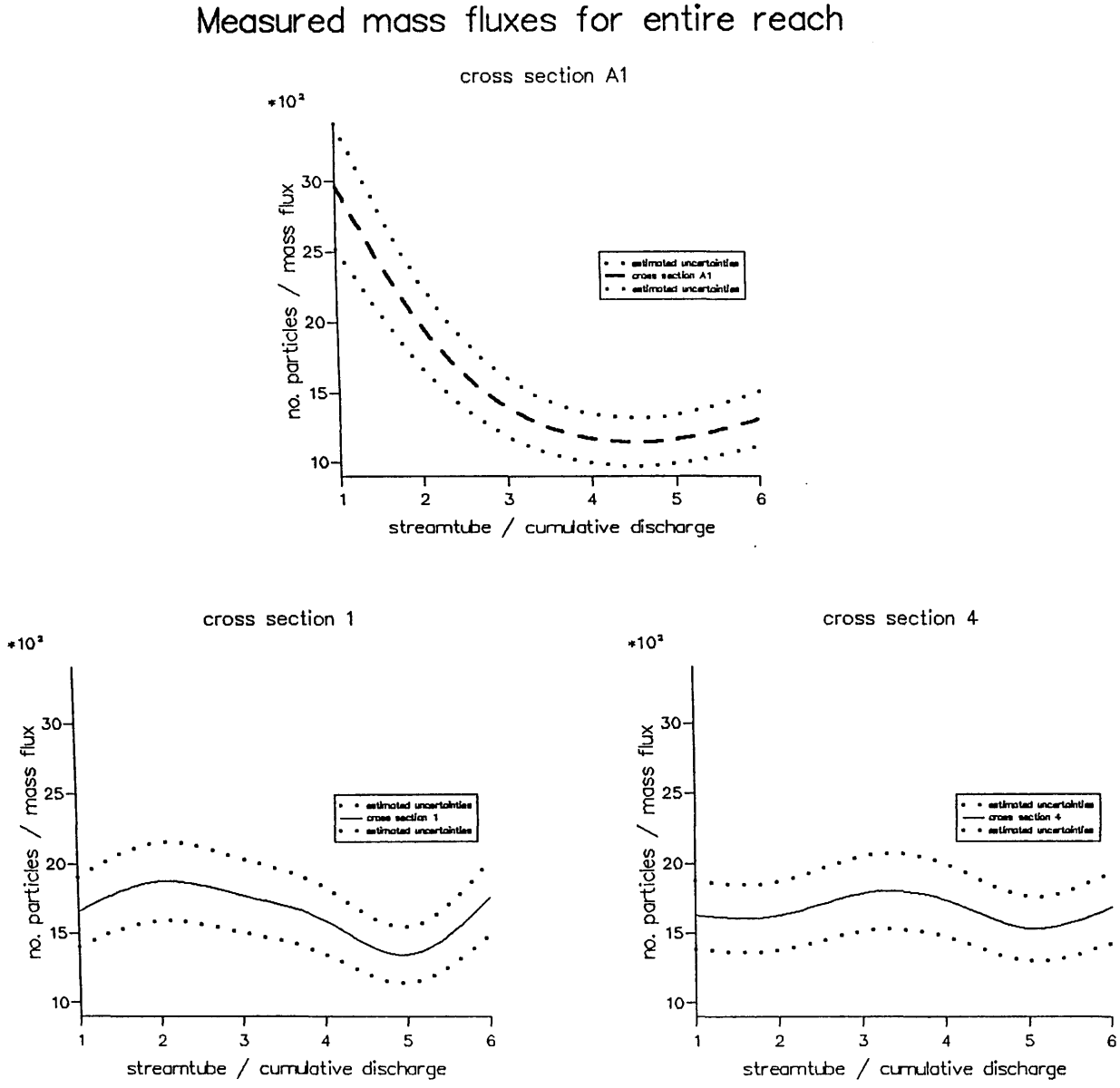
Measured mass fluxes for entire reach
cross section A1
*10³
no. particles / mass flux
30
25
20
15
10
1
2
3
4
5
6
streamtube / cumulative discharge
estimated uncertainties
cross section A1
estimated uncertainties
cross section 1
cross section 4

Fig.7.7

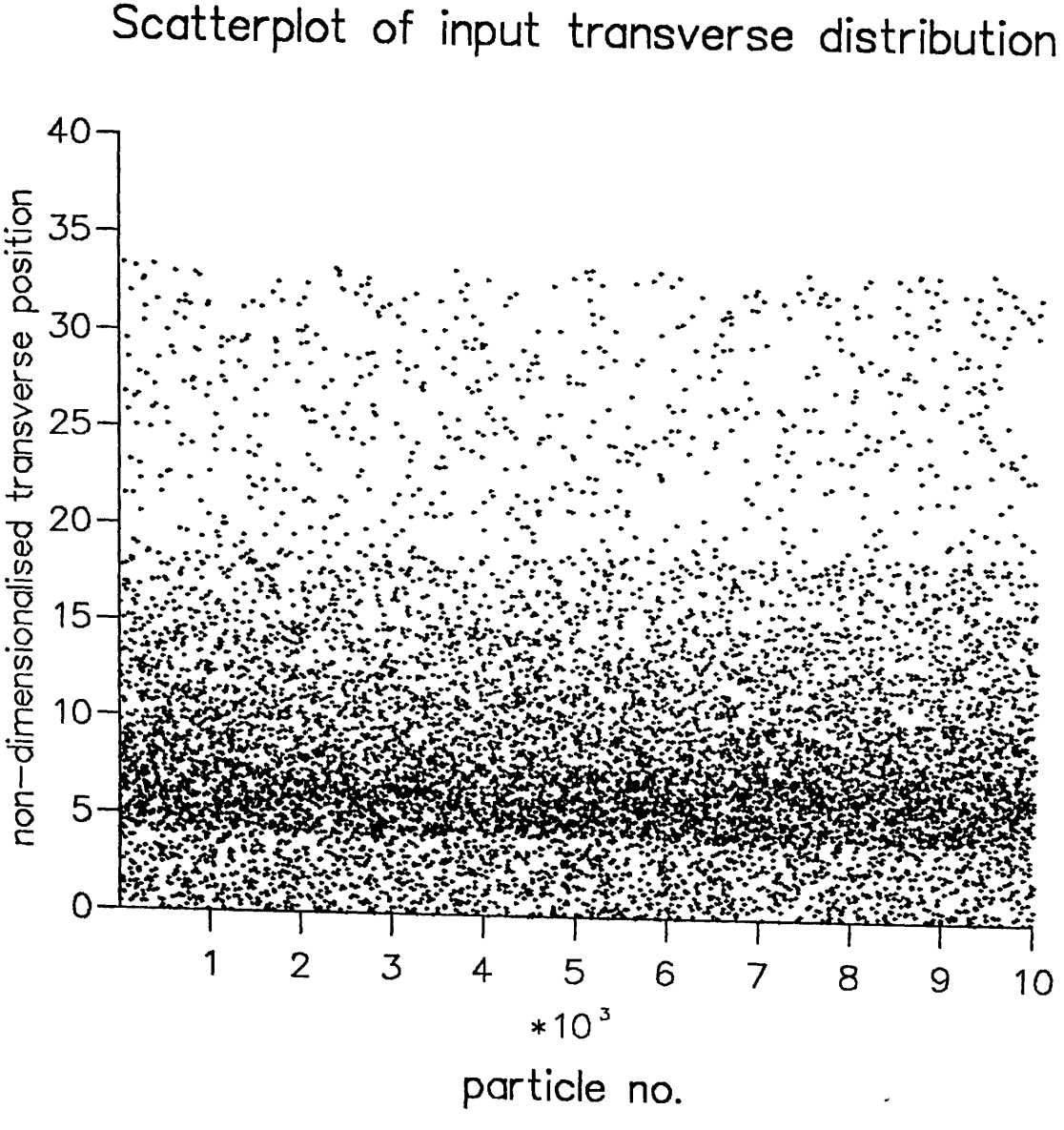
Scatterplot of input transverse distribution
non-dimensionalised transverse position
40
35
30
25
20
15
10
5
0
1
2
3
4
5
6
7
8
9
10
*10 3
particle no.

Fig.7.8

Frequency histogram of initial transverse particle distribution

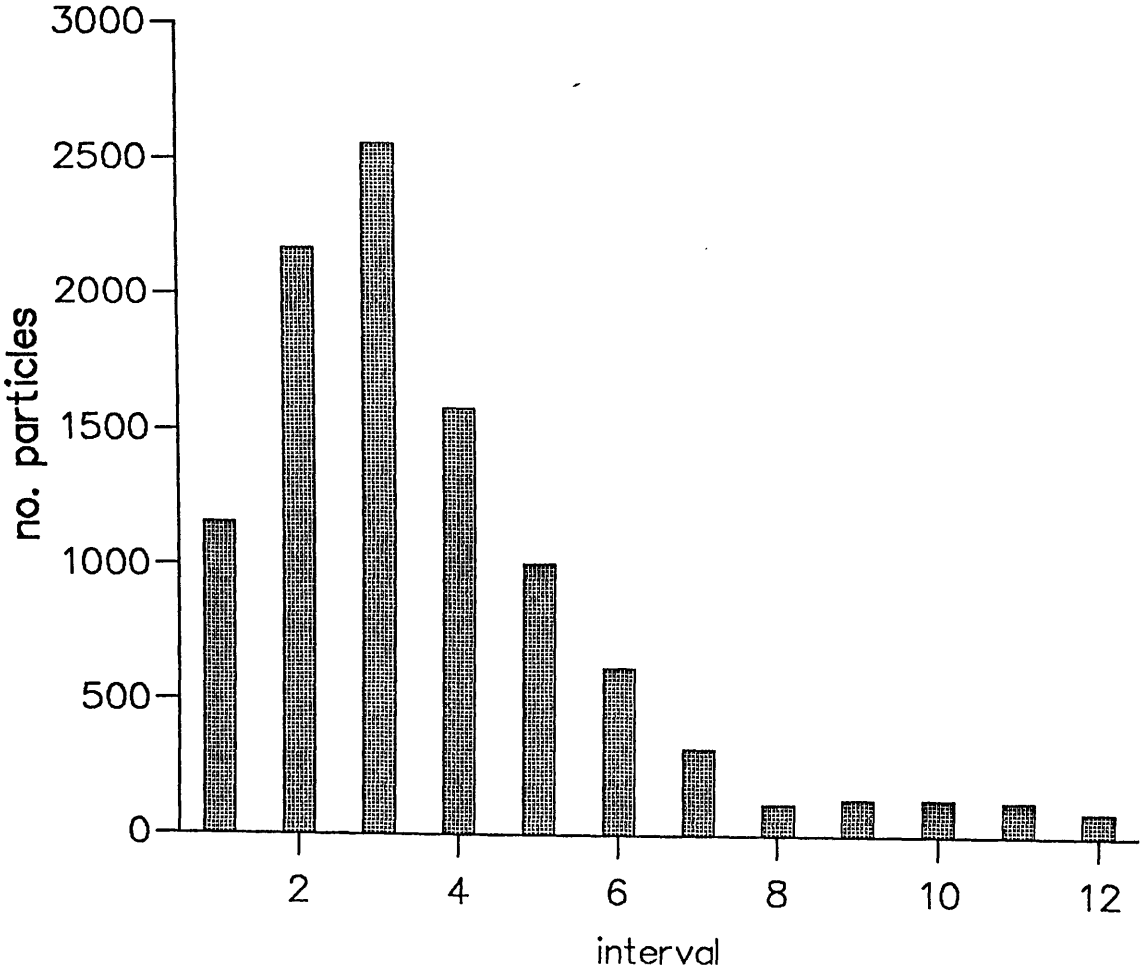

Fig.7.10

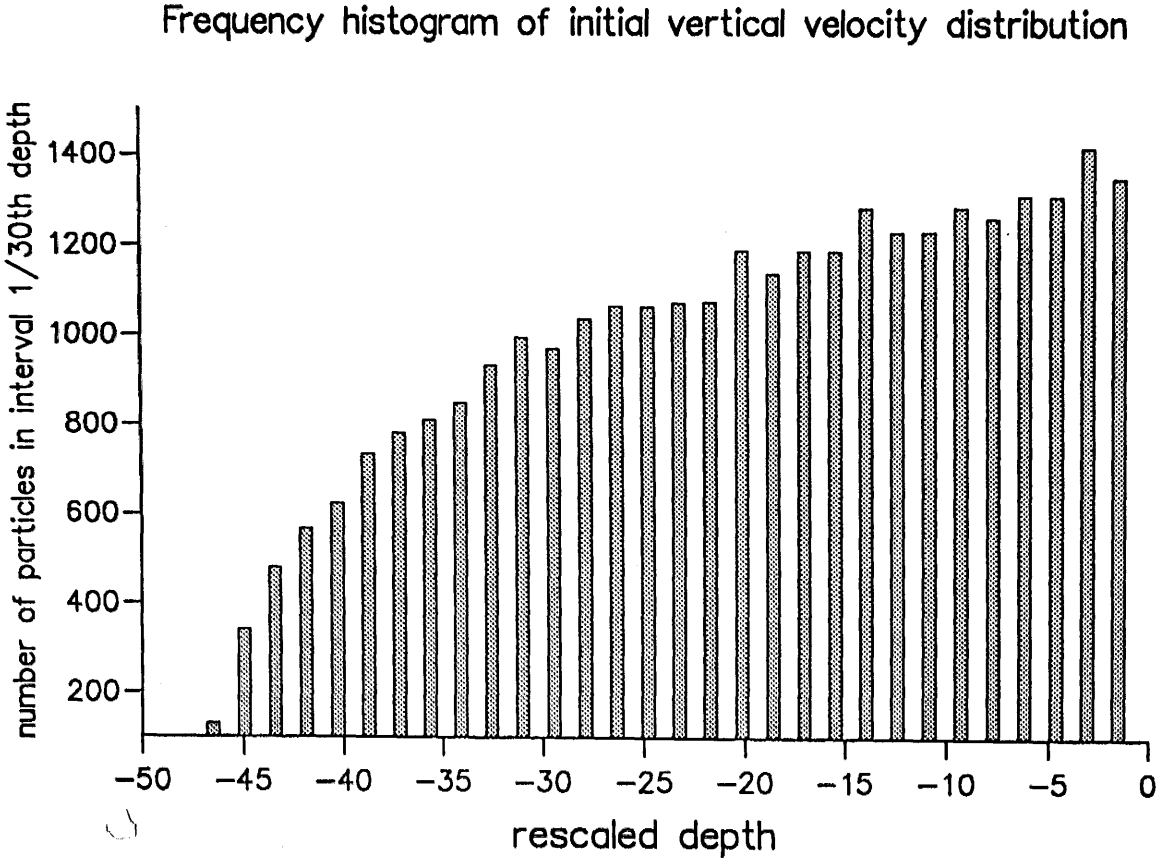
Frequency histogram of initial vertical velocity distribution
number of particles in interval 1/30th depth
1400
1200
1000
800
600
400
200
−50
−45
−40
−35
−30
−25
−20
−15
−10
−5
0
rescaled depth

Chapter 8

Sensitivity analysis of a random particle tracking model of the tracer dispersion characteristics in the reach of the River Lune.

8.1 Introduction.

This chapter describes a sensitivity analysis which was carried out on the simulation of the tracer dispersion in the reach of the river Lune. The extent to which it was necessary to calibrate the model before the measured concentration distributions could be reproduced to within estimated experimental uncertainties is discussed. This ultimately has implications on the quantity of fieldwork which it is necessary to undertake in order to operate the model to within given uncertainty bounds.

In section 8.2, the model equivalent of the conservation of mass and momentum laws are examined. The number of particles which were necessary to achieve steady state transverse distributions, to within acceptable uncertainty bounds is investigated.

In section 8.3 choice of the average size of the vertical perturbations in the random walk is explained so that the model exhibited the strong vertical mixing required to reproduce the field data.

In section 8.4 it is argued that the reach naturally divides into two sub-reaches, with most of the mixing taking place in the first sub-reach. The analysis is therefore divided into two sections, 8.5 and 8.6 which deal with the transverse mixing in the first and second sub-reaches respectively. In these sections the sensitivity of the model to

changes in the effective transverse dispersivity coefficient (e_y) are investigated, and the model is calibrated to within the estimated uncertainties using the measured tracer distributions. The value of e_y is estimated for each sub-reach, and its uncertainty bounds are estimated from the model sensitivity.

Section 8.7 examines the particle distributions in the reach as a whole, and a reach averaged value of e_y is estimated.

In section 8.8 the estimated values of e_y are compared with values determined from measurements made on similar rivers and are found to be in agreement, to within the estimated uncertainty bounds.

In section 8.9 numerical experiments are described in which a square wave distribution of particles are input to the model and the predicted particle distributions downstream are compared with approximate solutions of the cumulative discharge diffusion equation for the equivalent input distribution of mass flux, and having the same reach-averaged factor of diffusion. The two models exhibit similar cross-section averaged mixing characteristics which helped to confirm that the calibrated value of the transverse dispersivity coefficient was the correct order of magnitude.

Finally section 8.10 is a summary of the modelling work, which is also discussed further in chapter 9.

8.2 Preliminary tests on the model.

8.2.1 Conservation of total number of particles.

The particle tracking algorithms were initially tested to ensure that all of the particles remained within the flow domain. This was simply achieved by summing the

total numbers of particles which reached the cross-section at which the mass fluxes were calculated, and comparing this with the number of particles at the input. These tests were carried both with and without random velocity fluctuations. Conservation of mass is generally a simple matter to test for using random particle tracking models, since the particle number is simply the index of an outermost loop in the computer algorithm. Mass conservation is generally violated if the boundary conditions are inadequate.

8.2.2. Tests on the particle trajectories in the absence of random perturbations.

A test was devised to ensure that there were no spurious mixing effects in the absence of any random fluctuations. The transverse and vertical random components of the particle trajectories were set to zero so that the particles were advected under the influence of the mean interpolated velocities only. The number of particles in each streamtube was then determined at the last cross-section to be exactly the same as the number of particles which had been input into each streamtube. This result helped to confirm that the boundary and metric handling were performing correctly. Further checks were carried out during the run time operation of the model, such as the inclusion of statements which stopped the program if the particles went outside of the flow domain. Similar checks were carried out on the remainder of the interpolated variables.

The above test was then carried out with a non-zero vertical random component, such that vertical mixing was permitted but transverse mixing was not. The boundary handling, which was fully described in chapter 4 was used once again,

whereby if the random displacement would place the particle outside the boundary, then the particle remained at its current transverse or vertical position. In this way, the transverse mixing was uniquely dependent on the sizes of the transverse displacements, and was consequently more easily controlled. The transverse mixing effects due to the interaction of vertical motions with the bed topography in the real situation were therefore absorbed into the effective transverse dispersivity coefficient of the model.

8.2.3. Achieving a steady state in the particle distributions.

Although full three dimensional movement of particle trajectories was modelled, the modelled mass flux distributions could only be substantiated by the measured data in two dimensions, and consequently only the depth averaged mass flux distributions were examined. The model was run repeatedly using different random sequences for the random perturbations, and the mean numbers of particles in each streamtube at the output were determined. The coefficients of variability for the numbers of particles in each streamtube for these different runs were determined and these were averaged over the six streamtubes in a cross-section to give a measure of the variability in the model output due to the stochastic element of the random walk. Table 8.1 demonstrates the variability of the mass fluxes for different random number sequences, for 2000, 5000 and 10000 particles at cross-sections 1 and 4. A sample size of six different random sequences were used in the determination of each fractional deviation.

Table 8.1 Variation of standard deviation from the mean spread for repeated runs of the random walk having different random sequences, with total number of particles.

Cross-section	number of particles used	cross-section averaged coefficient of variability.
1	2000	0.07
1	5000	0.03
1	10000	0.02
4	10000	0.02

The table indicates a decrease in the uncertainties in the modelled distributions as the number of particles was increased at cross-section 1. The 2% variability in the modelled distributions at cross-sections 1 and 4 respectively which resulted when 10000 particles were used, were considered to be accurate enough for the sensitivity analysis, considering the size of the uncertainties in the measured distributions were 15%. These two measures of sensitivity come from different sources, the model variability from repeated computing experiments, and the uncertainties in the measurements from the estimated experimental error. If the particle tracking model is considered as a tool for investigating the mixing coefficient for the reach, the accuracy of the measurements on which the model is based is still the limiting factor in the determination of the value of the model mixing coefficient. 10000 particles were therefore used in all the following investigations. Fig. 8.1 demonstrates this variability graphically for the case of 10000 particles at cross-section 1. The curves have been smoothed using the minimum smoothing factor in a cubic-spline approximation on the graphics package, UNIRAS.

8.3 Vertical mixing.

The variance of the step sizes in the vertical direction was set at a fixed value throughout the reach, such that the average magnitude of the step sizes was approximately equal to one tenth of the reach averaged mean flow depth (mean flow depth was 0.3m, and the vertical step size was held at the value 0.03m). This value was sufficient to cause vertical mixing over the correct order of length scale, and has been used in the past by Allen (1982) and Van Dam (1992). This ensured that the particles rapidly diffused and were able to experience the entire vertical velocity distribution as they were advected between regions of different depths. The variance of the vertical step size was held constant for the remainder of the study, which was primarily concerned with transverse mixing. The effective vertical mixing coefficient was therefore constant, unless the time step was allowed to vary. The time step was allowed to vary spatially in the final model, in order to account for the observed variability in the turbulent time constants (as will be described in the next few sections).

8.4 Division of the reach into two sub-reaches.

The model needed to take into account several features of the flow which were considered to have a large influence on the mixing characteristics of the reach. These characteristics were apparent from direct observation and from the turbulence and dye concentration measurements and are outlined here.

From the measurements of concentration at cross-sections A1, 1 and 4 it was evident that most of the transverse mixing, at least in the main body of the flow, took place between cross-sections A1 and 1, as demonstrated in fig.7.6. This was thought to be mainly due to the secondary currents which were visible on the day of the tracer experiment, and can be identified in the region just after the bend entrance in fig.5.1. The sensitivity analysis was therefore concentrated on the study of the model behaviour between cross-sections A1 and 1.

Another difference between the two sub-reaches was evident from the turbulence and concentration time series analyses.

The first sub-reach showed a transverse variation in the turbulent time scales (tables 6.4), which can be attributed to the presence of two distinct regions of flow in the cross stream direction. There was a region of slow moving water close to the right bank at cross-section A1, and a region of fast moving water close to the left bank. However, the second sub-reach (1-4) comprised a riffle section, and the time scales measured at different cross stream positions at cross-section 4 indicated that the turbulence was homogeneous to within the accuracy of the measurements.

The transverse distributions in the time constants which were determined from the tracer concentration time series supported the above observation. Further, these time constants were considered to contain information about the large scale foldings or mixing of the dye in the river upstream of the measurements. The large time constants in the autocorrelations close to the right bank at cross-section 1, suggested that the deadzone close to the right bank had a strong influence in the first sub-reach.

The natural division of the reach into two sub-reaches was made use of throughout the sensitivity analysis.

8.5 Random particle tracking model applied to the first sub-reach.

In this section the sensitivity of the model to changes in the transverse step sizes and in the sizes of the time step are estimated. The transverse displacement size and the time steps are calibrated for each of the sub-reaches. The time steps are allowed to vary in the cross stream direction in the first sub-reach but are held constant in the second sub-reach, in accordance with the analysis of the E.C.M. measurements.

8.5.1. Average magnitude of the displacement sizes and time intervals for the random walk in the transverse direction in the first sub-reach(between cross-sections A1 and 1).

The model initially used a constant value for the variance of the transverse step size, and a constant time step for the entire sub-reach. This effectively meant that the modelled transverse eddy dispersivity coefficient was constant for the entire reach. The size of the variance could be changed through alteration of the size of the transverse step size multiplier, $\mathbf{f}_v$, in equation 7.14, using the same technique which was used the flume model.

It rapidly became apparent that the use of a single effective eddy dispersivity coefficient for the entire reach was insufficient to characterise the transverse dispersion characteristics (see for example the one time constant model results in fig. 8.2). This was to be expected from the large differences in the turbulent time constants which had

been determined from the turbulence measurements across-section A1. Further, the variation in transverse turbulent time scales across the channel at cross-section A1 was thought to be characteristic of much of the sub-reach due to the presence of a second 'dead zone' close to the right bank, although no measurements had been taken to substantiate this.

The model eddy dispersivity coefficient was therefore allowed to vary spatially to account for these inhomogeneities. This could be achieved in a number of ways, by either allowing the time step or the displacement size to scale with local properties of the flow. Initially the first sub-reach was examined, and the variance of the displacement size was kept spatially invariant, while the time step was varied in accordance with local turbulent time constants.

8.5.2 Localised values of time steps.

The time constants determined by measurement at cross-section A1 in table 6.4 show two distinct regions having slow and fast time scales. The corresponding two regions in the model framework were given two time scales which were the same order of magnitude as these measurements. The time step in the deadzone was set at 7 s (the measured value was 7 +/- 3s), and the time step in the other regions was set as 0.8s (the measured value for the first sub-reach was 0.8 +/- 0.3). Thus, the transverse eddy dispersivity was allowed to vary discretely in the transverse direction, analogously to the approach taken by Knight and Shiono (1989) for the problem of the overbank flow field, which was described in chapters 3 and 4. This approach was described fully in chapter 4, in which the overbank channel flow was divided into four regions, each of

which was attributed a different value of transverse eddy dispersivity coefficient. Knight and Shiono defined the boundaries of the regions by inspecting the cross-sectional variation of the measured transverse eddy dispersivity, rather than the measured time constants, as in this study.

Fig. 8.2 shows the immediate improvement to the modelled mass fluxes at cross-section 1, which was achieved by having two regions, A and B, instead of one, with effectively two different eddy dispersivity coefficients, the calibrated values of which are given in table 8.2:

Table 8.2 Boundaries and time steps for two-time constant model.

region / transverse location (m from L.Bank)		Time step(s)
A	0.0 - 4.8	0.6
B	4.8 - 8.6	7.0

The boundary of the deadzone was estimated by examining the downstream velocity distribution. The two time step sizes were varied between the ranges estimated from the turbulence measurements given above, in order to optimise the model fit to the data.

However, with only two regions, the model under predicted the mixing close to the left bank. This behaviour could not be accounted for in terms of the turbulent time constants, but was thought to be due to observed region of separation close to the left bank, which gave rise to rapid secondary advection. This feature which can be observed for the day of the tracer experiment in fig.5.1. Unfortunately, the separation

occurred a few meters below the measurement cross-section A1, on the day of the tracer experiment. This region of strong secondary advection would give rise to an enhanced transverse dispersion coefficient, which could be incorporated into the model by either increasing the displacement sizes, or through reducing the time step in a region close to the left bank. The latter approach was adopted for consistency. The minimum acceptable time step was estimated from dimensional reasoning to be approximately 0.1s, which for the displacement sizes in use corresponded to the maximum observed advective velocity of 0.8m/s. The region close to the left bank, in which this reduced time step was incorporated was kept as small as possible (0.5m), since the time constant was highly uncertain.

It was found that model could be further improved by incorporating three regions, A,B, and C with three time steps (and therefore dispersivity coefficients), as demonstrated by fig. 8.2, and where the calibrated values of the time steps in each region are given by table 8.3:

Table 8.3 Boundaries and values of time step for three-time constant model.

region / transverse location (m from L. bank)		Time step(s)
A	0.0 - 0.5	0.08
B	0.5 - 4.8	0.6
C	4.8 - 8.6	10.0

The time step in region A had to be reduced to a value which was just smaller than the estimated minimum time constant. The use of such a small time step is accepted as

being somewhat artificial, but this was carried out in order that the displacement size could be held constant for simplicity. The effective dispersivity coefficient for the model increases with the square of the displacement size in the random walk, whereas it is inversely proportional to the time step. The same enhanced dispersivity coefficient could therefore be attained by keeping the time step at a larger value and by increasing the displacement size by a proportionally smaller amount than the necessary reduction in the time step.

The variation in the time steps, combined with a constant vertical step size gave rise to a varying vertical mixing coefficient. The effects of this variation were not investigated (since the study was primarily concerned with the depth averaged mixing processes), although it was considered for example, that in a region of enhanced transverse mixing, the vertical mixing should also be enhanced.

It was only by using three dispersivity coefficients that the modelled mass fluxes could be fitted to the measured mass fluxes within the estimated uncertainties, as demonstrated in fig. 8.3. No further sub-regions were added to the model to avoid the use of even more degrees of freedom at the calibration stage.

8.5.3 Sensitivity of model to changes in the transverse dispersion coefficient.

The following exercise enabled the sensitivity of the model to increments in the variable parameter, $\mathbf{f_v}$, and in the time steps for the three regions to be investigated, while taking into account the random errors inherent to the model. It was more difficult to quantify the sensitivity of the model to changes in these parameters than had been possible in the channel flows due to the irregularity of the mass flux distributions.

8.5.3.1 Sensitivity of model to varying the f_v factor.

The model was run using three f_v factors over a small range of values, and the mean of the numbers of particles for the three values was taken for each streamtube. The coefficients of variability from these mean values for each streamtube was averaged over the cross-section, and used as an indication of the sensitivity of the model to the small increments in f_v. This was repeated for another range of f_v values in case the model sensitivity was dependent on the absolute values of the f_v factor. Table 8.4 shows the mean number of particles and the coefficients of variability, for each streamtube for two sets (of three localised values) of f_v using 5% increments(set 1: f_v=0.50,0.53,0.56 and set 2: f_v=1.05,1.10,1.15).

Table 8.4 Sensitivity of particle distributions to small (five percent) changes in the displacement sizes.

streamtube number	<N> for 3 intervals(set 1)	σ_{n-1}/N	<N> for 3 intervals(set 2)	σ_{n-1}/N
1	2246	0.01	1675	0.03
2	2179	0.01	1711	0.02
3	1595	0.02	1778	0.004
4	1420	0.02	1877	0.02
5	1150	0.001	1388	0.02
6	1410	0.003	1571	0.008
	$<\sigma_{n-1}/N>$ = 0.01		**$<\sigma_{n-1}/N>$ = 0.02**	

where $<\sigma_{n-1}/N>$ is the cross-sectional average value of the fractional standard deviation from the mean.

The cross-section averaged coefficient of variability from these means for the three values was determined to be between 0.01 and 0.02. This includes variations due

to systematic changes in $\mathbf{f_v}$, but is also subject to the random uncertainties discussed above. This coefficient of variability was the same order of magnitude as the random error incurred due to sampling the flow with 10000 particles, and the model could therefore be said to be insensitive to increments of this size. 10% increments in $\mathbf{f_v}$ were now examined, again using two sets of $\mathbf{f_v}$ values ($\mathbf{f_v}$=0.5,0.55,0.6 and $\mathbf{f_v}$=1.0,1.1,1.2) and the results are shown in table 8.5:

Table 8.5 Sensitivity of particle distributions to small (ten percent) changes in the displacement sizes.

streamtube number	set 1, <N> for 3 intervals	σ_{n-1}/N	set 2, <N> for 3 intervals	σ_{n-1}/N
1	2230	0.03	1666	0.04
2	2155	0.02	1719	0.05
3	1611	0.03	1784	0.006
4	1431	0.03	1869	0.03
5	1156	0.006	1391	0.05
6	1424	0.02	1576	0.02
	$<\sigma_{n-1}/N>$ =	0.02	$<\sigma_{n-1}/N>$ =	0.03

Here the cross-section averaged coefficients of variability from the mean show values 0f 0.02 and 0.03, which are slightly greater than the random error associated with the stochastic part of the model (0.02), and could therefore be attributed in part to small systematic changes in the mean particle numbers, due to the increments in $\mathbf{f_v}$. The $\mathbf{f_v}$ parameter was therefore optimised to within the accuracy afforded by using 10% increments.

8.5.3.2 Sensitivity of the model to changes in the values of the time steps.

A similar sensitivity analysis was applied to the variation the time steps in advance of the model calibration. This time steps in each of the regions A,B, and C were varied by 5% (set 1) and then 10% (set 2) about three localised values (T = 0.08, T = 0.6, T = 10.0) in each region. Since the time steps in each region could be varied independently of one another, there were many possible combinations of variations for the three regions. A representative sample of 8 of these combinations were examined for each set. The mean number of particles and the fractional standard deviation from these means in each streamtube were again determined for the different combinations, and are given in table 8.6:

Table 8.6 Sensitivity of particle distributions to small (five and ten percent) changes in the different time steps in the different regions.

streamtube number	set 1, <N> for 8 combinations	$\sigma_{n-1}/<N>$	set 2, <N> for 8 combinations	$\sigma_{n-1}/<N>$
1	1672	0.008	1711	0.036
2	1706	0.017	1767	0.025
3	1788	0.007	1766	0.008
4	1864	0.011	1839	0.027
5	1392	0.020	1388	0.018
6	1571	0.008	1530	0.019
	$<\sigma_{n-1}/<N>> = 0.01$		**$<\sigma_{n-1}/<N>> = 0.02$**	

The three sets of values for the three regions, A, B, and C, for set 1 and set 2 are given in table 8.7:

Table 8.7 Values of the time steps used in the sensitivity analysis.

region / transverse location (m)		Three sets of time step(s) using 5% increments (set1)	Three sets of time steps using 10% increments (set2)
A	0.0 - 0.5	0.080, 0.076, 0.084	0.08, 0.07, 0.09
B	0.5 - 4.8	0.57, 0.60, 0.63	0.54, 0.66, 0.60
C	4.8 - 8.6	10.0, 10.5, 9.5	9.0, 10.0, 11.0

8.5.4 Estimation of the uncertainty in the model value of effective transverse eddy dispersivity coefficient.

The transverse dispersivity coefficient was related to the reach averaged values of the step displacement size as given by equation 8.1:

$$e_y = \frac{3\langle f_V L_V \rangle^2}{\langle T \rangle} \qquad (8.1)$$

where the factor 3 arises due to the use of a random walk for which the displacements are selected from a normal Gaussian distribution (see section 2.2.5, equations 2.5 and 2.6). The uncertainty in the reach averaged value of e_y is determined from standard error analysis of 8.1 to give equation 8.2:

$$\Delta e_y^2 \approx \left(\frac{\partial e_y}{\partial f_V}\right)^2 \Delta f_V^2 + \left(\frac{\partial e_y}{\partial T}\right)^2 \Delta T^2 \qquad (8.2)$$

where the length scale L_V is constant, and effectively has no uncertainty. Evaluating the partial differentials, this gives equation 8.3:

$$\left(\frac{\Delta e_y}{e_y}\right)^2 = \left(\frac{2\Delta f_V}{f_V}\right)^2 + \left(\frac{\Delta T}{T}\right)^2 \qquad (8.3)$$

The fractional uncertainty in the values of $\mathbf{f_V}$ and T were then inferred from the sensitivity analyses in section 8.5.3. The model was found to be sensitive to at least 5% changes in the size of the $\mathbf{f_V}$ factor, and 5% changes in the time steps. Substitution into 8.3 results in an estimated sensitivity in the effective model dispersivity coefficient given by:

$$\Delta e_y / e_y = 0.11 \qquad (8.4)$$

8.5.5 Discussion of the effect of increasing the transverse dispersivity coefficient.

The transverse eddy dispersivity coefficient of the model was adjusted by varying the $\mathbf{f_V}$ parameter as described earlier. Fig. 8.3 demonstrates the effect of increasing $\mathbf{f_V}$ on the modelled distribution at cross-section 1, together with the input distribution at cross-section A1. As $\mathbf{f_V}$ was increased, the peak close to the left bank at cross-section 1 was gradually decreased in size until it approached the measured

relative mass flux value at cross-section 1. However, as $\mathbf{f_v}$ was increased another feature became apparent in the 4th and 5th streamtubes, which was not apparent in the data. This feature was of the same order of magnitude as the estimated experimental error in the measurements. The peak in the modelled mass flux for streamtube number 4 exceeds the upper uncertainty bound slightly, although it would be expected that some of the points would fall outside of the uncertainty bounds if these were truly representative of random experimental error.

The feature was nonetheless a characteristic of the model and might be attributed to the presence of a larger wave-like structure between streamtubes 4-6. If the central streamtube (5) of these three was a region of relatively high diffusivity in the model, then it would be expected that the particles would diffuse away in the transverse direction over many steps and accumulate in the two adjacent streamtubes. To support this, the numbers of particles in each of the adjacent streamtubes 4 and 6 were relatively large. By inspecting fig. 7.4, the 5th streamtube boundaries at cross-section 1 is much wider than the other streamtubes. This results from a relatively shallow, slow moving region of flow between the boundaries of streamtube 5. No provision had been made in the model for this large region of slow moving water in terms of increasing the time scale, (i.e. decreasing the eddy diffusivity) as had been done for the dead zone close to the right bank. Thus the eddy dispersivity was artificially too high in the fifth streamtube.

This effect implied that the size of the eddy dispersivity could be linked to the mean flow velocity. Therefore a model of the same form as NSCALE in the flume flow analysis was investigated, for which the velocity perturbations in the random walk scaled with the mean downstream velocity. However, the model could not be

calibrated so that it reproduced the data to within the estimated uncertainties. The main problem arose in the vicinity of the boundaries, and regions of sharp gradients in the downstream velocity gradient. Different approaches to handling the boundaries were investigated, such as having a minimum value for the effective dispersivity of the model. These trials were again unsuccessful, and this might be put down to the use of simple linear interpolations between the mean velocity measurements giving rise to the incorrect small-scale shear velocity gradients. The form of the shear velocity gradients strongly influence the dispersion, and in the absence of a more accurate mean velocity field, the modelling was continued using velocity perturbations which did not scale with the mean velocity.

The model predictions might be further improved by subdividing the channel into further sub-regions having different eddy dispersivities, but this was not carried out to avoid over parameterisation at the calibration stage. The modelling aimed to use the minimum amount of calibration under which was possible to collapse the measurement to within the estimated uncertainties, and this had already been achieved.

The three time constant model was therefore used, and was found to give a best fitting distribution to the measured mass fluxes for an $\mathbf{f}_v$ value of 1.1, which is shown in conjunction with the input and the estimated uncertainties in fig.8.4. This gave rise to an ensemble average transverse step size of : $\langle \mathbf{f}_v L_v \rangle = 0.08$m. The ensemble average time interval between steps was $\langle T \rangle = 1.6$s. The ensemble average effective eddy dispersivity coefficient of the model in the first sub-reach was therefore given by equation 8.5:

$$e_Y = \frac{3\langle f_V L_V \rangle^2}{\langle T \rangle} = 0.012 \pm 0.001 m^2 s^{-1} \qquad (8.5)$$

where the value quoted as an uncertainty has been estimated from the model sensitivity, using 8.4.

8.6 Optimisation of the multiplier on the transverse step size for the second sub-reach (cross-sections 1-6).

The model was expected to have a smaller effective transverse dispersivity coefficient in the second sub-reach since here the flow entered a riffle section where there were no obvious regions of flow separation or secondary circulation. The time steps between the random displacements were set at 0.6s, which was within the range of the characteristic time scales which had been determined from the turbulence measurements at cross-section 4. This was also the same as the time scale which had been used for the bulk of the flow in the first sub-reach in region B. Since there was not a transverse gradient in the turbulent time scales at cross-section 4, the time scale was held at this single value for the entire riffle section (the second sub reach). The multiplier, $\mathbf{f_V}$ was now optimised independently for the riffle section.

Fig. 8.5 shows that for a very small value of $\mathbf{f_V}$, the modelled mass flux distribution at cross-section 4 matches the measured distribution to within the estimated uncertainties. This implied that the tracer had almost completely mixed in the transverse direction by cross-section 1 and no further mixing was necessary to predict the distribution at cross-section 4. However, as $\mathbf{f_V}$ was increased from a small value,

the feature in the 5th streamtube, which was pointed out at cross-section 1, disappeared, showing the effects of increased mixing.

The maximum in the number of particles close to the left bank could not be reduced simply by increasing the $\mathbf{f}_V$ factor further. This suggested that there was an equilibrium in the number of particles which were entering and leaving the streamtube close to the left bank due to the zero flux boundary condition. The maximum was again a feature of the model, but complied with the measurements to within the uncertainties.

From inspection of fig. 8.5, the best fitting distribution corresponded to an fv value of 0.14, which gave rise to an average transverse step size of $<\mathbf{f}_V L_V> = 0.021$m. The best fitting distribution is given with the input and the estimated uncertainties in fig.8.6. The average time interval between steps was 0.79s, the model dispersivity coefficient was estimated to be:

$$e_Y = \frac{3\langle f_V L_V \rangle^2}{\langle T \rangle} = 0.0017 \pm 0.0002 m^2 s^{-1} \qquad (8.6)$$

8.7 Modelled mass fluxes for entire reach, and reach averaged transverse dispersion coefficient.

Fig. 8.7 show the modelled mass fluxes for the entire test reach for the fully calibrated model. The model predicts that the mass flux distribution remains well mixed following cross-section 4, although as described previously, no tracer concentrations were taken further downstream of cross-section 4 within the meander.

Fig. 8.8 gives a bi-linear interpolation of the modelled mass fluxes for the entire reach from the values which were saved at the measurement cross sections. Cross sections 5 and 6 are included in this plot, although there was no data available to compare with these distributions. However, the dye remained well mixed to within the 15% uncertainties which had been used between cross sections A1-4.

A reach averaged value of the transverse dispersivity coefficient was estimated from the values which were determined for the two sub-reaches. The sub-reach values were weighted according to the distances for which they applied to, given by equation 8.7:

$$e_y = \frac{24.6 \times (e_y)_{sub-reach1} + 66.6 \times (e_y)_{sub-reach2}}{(24.6 + 66.6)} = 0.0045 \pm 0.0003 \qquad (8.7)$$

where the uncertainty was estimated using standard error analysis of equation 8.7, using equation 8.8:

$$\overline{\Delta e_y}^2 = a^2 (\Delta e_y)^2_{sub-reach1} + b^2 (\Delta e_y)^2_{sub-reach2} \qquad (8.8)$$

where a = (24.6/91.2) and b = (66.6/91.2), which gave a 7% uncertainty in the reach averaged value of e_y.

8.8 Discussion of model dispersivity coefficient.

The $\mathbf{f_v}$ value was used as a multiplier to a length scale which had been estimated as being representative of the strength of the secondary currents in the first sub-reach, and was described in section 7.4.5. Since the calibrated $\mathbf{f_v}$ value was close to unity for the first sub-reach, the eddy dispersivity can already at this stage be said to be of the expected order of magnitude in the first sub-reach.

The estimations of the transverse dispersion coefficient for the two sub-reaches were now compared with values which have been determined on different rivers. The rivers included in table 8.8 were selected from previous investigations as having geometries and flow characteristics which were as close as possible to the reach on the River Lune.

Table 8.8 Summary of transverse dispersion characteristics from this study and from different studies on similar rivers.

River	sinuosity	width (m)	Q m^3/s	w/h	mean velocity m/s	u* (m/s)	e_y (m^2/s)	e_y/hu^*
Lune (A1-1)	1.4	10.2	0.35	34.0	0.12	0.036	0.012± 0.001	1.11±0 .09
Lune (1-4)	1.4	7.6	0.35	27.1	0.16	0.036	0.0017 ±.0002	0.17±0 .02
Lune reach	1.4	8.5	0.35	30.4	0.15	0.036	0.0045 ±.0003	0.45±0 .03
Beaver River/4	1.3	42.7	20.5	44.5	0.5	0.044	0.043	1.01
Kris-raba/1	mndr	10	8.0	9.4	0.8	0.069	0.011	0.16
Isere/5	mndr.	60-70	250	28.9	1.4	-	-	0.5-1.6
South River/3	1.0	18.3	-	7.3	0.18	0.040	.0046	0.26
Rea/2	1.0	6.7	0.75	37.2	0.73	0.075	0.004	0.24

where the references are:

/1 Symlyody(1977)

/2 Cotton and West (1980)

/3 Yotsukura and Cobb(1972)

/4 Beltoas(1980)

/5 Holley and Nerat(1984)

There have been very few investigations of the transverse dispersion coefficient for relatively shallow, sharply curved gravel bedded rivers such as the river Lune.

In a summary of previous literature, Fischer et al.(1979) concluded that for slowly meandering channels, the non-dimensional transverse dispersion coefficient lies between: $e_y/hu^* = 0.6 \pm 0.3$. It was also emphasised that sharp or rapid changes in channel geometry could give rise to higher values.

Rutherford (1994) similarly concluded for gently meandering rivers a value of: $0.3 < e_y/du^* < 0.9$, but that for more tightly curved channels, $1 < e_y/du^* < 3$, although no precise definition of curvature was given.

Beltoas (1980) gives a range of values having a larger mean dispersion coefficient of $0.4 < e_y/du^* < 2.5$. These values were mainly determined (with the exception of the Beaver River tabulated above) from channels over 100m wide, with large discharges.

The sinuosity (mean downstream distance divided by distance along the valley) or channel curvature clearly have a large effect on the values of the dispersion coefficient. The curvature leads to secondary currents which give rise to secondary advective mixing. Elhadi et al.(1984) examined the variation of e_y/du^* with width to depth ratio and sinuosity. e_y/du^* increased rapidly with sinuosity, but gradually decreased for large width to depth ratios.

That the transverse dispersion should change in the test reach of the River Lune is supported by detailed observations by Chang (1971) and Sayre and Yeh (1973) . These studies showed that e_y/du^* tends to vary periodically in the downstream direction, usually reaching a value of twice the average in the downstream portion of the bend and a minimum of about half the average in the upstream portion. In the River Lune a slightly larger value of e_y/du^* occurred at the upstream section than at the downstream section. This difference can be attributed to the particular geometry of the

Lune flow (the curvature was large between cross-section A1 and 1), and the observed distribution of the secondary currents, which have a large effect on the dispersion coefficient.

In summary, the estimated average dispersion coefficient for the reach falls within the range of values quoted by Fischer et al.(1979) and Rutherford(1994), for gently meandering rivers.

8.9 Comparison of the calibrated model with a simplified analytical solution.

The tracer concentration measurements at all of the measurement sites were required to calibrate the model by varying degrees. There was consequently no data set with which to test the model in a predictive sense. However, if a more simple input distribution was used, the predictions of the model could be compared with analytical solutions to the partial cumulative discharge equation (see section 1.3.5, equation 1.37) for the same input. This part of the study was only carried out for the first sub-reach, in which practically all of the tracer mixing had taken place.

The factor of diffusion (FOD - described in section 1.3.5) had to be assumed to have a constant value across the channel in order to use the analytical solution. From the preceding discussions, this is evidently a large approximation. The average value of the FOD for the first sub-reach, could nonetheless be estimated from using the calibrated particle tracking model to determine the ensemble average eddy diffusivity which was experienced by the particles. Having inserted the estimated average factor of diffusion into equations 1.38 and 1.39, for which the number of

image sources was set at 6 (recommended by Rutherford,1994), and non-dimensionalised the mass fluxes, the model output could be compared with the analytical solution for the same square wave input, shown in fig. 8.9.

The model prediction of the decrease in the relative height of the input maximum is supported by the analytical solution, although the maxima close to the left bank has not reduced by as much as for the random walk model. This is due to the the analytical solution relying upon a cross-sectional average transverse dispersivity, which is smaller than the large effective dispersivity coefficient close to the left bank in the random walk model. The random walk model also predicts that the mixing close to the right bank is poor, which is a reflection of the small, local effective dispersivity coefficient. It would again not be expected that the mixing be any less close to the right bank for the analytical solution, due to it using a constant, cross-section averaged effective dispersivity coefficient.

The analytical solution has therefore shown the expected behaviour, in that it is able to reproduce the overall mixing behaviour, but is unable to account for the smaller scale features to the mass flux distributions. The comparison of the random walk model results with the analytical solution helps confirm that the net diffusive (dispersive) behaviour of the random walk model, given its initial and boundary conditions, results in a similar net behaviour predicted by the analytical equations.

8.10 Summary and conclusions.

The random particle tracking, streamtube-based model, was able to be calibrated such that the particle distributions in regions of equal discharge matched the

relative tracer mass flux distributions to within the estimated experimental uncertainties. These uncertainties were large, but were not unreasonably large given the extent of the inhomogeneities which were prevalent in the system which was under study. The large uncertainties, however, give rise to a non-uniqueness in the type of model which can be used to collapse the data (for instance several different random walks based upon slightly different assumptions could be used to collapse the observed mass flux distributions to within the uncertainties). However, this appears to be an inescapable feature of investigations attempting to model complex environmental flows (based on the conclusions about equifinality of the results for different models, which were made following investigations on the flume flows). This property is discussed further in chapter 9.

The main difference between the river flow model which was developed here, and the models of the channel flows in earlier chapters, was that it had to account for the large scale inhomogeneities and non-uniform flow. The first characteristic was accounted for using a variable effective dispersivity coefficient, whilst the second characteristic was accounted for by the incorporation of streamtubes. The particles were advected in the downstream direction along streamlines which diverged or converged in accordance with the boundaries of regions of equal partial discharge (streamtubes).

It was found that the calibration of the model to give a fit to the data (to within the estimated uncertainties), was only possible if the effective transverse dispersivity coefficient was allowed to vary spatially in the transverse and downstream directions. This measure was supported by the variation in the measured turbulent time constants to a large degree, and by observations of strong secondary circulation. It was also

established from the tracing experiments that most of the mixing occurred within the first sub-reach, which was expected, since the curvature of the flow was the greatest in this region. This lead to the division of the test reach into two sub-reaches, for which the mixing behaviour was examined separately.

The effective transverse dispersivity coefficient of the model was estimated from the calibrated time step and displacement sizes, and its uncertainty was then estimated from a sensitivity analysis of these parameter values. The value of the estimated transverse dispersivity coefficients compared favourably with previous measurements on other rivers having similar features.

The limitations of the model, given the different approximations which were made in its construction (such as rescaling of velocities and flow depths, or linear interpolations between point measurements) and the relation of the modelled system to the actual system is discussed and expounded upon in chapter 9.

It is concluded that the model forms a robust, semi-empirical, but flexible tool in the investigation of the mixing characteristics of a complex environmental flow. The stochastic element of the random walk appears once more to be able to embody the effects which all the different scales of motion have on the tracer dispersion, to within the accuracy of the experiments, given a degree of empirical 'fitting' of variable, physical parameters.

Fig.8.1

Predicted mass fluxes at cross section 1 for different random seeds

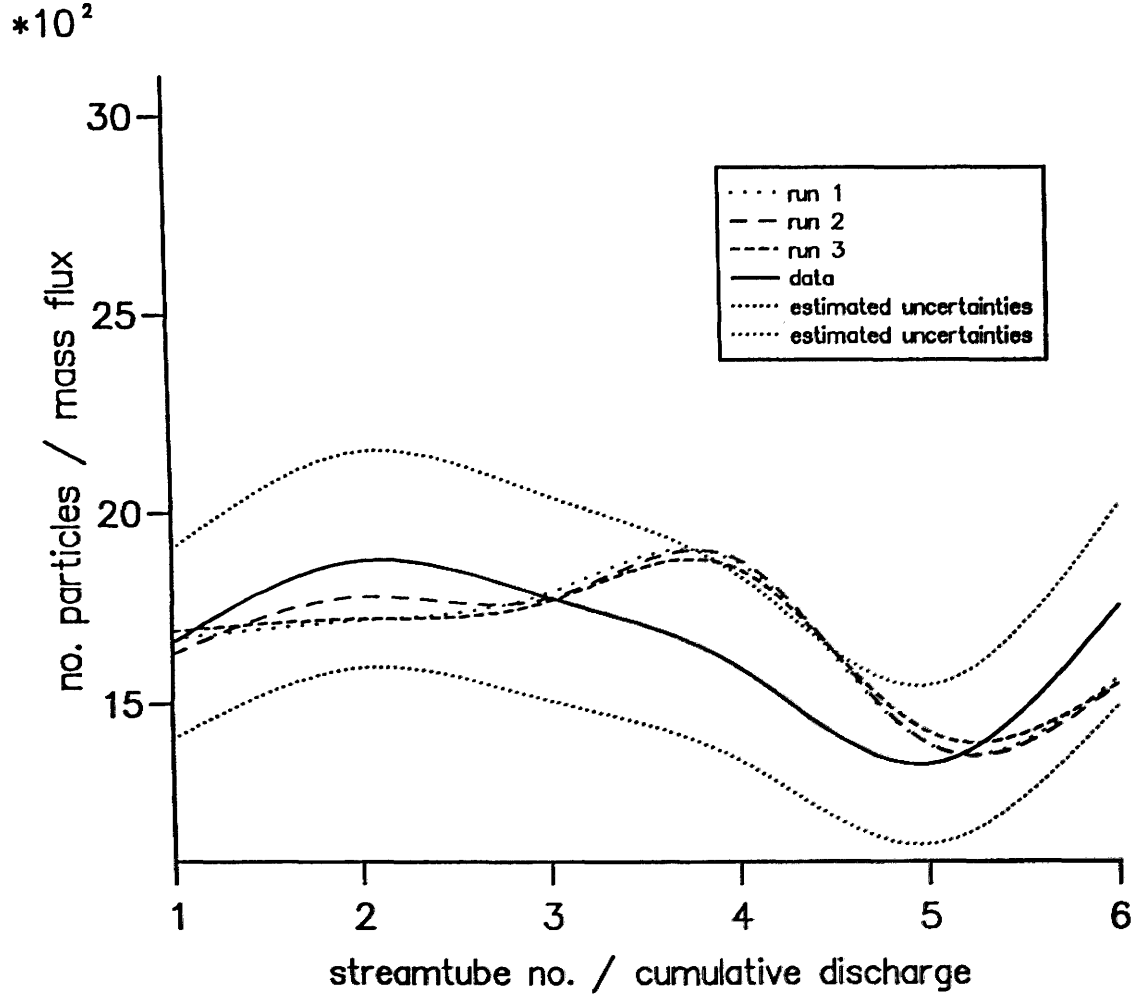

Fig.8.2

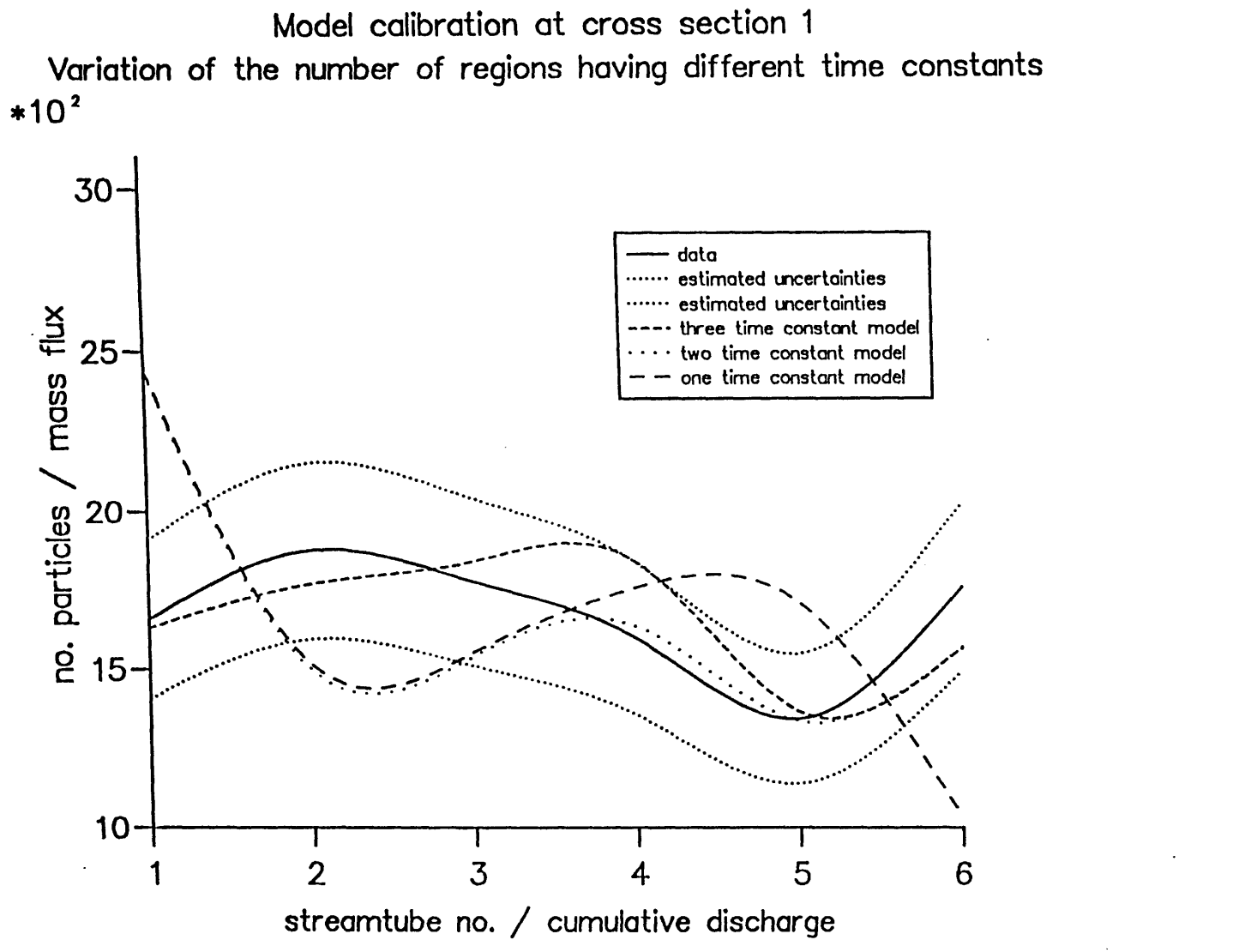
Model calibration at cross section 1
Variation of the number of regions having different time constants
*10²
30
25
20
15
10
no. particles / mass flux
1
2
3
4
5
6
streamtube no. / cumulative discharge
data
estimated uncertainties
estimated uncertainties
three time constant model
two time constant model
one time constant model

Fig.8.3

Predicted mass fluxes at cross section 1 for different values of the step size multiplier, fv (uncertainties omitted for clarity)

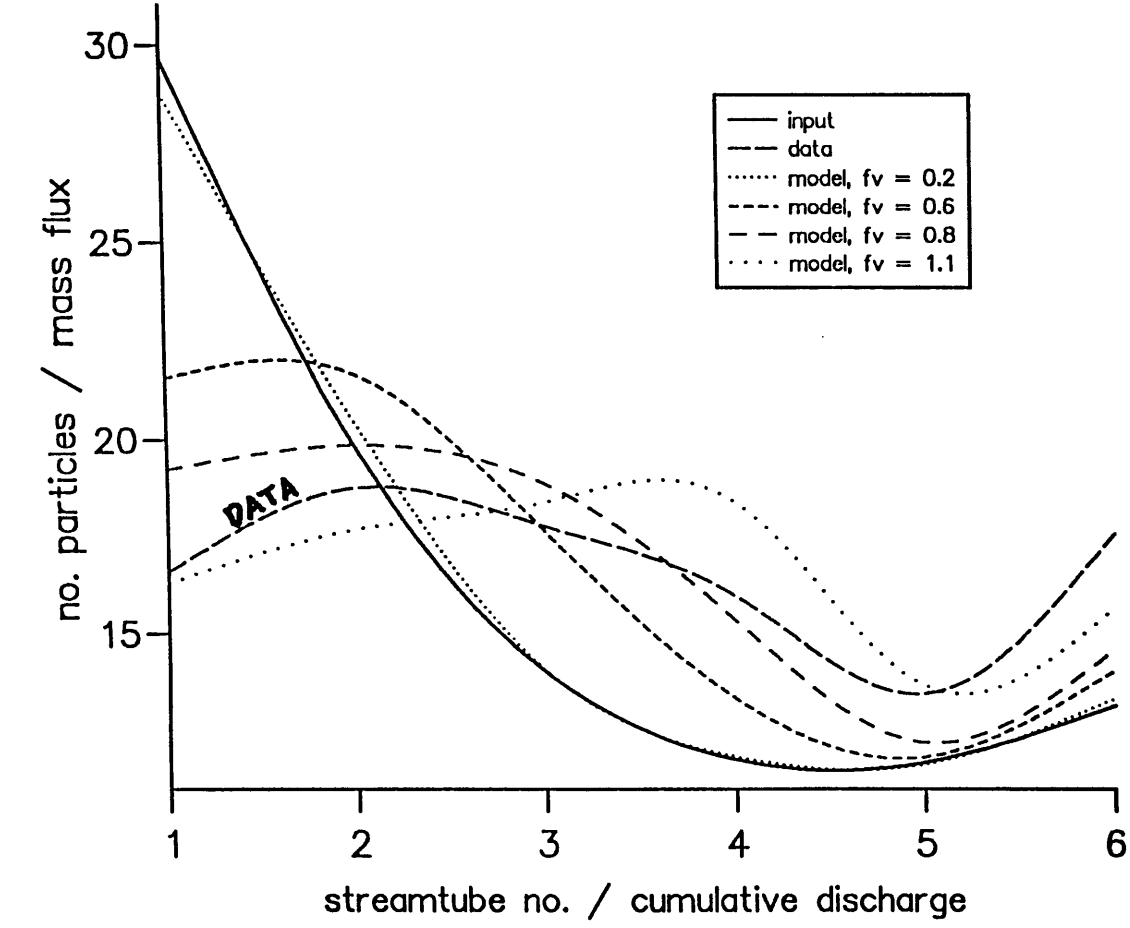

Fig.8.4

Mass flux distributions in the first sub–reach (A1–1)

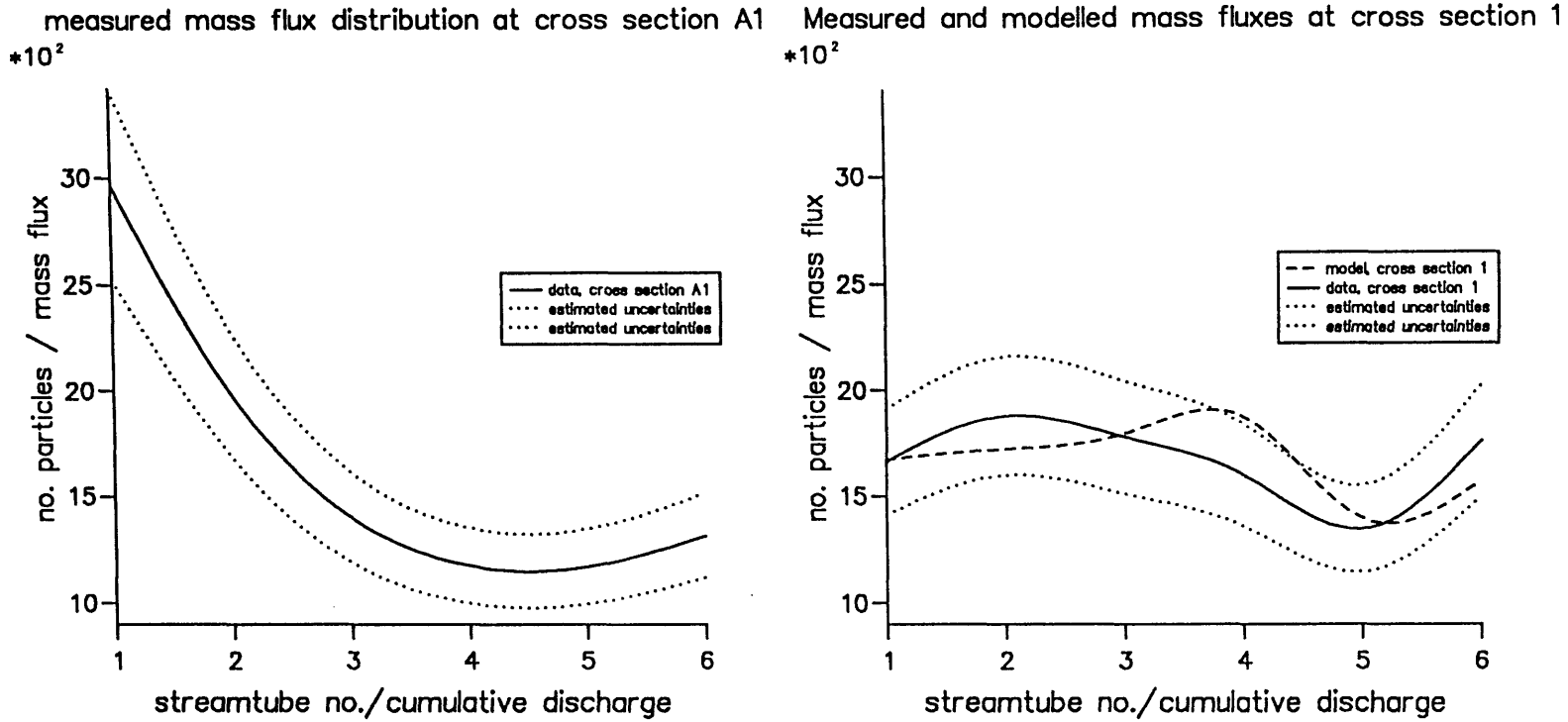

Fig.8.5

Model calibration at cross section 4
Response of the mass flux distribution to varying fv

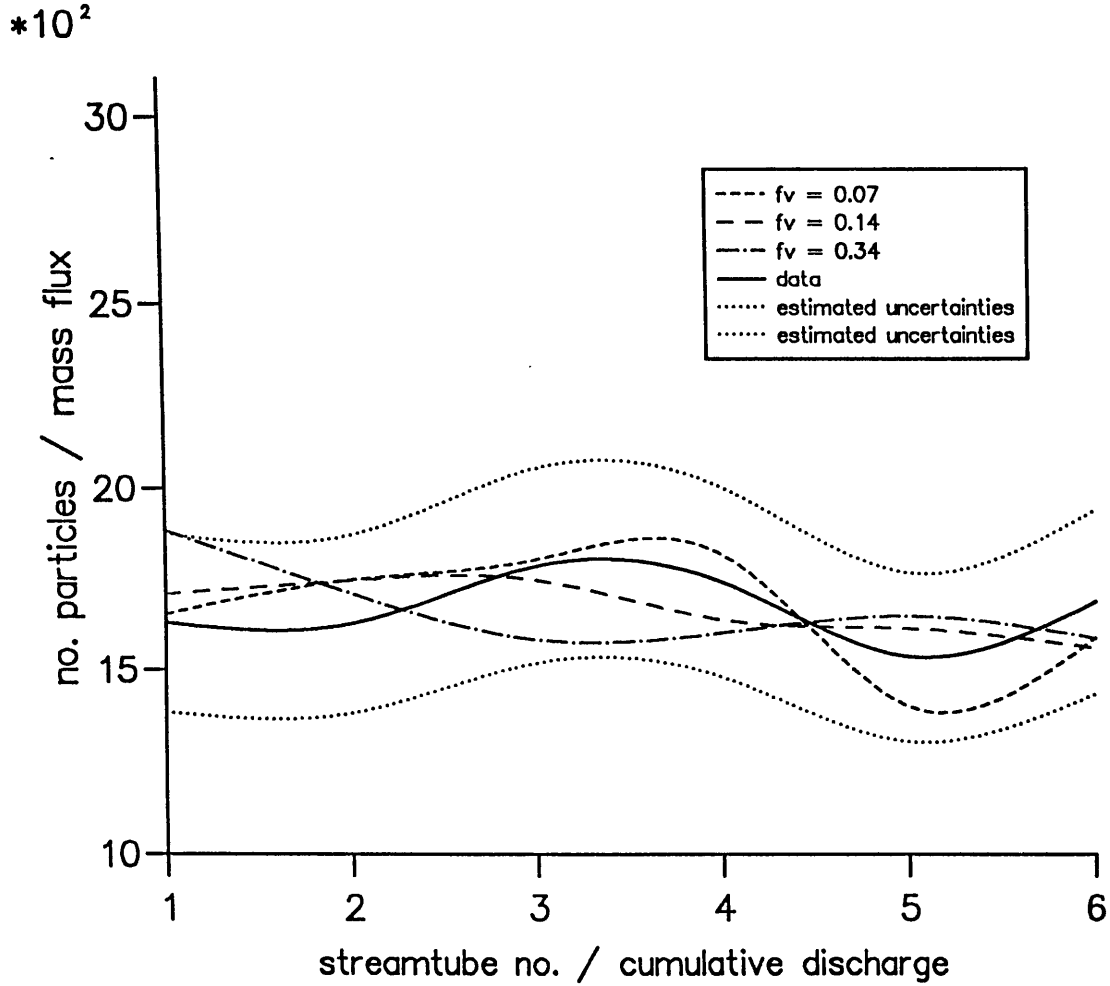

Fig.8.6

Measured and modelled mass flux distributions

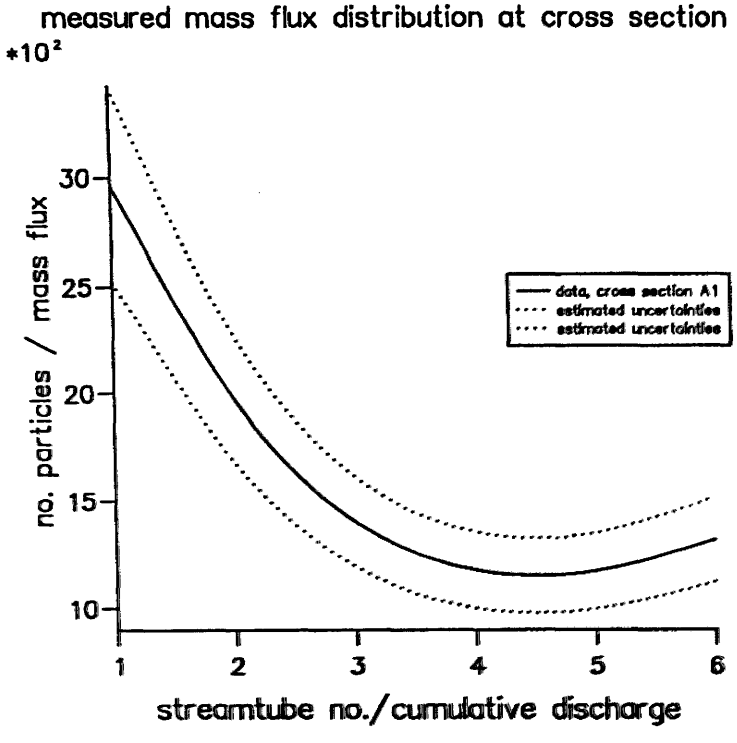

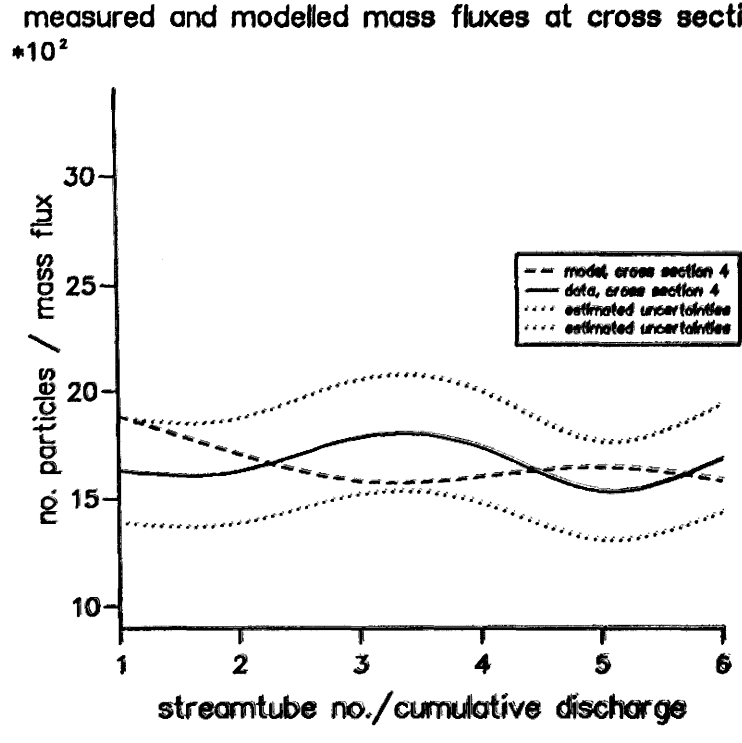

Fig. 8.7

Input and predicted mass flux distributions for X sections A1–4

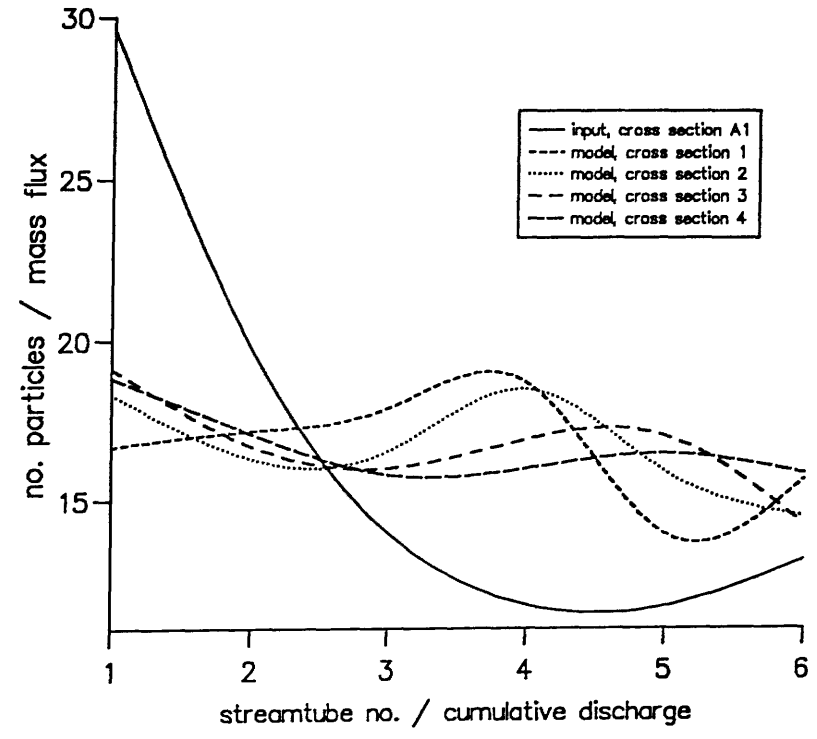

Fig.8.8

Interpolation of modelled mass fluxes for entire reach

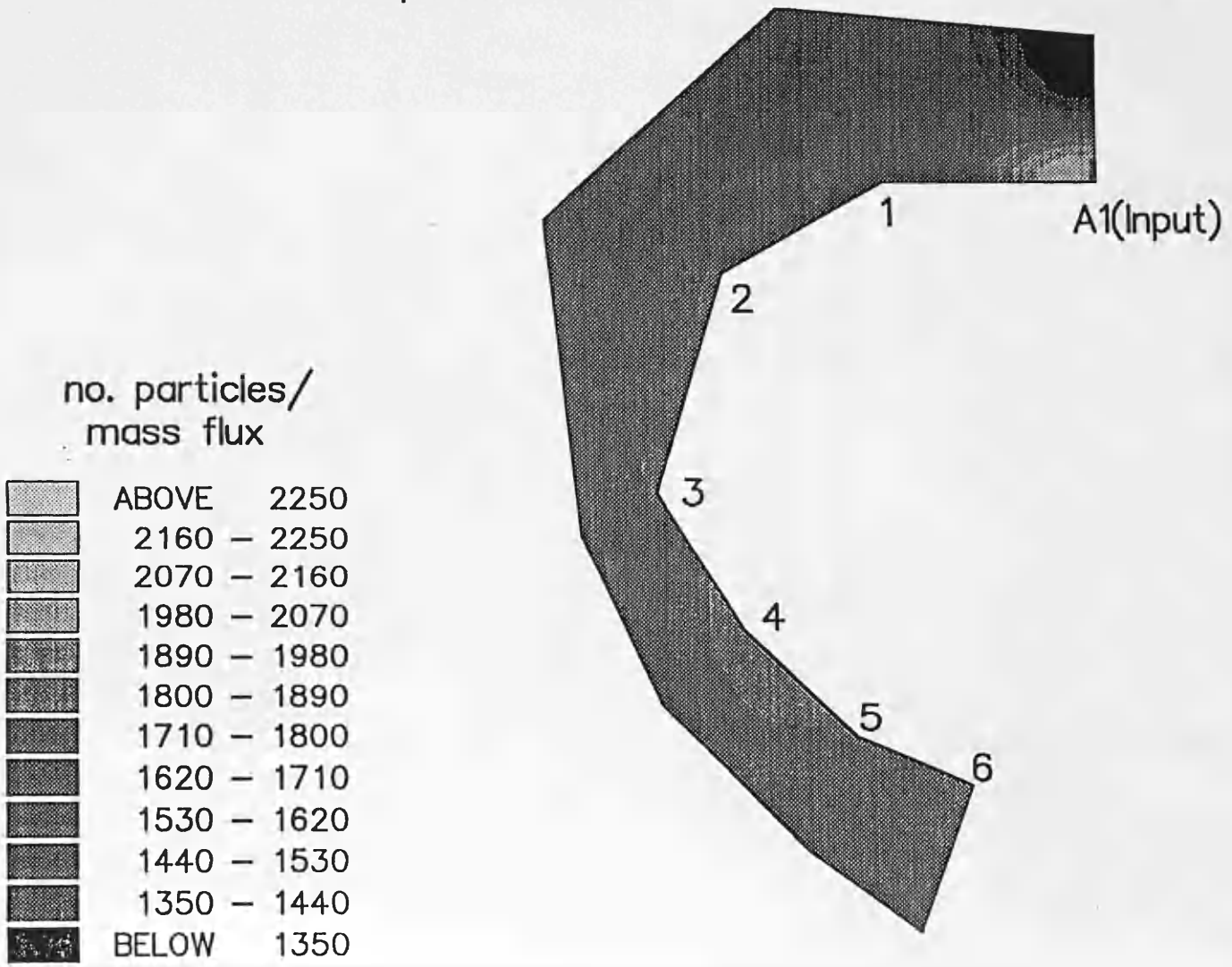

Fig.8.9

Solutions for the cumulative discharge diffusion equation for a square wave input to correspond with a similar input to the random particle tracking model, using the same factor of diffusion

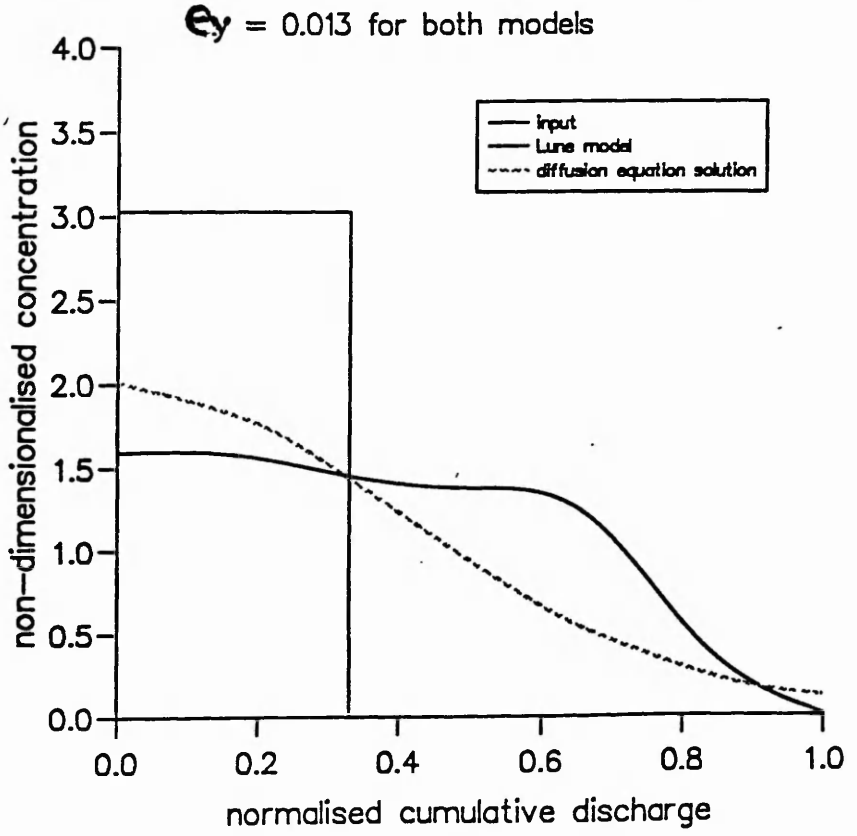

Chapter 9

Discussion, conclusions and suggestions for future work.

9.1 Introduction.

This chapter is a summary and discussion of the previous eight chapters with some suggestions for the direction in which the work might be continued. Section 9.2.1 crystallises the principal conclusions of the study, which the subsections (9.2.2 - 9.2.8) attempt to justify based on information from the previous eight chapters, and suggest possibilities for future work.

In section 9.3 suggestions for further research are given, which build on the success of the particle tracking technique in order to model momentum transfer in addition to mass transfer. Particle tracking models which allow for momentum transfer between particles (see for example Hoogerbrugge and Koelman, 1992) are suggested as being a credible alternative technique which could model the hydrodynamics of a flow in addition to the transport of a passive tracer by the flow. The desirability of such models is discussed with reference to other studies, and the construction of an algorithm and preliminary investigations are alluded to, as an indication of way in which such a model might be developed. Finally, section 9.4 summarises the principal conclusion of this thesis.

9.2 Discussion of chapters 1 to 8.

9.2.1 Principal conclusions.

In this study the dispersion characteristics of a passive pollutant in three different flows have been modelled on a semi-empirical basis using random walk particle tracking techniques. For the channel flows which were investigated, the macroscale dispersion characteristics of the particle distributions were found, in a sensitivity analysis, to be largely insensitive to the form of the fine structure (sub Lagrangian time scales) of the velocity perturbations, and the distributions from which the velocity perturbations were drawn.

The apparent equifinality of the predicted particle distributions for many of the models (especially for the in-bank flow case) arose because of their indistinguishability from the measured concentration distributions to within the estimated experimental uncertainties. This demonstrated an insensitivity of the current data set to discern which, if any, of the inferences about the velocity perturbations gave the best representation of the combined effects of the turbulence on the large scale tracer dispersion characteristics.

For all three flows, the collapse of the measured concentration distributions by the predicted particle distributions to within the estimated uncertainties leads to the conclusion that the random walk model appears to be able to embody the stochastic elements of these systems in such a way as to reproduce the net mixing characteristics of a tracer borne by such flows, to the accuracy afforded by the experiments. All this, despite the huge range of interacting, dynamically significant scales of motion, the

inhomogeneities, the anisotropies and, for the river flow, the rugged geometry which are all ubiquitous to complex natural flows.

9.2.2 Summary and further discussion of classical theory of fluid dynamics and tracer dispersion (chapter one).

The first chapter described aspects of the classical theory of fluid dynamics and tracer dynamics which were relevant to the study of tracer dispersion in turbulent flows, in order to provide a theoretical foundation to the following chapters. It was shown that the non-linear term was responsible for the interactions between all scales of dynamically significant motion in a turbulent flow. As the scale and Reynolds number of the flow of interest increases, so the number of degrees of freedom which must be modelled increases rapidly, and the computing power necessary to directly simulate all of these degrees of freedom, with all their interactions, boundary encounters and sensitivity to initial conditions, escalates way beyond the present computing capabilities for the kinds of flow which were examined in this thesis. If such computing power did become available, it would need to be accompanied by even better resolution measurements than those which have been described here, in order that the initial and boundary conditions could be specified with equal precision. Such measurements would be expensive and difficult to apply in the field, while the present study suggests that there is no guarantee that models with different behavioural aspects (such as the distribution of the velocity perturbations, or treatment of rough boundaries) would be resolved between on the basis of the data. For this reason the use of semi-empirical models which contain sufficient flexibility to cope with the

variability of conditions in an environmental flow is suggested as a promising approach in environmental flow modelling.

Direct numerical simulations and high order closure models of complex flows are highly desirable, and it is likely that these techniques will solve many engineering-flow problems in the near future, but the above conclusions suggest that the move towards higher and higher resolution models for the purpose of studying environmental flows, is unlikely to provide the entire solution.

9.2.3 Summary and further discussion of random walk theory (chapter two).

Chapter two introduced the concept of a random walk model as a simple and flexible alternative to conventional modelling techniques in studies of pollutant dispersion in turbulent flows. The random walk method can be used in the study of complex, inhomogeneous, high Reynolds number flows at all times, greater than the Lagrangian integral time scale, subsequent to the tracer release. This is not true of models which are based upon simple solutions to the Reynolds averaged advection diffusion equation, since the tracer must have been allowed sufficient time (the Taylor mixing period) to experience the entire transverse and vertical velocity field (for a uniform flow) before an average eddy diffusivity can be applied. More complex models of this sort, which allow for a spatially varying eddy diffusivity, require extensive calibration.

The simple, Lagrangian mode of application of the random walk is physically transparent, and is by definition exactly mass conserving, which is not necessarily the case with finite difference schemes, in which numerical errors may lead to violation of

conservation laws. Investigations in chapter 4 also suggests that there exists a simple linear relationship between the Lagrangian and Eulerian time averaged fluctuating velocity fields, for the relatively simple in-bank flow (although this flow was inhomogeneous and had a relatively large Reynolds number).

Since random walk models comprise repetitive tasks (application of the same rules to thousands of particles) they are suitable for parallel computing.

However, the form which the velocity perturbations in the random walk should take in order to best represent the motion of a passive tracer in an inhomogeneous flow-field is not known. For this reason the remainder of chapter 2 outlined a variety of random walk models which made different inferences as to the nature of the turbulent velocity perturbations. Some models for the in-bank flow included information from the measurements of the fluctuating velocity field, although this information was not available for the over-bank flow at the time of writing.

The different models attempted to account for the secondary advections (turbulence induced) which were known to be present in both flows, by the use of an effective eddy dispersivity. This lumped together the effects of dispersion due to both differential advection (caused by the secondary currents) and the diffusive behaviour of turbulence. Observations in chapter 4 suggest that, in the case of the over-bank flow, the drift in the centroids of the particle distributions, which was not observed in the centroid of the concentration distributions, were due to the combined effect of the asymmetric flow field, and the secondary circulations. Such a combination is frequently present in natural flows, although the asymmetry causing the drift in one direction, would more likely be balanced on average by a similar drift in the opposite direction, perhaps at a different depth or downstream distance, making the large-scale behaviour

stochastic and therefore more suitable to be modelled using a random walk. It would be an important part of future work to investigate this drift using random walk models which included secondary circulation.

However, the core investigation was into the sensitivity of the macroscale dispersion characteristics to the form of the velocity perturbations which were applied at the particle scale, and this was undertaken in chapter 4.

9.2.4 Summary and further discussion of the Flood Channel Facility flow and concentration measurements (chapter three).

The overall structure of this entire thesis, which concentrated initially on laboratory experiments and advanced to a complex environmental system, follows the same structure which is used in many studies of environmental systems, but because of scale effects associated with the dispersion process in complex flows, it was imperative that the laboratory flow was as large as possible in order that it be compatible with the river flow. These scaling effects render many tracer experiment sets inapplicable to this study because of their small scale.

Chapter 3 described the relatively large scale channel flows for which detailed sets of hydrodynamic and tracer concentration data were collected. The relatively high resolution measurements of velocity and concentration fields formed a good standard by which to carry out a sensitivity analysis of the different random walk models.

The study of two different flows at this stage of the analysis allowed the flexibility of the random walk model to be tested, although further flume studies,

especially meandering channel flows, would provide useful additional information under controlled conditions. The step in complexity which was made, in going from the study of the overbank flow to a complex environmental flow, could in this way be reduced. However, the course of the research was controlled by the data which was available at the time of writing, and the time restrictions of the research.

9.2.5 Summary and further discussion of chapter four.

The conclusions made in section 9.2.1 above are largely drawn from the observations which were made in chapter 4. The conclusions to be made about the different random walk models on an individual basis were discussed in chapter 4, but perhaps the most important observations come from viewing the modelling results collectively, for each flow.

Many of the random walk models were calibrated such that the particle distributions fitted the measured concentration distributions to within the estimated uncertainties for both of the channel flows. This demonstrates the flexibility of each individual model, but also it already indicates a certain degree of equality between all of the models. There are three main observations to make at this stage; firstly, given that some of the models incorporate finer structure (such as autocorrelations or cross-correlations) than the simple random walk (JUMP), and that this model is just as successful as its counterparts, there appears to be a redundancy in the incorporation of the additional information. Secondly, since the inclusion of the finer scale structure did not generally produce adverse effects on the models' mixing characteristics, these could be incorporated in more complex models which require more detailed knowledge

of the particle motion, such as sediment transport models. Thirdly, some of the models are based on different fluctuating velocity distributions (for example Gaussian as oppose to Gamma) and the resulting macroscale particle distributions are indistinguishable in terms of their closeness of fit to the data, since they lie within the uncertainty bounds of the data. This last observation might be expected, given that via the Central Limit Theorem, which states that in the limiting case, the trajectories of many particles undergoing random perturbations taken from any continuous distribution, approach a Gaussian distribution. However, this is only the case if the particles are undergoing random walks within a homogeneous medium. If the inhomogeneous velocity field is taken into account, then given two models for which, at each step the perturbation to the particle velocity is taken from different distributions, then there are no longer any physical grounds to suggest a collapse of the same ensemble trajectory for the two types of velocity distribution. Indeed, for the in-bank flow, the model TURJ2 accounts for the inhomogeneous velocity field, and yet there are no discernibly different facets to the macroscale dispersion characteristics (to within the accuracy of the experiment) of this model as compared with other models which do not account for the inhomogeneity.

Although the reasoning in the above arguments is well founded in terms of the physics, it must be borne in mind that none of the models presented here represent the true trajectories of the fluid elements. This is an obvious observation for the simple random walk model, such as JUMP, since it cannot possibly account for the inhomogeneities, (work by Sawford and Borgas,1993, showed that this kind of model was inconsistent with Kolmogorov scaling theory for homogeneous turbulence) but it is also true of the more complex models such as the random walks based on a Markov

sequence. A property of a Markov sequence is that although it is continuous in time, it is based upon an incremental equation (the Langevin equation) which is non-differentiable. Since the completely random part to the equation is instantaneous, in reality the equation would imply infinite accelerations (Legg and Raupach, 1985). Moreover, the Gaussian distributions used to model the distributions of the fluctuations were modelled without any degree of skewness, which is a necessary condition for the transfer of energy between scales (Legg and Raupach, 1985). However, the model would no longer be a Markov sequence if the fluctuations were taken from a non-Gaussian distribution (Sawford, 1985). It is therefore reasserted that the aim of these studies was not to search for the exact physical representation of the velocity perturbations at the individual fluid element scale, but more pragmatically, it was to search for the best representation of the velocity perturbations in the model which lead to the same macroscale distributions which were observed. Such an assertion has been made by many workers (for example Tampieri et al., 1992 ; Sawford, 1985).

Moving on to the stage of the research where the models were used to examine the evolution of the depth-averaged spread of the modelled tracer cloud with downstream distance, many of the models showed the same characteristically shaped curve, which if shifted along the ordinate, collapses to almost the same relationship. It is this behaviour which has essentially lead to the conclusions of equifinality in section 9.2.1. These conclusions were consolidated in the remainder of the sensitivity analysis, in which the predicted and measured concentration distributions were shown to be in agreement for most of the models of the in-bank flow and several of the models for the overbank flow at the furthest measurement site downstream.

The equifinality of these results would no doubt eventually be removed if more and more accurate measurements were made, and this would help to elucidate several points. Firstly, it would establish which of the models used the best representation of the turbulent velocity perturbations. Secondly, it would help to define the limits of the applicability of the different random walk models, so that unsuccessful ones could be eliminated. However, unless in the hypothetical case, the measurements were free from uncertainty, an infinite variety of assumptions which might be made about the form of the velocity perturbations would need to be examined before conclusions could be drawn about the universality of the random walk models in general. This assertion can only be made in the absence of a complete analytical understanding of the Lagrangian statistics of an inhomogeneous, anisotropic turbulent flow field, which was not known at the time of writing.

9.2.6 Summary and further discussion of the field measurements on a reach of the River Lune (chapter five).

At the commencement of this study, an upland gravel bedded-river flow was chosen in preference to, for example, a mildly inhomogeneous lowland river flow, in order to test the feasibility of the application of the particle tracking model to a complex situation. This is an extension of a general aim of environmental system modelling, in which the behaviour of the complete system is examined, rather than breaking it down into simpler blocks, the behaviour of which can be examined in more detail. The interactions between all of the different flow processes in the most complex flow combine together to give a net behaviour which is different from the behaviour

which would result if all of the different processes were isolated, and their individual effects were combined together.

The field studies which were reported in chapter five provided sufficient information with which to construct the particle-tracking dispersion model, which was described in later chapters. The acquisition of such information was not without mishap, and the problems which were encountered are summarised here, as an example of the difficulty involved in such studies of environmental systems. The three basic sets of measurements of velocity, turbulence and dye-tracer concentration each had problems associated with them, besides the logistical problems associated with taking the measuring equipment to the site. The velocity meters were originally calibrated incorrectly, (due to an incorrectly calibrated test flume) and later all had to be recalibrated. The turbulence meters were found to have larger offsets (by an order of magnitude) than expected, and a slight drift. The pump which drew water into the sample chamber of the fluorometer broke on one occasion and after repair it had a slightly different discharge. Several other tracer experiments (unreported) were carried out for the same reach, although these resulted in incomplete data sets.

Apart from the continuous geomorphologic changes to the river bed and banks, which were occurring over the duration of the study, a somewhat catastrophic landslide also took place between cross sections 4 and 6. Such events might be avoided in future experiments by carrying out all of the measurements in as short a period as possible. This was hindered to a large extent by the structure of this whole piece of research, since the model and the fieldwork were developed in tandem. Future investigations would have the benefit of the model having already been developed.

9.2.7 Summary and further discussion of the analysis of the field measurements (chapter six).

The analysis of the velocity, turbulence and concentration measurements in chapter 6 centred around the estimation of uncertainties. This was clearly important given the complexity of the system understudy, and these uncertainties ultimately set the bounds to the accuracy of the modelling work. The uncertainties in the flow observables were generally larger (by a factor of ~ 2) than their equivalent in the flume studies. In part, this was due to the measurements on the river being less spatially intense, but the extent of the inhomogeneities in the natural flow, as oppose to the controlled engineering-flow probably had the greater influence. The uncertainties in the measurements of observables in the river flow could be reduced further by a yet more intense field campaign, involving repetition of measurements wherever possible. In particular, the depth-wise concentration measurements (especially at the first cross section, A1) were found to be critical to the estimation of the total mass flux.

Additional future experimentation could include an analysis of the secondary velocity measurement technique. The vector addition technique which was used to measure the secondary flows in this study, could be compared with direct measurements made using the two-channel E.C.M. at different sites in the river.

9.2.8 Summary and further discussion of the construction and the sensitivity analyses of the different random walk models applied to the reach of the River Lune (chapters seven and eight).

Chapter 7 described the construction of the computer model of the flow and dispersion characteristics in the reach, based on the analysed data. Essentially, this comprised interpolation between measurement sites of depths, distances and velocities. Some of the data was collected for flows with different stages, which requires further interpolation or rescaling. These rescalings represent further approximations, but also made the model more flexible for future work, such as the analysis of different stage flows.

The model reproduced the measured relative mass flux distributions of the tracer to within the estimated experimental uncertainties, and was therefore successful to within the accuracy of the experiment. Classically, there is a problem with this conclusion, since the solution provided by the particle tracking model is non-unique. For example, many different random walk models, based on slightly different assumptions about the nature of the velocity perturbations, could be used to reproduce the observed behaviour to within the large uncertainties. The non-uniqueness problem could be investigated by testing the different models against consistency criteria. For example, the models could be tested against another data set from a different tracer experiment. To some extent, such testing was carried out in the models of the flume flows, although these flows were less complex. However, it was evident, even under these relatively high resolution measurements in the flume, that a non-uniqueness or

equifinality between models existed. Logistically, it would be difficult to carry out measurements on the river with the same accuracy as in the flume, let alone even more accurate measurements, which the results of this study suggest are required to distinguish between the macroscale behaviour of different models. However, although the non-uniqueness property is undesirable in a physical model, it appears to be characteristic in modelling environmental systems subject to uncertainty in observations and boundary conditions. Some of the empirical models developed here have been shown to give the correct macroscale dispersion behaviour to within experimental accuracy. Other models which were investigated which did not collapse the data to within the uncertainties have also been rejected.

The uncertainties in the mass fluxes were carefully estimated once again in chapters 7 and 8. Although these were derived from the propagation of experimental measurement errors in the flow observables, no account was directly taken of random or systematic errors which can be attributed to the approximation of the model 'architecture'(geometry and structure) to the real system. This type of error was estimated during different parts of the model construction (for examples, in the construction of the streamtube boundaries or in the approximation to the curvature in the downstream direction), and was minimised as far as possible, so that it was smaller than the uncertainties in the measurements of the different flow observables. In this way, the uncertainties which were estimated for the modelled flow observables were considered to be of at least the correct order. However, it is recognised that there could be systematic dependencies of uncertainties in the modelled flow observables with the model architecture, which could give rise to an underestimation of the error associated with the modelled flow observables. This could be investigated to some

extent, if the model was used on different data sets, and it consistently reproduced the mass flux distributions to within the estimated uncertainties. There could also be dependencies of the physically based parameters (such as the lengths of the random displacements and the time intervals between them) on the particular flow conditions. This could also be investigated to some extent, if the model was used on detailed data sets for different flows within the same reach, and it consistently reproduced the mass flux distributions to within the estimated uncertainties.

In the final analysis, the transverse dispersivity coefficient for the second sub-reach was estimated as being approximately the same as that for the first sub-reach. In this case, it might be asserted that the model could have been used in a more predictive sense for the second sub-reach, rather than carrying out further calibration. However, despite the similar sizes of the coefficients of dispersivity for the two sub-reaches, these are derived from a combination of length and time scales within each sub-reach. The relatively short time scales in the second sub-reach were representative of the behavioural aspect of the flow in this riffle section, whereas the longer time scales in the first sub-reach were synonymous with the presence of the slow moving 'deadzone' near to the right bank. The similarity in the sizes of the transverse dispersivity coefficients, might be explained by the presence of relatively strong turbulent mixing (and weak secondary advective mixing) in the riffle section, off-setting the relatively strong secondary advective mixing (and weak turbulent mixing) in the pool section.

The use of streamtubes, and mass flux distribution analysis in the river modelling work was suggested as an essential prerequisite to the use of random particle tracking models in systems with non-uniform geometry and flow. This also has

the advantage that the model results can be cross-validated to some extent using solutions to the streamtube or partial cumulative discharge diffusion equation.

The success of the model in reproducing the observed macroscale dispersion characteristics to within the accuracy of the experiment, and with regard for the differences between the natural and modelled system, consolidates the conclusions which were made in section 9.2.1. The statement that the combined effect of the huge range of dynamically significant scales of motion embodied by the Navier-Stokes equation on the macroscale dispersion characteristics of a passive tracer can be modelled using the relatively simple random walk model, can only be made for the macroscale, which has not yet been strictly defined for the river flow. Given that the largest scales of motion which are important to transverse mixing are due to the secondary currents, and since the effect of these have been lumped into the model's effective dispersivity coefficient, it is reasonable to assume that these scales define an absolute minimum to the macroscale. Given that the decorrelation time scale in the transverse direction, T_2 which was measured by the two-channel E.C.M. was on average ~1.2 seconds (reach averaged value from measurements), then a length scale associated with the downstream direction can be estimated from the dimensional construct, [$\langle U \rangle T_2$] , where $\langle U \rangle$ is the ensemble average downstream velocity ($\langle U \rangle$ ~ $0.25 ms^{-1}$). This gives approximately 0.3m as the minimum downstream length scale. The enhanced mixing of the tracer due to secondary circulation is essentially being modelled as a stochastic process, so for statistical stability in the result, at least 10 times this minimum length scale gives a representative resolution of approximately 3m, defining the order of magnitude of the macroscale discussed above. This length scale is smaller, by a factor of 3-4, than the resolution at which the mass fluxes were examined

in the downstream direction in this experiment. It also implies, that should the experiment be repeated with more spatially intensive measurements, then it should not be expected that the random walk models could reproduce facets in the measured concentration (mass flux) distributions to a smaller scale than ~3m.

9.3 Suggestions for extension of current work.

The above conclusion about the random walk, particle tracking model's ability to model the macroscale mixing characteristics of a passive tracer, also raises the question as to whether it would be possible to model the net effects of momenta transfer between 'fluid elements' in order to model the hydrodynamics as well as the tracer dispersion using random walk techniques. The modelled tracer particle motion is a representation of a marked fluid element in turbulent motion, and since each element carries momentum as well as mass, it would seem a natural step forward to include the transport and exchange of momentum in particle tracking models of environmental flows. This would hopefully provide a more satisfactory description of the mean, as well as the fluctuating velocity field, than the linear interpolation methods which were used in the current model. The linear interpolations cannot properly account for the inhomogeneities which are present at smaller scales than the resolution of the measurements.

In the Reynolds averaged advection diffusion equation, the mass transfer corresponding to terms such as $\overline{u'_i c'_j}$, are modelled using an eddy diffusivity, which relates this product to the mean concentration gradient. Similarly, in low order (up to second order) closure models of the RNS equations, the momentum transfer

corresponding to terms such as $\overline{u'_i u'_j}$, is again generally related via the gradient flux hypothesis, to the mean velocity gradient. Both forms of transport can equivalently be modelled using random walk models, and the following section explores the concept of a momentum transport model.

9.3.1 Towards a particle tracking model of flow in a natural channel.

The concept of a particle tracking, momenta exchange model comes from a larger class of models which are generally termed particle-particle (PP) models, which are generally used to solve many-body problems (Zannetti, 1990b). The motion of systems comprising three or more interacting particles, despite their being governed by the relatively simplistic Newtonian laws of motion (dealing with systems neither subject to quantum, nor relativistic effects), cannot generally be determined analytically, due to the non-linearity of the interactions. However, in PP models, the combination of the forces acting on any one particle (whether the forces be gravitational, electrostatic, etc.) within a system of particles can be evaluated instantaneously from the relative positions of all the other particles, and the resulting motion of each particle can then be evaluated by the integration of Newton's second law of motion, given by equation 9.1 (see Sugimoto, 1993):

$$u_j = \int_0^t \sum_{i=1}^{N-1} \frac{F_i}{m} dt \qquad (9.1)$$

where u_j is the velocity of particle j, and there are (N-1) particles of mass m, exerting a force F_i on particle j. The integral is then approximated by a summation over the accelerations between a discrete time step Δt in practice.

Such models find useful application in areas such as planetary physics, vortex dynamics and molecular dynamics. The models of many particle systems are by their nature multiple task-orientated, and lend themselves well to parallel computing. Further, task specific computer chips have been designed (Sugimoto, 1993), with the sole purpose of evaluating the force between two particles, given the particle separation. This type of technology reduces the cost of making such calculations, and makes research into PP models more feasible.

Returning specifically to fluid motion, there are many ways of building microscale models which lead to a given set of continuum equations, such as the Navier-Stokes equations (Frisch et al., 1986). The macroscopic motion of a fluid can theoretically be modelled from the interactions between particles at the molecular scale, for which the inter-particle forces of attraction due to electromagnetic and nuclear forces are well understood (Rapaport and Clementi , 1986), and all that is required to study the macroscale fluid motion are a sufficient number of modelled particles. However, such models require many thousands of particles to even model a few thousand atomic distances (Rapaport and Clementi used 100000 particles to model a flow of dimension 1000 Å), and the relative motions are updated with a time step which is ~ 1/100th of the average time it takes for a particle to travel a distance the length of the mean free path. In the above study, turbulent like structures such as eddies and periodic eddy shedding were observed around a cylindrical object in the flow field. However, there is little chance in the near future of scaling up the

computing power necessary to model flows on an environmental scale using molecular dynamics.

A different approach to building up macroscale flow from microscale interactions was taken by Frisch et al.(1986), with a lattice-gas automata model. Models of this sort have a completely discretised phase space, and are based around particle motion along a regular lattice, for which the time interval between interactions is compatible with the time it takes the particles to travel the mean free path length. The particles interact at the nodes of the lattice space, in accordance with semi-heuristic rules which conserve angular and linear momentum. Frisch et al.'s model, which was based on a 2d hexagonal lattice, was found to be consistent with the Navier-Stokes equations in the continuum limit (under low Mach numbers). Such models can be used to study flows having a Reynolds numbers which is limited by the ratio of the overall lattice size to the to the spacing in the lattice. However, it is difficult to envisage how inhomogeneous or anisotropic media could be represented using this framework. Further, the more complicated features that are added to the flow, the number of possible states which can occur per node increases dramatically, making an extension to complex flows difficult (Hoogerbrugge and Keolman, 1992)

Finally the most promising approach relevant to the kind of flow modelling investigated in this study, is a combination of the two models described above, which incorporated the flexibility of the grid-free molecular dynamics method, and the larger scales of motion represented by the particles in the lattice gas automata model.

This approach was used recently by Hoogerbrugge and Keolman (1992), whereby particles which are representative of fluid elements exchange momenta in accordance with physically based rules. Essentially, in Hoogerbrugge and Keolman's

model, the particle interaction (or exchange of momenta) comprised two parts, a 'damping term', dependent on the relative momenta of the interacting particles, and a 'heating up' term, which was a noise component. These two terms represent the effects of viscosity and pressure fluctuations, respectively. Both of these terms were weighted with a non-dimensional weighting function, which was dependent on the particles' separation.

These authors found that with relatively few particles, the average coarse grained dynamics of the particles were at a first approximation concordant with the Navier-Stokes equations. Further, the one particle velocity distribution over time demonstrated a Maxwell/Boltzman distribution, and the equations of state for pressure was closely matched for particle number densities (defined by N_i/r_c, where N_i is the number of particles in the system, and r_c is the distance over which particles can interact). The model also gave a constant viscosity similar to that of a Newtonian fluid. Moreover, for the specific case of flow around a cylinder in a rectangular duct, the model was shown to be able to reproduce the drag force on the cylinder in accordance with measurements.

These observations are promising for the future application of PP models to the modelling of environmental flows. Towards the end of this piece of research one such PP model was investigated, and some of the problems encountered during the short investigation are outlined below.

9.3.2 Some preliminary investigations into Particle Particle models: a suggestion for the direction of future work.

A simple PP algorithm was constructed on a parallel transputer system, in which thousands of particles exchanged momentum with each other and the bed in an (invented) open channel flow. The momentum exchange rules were derived from the shear stresses associated with a logarithmic vertical velocity profile, incorporating an eddy viscosity based on Prandtl's mixing length theory. These interactions were made proportional to local flow parameters, such as the positions and velocities of local particles. The precise form of the discretised interactions were not known, and the strength of the interactions was varied with the use of variable parameters which were multipliers to the interaction strength. These parameters were adjusted until the perturbations to the particle velocities at each time step were of the correct order of magnitude (of the order u*, for example, see Zannetti,1990b). A similar process was carried out for particles interacting with the bed. The discontinuity in the velocity gradient at the water surface was attempted to be accounted for through the use of image particles which exerted an equal and opposite force on particles close to the surface, to that which was exerted on them from particles below. The vertical velocity distribution was then investigated following many interactions (time steps).

These preliminary investigations indicated that the stability of the logarithmic distribution was sensitive to the form of the boundary interactions at the bed and at the surface, and that these require further investigation before the equilibrium state can be maintained for a long period of time.

The research aimed primarily to demonstrate that a simple macroscale (logarithmic) velocity distribution and an energy balance could be maintained by particles which exchange momenta in accordance with rules which are functions *only* of local flow variables. If this could be achieved, then given the initial and boundary flow conditions, the particles could be made to 'self assemble' into the correct macroscale distribution, following an adjustment period. If these interaction rules could then be shown to give stability for a variety of conditions, then the PP model would be a useful tool in the investigation of both the hydrodynamics and tracer dispersion in complex environmental flows.

9.4 Summary.

This chapter has discussed the conclusions which can be drawn from the studies of the random walk, particle tracking technique in the first eight chapters. It has been demonstrated that the a simple, flexible and semi-empirical approach to tracer dispersion modelling can be effective in the understanding of the mixing characteristics of a complex environmental flow. Further, an extension to of the use of particle tracking techniques has been suggested as a promising area of research in the modelling of the hydrodynamics of environmental flows.

This thesis has worked towards the development of a set of flexible computer modelling techniques that would allow the prediction (especially near and mid-field) of flow and transport of solutes in natural channels of complex geometry. These techniques, while partially empirical in nature, and allowing for equifinality in the

underlying description, have the potential to reflect the large scale flow structures such as 'deadzones', and secondary currents that are so important to the mixing characteristics in real (rather than laboratory) channels, and to do so in a computationally feasible way.

List of references

Acheson, D.J. 'Elementary Fluid dynamics', Clarendon Press, Oxford (1990).

Allen,C.M. , 'Numerical simulation of contaminant dispersion in estuary flows ' , Proc. R.Soc.Lond. A381 179-194 , 1982.

Allen,C.M. , 'Particle tracking models for pollutant dispersion' , Computing in the environment , 1992.

Anwar, H.O. 'A study of the turbulent structure in a river bend', Rept. no. IT 296, Hydraulics Research, Wallingford, 1985.

Bathurst, J.C. , Thorne,C.R. , Hey, R.D. 'Secondary flow and shear stress at river bends', Jn. Hydr. Div. ,p.1277, 1979

Beltoas, S, 'Transverse mixing tests in natural streams' Am. Soc. Civ. Eng.,106, 1980.

Bencala, K.E. and Walters, R.A. 'Simulation of solute transport in a mountain pool-and-riffle stream: a transient storage model', Wat. Resour. Res. vol 19 no.3. 1983.

Bencala, K.E., Kennedy, V.C. , 'Zellweger, G.W., Jackman, A.P., Avonzino, R.J. 'Interactions of solutes and stream bed sediment 1: An experimental analysis of cation and anion transport in a mountain stream.' vol 20 no.12 1984.

Bergeron,N.E. and Abrahams,D. ,'Estimating shear velocity and roughness length from velocity profiles', Water Resour. Res., 28, no.8 1992.

Bowles, R. 'Mathematical modelling, solutions and limitations', Procs. 'C.F.D. supercomputing and visualisation', University of London Computer centre, 8/7/94.

Bridge, J.S. and Jarvis, J , 'Flow and sedimentary processes in the meandering river South Esk, Glen Clova, Scotland' , Earth Surface Processes, vol 1 ,1976.

Brockie, N , Random Walk Modelling progress report ; Lancaster University internal report ; March 1991.

Chatwin, P.C. and Allen, C.M. , 'Mathematical models of dispersion in rivers and estuaries ' , Ann. Rev. Fluid Mechanics , 1985 .

Chatwin,P.C. and Sullivan, P , 'The structure and magnitude of concentration fluctuations' ,Boundary Layer Meteorology 62, 1993.

Clifford, N. , French, J.R. and Hardisty (Eds.) 'Turbulence: Perspectives on flow and sediment transport', Wiley. 1993.

Cokljat, D, 'Mathematical modelling of turbulent flows in tw stage channels', Transfer report, Dept. Engrg., City University, March 1991.

Cotton, A.P. and West, J.R. 'Field measurement of transverse diffusion in unidirectional flow in a wide, straight channel', Wat. Resour. Res. 14, 1980.

Dagpunar, J. 'Principles of random variate generation', Oxford science publications, 1990.

Daziel,S.B. , 'Decay of rotating turbulence : some particle tracking experiments', submitted to Dynamics of Atmos. and oceans , May 1992.

Demuren, A.O. and Rodi, W 'Calculation of flow and pollutant dispersion in meandering channels', J.Fluid. Mechs. vol. 172, 1986.

Durbin, P.A. 'A random flight model of inhomogeneous turbulent motion' Phys. of Fluids, vol 23, 1980.

Elder, J.W., 'The dispersion of a marked fluid in turbulent shear flow', J. Fluid mechs., vol 5 , p. 544-560, 1959.

Elhadi,N. , Harrington,A. , Hill,I , Lau,Y.L. ,Krishnappan, B.G. , ' River - A state of the art report ' , Can. J. Civ. Eng. vol. 11 ,1984.

Engelund, F, 'Dispersion of floating particles in uniform channel flow', 1969, Jn. Hydr. Div., ASCE 95, no Hy4, p1149-1162.

Ferro,V. Balamonte,G. 'Fow velocity profiles in gravel bed rivers', J.Hydr. Engrg. vol 120, 1994.

Fischer, H.B. 'Longitudinal dispersion and turbulent mixing in open channel flows',Ann.Rev. Fluid Dyn. , vol 5, 1973.

Fischer, H.B. et al. 'Mixing in inland and coastal waters' , H.; Academic Press 1979.

Frisch, U. , Hasslacher, B. , Pomeau, Y. ' Lattice gas automatafor the Navier-Stokes equation', Phys. Rev. Letters, vol. 56, no. 14.

Frisch,U and Orszag,S 'Turbulence: challenges for theory and experiment', Physics Today, Jan 1990

Guymer, I ,Brockie, N , Allen, C.M. , Beven, K. Hydraulics Research - SERC flood channel facility . 'Straight flood channel dispersion tests' . Dept. Civil. Engrg. , Herriot Watt University, Edinburgh ,1989 .

Grant, H.L., Stewart, R.W. , Moillet,A , 'Turbulence spectra from a tidal channel' , Jn. Fluid Mechanics 12, 1962. p 241.

Hansen, E. 'Lagrangian characteristics of surface turbulence', 1972, Jn. Hydr. Div. ASCE 98, no. HY7, p1255.

Heathershaw,A.D. , 'The turbulent structures of the bottom boundary layer in a tidal current', Geophys. J.R. Astr. Soc., 58, 1979

Heslop, S. ,Allen, C.M. , 'Modeling contaminant dispersion in the River severn using a random walk model' , J. of Hydr. Research vol 31(3) ,1993.

Holland, M.J. Allen, C.M. , Heslop,S.E. , Beven, K.J.B.. 'Detailed analysis of turbulence data and flow structures on the river Severn' , final report I.E.B.S. Lancaster University . 1989

Holley, E.R. 'Transverse mixing in rivers', Rep. S132, Delft Hydr. lab. , Delft , Netherlands, 1971

Holley, E.R. , Siemons, ,J. and Abraham, G. 'Some aspects of analysing transverse dispersion in rivers', J. Hydr. Res. ,vol 10(1) ,1972

Holly, M. Jr., Nerat, G. 'Field calibration of Stream-tube dispersion model', Jn. Hydr. Engrg. vol.109, no.11, 1983.

Hoogerbrugge, P.J. , Koelman, J.M.V.A.'Simulating microscopic hydrodynamic phenomena with dissipative particle dynamics.', Europhys. Lett. , 19(3) pp155-160, 1992.

Kelsey, A. ,'Sediment transport modelling', Thesis. Dept. Env.Science, Lancaster,1994.

Kinzelbach, W. , ' Particle tracking methods and fractal statistics in groundwater modelling ' , from ' Modelling and application of transport phenomena in porous media ' , Von Karman inst. for fluid dynamics ' , 1990.

Knight, D.W. and Samuels, P.G., Shiono, K. 'River flow simulations : Research and Developments', J. IWEM,4, 1990.

Knight, D.W. and Shiono,K, ' Turbulence measurements in a compound overbank flow', Jn. Hydr. Research , vol.28 no.2 1989.

Krogstadt,P.A. Antonia, R.A. Browne, L.W.B. ,'Comparison between rough and smooth-wall turbulent boundary layers', J. Fluid Mechs., March 1992.

Lau, L., Krishnappan, B.G. 'Modelling Transverse mixing in natural streams', Jn. of the Hydr. Div. , vol 107, 1981.

Ley, A.J, 'A random walk simulation of two dimensional turbulent diffusion in the neutral surface layer', Atmos. Envir. vol. 16 no.12 ,1982.

Lovejoy, S and Schertzer,D. 'Multifractals in Geophysics' , AGU Spring Meeting, Montreal: May, 1992. One day seminar.

Luchik, T.S. , Tiederman, W.G. ' Timescale and structure of ejections and bursts in turbulent channel flows', J. Fluid Mechs. , 174, p529-552, 1987.

Lu,S.S. and Willmarth, W.W. 'Measurements of the structure of the Reynolds stress in a turbulent boundary layer', Jn. Fluid Mechs. vol.60 p 481 , 1973.

Mandelbrot,B.B , 'A fast fractional Gaussian noise generator' , vol. 7 ,no.3 Water Resour. Res. ' , 1971.

Marcus, D.L., Bell, J.B. 'Numerical simulation of a viscous vortex ring interaction with a density interface', Phys. of Fluids, 6(4) , April, 1994

Matalas, N.C. 'Introduction to random walk theory and its application to open channel flow', Research Hydrologist, U.S. Geological survey, Washington D.C. ,U.S.A.

McComb, W.D. 'The physics of fluid turbulence', Oxford Science publications, Clarendon Press, 1991.

Morgan, A.J. 'Initial mixing in an upland reach of the River Lune near Tebay in Cumbria', Msc. dissertation, I.E.B.S. Lancaster University. 1993 .

Moser,R.D. ' Kolmogorov inertial range spectra for inhomogeneous turbulence', Phys. of Fluids 6(2), p794 , Feb. 1994.

Mullen, P., 'Measurement of three dimensional turbulent velocity fluctuations', Undergraduate dissertation, I.E.B.S. Lanster University, 1993.

NAG- The NAG Fortran library manual, mark 12, (The numerical algorithms group ltd.) 1987.

New Scientist 'Over bank flow flood relief' , 8th Jan. 1994.

Perkins, P.J. , Hunt, J.C.R. 'Particle tracking in turbulent flows', Advances in turbulence 2, Springer-Verlag, Heidelberg 1989.

Rapaport,D.G. and Clementi, E. 'Eddy formation in obstructed fluid flow: a molecular dynamics study', Phys. Rev. Letters, vol.57, no.6., 11/8/86.

Raupach, M.R. Antonia, R.A. Rajagopalan, 'Rough wall turbulent boundary layers' , Appl.Mech. Rev. ,44, no.1, Jan 1991.

Reid,J.D. 'Markov chain simulations of vertical dispersion in the neutral surface layer for surface layer and elevated releases ' , Boundary Layer Meteorology 16 3-22,1979.

Reynolds, O ; Phil. trans. R. Soc. Lond. 174, p935-82, 1883.

Rutherford, J.C. 'River mixing', Wiley, 1994.

Sawford,B.L. 'Lagrangian Statistical Simulation of concentration mean and fluctuation fields', Jn. of App. Meteorlogy, 24 ,1985.

Sawford, B.L. ' Recent developments in the Lagrangian stochastic theory of turbulence dispersion' , 1993a, Bound. Lay. Met. , vol 62, p.197.

Sawford, B.L. , Borgas, M.S. 'On the continuity of stochastic models for the Lagrangian velocity ' , Physica D (special issue) 'Chaotic advection , tracer dynamics and tubulent dispersion ' , 1993b.

Sawford, B.L. , Borgas, M.S. , 'Stochastic equations with multifractical random increments for modelling turbulent dispersion ' , Physics of Fluids , 6 (2) Feb. 1994.

Shiono,K and W.Knight, W. ,' Turbulent open channel flows with variable depth across the channel - a general model and new data ' , Jn. Fluid Mechs. , vol. 222, Jan 1991.

Shiono,K and W.Knight, W. , 'Mathematical models of flow in two or multistage straight channels' ; International Conference on River Flood Hydraulics ,17-20 Sept . 1990.

So, R.M.C. , Lai, Y.G. , Zhang, H.S. 'Second order near-wall turbulence closures: a review', A.I.A.A. Journal. vol 29 no.11, 1991.

Somlyody,L 'An approach to the study of transverse mixing in streams', Jn.Hydr.Res.,20 1982.

Speziale ,C.G. 'Reynolds-Stress closures in turbulence' , Jn. of Fluid Mechs.,107-153 1985.

Sullivan, P.J 'Insantaneous velocity and length scales in a turbulent shear flow' , Advances in Geophysics, 1974.

Sugimoto, D. 'A pipeline approach to many body problems', Physics world, nov. 1993, p32.

Tampieri ,F ,Scarani,C , Giostra,U , Brusasca,G , Tinarelli,G , Anfossi,D and Ferrero,E ; 'On the application of random flight dispersion models in inhomogeneous turbulent flows ', Ann. Geophysicae , 749-758, 1992.

Taylor, G.I. 'Diffusion by continuous movements', procs. of the London Math. Soc., ser 2, vol.20, 1921.

Taylor, G.I. 'Spectrum of turbulence', procs. Roy. Soc. London, Ser. A, Vol.219 p.476, 1938.

Taylor, G.I. 'The dispersion of matter in turbulent flow through a pipe', Procs Roy. Soc. , vol. 223, p446-68, 1954.

Tennekes, H, Lumley, J.L., 'A first course in turbulence', MIT Press, Cambridge, MA 1972.

Thomson, 'Criteria for the selection of stochastic models of particle trajectories in turbulent flows', Jn. Fluid Mechs., vol 180, 1987.

Tominaga,A and Nezu,I. , 'Turbulent structure in compound open channel flows ' , A. Jn. Hydr. Egrg. , vol 117 ,no.1 1990.

Tominaga,A and Nezu,I et al., 'Three dimensional turbulent structure in straight open channels' ; Jn. of Hydraulic Res. , 27 1989.

Tritton, D.J. 'Physical Fluid Dynamics', 2nd ed. ,Oxford Science Publications, 1990

Van Dam, G.C. 'The study of shear dispersion in tidal waters by applying discrete particle techniques', technical paper, Rijkswaterstaat, P.O. Box 20907, Tidal waters division, The Hague, Holland, 1992.

Van Dop,H. Nieuwstadt, F.T.M , Hunt, J.C.R. 'Random walk models for particle displacements in inhomogeneous unsteady turbulent flows ' , Physics of Fluids,28(6) June 1985.

Wang, L.P. and Stock, D.E. 'Stochastic trajectory models for turbulent diffusion: Monte Carlo process versus Markov chains', Atmos. Environment. vol 26a (1992).

Wallis, S.G., Blakeley, C and Young, P.C. 'A microcomputer-based fluorometric data logging system for flow and dispersion measurements', Jn. Inst. Water Eng. and Scientists. vol. 41 1987.

West, J.R., Cotton, A.P., 'Field measurement of transverse diffusion in unidirectional flow in a wide straight channel', Water Research, vol. 14, 1980.

Williams, J.J. , Thorne, P.D. , Heathershaw, D., 'Measurements of turbulence in the benthic boundary layer over a gravel bed' , Sedimentology36, p956, 1989.

Wilson, J.D. and Zhuang,Y.,'Restriction on the timestep to be used in stochastic lagrangian models', Boundary Layer Met., 49, 1989.

Yotsukura, N and Cobb, 'Transverse diffusion of solutes in streams, U.S. Geol. Surv. Prof. paper No. 582-C , 1972

Yotsukura, N, Fischer,H.B., Sayre, W.W., 'Measurements of mixing characterisics of the River Missouri between Sioux City, Iowa and Plattsmouth, Nebraska', U.S. geological survey paper, 582-c. 1970.

Yotsukura, N. , Sayre, W.W. , 'Transverse mixing in natural channels', Water Resour. Res. , vol 12 no.4 , 1976.

Young,A.D.'Boundary Layers',B.S.P. Professional books. Page 144. 1989.

Younis,B. , Proceedings of I.A.H.R. meeting : ' Is turbulence modelling any use ? ',1992.

Zannetti, P. 'Air pollution modeling' , Computational mechanics publications ,1990a.

Zannetti, P.'Computer simulation using particle modelling', procs. particle tracking course, 23/11/ 1990b, Southhampton.